DISSERTATION

Studies on the nonlinear beam dynamics for future particle colliders

Ausgeführt zum Zwecke der Erlangung des akademischen Grades eines Doktors der technischen Wissenschaften unter der Leitung von

Privatdoz. Dipl.-Ing. Dr.techn. Michael Benedikt

Atominstitut (E141) und

European Organization for Nuclear Research (CERN)

eingereicht an der Technischen Universität Wien

Fakultät für Physik

von

Dipl.-Ing. Michael HOFER, BSc

[redacted]

[redacted]

Wien, am 15.05.2023

TECHNISCHE UNIVERSITÄT WIEN

Abstract

Studies on the nonlinear beam dynamics for future particle colliders

by Dipl.-Ing. Michael HOFER, BSc

Particle colliders serve as unique tools to study constituents of matter and understand their interactions. For studying rare events, the collision energy of the particle beam is key in determining which events can be observed, while the achievable collision rate gives the number of observable events during the operation time of the machine. Naturally, current and future collider designs have aimed for ever-increasing collision rates to accurately study rare events with high statistical significance. Beam losses are detrimental to the performance due to reducing the number of potential colliding particles. Such losses may be generated by amongst others nonlinear magnetic fields, introduced either by errors or to counteract other beam loss mechanisms. A good understanding of the impact of those fields and their interplay is thus critical as means to study mitigation measures that help increase the collider performance.

In this thesis, studies on the impact of such nonlinear fields on the beam dynamics have been conducted with focus on issues in potential future colliders. Simulations were conducted for such a future collider design to define tolerances on the magnetic field errors. To benchmark these simulations, experiments in currently running machines were conducted where errors have been artificially introduced. A theory was developed to quantify the interplay between different effects in order to help explain observations made during the operation of the Large Hadron Collider at CERN. Further measurements have been conducted at the IOTA accelerator at Fermilab to quantify the impact of sextupole fields on the beam dynamics.

TECHNISCHE UNIVERSITÄT WIEN

Zusammenfassung

Studies on the nonlinear beam dynamics for future particle colliders

von Dipl.-Ing. Michael HOFER, BSc

Teilchenbeschleuniger sind unentbehrliche Instrumente um die Zusammensetzung von Materie und ihre Wechselwirkungen zu studieren. Entscheidend für die Studie von seltenen Prozessen sind vor allem die Kollisionsenergie, ausschlaggebend für welche Vorgänge beobachtbar sind, sowie die Kollisionsrate, welche die Anzahl der möglichen beobachtbaren Vorgänge während der Laufzeit des Beschleunigers angibt. Gegenwärtig laufende und mögliche zukünftige Collider Projekte streben höhere Kollisionsraten an um seltenere Vorgänge mit hoher statistischer Signifikanz zu untersuchen. Durch übermäßigen Verlust von Teilchen wird die Kollisionsrate verringert, wodurch die Leistungsfähigkeit eingeschränkt wird. Teilchenverluste können unter anderem durch nichtlineare Magnetfelder verursacht werden, welche durch Feldfehler eingeführt werden können, aber auch um andere Verlustmechanismen zu unterbinden. Als solches ist ein gutes Verständnis von den Auswirkungen die diese Felder haben sowie deren Wechselwirkungen wichtig um mögliche Gegenmaßnahmen zu studieren, welche die Leistungsfähigkeit des Beschleunigers verbessern können.

In dieser Arbeit werden Studien über den Einfluss von nichtlinearen magnetischen Feldern auf die Strahldynamik präsentiert, mit Fokus auf Probleme in möglichen zukünftigen Beschleunigern. Simulationen für ein Colliderdesign wurden durchgeführt um Feldfehlertoleranzen zu definieren. Um die Glaubwürdigkeit dieser Simulationen zu beurteilen, wurden Experimente in einem gegenwärtig laufenden Beschleuniger durchgeführt, in welchen künstlich Feldfehler eingeführt wurden. Eine Theorie wurde entwickelt um die Wechselwirkung zwischen verschiedenen Effekten zu quantifizieren und um Beobachtungen im Large Hadron Collider am CERN zu erklären. Weitere Messungen wurden am IOTA Beschleuniger am Fermilab durchgeführt um den Einfluss von Sextupolefeldern auf die Strahldynamik festzustellen.

Contents

List of Figures

List of Tables

Introduction

Driven by the research of the nature of the atoms and its constituents and the need for high energy particles to probe matter, the field of particle accelerator physics has evolved significantly since its inception in the 1930s. With each new particle collider generation shattering records held by its predecessors, either in terms of collision energy, size, or collision rate, major advances in particle physics became possible, such as the discovery of the Higgs-Boson in the LHC or the top-quark in the Tevatron. While still an essential tool for particle research, particle accelerators also increasingly play an important role in other fields, such as cancer therapy, as a source of synchrotron radiation for spectroscopy, or as driver for a nuclear reactor. The wide range of applications for particle accelerators has also spawned multiple different accelerator types with differing design principles.

One particular important design principle is based around the idea of alternating-gradient focusing, proposed by E. Courant, M. Livingston, and H. Snyder and independently by N. Christofilos [1]. This proposal has led to the focusing and steering component being handled by separate magnetic elements, whereas in the constant-gradient focusing approach used before both tasks had to be accomplished by shape of the guiding magnetic field. The new approach enabled for stronger focusing and hence smaller beams, in turn reducing the need for large aperture magnets, which in the end allowed for larger synchrotrons, achieving energies previously thought unattainable. In the developed theory of the alternating-gradient synchrotron, only elements with a magnetic field linear in the displacement to the origin are taken into account, in turn ideal machines consisting only of dipole and quadrupole magnets. As such, the stability of the particle motion can easily be inferred via methods derived from linear algebra.

However, in the pursuit of higher energy, higher intensity particle accelerators, the presence of nonlinear elements such as sextupoles has become inevitable. The presence of such magnets may be by design to allow to compensate for effects that could lead to a severe loss of particles, such as the electromagnetic interaction of the particle beam with machine elements potentially leading to collective instabilities, or erroneously introduced via effects such as misalignments. While itself posing as a valuable resource to correct for effects that could cause particle loss and may end up as intensity limitation, nonlinear magnetic elements itself are also able to induce unbounded motion of particles which then may be lost. Unlike the previous case of the linear beam optics theory, given the initial conditions of the particle trajectory, at present, the stability of motion in the presence of strong nonlinear fields cannot be analytically determined. In the absence of a general solution of this problem, a plethora of tools and methods have been developed in the past to analyse specific scenarios and identify individual solutions.

In this thesis, studies on the single-particle transverse dynamics are presented, focusing in particular on the effects of nonlinear magnetic fields on the particle motion.

The focus lies on assessing the issues these fields might pose for the next generation of particle accelerator.

In Chapter 1, a brief overview of particle collider currently in operation and plans for the next generation is given. Chapter 2 then highlights beam dynamics aspects relevant for the following chapters. Studies on the impact of magnetic field errors on the beam dynamics for one of the potential successors to the LHC, an energy upgrade named the HE-LHC, are described in Chapter 3. Inspired by the situation faced in the previous chapter, an experimental study has been conducted in the LHC and its analysis and results are presented in Chapter 4. In the following Chapter 5, a theory is developed and presented on the interplay between (non-)linear magnetic fields and coupling between the transverse planes and benchmarked against simulations. Further experimental studies aiming to quantify the impact of nonlinear fields on the beam dynamics are presented in Chapter 6 for the case of an accelerator based on an evolution of the alternating-gradient synchrotron, incorporating nonlinear fields not as a perturbation but as main component to allow for nonlinear bounded motion.

Chapter 1

The particle collider landscape and its future

This chapter aims to provide a brief overview over the particle colliders either in operation or in planning at the time of writing, of which some were studied in detail as part of this thesis. First, an overview over the timeline and technical aspects of the Large Hadron Collider (LHC) will be presented, followed by a description of its planned upgrade, the HL-LHC. In the following section, the colliders studied as part of the Future Circular Collider (FCC) study, which provide the framework in which this thesis was written under, are discussed. In the last section, other collider projects will be briefly introduced, to which some of the concepts and problems treated in this thesis may also apply.

1.1 LHC and HL-LHC

The earliest idea of the LHC can be traced back all the way to the design phase of its predecessor, the Large Electron Positron Collider (LEP), in the 1970s [2]. Here, the design of the to date highest energy lepton collider was chosen such that eventually the same tunnel can be reused to later on host an hadron collider, in this case for colliding two protons beams. Midway through the runtime of the LEP, which began in 1989 and ended in 2000 [3, 4], the LHC was approved in 1994 by the CERN Council, not long after the competing Superconducting Super Collider (SSC) in the United States of America was canceled [5]. First beam was injected in the LHC in 2008 [6], and with the first collision data taking during run I commencing in 2009 [7]. With a design center of mass energy of 14 TeV, the LHC exceeds the previous record holder, the Tevatron, by about a factor 7 [8]. This energy reach allows to study the standard model of particle physics at an unprecedented level, which eventually allowed the discovery of the Higgs Boson [9, 10]. These observations were reported by the two high-luminosity experiments ATLAS [11] and CMS [12] in the LHC, which are complemented by two further experiments, ALICE [13] and LHCb [14].

In order to extend the discovery potential of the LHC, the High Luminosity LHC (HL-LHC) project was launched in 2010 [15]. Its aim is to increase the luminosity of the LHC by a factor 5, relying on, amongst other factors, on the use of crab cavities and the installation of superconducting magnets featuring an increased peak field of around 11 T, made possible by the use of Nb_3Sn instead of NbTi as superconductor. Operation is projected to start around 2026, running for about 15 years [16], with the center of mass collision energy of the HL-LHC remaining at 14 TeV.

1.2 Future Circular Collider study

Following the update provided by the European Strategy Group for Particle Physics in 2013 and its full support by the CERN Council [17, 18], the Future Circular Collider study was launched in 2014 to study the design of accelerators for a post-LHC era. Hosted by CERN, the study combines efforts from over 136 institutes and 32 companies from 34 different countries, covering a range of aspects such as accelerator design, hardware development, and implementation studies [19]. Circular collider scenarios studied fall into three categories: hadron-hadron collider, lepton-lepton collider, and lepton-hadron collider.

The two hadron collider scenarios investigated as part of the FCC study are the High Energy LHC and FCC-hh, both aiming to achieve proton-proton collision at a center of mass energy energy far above the 14 TeV from the LHC. The HE-LHC aims to do so by using new dipole magnets using Nb_3Sn as superconductor and with a field strength of 16 T compared to the 8.33 T of the LHC dipoles, which should allow to reach a collision energy of 27 TeV while reusing the LHC tunnel. The FCC-hh on the other hand would be hosted in a new tunnel in the Geneva Basin, which has a circumference of about 100 km and together with the 16 T dipoles would allow to reach a center of mass energy of 100 TeV. The same 100 km may be used also to host an electron-positron collider, referred to as the FCC-ee, with multiple operational collision energies ranging from 90 GeV to 365 GeV envisaged to study in detail specific processes, exceeding the 209 GeV reached in the last year of LEP operation [20]. Similar to case of the LEP and LHC, the FCC integrated project aims to build the FCC-ee first and later on install the FCC-hh in the same tunnel [21]. The last option, the FCC-eh, is intended to work alongside the FCC-hh by colliding one of the proton beams with an electron beam coming from an outside energy recovery linac.

The studies on the design of these four machines and associated particle physics opportunities over a 5 year span have been compiled into four conceptual design reports [22–25] to serve as input to the 2020 update of the European Strategy for Particle Physics. Following the recommendation of further investigating technical and financial feasibility of both a future hadron collider with a center of mass energy of about 100 TeV and a preceding electron-positron collider, further studies are conducted as part of the Future Circular Collider Innovation study to serve as input for the 2025 update of the European Strategy for Particle Physics [26].

1.3 Other collider projects

Similar particle collider studies at the forefront of the energy frontier are not only being pushed at CERN, but also at other accelerator laboratories.

One such study, similar to the FCC-ee, focuses on the Circular Electron Positron Collider (CEPC), a lepton collider which targets to collide at center of mass energies of up to 240 GeV [27]. Led by the Institute of High Energy Physics of the Chinese Academy of Sciences, the installation of this double-ring collider is currently planned to take place in China. Similar to the case of the FCC integrated project, the CEPC tunnel may later on be reused to host a hadron collider, called the Super Proton Proton Collider (SppC), with an initial center of mass energy of 75 TeV. Unlike the FCC-hh with its 16 T, Nb_3Sn dipoles, the preliminary dipole designs for the SppC foresee the use of iron based high temperature superconductors, initially

reaching a field strength of 12 T. Later upgrades may then push the field strength to 20 T to 24 T, which would allow to increase the center of mass energy to 125-150 TeV.

Due to the significant energy loss from synchrotron radiation at collision energies above those of the FCC-ee or CEPC, accelerator studies for machines able to achieve these higher energies focus on linear colliders. Two design studies, both part of the Linear Collider Collaboration, have been brought forward. One of the key differences between the two machines is the use of different accelerating technologies. The International Linear Collider (ILC) is a design for a linear electron positron collider with a center of mass energy of 250 GeV [28], which could be extended up to 1 TeV [29]. Its design is based on the use of superconducting RF-cavities made out of Nb_3Sn. The Compact Linear Collider (CLIC) on the other hand is based on the use of a two-beam acceleration scheme, with collision energies ranging from 380 GeV in the initial operations phase up to 3 TeV in the ultimate stage [30]. In this two-beam acceleration scheme, the main beam is accelerated in normal conducting cavities by the power extracted from a secondary, low-energy, high-charge beam.

A similar concept to the LHeC [31] and the FCC-eh is the proposal of the EIC, a dedicated electron ion collider building on the already existing and running Relativistic Heavy Ion Collider (RHIC) [32]. The design foresees collision of polarized, 15.9 GeV electrons, delivered by an Energy Recovery Linac, with either polarized, 250 GeV protons or heavy ions such as to fully stripped, 100 GeV/u Uranium- or Gold-ions. Unlike the FCC-eh or LHeC, collisions in the EIC are possible in two interaction regions, made possible by putting the recirculating rings in the same tunnel as the RHIC.

Other accelerator facilities already under construction are the NICA accelerator complex [33] in Dubna, Russia and the Facility for Antiproton and Ion Research [34] at the GSI Helmholtz Centre for Heavy Ion Research in Germany. The former allows colliding one ion beam with either an ion or proton beam or for extraction of the ion beam to a fixed target station, whereas the latter aims to provide beams ranging from (anti-)protons up to uranium over a wide range of energies and intensities to various further storage rings or to target stations.

Lastly, at Fermi National Accelerator Laboratory as part of the Long Baseline Neutrino Experiment, studies are undertaken to high power proton beams to a fixed target station. With the currently ongoing upgrades to reach the targeted beam power of 1.2 MW, put forward in Proton Improvement Plan-II (PIP-II) [35], further studies are undertaken using a new Rapid Cycling Synchrotron to achieve an eventual beam power of 2.4 MW [36]. Amongst other key factors for this machine is the use of nonlinear integrable optics [37] to ensure suppression of transverse instabilities while keeping particle losses due to chaotic motion at a minimum, a concept which is currently being tested at the IOTA accelerator at FNAL [38].

Chapter 2

Theory of beam physics

In this chapter the main concepts of accelerator beam dynamics relevant for the following chapters is introduced. For a more extensive discussion on these topics, the reader is referred to standard textbooks such as [39–43] as well as the proceedings of CERN Accelerator Schools, which were also the basis for the following introduction.

2.1 Coordinate System

The motion of a single particle in a circular accelerator is most commonly described by a co-moving Frenet-Serret coordinate system, characterized by (x, y, z). These coordinates are defined with respect to an ideal particle traveling on a reference orbit with a design momentum p_0 and a location s along the path. The coordinate z is tangent to the reference orbit, with x and y perpendicular to z and referring to the transverse offset of a given particle. The location of a particle in phase space is then fully described by these coordinates and the associated momenta p_x, p_y, and p_z. An orbit which closes upon itself is termed a closed orbit, that is, after a given number of revolutions n which is usually $n = 1$, the particle arrives at the initial location s_0 with the same transverse offset and momentum,

$$x(s_0 + nC) = x(s_0), \tag{2.1}$$
$$p_x(s_0 + nC) = p_x(s_0), \tag{2.2}$$
$$y(s_0 + nC) = y(s_0),$$
$$p_y(s_0 + nC) = p_y(s_0),$$

with C the circumference of the circular accelerator. Usually, one defines a reference orbit, that is, the closed orbit of the machine neglecting any errors such as misalignments. In most accelerator designs, the reference orbit passes through the magnetic center of each element and is only defined by the dipole magnets with a local radius of curvature $\rho(s)$ depending on the dipole field strength. Usually, bending only occurs in one transverse plane, which is commonly taken to be in x.

2.2 Guiding Force

The preference to use dipole magnets over electrostatic elements in accelerators to guide relativistic particles ($v \simeq c$) can be seen by looking at the Lorentz force

$$\vec{F} = \frac{d\vec{p}}{dt} = q\left(\vec{E} + \vec{v} \times \vec{B}\right), \tag{2.3}$$

where $\vec{E}$ is the electrical field, $\vec{v}$ the velocity of the particle and $\vec{B}$ the magnetic field. While magnetic fields with a strength of above 1 T have been easily achieved by electromagnets in the past, an equivalent electric field with a strength of $3 \cdot 10^8$ Vm^{-1} is currently not achievable due to vacuum breakdowns [44], making magnetic fields the sole option. In the absence of any transverse steering electric fields and for a circular orbit, the Lorentz force is equal to the inertial force, which gives

$$B\rho = \frac{p}{q} \tag{2.4}$$

where $B = B_y$ is the field strength perpendicular to the bending plane, ρ then bending radius, p the particle momentum, and q the charge of the particle. The term $B\rho$ is also commonly called the beam rigidity. Equation 2.4 also illustrates that in synchrotrons, where the bending radius is fixed, the magnetic field strength needs to follow synchronously the particle momentum to keep the particles on the same orbit. In turn, the maximum particle energy a synchrotron can achieve is then defined by its radius and the maximum field strength that can be achieved by the dipoles.

2.3 Equations of motion

To describe the motion of a particle under the influence of external forces in a general way, the Hamilton equations

$$\frac{dx}{dt} = \frac{\partial H}{\partial p_x}, \frac{dy}{dt} = \frac{\partial H}{\partial p_y}, \frac{dp_x}{dt} = -\frac{\partial H}{\partial x}, \frac{dp_y}{dt} = -\frac{\partial H}{\partial y} \tag{2.5}$$

are used, where the system is described by Hamiltonian H, x, y being the canonical coordinates and $p_{x,y}$ the conjugate momenta, and t the time. Assuming that no electric fields ϕ are present, the Hamiltonian of a relativistic particle inside an accelerator is then given by

$$\begin{aligned} H(x, p_x, y, p_y, \delta_p, ct, s) &= \left(1 + \frac{x}{\rho}\right) \times \\ &\left[\frac{q}{p_0} A_z(s) + \sqrt{(1+\delta_p^2) - \left(p_x - \frac{q}{p_0} A_x(s)\right)^2 - \left(p_y - \frac{q}{p_0} A_y(s)\right)^2}\right], \end{aligned} \tag{2.6}$$

where $\delta_p = \frac{p_z - p_0}{p_0}$ is the relative momentum deviation from the reference momentum p_0, A_u the vector potential in the plane $u \in \{x, y, z\}$. Often, a hard edge model is assumed, that is, the field strength between different strength elements jumps abruptly. By neglecting these transition areas called fringe fields, A_x and A_y are $A_x = A_y = 0$ and by further assuming $p_z \gg p_x$ and $p_z \gg p_y$, the square root in the

Hamiltonian 2.6 is then expanded, yielding

$$H(x, p_x, y, p_y, s) = -\left(1+\frac{x}{\rho}\right)\left[1+\delta_p - \frac{p_x^2+p_y^2}{2(1+\delta)} + \frac{q}{p_0}A_z(s)\right]. \tag{2.7}$$

For a region free of magnetic field, commonly referred as drift space, $A_z = 0$, and the Hamiltonian for a drift space is expressed as

$$H(x, p_x, y, p_y, s) = \sqrt{(1+\delta_p^2) - p_x^2 - p_y^2} \approx \frac{p_x^2+p_y^2}{2(1+\delta)}. \tag{2.8}$$

Here, the first equality is the exact Hamiltonian for a drift space based on Eq. 2.6, whereas the second is based on the approximate Hamiltonian from Eq. 2.7.

In a region free of currents, the vector potential A_z can be written as the following multipolar expansion

$$\frac{q}{p_0}A_z(s) = -\Re\sum_{n=1}^{\infty}\frac{1}{n}[K_n(s)+iJ_n(s)](x+iy)^n, \tag{2.9}$$

with $n = 1$ corresponding to a dipole. Using $\vec{B} = \nabla \times \vec{A}$, the magnetic field can then be written in complex form

$$B_y(x, y, s) + iB_x(x, y, s) = \sum_{n=1}^{\infty}[K_n(s)+iJ_n(s)](x+iy)^{n-1}, \tag{2.10}$$

where the coefficients K_n and J_n represent the strength of the multipole component and are defined as

$$K_n(s) = \frac{1}{B\rho(n-1)!}\frac{\partial^{n-1}B_y}{\partial x^{n-1}} \tag{2.11}$$
$$J_n(s) = \frac{1}{B\rho(n-1)!}\frac{\partial^{n-1}B_x}{\partial x^{n-1}}.$$

For the case of an on-momentum particle ($\delta_p = 0$) in a normal quadrupole ($\rho = \infty$), the Hamiltonian from Eq. 2.7 is then (neglecting constant terms as they will not affect the equations of motion)

$$H(x, p_x, y, p_y, s) = \frac{p_x^2+p_y^2}{2} + K_2(s)\frac{x^2-y^2}{2}. \tag{2.12}$$

2.4 Hill's equation and Twiss parameters

Using the Hamiltonian for a quadrupole from Eq. 2.12 together with Hamilton's equations, stated before in Eqs. 2.5, whilst switching the independent variable from t to s, one obtains the following equation

$$\frac{d^2u}{ds^2} + K_2(s)u = 0,\ u \in \{x, y\}. \tag{2.13}$$

Note that by choice of the Hamiltonian here only the focusing from quadrupole magnets is taken into account. An additional weak focusing term $(1/\rho(s)^2)$ in the bending plane is obtained from dipole magnets.

For a circular accelerator, the focusing $K_2(s)$ constitutes a periodic function

$$K_2(s) = K_2(s + C) \tag{2.14}$$

with a period of C, which is the circumference of the accelerator. With the constrain 2.14, Eq. 2.13 now constitutes the well known Hill's equation. The solution for Hill's equation are found to be

$$\begin{aligned} u(s) &= \sqrt{2J_u\beta_u(s)}\cos\left(\psi_u(s) + \psi_{u,0}\right) \\ u'(s) &= -\frac{\sqrt{2J_u}}{\beta_u(s)}\Big[\alpha(s)\cos\left(\psi_u(s) + \psi_{u,0}\right) + \sin\left(\psi_u(s) + \psi_{u,0}\right)\Big], \end{aligned} \tag{2.15}$$

which describes a the pseudo-harmonic oscillation of a particle around the reference orbit. Here, $'$ indicates a derivative with respect to s, that is $\frac{\delta}{\delta s}$. J_u is the action of a particle and a constant of motion, and together with the phase-offset $\psi_{u,0}$ make up the initial conditions of a particle. The betatron-function $\beta_u(s)$ is the position dependent oscillation amplitude and a sole property of the accelerator lattice. The term $\sqrt{2J_u\beta_u(s)}$ describes the maximum amplitude of a particle at a given position s. The α-function is defined as $\alpha_u(s) = -\frac{\beta_u'(s)}{2}$, which together with the β-function and γ-function $\gamma_u(s) = \frac{1+\alpha_u^2(s)}{\beta_u(s)}$ make up the so-called Courant-Snyder parameters. The phase-advance $\psi_u(s)$ relates to the β-function via

$$\psi_u(s) = \int_{s_0}^{s} \frac{d\tau}{\beta_u(s)}\,. \tag{2.16}$$

The phase-advance over the whole accelerator ring, divided by 2π, is called the tune Q_u

$$Q_u = \frac{1}{2\pi}\oint \frac{d\tau}{\beta_u(s)}\,, \tag{2.17}$$

and gives the number of betatron oscillations per revolution.

Combining the equations from Eq. 2.15 and solving for $2J_u$, one obtains

$$\gamma_u(s)u(s)^2 + 2\alpha_u(s)u(s)u'(s) + \beta_u(s)u'(s)^2 = 2J_u. \tag{2.18}$$

For a given location s, this equation describes an ellipse in trace space u, u', fully determined by the parameter $\beta_u, \alpha_u, \gamma_u$ and the action J_u, as is illustrated in Fig. 2.1.

The position of a particle with a given action J_u on the ellipse will change turn-by-turn depending on the tune Q_u of the accelerator. Given the dependence on the optics functions, the shape and orientation of the ellipse varies around the ring, while the area remains constant.

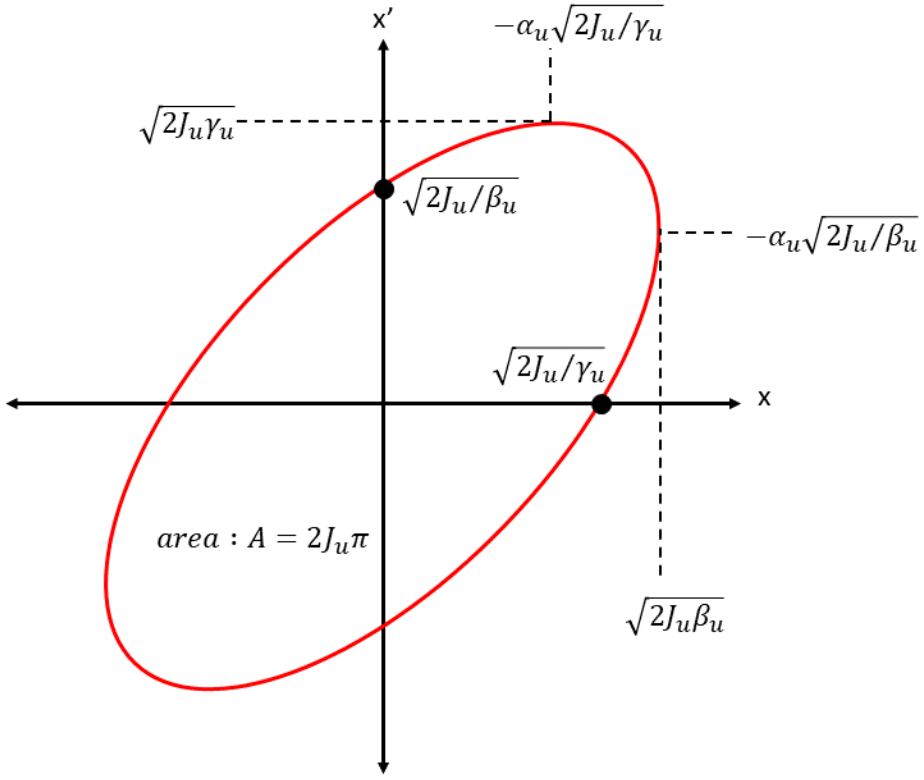

FIGURE 2.1: Ellipse in trace space diagram described by the Courant Snyder parameter $\beta_u, \alpha_u, \gamma_u$ and the action J_u.

2.5 Transfer maps

With the Hamiltonian of an element of given length and strength, a transfer map $\mathcal{M}$ can be defined, which allows to express the final coordinates as polynomial functions of the initial coordinates. As example, for the coordinate $q \in \{x, p_x, y, p_y\}$ the propagation from point s_0 to s_1 as a Taylor series is

$$q(s_1) = q(s_0) + (s_1 - s_0)\frac{dq}{ds} + \frac{(s_1 - s_0)^2}{2}\frac{d^2q}{ds^2} + \cdots = \sum_{n=0}^{\infty}\frac{(s_1 - s_0)^n}{n!}\frac{d^nq}{ds^n}. \tag{2.19}$$

The total derivative $\frac{dq}{ds}$ can then be rewritten as a function of the Hamiltonian H, using

$$\begin{aligned}\frac{dq}{ds} = \quad & \frac{\partial q}{\partial x}\frac{\partial x}{\partial s} + \frac{\partial q}{\partial p_x}\frac{\partial p_x}{\partial s} + \frac{\partial q}{\partial y}\frac{\partial y}{\partial s} + \frac{\partial q}{\partial p_y}\frac{\partial p_y}{\partial s} = \\ & \frac{\partial q}{\partial x}\frac{\partial H}{\partial p_x} - \frac{\partial q}{\partial p_x}\frac{\partial H}{\partial x} + \frac{\partial q}{\partial y}\frac{\partial H}{\partial p_y} - \frac{\partial q}{\partial p_y}\frac{\partial H}{\partial y}.\end{aligned} \tag{2.20}$$

The last equation may be more conveniently expressed as a Lie operator $: H :$, which is defined as

$$: H := \frac{\partial H}{\partial x}\frac{\partial}{\partial p_x} - \frac{\partial H}{\partial p_x}\frac{\partial}{\partial x} + \frac{\partial H}{\partial y}\frac{\partial}{\partial p_y} - \frac{\partial H}{\partial p_y}\frac{\partial}{\partial y}. \tag{2.21}$$

The Lie operator now allows to rewrite Eq. 2.19 as follows

$$q(s_1) = \sum_{n=0}^{\infty} \frac{(s_1 - s_0)^n}{n!} \frac{d^n q}{ds^n} = e^{-(s_1-s_0):H:} q(s_0). \tag{2.22}$$

Using the Hamiltonian for a quadrupole as defined above (see Eq. 2.12) with a length L, one may now express the coordinates after passing through the element as

$$\begin{pmatrix} x_1 \\ p_{x_1} \\ y_1 \\ p_{y_1} \end{pmatrix} = e^{-L:K_2(s)\frac{x^2-y^2}{2}:} \begin{pmatrix} x_0 \\ p_{x_0} \\ y_0 \\ p_{y_0} \end{pmatrix} = \begin{pmatrix} 1 & 0 & 0 & 0 \\ -K_2L & 1 & 0 & 0 \\ 0 & 0 & 1 & 0 \\ 0 & 0 & K_2L & 1 \end{pmatrix} \begin{pmatrix} x_0 \\ p_{x_0} \\ y_0 \\ p_{y_0} \end{pmatrix} \tag{2.23}$$

Note that here the effect of the quadrupole of the length L was replaced by a single kick at one location with the same integrated strength, which also allows to omit the kinematic $\frac{p_x^2+p_y^2}{2}$ of the Hamiltonian. This approximation, where the element is then assumed to have zero length, is called thin lens approximation.

For the case of a thick quadrupole of length L and focusing in the horizontal plane ($K_2 > 0$), the transfer matrix M can also be obtained as general solution of Eq. 2.13 and is

$$M = \begin{pmatrix} \cos(\sqrt{K_2}L) & \frac{\sin(\sqrt{K_2}L)}{\sqrt{K_2}} & 0 & 0 \\ -\sqrt{K_2}\sin(\sqrt{K_2}L) & \cos(\sqrt{K_2}L) & 0 & 0 \\ 0 & 0 & \cosh(\sqrt{K_2}L) & \frac{\sinh(\sqrt{K_2}L)}{\sqrt{K_2}} \\ 0 & 0 & \sqrt{K_2}\sinh(\sqrt{K_2}L) & \cosh(\sqrt{K_2}L) \end{pmatrix}. \tag{2.24}$$

For the case where $K_2 = 0$, the transfer matrix M is

$$M = \begin{pmatrix} 1 & L & 0 & 0 \\ 0 & 1 & 0 & 0 \\ 0 & 0 & 1 & L \\ 0 & 0 & 0 & 1 \end{pmatrix}. \tag{2.25}$$

Note that the exact representation of the transfer map as a matrix is only possible for elements where the magnetic field is either constant or depends linearly on the transverse position of the particle. For elements such as sextupoles with a magnetic field described by

$$B_y(x, y, s) + iB_x(x, y, s) = K_3(s)(x + iy)^2, \tag{2.26}$$

and the associated Hamiltonian

$$H = \frac{K_3}{3!}(x^3 - 3xy^2), \tag{2.27}$$

such an approach is not possible anymore.

For an accelerator lattice consisting of n elements with associated transfer maps $\mathcal{M}$, the change of the initial coordinates (u, p_u) over one full turn can be expressed by the one turn map

$$\mathcal{M}_{OTM} = \mathcal{M}_n \cdot \mathcal{M}_{n-1} \cdot ... \cdot \mathcal{M}_2 \cdot \mathcal{M}_1, \tag{2.28}$$

which is a concatenation of the individual transfer maps. For the case of only taking into account linear elements, the one-turn map $\mathcal{M}_{OTM}$ then simplifies to a matrix

$$\mathcal{M}_{OTM} = \begin{pmatrix} \cos(2\pi Q_u) + \alpha_u \sin(2\pi Q_u) & \beta_u \sin(2\pi Q_u) \\ -\gamma_u \sin(2\pi Q_u) & \cos(2\pi Q_u) - \alpha_u \sin(2\pi Q_u) \end{pmatrix}, \quad (2.29)$$

using the Courant-Snyder parameters β_u, α_u, and γ_u at a given location s.

The linear motion in an accelerator can be further simplified by introducing the Courant-Snyder coordinates $\hat{u}$, $\hat{p}_u$, which are obtained by the following transformation

$$\begin{pmatrix} \hat{u} \\ \hat{p}_u \end{pmatrix} = \begin{pmatrix} \frac{1}{\sqrt{\beta_u}} & 0 \\ \frac{\alpha_u}{\sqrt{\beta_u}} & \sqrt{\beta_u} \end{pmatrix} \begin{pmatrix} u \\ p_u \end{pmatrix}. \quad (2.30)$$

The newly obtained linear normalized phase space coordinates

$$\begin{aligned} \hat{u} &= \sqrt{2J_u} cos(\psi_u) \\ \hat{p}_u &= -\sqrt{2J_u} sin(\psi_u) \; u \in (x, y), \end{aligned} \quad (2.31)$$

are defined by the action-angle coordinates J_u and ψ_u. In these coordinates, the one-turn map from Eq. 2.29 becomes a simple rotation matrix in phase space

$$\hat{\mathcal{M}}_{OTM} = \begin{pmatrix} \cos(2\pi Q_u) & \sin(2\pi Q_u) \\ -\sin(2\pi Q_u) & \cos(2\pi Q_u) \end{pmatrix}. \quad (2.32)$$

It follows that compared to the trace-space plot in Fig. 2.1, in the normalized coordinates the phase space plot is simply a circle with a radius of $\sqrt{2J_u}$.

When taking into account nonlinear elements, a more general approach is used, which is described in Sec. 5.2.

It should be noted that in the previous sections and some of the literature $u' = \frac{du}{ds}$ and p_u are used interchangeably. This approximation is valid for high energy machines, where $p_z \gg p_x, p_y$, as will be demonstrated in the following. Using the Hamilton of the drift space from Eq. 2.8 and Hamilton's equation of motion with s as the independent variable

$$u' = \frac{du}{ds} = \frac{\partial H}{\partial p_u}, \quad (2.33)$$

one arrives at

$$u' = \frac{p_u}{\sqrt{(1+\delta)^2 - p_x^2 - p_y^2}} \approx \frac{p_u}{1+\delta}. \quad (2.34)$$

One commonly refers to u, p_u as the phase space, whereas u, u' is called trace space.

2.6 Longitudinal Motion

Using Eq. 2.3, the change of the kinetic energy is given by

$$\Delta E_{kin} = \int_{s_0}^{s_1} \vec{F} d\vec{s} = \int_{s_0}^{s_1} q\vec{E} \cdot d\vec{s} + \int_{t_0}^{t_1} \underbrace{q\left(\vec{v} \times \vec{B}\right) \cdot \vec{v}}_{=0} dt. \tag{2.35}$$

Equation 2.35 indicates that only electric fields in the direction of motion can be used to increase the kinetic energy of a charged particle. While electrostatic fields are used for acceleration in the some accelerator types, in synchrotron radio frequency (RF)-cavities are used. The longitudinal field E_z in those cavities follows

$$E_z(t) = E_{z,0} \sin\left(2\pi f_{RF} t + \phi_s\right) \tag{2.36}$$

with f_{RF} the RF frequency and ϕ_s the synchronous phase. For a particle to arrive at the same phase at the cavity, the RF frequency needs to fulfil

$$f_{RF} = h f_{rev}, h \in \mathbb{Z}, \tag{2.37}$$

where f_rev is the revolution frequency and h an integer called harmonic number. The harmonic number h determines the number of fixed stable synchronous points in the accelerator. Using Eq. 2.4, the revolution frequency is given by

$$f_{rev} = \frac{v}{C} = \frac{qc^2}{E_0} \frac{\rho}{C} B, \tag{2.38}$$

with C the circumference of the accelerator, q and E_0 the charge and rest energy of the particle. Keeping the bending radius ρ constant, the change of the momentum is proportional to the change of the bending field B

$$\frac{dp}{dt} = q\rho \frac{dB}{dt}. \tag{2.39}$$

The change over one turn is

$$\Delta p = q\rho T \frac{dB}{dt} = \frac{q\rho C}{v} \frac{dB}{dt} \tag{2.40}$$

which with $\Delta E_{kin} = v\Delta p$ and change of energy equal to the energy gain from the RF-cavities leads to

$$\Delta E_{kin} = \frac{q\rho C}{v} \frac{dB}{dt} = qV \sin\phi_s. \tag{2.41}$$

From this equation, it follows that the synchronous phase ϕ_s follows the change of the magnetic field

$$\phi_s = \arcsin\left(\frac{\rho C}{V}\frac{dB}{dt}\right) \tag{2.42}$$

and in the case of no acceleration $dB/dt = 0$, the synchronous phase is either $\phi_s = 0$ or $\phi_s = \pi$.

To keep the synchronicity, a particle with deviation from the reference momentum p will experience a change in orbit length and revolution period.

One defines the momentum compaction factor α_c as the relative change of circumference with relative momentum change

$$\alpha_c = \frac{\Delta C/C}{\Delta p/p} \tag{2.43}$$

and the slip factor η the relative change of revolution time $T = \frac{1}{f_{rev}}$ with relative momentum change

$$\eta = \frac{\Delta T/T}{\Delta p/p}. \tag{2.44}$$

The change of circumference with momentum is determined by the transverse optics. With the revolution time $T = C/v = C/(\beta_{rel}c)$, the relative change is given by

$$\frac{dT}{T} = \frac{dC}{C} - \frac{d\beta_{rel}}{\beta_{rel}} = \alpha_c\frac{dp}{p} - \frac{1}{\gamma_{rel}^2}\frac{dp}{p}, \tag{2.45}$$

where $\beta_{rel} = v/c$, the Lorentz factor $\gamma_{rel} = (1-\beta_{rel}^2)^{-1/2}$, and $\frac{dp}{p} = \gamma_{rel}^2\frac{d\beta_{rel}}{\beta_{rel}}$ have been used. From Eq. 2.45, it can be inferred that the slip factor η is given by

$$\eta = \alpha_c - \frac{1}{\gamma_{rel}^2}. \tag{2.46}$$

Two regimes can be identified, one where $\alpha_c > \gamma_{rel}^{-2}$, thereby $\eta > 0$ and an increase in momentum leading to an increase/decrease in revolution time/frequency, and the other where $\alpha_c < \gamma_{rel}^{-2}$ and the opposite is the case. One defines the transition energy as the energy where $\eta = 0$, thus $\gamma_{rel,t} = \alpha_c^{-1/2}$.

Defining the following variables with respect to the synchronous particle

$$\begin{aligned}\Delta\phi &= \phi - \phi_s,\\ \Delta p &= p - p_0,\\ \Delta E &= E - E_0,\\ \Delta\omega &= \omega - \omega_s,\end{aligned} \tag{2.47}$$

it can be shown (e.g. in [45]) that the following equation governs the longitudinal motion of a particle

$$\frac{d}{dt}\Big[\frac{C_s p_0}{h\eta 4\pi^2 f_{rev,s}}\frac{d\phi}{dt}\Big] + \frac{qV}{2\pi}\Big(\sin\phi - \sin\phi_s\Big) = 0. \tag{2.48}$$

Assuming that parameters C_s, p_s, $f_{rev,s}$, and η vary slowly in time Eq. 2.48 simplifies to

$$\frac{d^2\phi}{dt^2} + \frac{\Omega_s^2}{\cos\phi_s}(\sin\phi - \sin phi_s) = 0 \tag{2.49}$$

with

$$\Omega_s = \sqrt{\frac{h\eta f_{rev,s} qV\cos\phi_s}{2\pi C_s p_s}} \tag{2.50}$$

the synchrotron frequency. Using $\sin\phi - \sin\phi_s \approx \Delta\phi\cos\phi_s$, Eq.2.49 simplifies to the equation of a harmonic oscillator

$$\frac{d^2\phi}{dt^2} + \Omega_s^2\Delta\phi = 0. \tag{2.51}$$

The synchrotron tune Q_s is given by

$$Q_s = \frac{\Omega_s}{2\pi f_{rev}}. \tag{2.52}$$

The longitudinal motion is stable if Ω_s^2 is positive, which leads to the following requirement

$$\eta\cos\phi_s > 0. \tag{2.53}$$

From this condition, it follows that below the transition energy ($\eta > 0$), for acceleration the synchronous phase is $0 < \phi_s < \frac{\pi}{2}$, whereas above transition energy $\frac{\pi}{2} < \phi_s < \pi$ holds.

Using either the Eq. 2.49 or the approximation Eq. 2.51 describing the longitudinal motion, it follows that in a limited range around the synchronous phase, the motion is stable. For the case above transition energy ($\eta > 0$), a particle with an initially higher energy than the synchronous particle will arrive earlier at the RF-cavity, where due to the larger voltage, the energy increase will be larger. Due to the effect of the path lengthening dominating ($\eta > 0 \rightarrow \alpha_c > \frac{1}{\gamma_t^2}$), the orbit length of a particle with a higher energy will be larger than that of the synchronous particle, thereby increasing the revolution time. Due to the increased revolution time, the difference in arrival time or phase between the higher momentum particle and the synchronous particle will decrease. Conversely, a lower energy particle will arrive after the synchronous particle, where the energy gain will be less. This will lead to a shorter orbit length, with an associated shorter revolution time, which will decrease the phase

difference between the particles. For the case below transition energy ($\eta < 0$), the opposite is the case. Here, a particle with a larger momentum will arrive before the synchronous particle where the energy gain will be less. By repeatedly gaining less energy than the synchronous particle, the initial phase difference will decrease. Both cases are illustrated in Fig. 2.2.

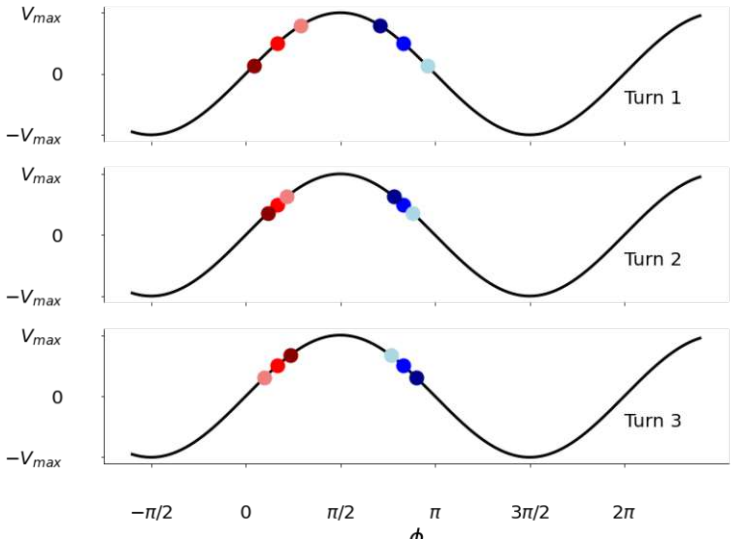

FIGURE 2.2: RF voltage as function of the phase for a synchronous particle below (red) and above (blue) transition energy. The darker shaded point shows a particle with an initially higher momentum than the synchronous particle, whereas the lighter point represents a particle with a lower momentum.

Another way of illustrating the longitudinal motion around the synchronous particle is in a phase space plot, as is done in Fig. 2.3.

The phase space is separated into two different regions. Trajectories within the separatrix are closed and particles with a momentum and phase offset with respect to the synchronous particle within the separatrix will oscillate around this particle. Outside the separatrix, the motion is unstable and particles will get lost. The area within the separatrix is also being referred to as the RF-bucket and gives the RF-acceptance of the accelerator. The size of the RF bucket depends on the synchronous phase and is largest at either $\phi_s = 0$ below transition energy and $\phi_s = \pi$ above transition energy.

2.7 Perturbations and resonances

A dipole where the bending angle differs to the design one by $\Delta\theta$ will result in a closed orbit distortion $\Delta u(s)$. This change in the orbit is described by

$$\Delta u(s) = \frac{\sqrt{\beta_u(s)\beta_u(s_0)}}{2\sin(\pi Q_u)}\Delta\theta\cos(\pi Q_u - |\psi_u(s) - \psi_u(s_0)|), \tag{2.54}$$

where s_0 represents the position where the erroneous kick occurs. Notably, in the case where the tune Q_u is equal to an integer, the denominator will be zero and thus

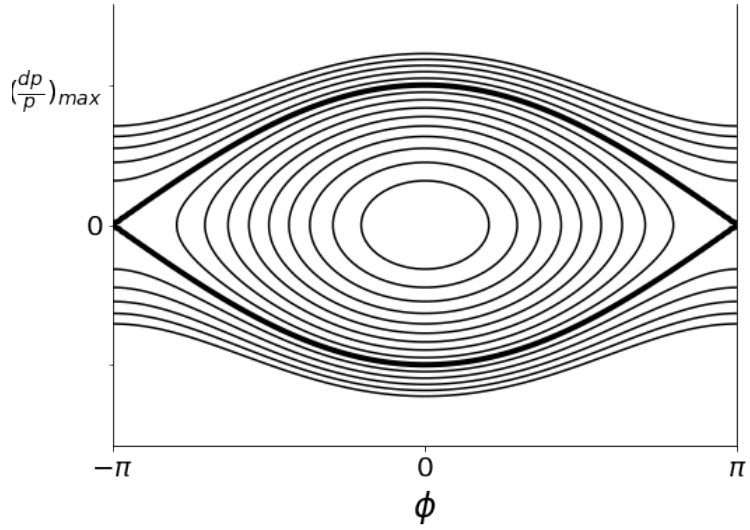

FIGURE 2.3: Phase space diagram of the longitudinal motion. Stable trajectories is found within the separatrix outlined by the thick black line. The synchronous phase is set to $\phi_s = 0$ in this case.

the closed orbit distortion will diverge to infinity. Similarly, in the case of gradient field errors in the quadrupoles, the β-function and phase, and subsequently the tune, will be perturbed. The relative deviation of the β-function, called the β-beating, can be expressed as

$$\frac{\Delta\beta_u}{\beta_u}(s) = \frac{\beta_u(s_0)}{2\sin(2\pi Q)}\Delta K_2 L \cos\left(2\pi Q_u - 2|\psi_u(s) - \psi_u(s_0)|\right), \tag{2.55}$$

where $\Delta K_2 L$ represents the quadrupole gradient error integrated of the length L of the magnet. The deviation of the phase can then be obtained by using Eq. 2.16 and Eq. 2.55, which gives

$$\Delta\psi_u(s) = \int_{s_0}^{s} \frac{d\tau}{\beta_u(\tau)}\left(\frac{1}{1+\frac{\Delta\beta_u}{\beta_u}(\tau)} - 1\right). \tag{2.56}$$

Again, in cases where the denominator $\sin(2\pi Q_u)$ is either integer or half integer, the β-beating will diverge and particle motion becomes unstable.

Using perturbation theory, similar equations can be found determining the evolution of the action $J_{x,y}$ in the presence of higher order magnetic fields [46]. From these, the resonance condition

$$mQ_x + nQ_y + oQ_s = p, (m, n, o, p \in \mathbb{Z}) \tag{2.57}$$

arises, where Q_x and Q_y are the tunes in the transverse planes and Q_s the synchrotron tune. In Fig. 2.4, Eq. 2.57 is visualized in form of resonance lines up to order $|m| + |n| = 5$ in a tune diagram together with a potential working point far from resonances.

To note, the effect of a resonance on the particle motion is not only present when the

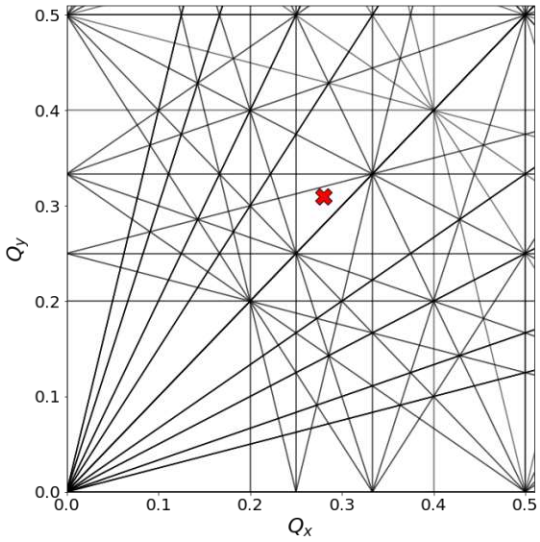

FIGURE 2.4: Tune diagram with resonances up to order $|m| + |n| = 5$ and with the working point of LHC at injection energy of $Q_x = 0.28/Q_y = 0.31$. Synchrobetatron resonances ($o \neq 0$) have been omitted here.

resonance condition Eq. 2.57 is fulfilled, but also in the vicinity of a resonance. The region of effect is called the stop band and the width of this stop band is dependent on the strength of a given resonance [40].

2.7.1 Linear Coupling

In the above introduction of the Courant-Snyder parameters, Eq. 2.13 and its solution do not consider the presence of either skew quadrupole or solenoidal fields. This has allowed to treat the two planes separately, whereas in the presence of such elements the motion in the two planes is coupled. If these sources are taken into account, the one turn map does not retain its block diagonal form anymore. Two methods are available to describe the coupled motion in terms of their eigenmodes, one developed by Edward and Tengs and another by Mais and Ripken [47]. In the presence of coupling, the tunes Q_x and Q_y are also replaced by the eigentunes

$$Q_1 = Q_x - \frac{\Delta}{2} + \frac{1}{2}\sqrt{\Delta^2 + (C^-)^2} \tag{2.58}$$

$$Q_2 = Q_y - \frac{\Delta}{2} - \frac{1}{2}\sqrt{\Delta^2 + (C^-)^2}, \tag{2.59}$$

where Δ represents the uncoupled tune split $\Delta = |Q_x - Q_y|$ and C^- the coupling coefficient, being the sum of each source weighted by $\sqrt{\beta_x \beta_y}$.

It should be noted that the motion near the difference resonance $Q_x - Q_y$, excited by skew quadrupole fields, and far from other resonances is stable and thus by itself does not induce an particle loss [48].

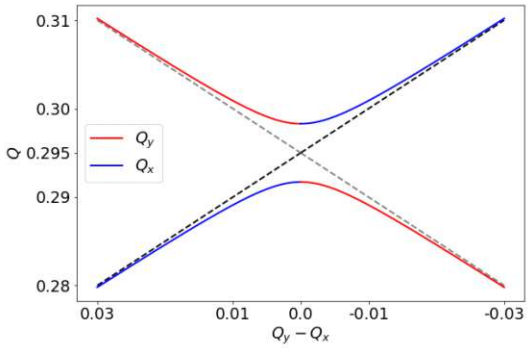

FIGURE 2.5: Illustration of the behaviour of the transverse tunes with varying tune split in the presence of linear coupling.

2.7.2 Dispersion and Chromaticity

The solution Eqs. 2.15 takes into account particles with the reference momentum. To treat a particle with $\delta_p \neq 0$, Hill's equation has to be extended as follows

$$\frac{d^2u}{ds^2} + \Big(\frac{1}{\rho(s)^2} - K_2(s)\Big)u = \frac{\delta_p}{\rho(s)},\ u \in (x,y). \tag{2.60}$$

The solution for the position coordinate $u \in (x,y)$ to the above equation then consist of the homogeneous solution shown in Eq. 2.15 and a special solution

$$u(s) = D_u(s)\delta, \tag{2.61}$$

where $D_u(s)$ is called the dispersion function, given by

$$D_u(s) = \frac{\sqrt{\beta_u(s)}}{2\sin(\pi Q_u)} \int_s^{s+C} \frac{\beta_u(\tau)}{\rho(\tau)} \cos\left(\psi(\tau) - \psi(s) - \pi Q\right) d\tau. \tag{2.62}$$

Particles with a momentum deviation not only experience a different trajectory than on-momentum particles, but also the focusing strength of the quadrupole is affected. Due to the different focusing of the quadrupoles, the tune of the machine is changed. The variation of the tune with the relative momentum deviation δ_p is called chromaticity and described by

$$Q_u(\delta_p) = Q_u + Q'_u\delta_p + \frac{1}{2!}Q''_u\delta_p^2 + \frac{1}{3!}Q'''_u\delta_p^3 + ...,\ u \in (x,y) \tag{2.63}$$

The terms $Q_u^{(n)} = \frac{\delta^n Q_u}{\delta\delta_p^n}$ are referred to as chromaticity of order n. Usually, Q' is referred to as (linear) chromaticity, whereas the higher order terms Q'', Q''' etc. are called nonlinear chromaticity. To compensate for the momentum dependent focusing of the quadrupoles, sextupoles are introduced as the feature a transverse position dependent gradient. These are placed in dispersive regions where particle displacement is proportional to their momentum deviation. It can then be shown that the first order chromaticity of a ring is

$$Q'_u = \mp\frac{1}{4\pi}\oint \beta_u\Big(K_2(s) - K_3(s)D_x\Big)ds. \tag{2.64}$$

2.7.3 Amplitude Detuning

Similar to chromaticity, the tune may also vary with the action J_u of a particle. This is referred to as amplitude detuning and similar to the chromaticity can be expressed as a Taylor series

$$Q_u(J_x, J_y) = Q_u + \frac{\partial Q_u}{\partial J_x} J_x + \frac{\partial Q_u}{\partial J_y} J_y + \frac{1}{2}\left(\frac{\partial^2 Q_u}{\partial J_x^2} J_x + \frac{\partial^2 Q_u}{\partial J_x J_y} J_x J_y + \frac{\partial^2 Q_u}{\partial J_y^2} J_x\right) + ..., \; u \in (x, y). \tag{2.65}$$

Such a behaviour is introduced by nonlinear magnetic fields, such as octupole fields. Taking the Hamiltonian of an octupole

$$H = \frac{K_4}{4!}(x^4 - 6x^2y^2 + y^4) \tag{2.66}$$

and using

$$\begin{aligned} x &= \sqrt{2J_x\beta_x}cos(\psi_x) \\ y &= \sqrt{2J_y\beta_y}cos(\psi_y), \end{aligned} \tag{2.67}$$

one obtains

$$H = \frac{K_4}{4!}\left[4J_x^2\beta_x^2cos^4(\psi_x) - 24J_x\beta_xcos^2(\psi_x)J_y\beta_ycos^2(\psi_y) + 4J_y^2\beta_y^2cos^4(\psi_y)\right]. \tag{2.68}$$

The tune shift of a Hamiltonian is given by

$$\Delta Q_u = \frac{1}{2\pi}\frac{\partial\langle H\rangle}{\partial J_u}, \tag{2.69}$$

where $\langle H\rangle$ is the Hamiltonian average over the phase space angle

$$\langle H\rangle = \frac{1}{4\pi^2}\int_0^{2\pi}\int_0^{2\pi} H d\psi_x d\psi_y. \tag{2.70}$$

For the aforementioned octupole, the average Hamiltonian $\langle H\rangle$ is then given by

$$\langle H\rangle = \frac{K_4}{4!}\left(\frac{3}{2}\beta_x^2J_x^2 - 6\beta_x\beta_yJ_xJ_y + \frac{3}{2}\beta_y^2J_y^2\right). \tag{2.71}$$

Following Eq. 2.69, the tune shift induced by a single octupole with an integrated strength of K_4 is then

$$\begin{aligned} \Delta Q_x(J_x, J_y) &= \frac{3K_4}{8\pi}\left(\beta_x^2J_x - 2\beta_x\beta_yJ_y\right) \\ \Delta Q_y(J_x, J_y) &= \frac{3K_4}{8\pi}\left(\beta_y^2J_y - 2\beta_x\beta_yJ_y\right), \end{aligned} \tag{2.72}$$

clearly indicating a dependence on the action in both transverse planes. Note that for a single sextupole with a Hamiltonian

$$H = \frac{K_3}{3!}\left[x^3 - 3xy^2\right], \tag{2.73}$$

no amplitude detuning is found. However, for the case where two or more sextupoles are present in the accelerator, amplitude detuning is introduced via second order effects [49].

2.7.4 Feeddown

Due to either dipole errors or due to misalignment, the closed orbit may not pass through the magnetic center of a given element, but off axis. In this case, the beam will not only be subject to the primary field component of the element, but also to lower order components, which is an effect called feed-down. This can be illustrated by for example taking a sextupole field and adding an offset Δx to the horizontal position, illustrated as

$$B_y(x+\Delta x, y, s) + iB_x(x+\Delta x, y, s) = K_3(s)(x+\Delta x+iy)^2 = \\ K_3(s)(x+iy)^2 + K_3(s)\Delta x^2 + 2K_2(s)x\Delta x + 2iK_3(s)y\Delta x.$$

Here, the term $2K_3(s)x\Delta x$ corresponds to an additional quadrupole kick experienced by the beam passing off center through the sextupole.

2.7.5 Dynamic Aperture

Through the aforementioned effects of amplitude detuning or chromaticity, it is clear that particle bunch with a given distribution of δ_p, J_x, and J_y will exhibit a tune spread, determined by the strength of the nonlinear magnetic fields. Even for a working point $Q_{x,0}, Q_{y,0}$ far from resonances, detuning $Q_x(J_x, J_y, \delta_p), Q_y(J_x, J_y, \delta_p)$ will change the tune of particles with a large enough deviation from the reference particle to fulfill the resonance condition Eq.2.57 and thereby lead to a growth of oscillation amplitude until particles hit the physical aperture of the accelerator and are lost. Such is illustrated in Fig. 2.6, where the tune spread of a particle bunch due to amplitude detuning generated by octupoles is shown together with resonance lines up to order 7.

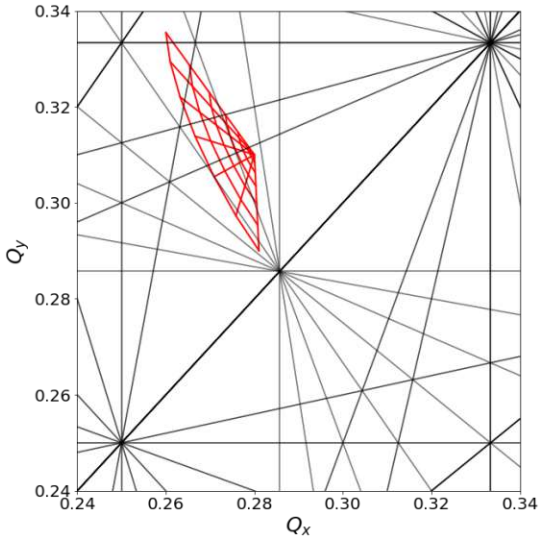

FIGURE 2.6: Resonance diagram with resonances up to order $|m| + |n| = 7$ and illustrating the tune spread of a particle bunch in the presence of amplitude detuning.

In this plot, some particles with a large amplitude will be close to the resonance $3Q_y = p$, excited by skew sextupole fields. In the presence of strong, uncompensated skew sextupole fields, this resonance will result in the loss of these large amplitude particles. Thus, depending on the strength of the resonance, after a certain number of turns all particles in a bunch with a large enough action will be lost, effectively introducing an upper limit for the attainable action.

One can then define the dynamic aperture (DA) as the boundary in phase space above which all particles are lost due to a rapid growth of oscillation amplitude. Conversely, the oscillation amplitude of particles within the DA remains bounded.

Depending on the strength of different resonances, the speed with which the oscillation amplitude increases may vary for different particles, such that the amplitude above which particles are lost will steadily decline with the increasing number of turns. It is then practical to quote the DA $\mathcal{D}(N)$ for a given number of turns N, with $\mathcal{D}_\infty$ the asymptotic value for an infinite amount of turns. While for simple nonlinear systems such as a Hénon-Heiles system [50], $\mathcal{D}_\infty$ can be found analytically, in more complex systems one usually has to resort to tracking a grid of particle for given amount of turns to then infer $\mathcal{D}(N)$. Based on the evolution of $\mathcal{D}(N)$ for an increasing number of turns N, models have been derived to estimate D_∞ [51].

For tracking particles in an accelerator model, some basic precautions are necessary. As described in Eq. 2.28, the accelerator ring can be modelled as a concatenation of transfer maps. For studying systems governed by a Hamiltonian, one key property of the map is that it is sympletic, that is, the area in phase space is conserved. In general, a thick element with a length L cannot be described by a sympletic map. It is thus common to split a thick element into a number of thin elements with $L \to 0$ and separated by drift spaces. The map of a thin element, which only changes the momentum coordinates and thus commonly referred as a kick, is sympletic. Algorithms such as the TEAPOT [52] have been devised to split a thick element into N thin elements while keeping the error that is introduced by doing so minimal.

On a practical note, in any real accelerator, the maximum oscillation amplitude of particle is limited by the (normalized) physical aperture of the machine. As such, for studying the DA in real accelerators, one can only measure the DA up to the physical aperture. In tracking studies on the other hand, the physical aperture in the model can be set to a sufficiently high value. Complementary to the loss of particle when hitting the aperture, two other methods are implemented in the tracking code SIXTRACK [53] used for the studies below. For each coordinate on the initial grid, two particles separated by small distance are initialized. The *distance* method examines the final distance between the particles, which if exceeding a certain threshold is considered lost, whereas the *slope* method examines the evolution of the distance between the particles and considers unbounded motion if the slope is outside a given range of values [54].

2.8 Emittance and beam size

The previous sections have so far treated the motion of a single particle in an accelerator. However, the bunches in any accelerator usually consist of multiple particles. For the case of the LHC and its upgrades, the number of protons in one bunch ranges

from $5.0 \cdot 10^9$ [55] to $2.2 \cdot 10^{11}$[56]. Notably, there have been instances where single particles were stored in an accelerator, such as VEPP-3 [57], MLS [58], and more recently in the IOTA accelerator [59].

The bunch is then an ensemble of particles with different initial conditions J_u and $\psi_{u,0}$. To describe the distribution of particles, one natural measure is the average action of the ensemble

$$\langle J \rangle = \frac{1}{N} \sum_i^N J_{u,i}, \tag{2.74}$$

which given that the action of a particle is a constant of motion, the average is constant around the ring.

To describe the evolution of any distribution, one can also define the the σ-matrix as follows

$$\sigma = \begin{pmatrix} \frac{1}{N}\sum_i^N x_i x_i & \frac{1}{N}\sum_i^N x_i x_i' \\ \frac{1}{N}\sum_i^N x_i' x_i & \frac{1}{N}\sum_i^N x_i' x_i' \end{pmatrix} = \begin{pmatrix} \langle \overline{x}^2 \rangle & \langle x x' \rangle \\ \langle x x' \rangle & \langle \overline{x'}^2 \rangle \end{pmatrix} \tag{2.75}$$

and for the normalized distribution as

$$\overline{\sigma} = \begin{pmatrix} \frac{1}{\sqrt{\beta_0}} & 0 \\ \frac{\alpha_0}{\sqrt{\beta_0}} & \sqrt{\beta_0} \end{pmatrix} \sigma \tag{2.76}$$

using the normalization to the Courant-Snyder coordinates from Eq. 2.31.

With this definition, a beam distribution is called matched to a specific point with optics function β_0 and α_0 if $\overline{\sigma}$ is invariant under rotation, that is $\langle \hat{x}\hat{x}' \rangle = 0$ and $\langle \overline{\hat{x}}^2 \rangle = \langle \overline{\hat{x}'}^2 \rangle$. For this case the σ-matrix is then

$$\sigma = \epsilon_{RMS} \begin{pmatrix} \beta_0 & -\alpha_0 \\ -\alpha_0 & \gamma_0 \end{pmatrix} \tag{2.77}$$

,

where ϵ_{RMS} is the RMS emittance of the beam, given by

$$\epsilon_{RMS} = \sqrt{\langle x^2 \rangle \langle x'^2 \rangle - \langle x x' \rangle^2} = \langle J \rangle. \tag{2.78}$$

The RMS beamsize and divergence at a location s_0 are given by

$$\sigma_x = \sqrt{\langle \overline{x}^2 \rangle} = \sqrt{\beta(s_0)\epsilon_{RMS}} \tag{2.79}$$

$$\sigma_{x'} = \sqrt{\langle \overline{x'}^2 \rangle} = \sqrt{\gamma(s_0)\epsilon_{RMS}}. \tag{2.80}$$

In case of no beam acceleration and neglecting any interaction between the particles in a bunch, the emittance remains constant during the bunch circulation. However, for the case where particles are accelerated by the RF-cavities, the emittance decreases via a process called adiabatic damping. This follows from $x' = \frac{p_x}{p_s}$, which in the case of constant p_x decreases due to the increase in p_s. For the operation of accelerators with an energy ramp, it is convenient to defined the normalized emittance ϵ_n as

$$\epsilon_n = \beta_{rel}\gamma_{rel}\epsilon_{RMS} \tag{2.81}$$

with $\beta_{rel} = v/c$ and $\gamma_{rel} = (1 - \beta_{rel}^2)^{-1}$, which is constant during the acceleration.

So far, the emittance has only been discussed in the context of a linear lattice. However, as discussed above, nonlinear magnetic fields also introduce a variation of the phase ψ_u with the action J_u. Assuming a particle bunch initially on the reference orbit receiving a strong transverse kick, the bunch will then oscillate around the reference orbit following

$$u(s) = \sqrt{(2J_u + 2J_{u,kick})\beta_u(s)}\cos\left(\psi_u(s) + \psi_{u,0}\right), \tag{2.82}$$

where $J_{u,kick}$ is the so called kick action. In the linear lattice, the beamsize as such is not directly affected by only being offset. In the case with nonlinearities, the spread in tune will lead to particles distributed across the phase space trajectory after a certain number of turns, leaving a larger emittance and thereby beamsize. This process is called filamentation and is illustrated in Fig. 2.7.

Here, the case of a single excitation and the ensuing unpreventable emittance blow-up is shown. It should be noted that by coherently exciting the beam, the beam can be adiabatically brought to large amplitudes and back to the original orbit with minimal emittance blow-up [60].

Following the discussion on resonances, in the vicinity of resonances the action of a particle will grow rapidly, leading to a rapid emittance growth or beam loss.

For the studies presented in this thesis, other effects affecting the beam emittance such as radiation damping or intrabeam scattering have only played a negligible role, and will not be discussed here. A detailed description of those can be found in e.g. [40].

2.9 Luminosity

The performance of any particle collider is usually quantified by its center of mass energy and the achievable number of generate events. The number of events R per unit of time for a given process with a cross section σ_p is given by

$$\frac{dR}{dt} = \mathcal{L}\sigma_p \tag{2.83}$$

where $\mathcal{L}$ is the instantaneous luminosity. It is a process-independent measure of the capability of the collider to produce a certain number of collisions.

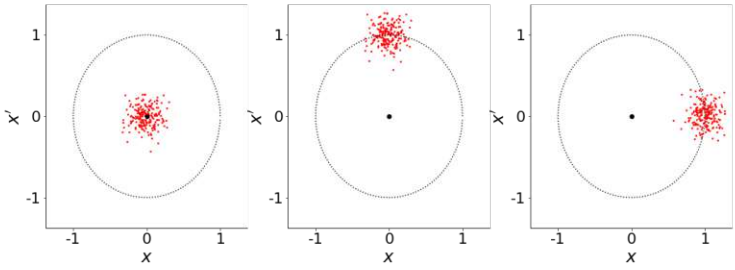

(A) Evolution of a kicked beam in a linear lattice

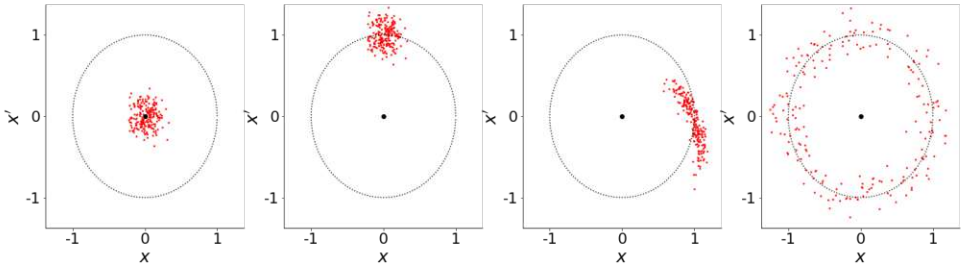

(B) Evolution of a kicked beam in a lattice with amplitude dependent tune

FIGURE 2.7: Illustration of the evolution of a kicked beam (A) in the linear case and (B) for the case of an amplitude detuning. The leftmost plot shows the beam distribution before the excitation, and the plot to the right the distribution after receiving a transverse kick. In the lower plot, the change of the beam distribution is shown for a small number of turns in the third plot, whereas the right plot shows the filamented beam after many turns.

It can be calculated using the overlap integral [61]

$$\mathcal{L} = 2N_1N_2fN_b \iiint_{-\infty}^{\infty} \rho_{x,1}(x)\rho_{y,1}(y)\rho_{z,1}(z-z_0)\rho_{x,2}(x)\rho_{y,2}(y)\rho_{z,2}(z+z_0)dxdydzdz_0 \tag{2.84}$$

where the subscripts $_{1,2}$ denotes the different beams, N is the number of particles in a bunch, f the revolution frequency, N_b the number of colliding bunches. Here, it was assumed that the particle distributions $\rho_{x,y,z}$ are uncorrelated between the different planes. Assuming Gaussian beams with equal bunch length, the instantaneous luminosity is given by

$$\mathcal{L} = \frac{N_1N_2fN_b}{2\pi\sqrt{\beta^*_{x,1}\epsilon_{x,1} + \beta^*_{x,2}\epsilon_{x,2}}\sqrt{\beta^*_{y,1}\epsilon_{y,1} + \beta^*_{y,2}\epsilon_{y,2}}}, \tag{2.85}$$

where $\beta^*_{x,y}$ the β-function at the interaction point.

In regular machines, additional complications arise, reducing the achievable luminosity. For one, in Eq. 2.85 is also assumed that the dispersion at the interaction point is negligible. It is also assumed that the β-function is constant over the collision region. However, with the β-function in the collision region following

$$\beta_{x,y}(s) = \beta^*_{x,y} + \frac{s^2}{\beta^*_{x,y}}, \tag{2.86}$$

the beam size $\sigma_{x,y} = \sqrt{\beta_{x,y}\epsilon_{x,y}}$ increases linearly with the distance and accordingly the luminosity. Following the shape of the β-function, this effect is called hourglass effect. Similarly, in the presence of optics errors, the minimum of the β-function is shifted with respect to the collision point, thereby affecting the beam sizes at the collision point. In the LHC, bunches travel for about 120 m in a common beam pipe around the interaction point. To avoid unwanted collision anywhere outside the interaction point, the orbit is adjusted such that the bunches collide with a crossing angle α. Through this, the overlap between the bunches is reduced by a factor $S = \frac{1}{\sqrt{1+(\frac{\sigma_z}{\sigma_x}\tan\alpha)^2}}$. Lastly, any transverse separation between the bunches will also decrease the luminosity.

In addition, for a collider project not only optimizing the instantaneous luminosity is key, but also the so-called integrated luminosity. It is given by

$$\mathcal{L}_{int} = \int_0^T \mathcal{L}(t)dt \tag{2.87}$$

where T is the time spent in collision over the lifetime of the project. Following Eq. 2.83,

$$R = \mathcal{L}_{int}\sigma_p \tag{2.88}$$

gives the numbers of observable events R.

From an operational point, it is thus crucial to maximise the time spent in collisions while keeping the down time due to e.g. equipment failure low. Similar so, the instantaneous luminosity should be maximised by keeping a well controlled linear optics in the collision point and reducing any loss of particles.

Chapter 3

Dynamic aperture studies for the HE-LHC

The results presented in this chapter have been in parts published as conference proceedings under
M. Hofer *et al.*, "Integrated Full HE-LHC Optics and Its Performance", in *Proc. IPAC'18*, Vancouver, Canada, Apr.-May 2018, pp. 348–351. doi:10.18429/JACoW-IPAC2018-MOPMK002 and
M. Hofer, M. Giovannozzi, J. Keintzel, R. Tomás, F. Zimmermann, and L. van Riesen-Haupt, "Dynamic Aperture at Injection Energy for the HE-LHC", in *Proc. IPAC'19*, Melbourne, Australia, May 2019, pp. 480–483. doi:10.18429/JACoW-IPAC2019-MOPMP023

3.1 Introduction

Part of the Future Circular Collider (FCC) study is the study of two accelerator options at the energy frontier, both serving as a potential successor the Large Hadron Collider (LHC). Following the simple equation

$$B\rho = \frac{p}{q}, \tag{3.1}$$

the momentum p, and equivalently the energy, of a particle of given charge q can be increased by increasing the radius ρ of a synchrotron or the magnet field strength B, or via a combination of both.

To achieve its design collision energy of 100 TeV, the FCC-hh design features a synchrotron with radius roughly a factor 3.5 larger than the LHC and intends on using dipole magnets with a field strength about a factor 2 stronger than the LHC dipoles. To house the accelerator ring with a circumference of 97.75 km, a new tunnel in the Geneva basin would need to be excavated and accompanying infrastructure would need to be built, requiring both significant financial investment and construction time.

The premise of the High-Energy LHC (HE-LHC) on the other hand is to reuse the tunnel built for the LEP and where the LHC currently resides and achieve an increase in the collision energy by using stronger dipoles. The reuse of the preexisting tunnel in turn would allow substantial savings as only minor modifications are needed in terms of infrastructure. The increase in collision energy is then solely achieved by

the increase in magnetic field strength. In the considered case, by going from a field strength of 8.33 T to 16 T, the collision energy of the HE-LHC then tops out at about 27 TeV.

The HE-LHC is set to reuse the existing CERN injector chain, starting with LINAC4, followed by the PSB, PS, and the SPS before injecting into the collider rings. Injection scenarios for HE-LHC include injection from the current SPS with an injection energy of 450 GeV or the use of a newly built synchrotron hosted in the SPS tunnel and using superconducting magnets, which could allow for an injection energy of up to 1.3 TeV.

In general, for machines using superconducting magnets, the field quality, that is, the strength of fields other than the main field of the main dipoles is of major concern at injection energy. Effects such as persistent current effects are particularly pronounced at the low field strength required at injection, which together with any contribution from geometry of the coil may lead to strong nonlinear fields in the main dipoles. These strong nonlinear fields, together with the vast number of dipoles in a machine like the HE-LHC, may in turn lead to significant beam losses. These losses are due to particles approaching certain resonances, resulting in a growth of the oscillation amplitude until the particle hits the aperture and is lost. Particles with a higher oscillation amplitude receive stronger kicks and are thus likely to be lost sooner. To quantify the impact of the nonlinear fields, the dynamic aperture is introduced, which is defined as the maximum oscillation amplitude up until which all particles experienced constrained motion for a given number of turns.

The assessment of the impact of the nonlinear fields of the dipoles on the dynamic aperture at injection energy is of particular importance in the HE-LHC. Compared to the LHC, the field quality is expected to be worse due to the use of a different superconductor, which due to its larger filament diameter is expected to have a stronger persistent current contribution. Additionally, to reach the the target energy while keeping the main dipole field below 16 T, lattice designs with a larger number of main dipoles than the LHC are investigated. Due to the larger number of dipoles, the impact of the worse field quality on the particle motion may be larger. As such, careful assessment of the dynamic aperture is required and potential mitigation strategies need to be investigated. These may include the efficacy of correctors in increasing the dynamic aperture as well as providing input to the magnet design.

In the following chapter, studies on the impact of the field quality of the main dipoles on the dynamic aperture are presented. Section 3.2 will present an introduction to the HE-LHC lattice design and considerations for the following studies. In the following Section 3.3, an introduction to magnetic field errors, their origin and correction schemes is presented. Studies on the dynamic aperture in the HE-LHC are then treated in Section 3.4. Lastly, sorting schemes for the dipoles and their impact on the DA are presented in Section 3.5.

3.2 HE-LHC Lattice Design

Linked to continuous exploration of ways to increase the field strength of superconducting magnets by using different materials, the idea of using those magnets then to increase the energy of the LHC has been around even before the LHC completed

its construction [62]. Starting in 2010, a dedicated working group was launched at CERN, investigating the feasibility of an energy upgrade of the LHC [63, 64]. First designs of the HE-LHC were based on using dipole magnets with a field strength of 20 T, which would allow to achieve a collision energy of 33 TeV. Following the integration of the HE-LHC design study into the FCC study, which was launched in 2014, key parameters of the HE-LHC design were adapted. Notably, the dipole design follows the one for the FCC-hh, those using Nb_3Sn as a superconductor and with an operational field strength of 16 T. One minor difference is that in the design of the HE-LHC, the dipoles are curved, whereas in the FCC-hh design the dipole magnets are straight. The target collision energy for the HE-LHC is then set to 27 TeV. Further key parameters and a comparison with the FCC-hh and the (HL-)LHC are presented in Tab. 3.1.

Parameter	(HL-)LHC	HE-LHC	FCC-hh
Centre-of-mass energy [TeV]	14	27	100
Peak arc dipole field [T]	8.33	16	16
Circumference [km]	26.7	26.7	97.8
Straight-section length [m]	528	528	1400
Beam current [A]	0.58 (1.12)	1.12	0.5
Bunch population [10^{11}]	1.15 (2.2)	2.2	1.0
Number of bunches per beam	2808 (2760)	2808	10400
Normalized transverse rms emittance [μm]	3.75 (2.5)	2.5	2.2
Bunch spacing [ns]	25	25	25
Number of high-luminosity IPs	2	2	2

TABLE 3.1: Comparison of key parameters between the (HL-)LHC, HE-LHC, and FCC-hh [25].

The reuse of the existing tunnel without performing major civil engineering modifications necessitates that many design aspects of the HE-LHC have to follow those of the LHC. On one hand, the length of the straight sections and the arc sections as well as the curvature of the latter are fixed. As such, potential arc designs for the HE-LHC should closely follow the reference path set out by the LHC and LEP. On the other hand, the design of the arc cells should aim to achieve the largest possible dipole filling factor in order to achieve a high beam energy while keeping the required dipole field strength low. These two considerations however result in conflicting design measures. In order to not deviate from the reference path too much, shorter arc cells are preferred, whereas longer cells with more dipoles and a higher dipole filling factor are favoured in order to reach the targeted beam energy. Thus, a middle ground in terms of cell length and thereby also the number of cells has to be found to provide a sufficient dipole filling factor while not significantly deviating from the reference path of the previous two accelerators. To provide more space for the dipoles, the phase advance over the cells can also be lowered, resulting in a decrease of the required integrated quadrupole strength, which in turn allows for shorter quadrupoles. The side effect of lowering the phase advance is that the maximum β-function and dispersion in the arcs increase.

A further constraint is added by taking into account the injector scenario. For the same injection energy, designs with a larger number of arc cells using also a high phase advance are preferred, as those feature a smaller beam size. For the same

beam pipe aperture, a smaller beam size, or equivalently a larger normalized distance between the beam and the aperture around the ring is preferred in terms of collimation and machine protection.

However, an increased injection energy results in a smaller injected beam size for the same optics, alleviated the concerns raised before, while requiring a potentially costly injector upgrade.

Taking all the above mentioned constraints and considerations into account, various lattice design options were considered [65, 66]. In these early studies, no design could be found satisfying all the constraints and two lattice options have been chosen as main options, covering separate scenarios.

In the first chosen lattice design, each arc section is comprised of 18 FODO cells, with a phase advance of 90 degree per cell. In the following, this design will be called `18x90` or 18 cells design. In order to achieve the targeted collision energy of 27 TeV, a higher dipole filling factor than in the LHC is required, which is the case in this layout with each FODO cell containing 8 dipoles.

The second design under study is an LHC-like lattice with 23 FODO cells per arc section, each cell matched to a phase advance of 90 degree in both planes. Accordingly, this layout is referred to as `23x90` or 23 cell layout in the following. The cell layout has been slightly modified with respect to the LHC to comply with specific constraints imposed by the Nb_3Sn dipoles design. Compared to the other investigated design, the dipole filling factor is lower in this design and the targeted collision energy cannot be achieved with a dipole field strength of 16 TeV.

In Tab 3.2, the arc cell parameters for both designs are presented.

Parameter	**18 Cells**	**23 Cells**
Cell length [m]	137.227	106.9
Cell Phase advance [°]	90	90
Number of dipoles per Cell	8	6
Total number of dipoles	1280	1232
Dipole Length [m]	13.95	13.83
Quadrupole Length [m]	2.8	3.5
Sextupole Length [m]	0.5	0.836
Dipole field for 13.5 TeV [T]	15.83	16.59
Beam energy at 16 T [TeV]	13.64	13.005

TABLE 3.2: Arc cell parameters for the two studied HE-LHC lattices.

The optics for the designs as well as the arc cell layout is presented in Fig. 3.1, where the magnet naming convention from the LHC was used [67].

For both arc designs, the beam stay clear was determined using the `APERTURE` module of `MAD-X` [68] and the aperture parameter specified in [69] and assuming a mechanical tolerance of 1 mm. As the synchrotron radiation load in the HE-LHC will be similar to the one in the FCC-hh [70], for these evaluations the beam screen design developed for the FCC-hh [71] was used instead of the LHC beam screen design. In Fig. 3.2, the beam stay clear for the two design is presented, together with the minimum beam stay clear considered to be safe for the HL-LHC of 12.6 σ [69].

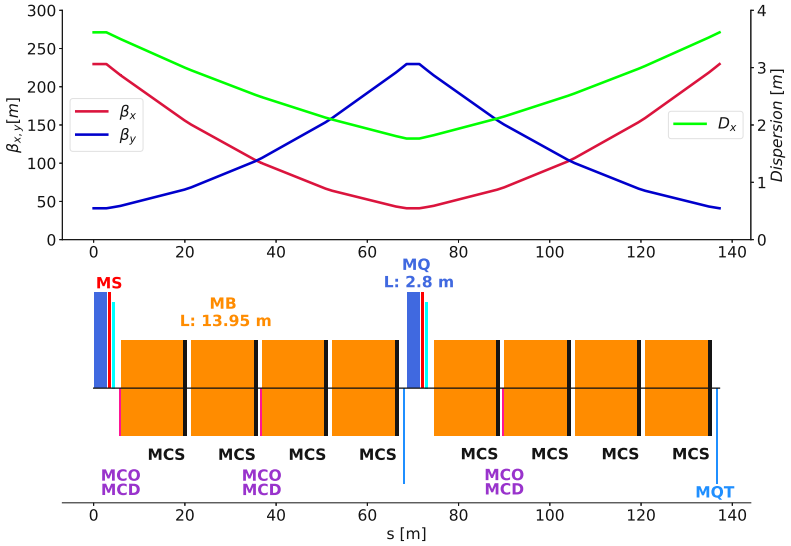

(A) Optics in one arc cell in the 18 cells layout

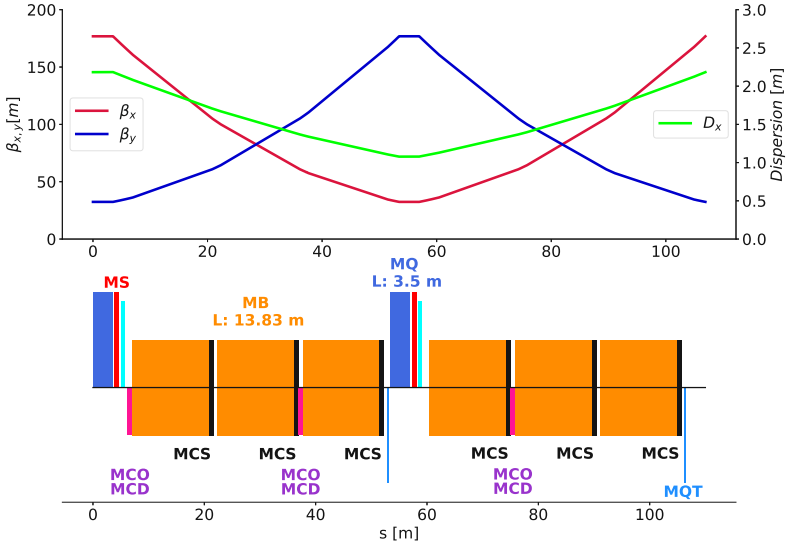

(B) Optics in one arc cell in the 23 cells layout

FIGURE 3.1: Comparison of the cells in both lattices.

Using the beam stay clear of the HL-LHC as a reference, the target collision energy could only be achieved using the 18x90 layout and with an injection energy above 1.3 TeV. Using the LHC-like, 23x90 layout, on other hand would allow for an injection energy of about 900 GeV. In both layouts, the beam stay clear at an injection energy of 450 GeV is below the required level and thus seems currently not feasible. Studies were undertaken in the LHC to see the impact of operating with tighter collimator gaps, in view of potentially allowing for a decreased minimum beam stay clear [72]. However, while promising results were achieved in these studies, no conclusion on the feasibility of operating with a beam stay clear of 10 σ, required for the case of the 23x90 layout at 450 GeV, has been made.

For the full lattice, LHC-like dispersion suppressor were used in both layouts [67]. New layouts for the high luminosity experimental insertions in IR1/5 and the RF-insertion in IR4 have been implemented [73, 74]. Compared to the LHC, the insertion

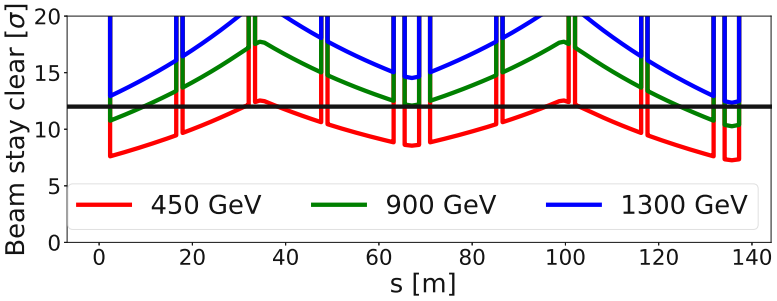

(A) Beam stay clear in one arc cell in the 18 cells layout

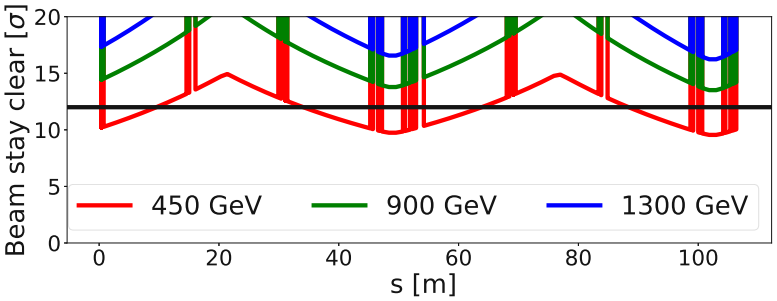

(B) Beam stay clear in one arc cell in the 23 cells layout

FIGURE 3.2: Comparison of the beam stay clear for both lattices.

in Point 4 features two more quadrupoles, which provide more flexibility in adjusting the phase-advance over the insertion. For the remaining insertion, the layouts used in the LHC were integrated and matched. The optics in the arcs 23, 34, 67, and 78 were adjusted to match the tunes of the ring to 0.31/0.32. A phase advance of $\pi/2$ has been kept in the arcs adjacent to the high luminosity experimental insertions to ensure for an efficient correction of the chromaticity.

As the HE-LHC is constrained by the geometry of the existing tunnel, the offset of these machines to the survey of the LHC has to be checked. While offsets in the insertions are less critical as these are located in wide caverns, a spurious excursion in the arc sections cannot be easily compensated given the fixed tunnel width. The radial offset of both lattices with respect to the LHC is presented in Fig 3.3. As the

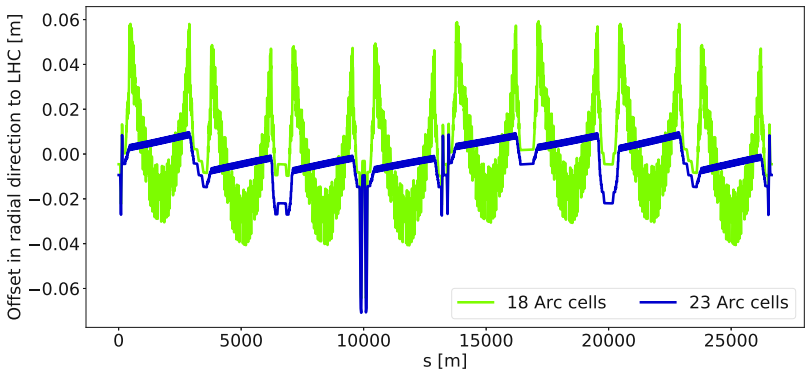

FIGURE 3.3: Radial offset of the HE-LHC lattice options with respect to the LHC

23x90 follows closely the LHC layout, with only minor changes in the arc cells due

to change in the required inter-magnet distance, it exhibits only a minor offset with respect to the LHC layout. The 18x90 layout on the other hand presents a peak offset of close to 6 cm around the dispersion suppressors in each arc. However, at present, further tunnel integration studies are required, taking into account also outer cryostat width and safety margin to other elements, to determine the maximum allowed survey offset. The offset around 10 km, present in both lattices, is explained by the change of the layout of the insertion at Point 4, where the separation dipoles were moved to provide more space for the RF-cavities [73].

In conclusion, two lattices are being studied in the HE-LHC, covering different scenarios. Assuming a maximum dipole of 16 T, the targeted collision energy of 27 TeV can only be reached by the 18x90 layout. However, assuming presented aperture consideration, an upgrade of the injectors would be required in order to increase the injection energy. The 23x90 lattice can only achieve a collision energy of 26 TeV with a maximum dipole field of 16 T, but allows for operation at a lower injection energy than the 18x90 layout. The feasibility of operating either HE-LHC lattice at an injection energy of 450 GeV, which would not require an upgrade of the injector, is subject to further studies.

Note that here the designs used for the studies presented in the following sections were described, which are available under [75]. Later studies have reexamined other arc layouts [76, 77], but concluded that no change of the choice of the studied lattices is required. Further optimisation of certain aspects of the lattice design such as reducing the offset with respect to LEP were conducted [78]. Given that one aspect of the presented work is to assess how the dynamic aperture changes with the field quality of specific dipole designs, all studies should be performed using the same optics and layouts. As such, it was decided to perform all studies with the same lattice version as described above.

3.3 Magnetic field errors and correction systems

The design of the electromagnets used in accelerators can be roughly be divided in two types, coil-dominated designs, and iron-dominated ones [79]. They differ in that the magnet field in an iron-dominated design is mainly determined by the shape of the (iron-)yoke, whereas in a coil-dominated magnets, the distribution of conductors and as such the current distribution is of importance. As the LHC and HE-LHC superconducting dipoles design is a coil-dominated design, in the following only specifics of this design are discussed.

It can be shown that an ideal dipole field may be achieved by using a cylindrical current bearing shell, where the current distribution follows $J(\theta) = J_0 * \cos(\theta)$, with θ the angle to the horizontal axis [80]. Due to the angle dependence of the current, such designs are called 'cosine-theta' designs, with one such being schematically depicted in Fig. 3.4.

The strength of the vertical field component inside the shell then depends next to the current density also on the coil width. Notably, due to up/down symmetry of the design no horizontal field component is present. However, such an ideal design cannot be reproduced in practice and instead of a cylindrical shell, coil blocks are used. As a result, next to the dipole field, also higher order magnetic fields are then introduced. The specific components which are introduced can be deduced from

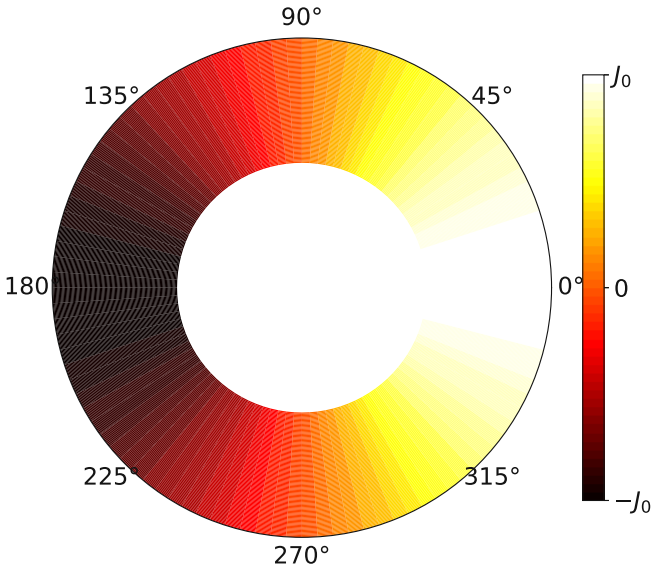

FIGURE 3.4: Cylindrical shell with a $cos(\theta)$-dependent current distribution.

symmetry considerations. In case of an up/down symmetry of the design, no skew components should be present. If additional left/right anti-symmetry is introduced, only odd higher order multipole components such as a sextupole field or a decapole field are introduced, which follow a $J(\theta) = J_0 * \cos(3\theta)$ and $J(\theta) = J_0 * \cos(5\theta)$ current distribution, respectively.

Such multipole components which are inherent to the design due to symmetry properties are called 'allowed multipoles'. However, such allowed harmonics can be minimized by carefully designing the magnet. Other 'nonallowed multipoles' present in a real magnet then may stem from manufacturing tolerances, leading to a symmetry breaking.

We note that the above described 'cosine-theta' design is the baseline option for the 16 T dipoles for the FCC-hh and the HE-LHC [24]. Other designs are also being explored but were not considered for the studies in the next sections.

To use the field quality of an accelerator magnet in further beam simulation codes, it is then convenient to separate the magnetic field $\vec{B}$ into separate multipole coefficients, which depend on the main field of the magnet. The magnetic field $\vec{B}$ in the transverse x-y plane is described by [81]

$$B_y + iB_x = \sum_{n=1}^{\infty} (B_n + iA_n) \left(\frac{x + iy}{R_r} \right)^{n-1}, \tag{3.2}$$

where n corresponds to the order of the multipole, which, following the European

convention, is $n = 1$ for a dipole, $n = 2$ for a quadrupole and so forth. B_n and A_n refer to the field strength of the given multipole in units of Tesla at a reference radius R_r. Finally, the field is then expanded relative to the main field B_N in case of a normal magnet or A_N for a skew magnet as follows

$$B_y + iB_x = \begin{cases} B_N \sum_{n+1}^{\infty} (b_n + ia_n)(\frac{x+iy}{R_r})^{n-1}, & \text{if normal magnet} \\ A_N \sum_{n+1}^{\infty} (b_n + ia_n)(\frac{x+iy}{R_r})^{n-1}, & \text{if skew magnet.} \end{cases} \tag{3.3}$$

The dimensionless coefficients b_n and a_n then represent the field strength of the magnetic field of order n relative to the main field. For a dipole with a bending angle of α, the integrated normalised strength of a given multipole n is then [82]

$$K_n L = \begin{cases} \alpha(n-1)! \frac{b_n}{R_r^{n-1}}, \\ \alpha(n-1)! \frac{a_n}{R_r^{n-1}}. \end{cases} \tag{3.4}$$

The coefficients b_n and a_n can then be further separated into the error sources and systematic or random errors. Field error tables for the LHC and following machines follow the procedure laid out in [82], where each harmonic b_n/a_n is described by three components, defined as systematic b_{nS}/a_{nS}, uncertainty per production line b_{nU}/a_{nU}, and purely random component b_{nR}/a_{nR}. For the case of the main dipoles, it is then further assumed that a systematic component is common to all magnets as it is inherent to the design, whereas the uncertainty component is present in all dipoles coming from one production line, with the nominal installation strategy being that magnets from the same production line will be installed in the same arc. Each harmonic in the dipole is then described by

$$b_n = b_{nS} + \frac{\xi_U}{1.5} b_{nU} + \xi_R b_{nR}, \tag{3.5}$$

$$a_n = a_{nS} + \frac{\xi_U}{1.5} a_{nU} + \xi_R a_{nR}, \tag{3.6}$$

where ξ_U and ξ_R are random numbers drawn from a Gaussian distribution cut at $1.5\,\sigma$ and $3.\,\sigma$, respectively. Following the above mentioned considerations, the same random number ξ_U is used for all dipoles in one arc, whereas ξ_R changes for each dipole. For the HE-LHC, the same procedure as used during the design phase of the LHC and described above is used. However, given the early state of development, in the field quality evaluations the uncertainty component and random component are assumed to be the same [83]. The random component is evaluated in simulation based on the experience of the alignment tolerances of the coil blocks in LHC and HL-LHC.

The presence of field components may disrupt the operation of an accelerator and decrease the performance via effects such as optics distortions or excess particle losses due to decrease of the dynamic aperture. Thus, corrections are applied for field components deemed critical for the success of the accelerator operation.

Correction strategies of unwanted higher order fields can broadly be separated in two categories, a local error correction or a global correction.

In the local correction approach, the unwanted higher order field component of a magnetic element is corrected by an adjacent magnet of that order. As an example,

to correct for field imperfection of the final focus triplets the LHC experimental insertion, a combined sextupole/dodecapole corrector is installed [84]. The required strength of the corrector is then set based on either using magnetic measurements or from beam-based measurements [85].

Contrary to that, instead of correcting the errors where they occur, in the global correction approach the adverse effects are corrected for. In the LHC, such a scheme is chosen for example to correct the tunes. Here, spurious quadrupole fields are not corrected for where they occur, but rather their impact on the tunes is corrected by distributed trim quadrupoles. Their location and powering scheme have been chosen such that they act only the tune and do not introduce a large increase in β-beating.

For the correction of specific error sources, the HE-LHC follows largely the correction schemes used in the LHC [82]. In Fig. 3.5, the layout of a half-cell is illustrated, with the corrector elements described in the following.

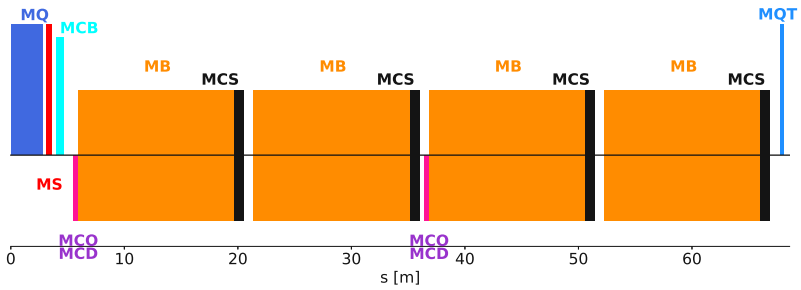

(A) One half-cell in the 18 cells layout

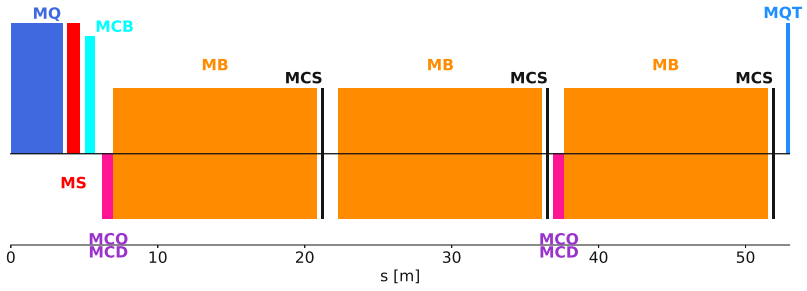

(B) One half-cell in the 23 cells layout

FIGURE 3.5: Corrector layout in the HE-LHC designs. Here, MQ refers to a main quadrupole, MQT to a tune quadrupole, MS to chromaticity sextupole, MCB to an orbit corrector, MB to an main dipole, MCS to a sextupole spool piece corrector, and MCO/MCD to a nested octupole/decapole corrector.

Both for the correction of tune and chromaticity, global correction schemes were implemented. For the tune correction, tune quadrupoles are installed next to both the focusing and defocusing quadrupoles in the four arc cells on both extremities. For tune matching, the tune quadrupoles are separated into two families, depending if the tune quadrupole is sitting next to a focusing or a defocusing quadrupole. Here as in the following, assigning correctors to one family means that these will have the same strength.

The chromaticity sextupoles as well as orbit correctors are located on the other side of the arc quadrupoles. These sextupoles are installed next to all arc quadrupoles except for four quadrupoles, where instead skew sextupoles are installed [86]. For adjusting the chromaticity, sextupoles were split in two families, based on if located next to a focusing or defocusing quadrupole. We note that in the LHC, sextupoles are split further into four families [87], though this further distinction is only used with special types of optics [88].

For the correction of the field errors of the main dipoles, a local correction scheme is used.

To correct the sextupole component of main dipoles, sextupole spool pieces are attached to each dipole. In the LHC scheme, all sextupole spool piece correctors in one arc are part of one family. Their strength is set such to correct for the average sextupole component of the main dipoles in one arc. This scheme has also been assumed as the baseline scheme for the HE-LHC.

The LHC octupole and decapole components are corrected by nested corrector coils, attached to every second dipole. As for the sextupole spool piece correctors, all nested correctors of the same multipole order in one arc belong to one family and are set to correct for the average octupole and decapole components.

Other correctors such as skew quadrupoles and skew sextupoles have been implemented in the HE-LHC lattices, but were not used in the studies presented in the next two sections and will not be described here.

3.4 Assessment of the Dynamic Aperture and limiting factors

In the design phase of a hadron collider, the assessment of the dynamic aperture (DA) in all phases of operation is critical for defining the expected performance. Here, the performance is usually linked to the luminosity which depends amongst other factors on the number of colliding particles. As the dynamic aperture is linked to particles loss, given that particles outside of the DA are lost, a too low DA would thus result in a severe decrease of colliding particles and thus of luminosity.

For machines like the LHC, different contributions play a role for the various phases during operation. In case of the LHC, the operational cycle is roughly divided into three phases, injection, energy ramp, and collision. At collision, the beams are focused by the quadrupoles of the triplet to achieve the smallest feasible beam size in the interaction point and thereby increase the luminosity. Conversely, the beam size in the final focus quadrupoles is large and thus susceptible to field errors of the final focus quadrupoles and separation dipoles. As such, the DA at collision energy is expected to be dominated by the field quality of these magnets, not taking into account the effects of the beam-beam interaction.

On the other hand, DA at injection energy is dominated by the field errors in the main dipoles, due to the number of dipoles in the machine and that beam occupies most of the available aperture [89], which is the focus of the following studies for the HE-LHC. Dynamic aperture studies for the HE-LHC at collision energy taking into account the expected field quality of the final focus quadrupoles have been performed and are presented elsewhere [90].

For the tracking studies, the MAD-X [68] models of the HE-LHC lattices were used and using the SixDesk [91–93] environment, SixTrack [53, 94, 95] tracking studies were set up. For these studies, only single particle effects were considered, that is no interaction between particles is assumed, which allows for full parallelization in that each particle can be tracked in a separate process with no inter-process communication required. Note that for every tracking process, SixTrack actually tracks two particles with a small difference in the initialization amplitude. By studying the evolution of the distance of the two particles, the Lyapunov exponent can be evaluated and allows determination on the stability of motion [96]. Particles are initialized in radial direction in steps of 1 σ, where the nominal normalized emittance of 2.5 μm was used. Particles were initialized using five different emittance ratios $\sqrt{(\epsilon_y/\epsilon_x)}$, corresponding to angles in x-y space. Angles were determined using

$$\theta_i = \frac{90° i}{N+1} = arctan(\frac{\epsilon_y}{\epsilon_x}), \text{ with } 1 \geq i \geq N, \tag{3.7}$$

where N is the number of angles probed. For the study case, 60 different realizations of the probed HE-LHC lattice were used, that is, 60 different seeds were used to determine the random numbers used for magnet error assignment.

While for circular lepton accelerators, where particles experience strong radiation damping, studies only require tracking for a few thousands of turns, in hadron machines where such a damping effect is weak, tracking should ideally be conducted for the the operational cycle length. To account for losses due to the dynamic aperture in the LHC at injection, where the injection of all bunches for a physics fill may take about 90 minutes [97], tracking should be performed for about $5 \cdot 10^7$ turns at injection energy. However, with current computational power, performing tracking studies for such amount of turns is not feasible in a reasonable amount of time. For the presented studies, particles were tracked for 10^5 turns, corresponding to around 11 s of machine time.

Using a similar set of parameters, it was determined that the DA results from different computing architectures may differ by up to 0.5 σ [98]. Studies presented in [99] show that by better sampling of the parameter space by either increasing the number of probed angles or seeds, the found minimum DA might decrease by 1 σ. However, given the vast number of tracking studies performed (60 seeds $\times$ 5 angles $\times$ 20 amplitudes = 6000 tracking jobs for one lattice and one energy), it was decided to keep using the presented numbers in order to keep the computation load at a reasonable level.

Full 6D tracking is performed, with the RF-parameter used as presented in Tab. 3.3.

Energy	**18 arc cell lattice**		**23 arc cell lattice**	
[GeV]	Voltage [MV]	$\Delta p/p$ [10^{-4}]	Voltage [MV]	$\Delta p/p_0$ [10^{-4}]
450	10.7	6.53	10.4	8.27
900	10.8	4.61	10.5	5.84
1300	10.8	3.84	10.6	4.86

TABLE 3.3: RF parameters for both HE-LHC lattices [25]. The $\Delta p/p$ corresponds to 75% of the bucket height.

Magnetic field errors are assigned to all main dipoles following the procedure outlined in the previous section. Care is taken that the sign of the even harmonics changes between the inner and outer aperture [81]. Furthermore, harmonics b_1, a_1, b_2, and a_2 were not used and potential misalignments of any elements were not taken into account to exclude any linear harmonics through feed-down. This is to ensure that the linear optics is the same for all the studied cases and avoid any potential influence of β-beating or linear coupling on the DA. The spool piece correctors are set following the correction scheme described above. Lastly, after application and correction of the magnetic field errors, the fractional tunes are matched to $Q_x = 0.28/Q_y = 0.31$ and chromaticity is matched to $Q'_x = Q'_y = 0$.

The results from the tracking are then processed to infer the DA using SixDB [100]. Note that particles are considered lost in SixTrack once they cross the aperture limitation, set to 1 m in the x-y plane [53].

In the following, only the minimum DA from the 5 angles in x-y space and from the 60 seeds is given.

The minimum DA from tracking simulations considered acceptable for machine implementation is 12 σ, as was used during the design of the LHC [101]. For the LHC, this number was concluded on assuming a variety of modelling uncertainties and safety margins, which in the worst case should yield an eventual DA in the machine of 6 σ, which is also the physical aperture of the collimation system. However, experiments in the past have demonstrated excellent agreement between models and measurements [102, 103], making this target DA potentially too stringent. While currently studies are ongoing aiming to provide a realistic description of beam losses and as such beam lifetime using tracking studies [104], these are currently still in an exploratory phase and as such using beam lifetime as a potentially more tangible target parameter was not considered an option. As such, the above mentioned target DA of 12 σ is kept, assuming that meeting this target will ensure sufficient beam lifetime and that, while quite stringent, it should allow for a good classification of which scenarios are feasible for the HE-LHC. Furthermore, it may also provide sufficient margin for special operation conditions, such as if for mitigation of transverse instabilities, running with a higher chromaticity or with strong Landau octupoles is required, both of which likely resulting in a decrease of dynamic aperture. Given the involved hardware and process dependent nature of the beam stability mechanism, estimating a reasonable range of settings in the conceptual design phase of this machine to cope with all possible instability scenarios is rather complicated, which is why only this baseline scenario with a high safety margin is studied. In case the HE-LHC study moves forward, targeting a technical implementation, more studies may be performed with the chosen scenario to assess in detail the requirements in terms of long time stability.

Initial tracking studies were performed assessing the DA in both lattices and at all injection energies without implementing any field errors. Thin lattice versions were used together with a simplified Hamiltonian, using the small-angle approximation to expand the accelerator Hamiltonian instead of its "exact" form [105], which was done in an effort to reduce computation time. In this setup, the only sources of nonlinear fields are the chromaticity sextupoles in the arcs, powered such to correct the natural chromaticity. In Tab. 3.4, the minimum DA for both lattices and at three different injection energies is presented.

Lattice	Injection Energy [GeV]		
	450	900	1300
18 arc cells	58 σ	97 σ	123 σ
23 arc cells	42 σ	61 σ	75 σ

TABLE 3.4: Minimum DA for both HE-LHC lattices and at different injection energies.

Notably, the 18x90 layout shows a higher dynamic aperture in all cases, which is attributed to the difference in the sextupole powering. In the 18x90 layout, which has the smaller number of chromaticity sextupoles compared to the other layout though these being located at locations with larger β-functions and dispersion function, the required integrated normalised strength of one focusing/defocusing sextupole is $k_3L = 8.81 \cdot 10^{-3}$ m^{-2}/ $-1.80 \cdot 10^{-2}$ m^{-2}, whereas $k_3L = 2.33 \cdot 10^{-2}$ m^{-2}/ $-3.75 \cdot 10^{-2}$ m^{-2} is used in the 23x90 layout.

For the following studies, field errors were applied to all main dipoles using the values presented in Tab. A.1. Here, no correction was applied by the spool piece correctors, only chromaticity was matched to the aforementioned values using the chromaticity sextupoles. The resulting DA is presented in Tab. 3.5.

Lattice	Injection Energy [GeV]		
	450	900	1300
18 arc cells	0 σ	0 σ	0 σ
23 arc cells	1.3 σ	1 σ	2 σ

TABLE 3.5: Minimum DA for both HE-LHC lattices and at different injection energies using the field errors presented in Tab. A.1.

Compared to previous case, a reversed picture is presented, with 23x90 layout showing a non-zero DA in all cases, whereas all particles were lost in the studies with the 18x90 layout. The decrease of the DA when going from 450 GeV to an injection energy of 900 GeV may be explained by the increase of the systematic sextupole component from $-35 \cdot 10^{-4}$ units to $-55 \cdot 10^{-4}$ units. All cases being far away from the target DA, these studies illustrate the necessity of the application of the spool piece correctors to correct for the field errors in the dipoles.

In the following studies, the effect of single components and its correction are assessed. Following the provided correction scheme of the LHC, sextupole, octupole, and decapole components were included and corrected. The results are presented in Tab. 3.6.

Here, as also in the previous presented case where no corrections were applied, the 23x90 lattice shows a higher DA in every scenario compared to the 18x90 layout. Furthermore, in both layouts, foregoing the correction of the b_3 component results in the smallest DA in all cases. Moreover, even with only the sextupole component in the dipoles and correction provided by the spool piece correctors, the DA in all but one case is below the target. Similarly so, the b_5-component, if uncorrected, results in a significant decrease of the minimum DA. However, using the LHC correction scheme for this decapole component, the minimum DA is met in both lattices at the highest injection energy of 1.3 TeV, and also in the 23x90 layout for the case of an injection energy of 900 GeV. The octupole component, and here in particular only the

Lattice	Scenario	Injection Energy [GeV] 450	900	1300
18 arc cells	b_3	0 σ	0 σ	0.3 σ
	b_3 + correction	2.2 σ	4.5 σ	7.4 σ
	b_4	10.6 σ	15 σ	18.6 σ
	b_4 + correction	22 σ	32 σ	40 σ
	b_5	2 σ	2.9 σ	6.3 σ
	b_5 + correction	8 σ	11.3 σ	18.4 σ
23 arc cells	b_3	1.5 σ	1.5 σ	2.7 σ
	b_3 + correction	3.3 σ	7.5 σ	12.6 σ
	b_4	11.2 σ	17.3 σ	20.6 σ
	b_4 + correction	24.2 σ	40.3 σ	48.7 σ
	b_5	4.1 σ	6.8 σ	11.6 σ
	b_5 + correction	11.8 σ	20.5 σ	32.3 σ

TABLE 3.6: Minimum DA for both HE-LHC lattices and at different injection energies using certain field components and corresponding correctors.

component arising from mechanical tolerances, and its correction only play a role at the lowest considered injection energy of 450 GeV, as in all other considered scenarios, the minimum DA is above the target. Including all components and correction for the aforementioned three components reflects the behaviour seen before for only the case of the sextupole component, as is illustrated in Tab. 3.7.

Lattice	Injection Energy [GeV] 450	900	1300
18 arc cells	1.5 σ	4.2 σ	7.6 σ
23 arc cells	2.7 σ	7.0 σ	12.1 σ

TABLE 3.7: Minimum DA for both HE-LHC lattices and at different injection energies using all field errors presented in Tab. A.1 and correction for the b_3, b_4, and b_5 components.

For the estimated field quality of Tab. A.1, only one scenario, namely the 23x90 at the highest considered injection energy, meets the aforementioned target DA of 12 σ. However, this scenario is considered the most undesirable, given that the 23x90 layout only allows for a collision energy of 26 TeV, while due to its smaller beam size it is the more feasible design at lower injection energies. From these results, it is concluded that the main driver for the reduction of the dynamic aperture is the sextupole component of the dipoles and its correction is critical in improving the DA.

First studies to guide the magnet design looked into the impact of systematic sextupole component compared to the random one. The uncertainty component is kept as before, while it is assumed that the correction being on a per arc basis can cope well with shift of all dipoles. Studies were performed only for the worst performing scenario, being the 18x90 layout at an injection energy of 450 GeV.

From the result of the tracking studies presented in Tab. 3.8, it is apparent that a

		b_{3R}		
		2	6	10
b_{3S}	30	6.3 σ	3.7 σ	1.9 σ
	20	7.5 σ	4.0 σ	2.3 σ
	10	8.8 σ	4.0 σ	2.3 σ

TABLE 3.8: Minimum DA in the layout at an injection energy of 450 GeV, with only sextupole field components included in the dipoles and corresponding correction.

reduction of the random sextupole component is more beneficial in terms of the DA compared to reducing the systematic component. This may be seen as a result of the correction strategy, which only corrects for the average sextupole component of the dipoles, with the deviation of the individual dipoles remaining uncorrected. As such, the reduction of the spread due to the random sextupole component allows for a more efficient correction, in terms improving the DA. However, it has to be noted that even for systematic and random sextupole components similar to what was foreseen for the LHC [106], the DA in the 18x90 does not reach satisfactory levels.

Following these studies, the next version of the main dipole design features a significantly reduced random sextupole component, akin to the random component of the LHC main dipole during the design phase. Compared to the previous error table, here improvements in the Nb_3Sn superconductor development were included which allow a reduction of the persistent current contribution, in turn causing the reduction almost all error components [107]. The full error table is presented in Tab. A.2. Compared to the previous field quality table, the systematic sextupole component is also significantly reduced, with the highest now observed at 450 GeV instead of 900 GeV observed before. In Tab. 3.9 the minimum DA for the updated field quality table are presented, using the LHC correction scheme as explained in Sec. 3.3.

Lattice	**Injection Energy [GeV]**		
	450	900	1300
18 arc cells	5.3 σ	8.8 σ	11.3 σ
23 arc cells	8.4 σ	12.7 σ	15.3 σ

TABLE 3.9: Minimum DA for both HE-LHC lattices and at different injection energies using all field errors presented in Tab. A.2 and correction for the b_3, b_4, and b_5 components.

Due to the significant improvements in the field quality, an increase of the minimum DA across all study cases is observed. Using the aforementioned 12 σ as threshold, the 23x90 layout presents two viable options at 900 GeV and 1300 GeV, both in terms of physical aperture as well as dynamic aperture. As with the previous table, the 18x90 layout performs worse in terms of DA compared to the other layout, with only the scenario with the highest injection energy close to the required DA.

Further studies looked in the changes in global observables like amplitude detuning as a way to identify specific quantities which may explain the increase in DA and difference between the two lattice versions. Focus was put on the cases with an injection energy of 450 GeV where the most significant increase occurred for both lattices. First studies looked into difference of the amplitude detuning between the

two error tables, including all field components and correcting for the b_3, b_4, and b_5 components. In Fig. 3.6, histograms of the amplitude detuning of 60 different realizations of the 18x90 layout are presented, evaluated using MAD-X PTC.

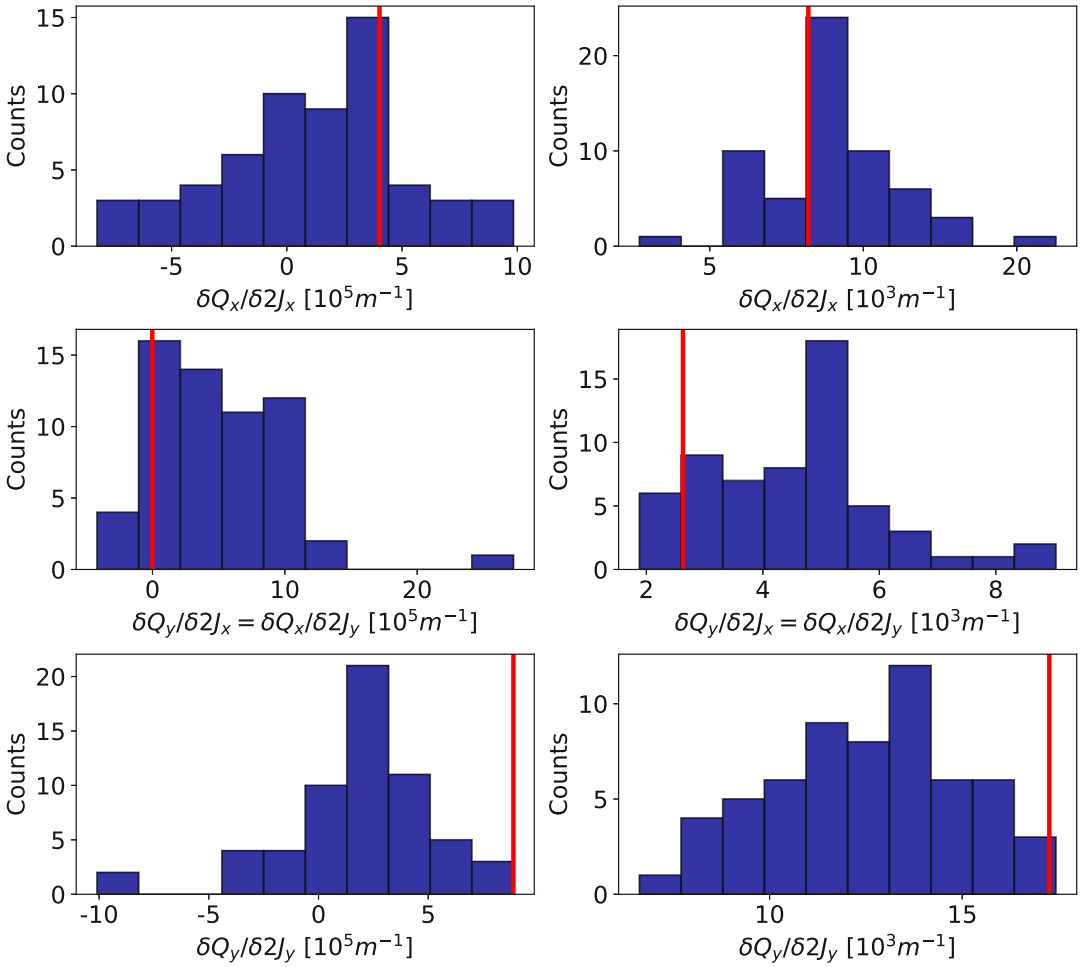

(A) Amplitude detuning for 60 different lattices using the field quality from Tab. A.1.

(B) Amplitude detuning for 60 different lattices using the field quality from Tab. A.2.

FIGURE 3.6: Amplitude detuning for 60 different realizations of the 18x90 lattice at an injection energy of 450 GeV. Marked in red are the values for the worst performing seed.

Compared the results from the previous error table illustrated in Fig. 3.6a to the results presented in Fig 3.6b for the updated error table, a significant decrease in the amplitude of about one order of magnitude is observed for all three components. First order amplitude detuning ($\delta Q/\delta 2J$) is driven by the first order contribution from the octupole and as a second order contribution from sextupoles [108]. While Tab. A.2 shows a systematic octupole component not present in the previous error table, this component is an order of magnitude smaller than the random and uncertainty component, which have remained the same between these versions. As such, the decrease of the amplitude detuning is mainly attributed to the changes of the sextupole components. Notably, the worst performing seed (marked with a red line) shows a similar behaviour in both cases, in that while horizontal direct detuning ($\delta Q_x/\delta 2J_x$) and cross plane detuning ($\delta Q_x/\delta 2J_y = \delta Q_y/\delta 2J_x$) show behaviour similar to other seeds, the direct detuning in the vertical plane ($\delta Q_y/\delta 2J_y$) is in both

cases at the upper end of the scale. In both cases, the minimum DA is reported for the case where the angle is 45°.

The same studies were performed for the 23x90 layout and are presented in Fig. 3.7.

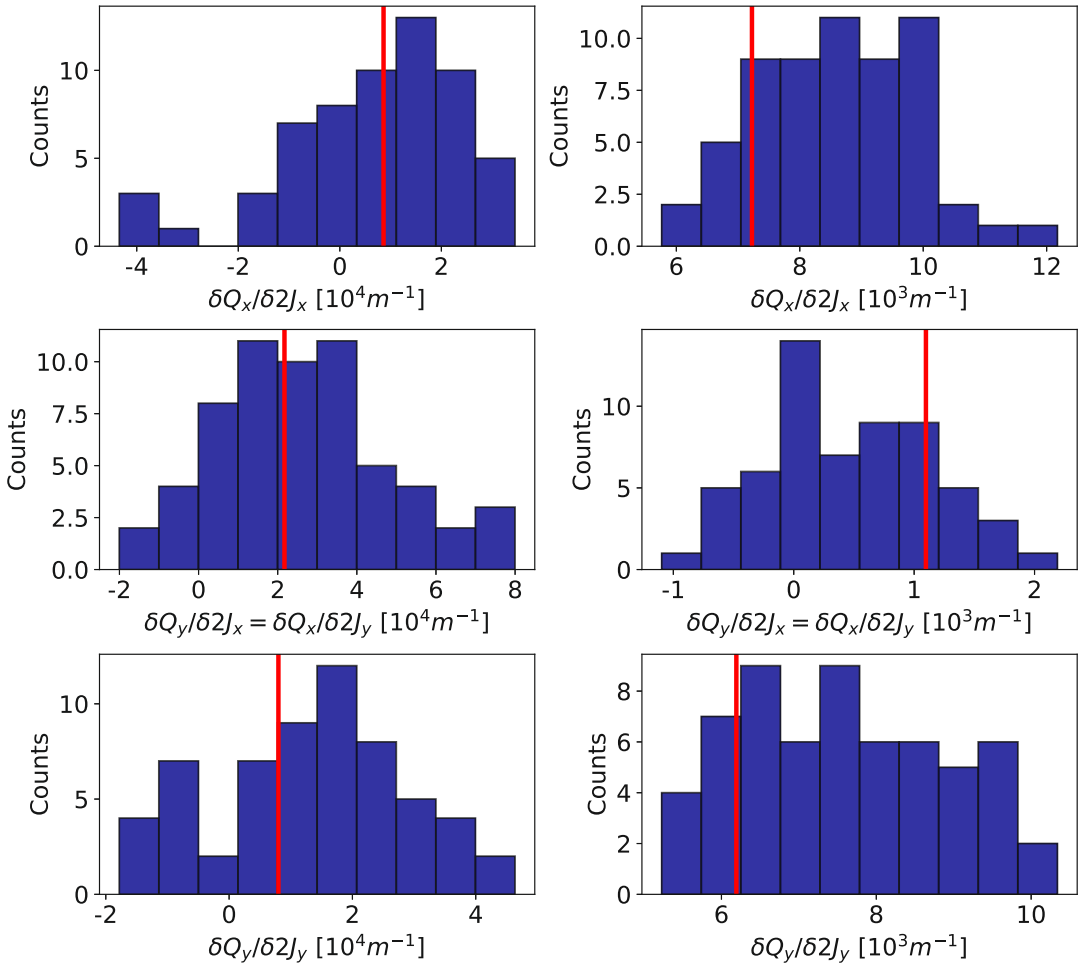

(A) Amplitude detuning for 60 different lattices using the field quality from Tab. A.1.

(B) Amplitude detuning for 60 different lattices using the field quality from Tab. A.2.

FIGURE 3.7: Amplitude detuning for 60 different realizations of the 23x90 lattice at an injection energy of 450 GeV. Marked in red are the values for the worst performing seed.

Similar to the 18x90 case, a stark decrease of the amplitude detuning is observed between the two error tables, which again is mostly attributed to the change of the sextupole component. However, the 23x90 also shows a smaller amplitude detuning in all three components by an order of magnitude compared to the other layout, which partly explains the larger DA observed in this LHC-like layout. Unlike the 18x90, no distinct behaviour can be made out for the worst performing seed, where again particle loss is reported for case where the angle is 45°.

Another global observable investigated is the second order chromaticity, which unlike the first order chromaticity is not directly corrected for. Where first order chromaticity stems from quadrupole and sextupole sources, second order chromaticity

additionally is created by octupoles and by sextupoles as a second order contribution [108]. As 6D tracking is performed for the DA studies where particles are initialized with a momentum offset as noted in Tab. 3.3, particles loss due to momentum detuning may also contribute to a low DA. In Fig. 3.8, the second order chromaticity ($\delta^2 Q/\delta(\frac{\Delta p}{p_0})^2$) in both planes of 60 different realizations of the 18x90 layout is shown.

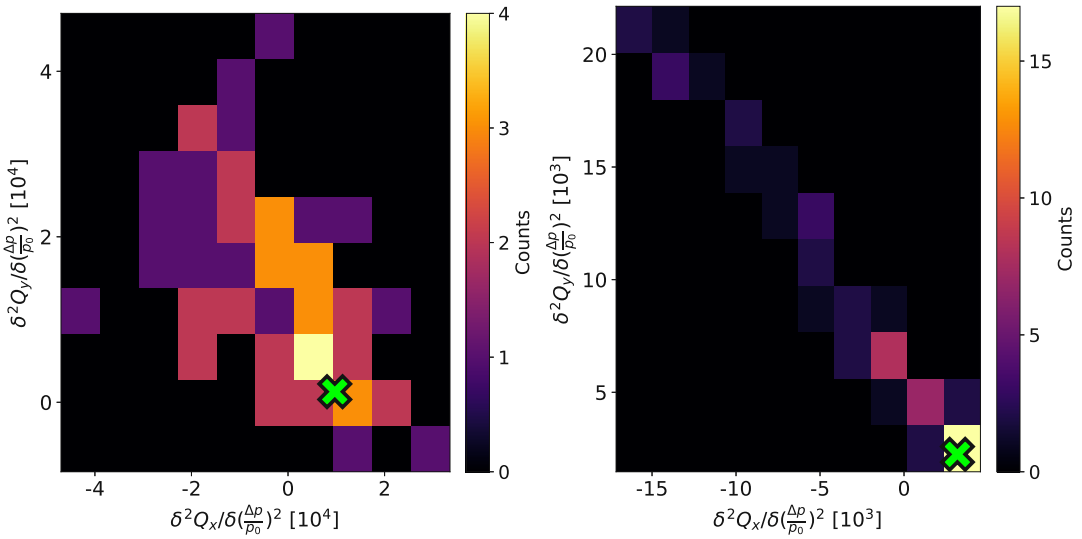

(A) Second order chromaticity for 60 different lattices using the field quality from Tab. A.1.

(B) Amplitude detuning for 60 different lattices using the field quality from Tab. A.2.

FIGURE 3.8: Second order chromaticity for 60 different realizations of the 18x90 lattice at an injection energy of 450 GeV. The values for the worst performing seed are marked with a lime cross.

Similarly to what was observed for the case of the amplitude detuning, a decrease of about a factor 2 is observed between the two error table. Additionally, a reduction in the spread of the second order chromaticity is observed, which the results for new field quality table also showing a narrow distribution. The second order chromaticity of the worst performing seed (marked with a lime cross) is in both cases close to highest bin, which itself is far off the maximum of the encountered absolute values, as such indicating that the momentum detuning does not play a significant role in the low DA for this specific seed.

In Fig. 3.9, the results of the second order chromaticity studies for the 23x90 lattice are presented.

As before, the new field quality table results in a stark decrease of the maximum second order chromaticity encountered, as well as the spread. Both in the case of the 18x90 and the 23x90 layout, the results for the updated field quality table show a strong correlation between the horizontal and the vertical second order chromaticity. Again, the values of the worst performing seed are not found to be at the upper or lower limit of the 60 cases, again indicating that the second order chromaticity alone is not the deciding factor for this seed.

To further investigate the effect of the momentum offset on the minimum DA, tracking studies were performed using the same lattices and error tables, but with a reduced momentum offset to what is presented in Tab. 3.1. The results of those studies

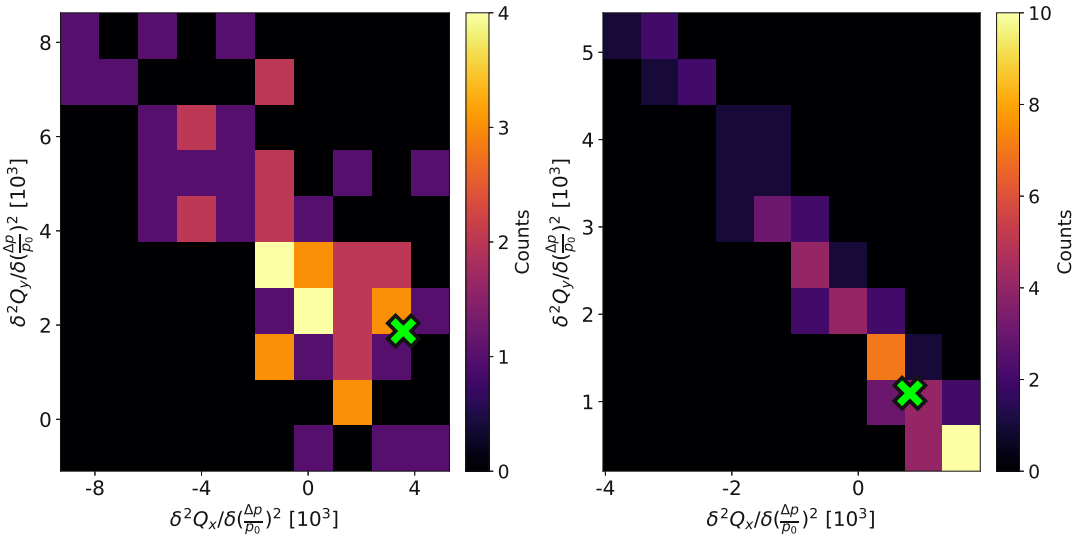

(A) Amplitude detuning for 60 different lattices using the field quality from Tab. A.1.

(B) Amplitude detuning for 60 different lattices using the field quality from Tab. A.2.

FIGURE 3.9: Second order chromaticity for 60 different realizations of the 23x90 lattice at an injection energy of 450 GeV. The values for the worst performing seed are marked with a lime cross.

are presented in Tab. 3.10.

Lattice	**Error table**	**Percentage of the nominal** $\Delta p/p_0$ 25%	50%	75%	100%
18 arc cells	Tab. A.1	2.2 σ	2.0 σ	1.8 σ	1.5 σ
	Tab. A.2	6.9 σ	7.0 σ	6.2 σ	5.3 σ
23 arc cells	Tab. A.1	4.5 σ	3.5 σ	3.7 σ	2.7 σ
	Tab. A.2	11.1 σ	10.6 σ	9.0 σ	8.4 σ

TABLE 3.10: Minimum DA for both HE-LHC lattices at an injection energy of 450 GeV, for different initialization of the momentum offset.

Notably, in all cases, with decreasing the momentum deviation, also the angle at which the lowest DA is found decreases. In all cases where tracking was performed using 25% of the nominal momentum offset, the minimum DA is found at an angle of 15°, compared to the 45° found in the nominal case.

For the same dipole design, another error table using conductor parameter deemed more realistic is presented in Tab. A.3. This realistic conductor parameters foresee thus resulting in a slightly increased persistent current contribution and thus an increase of most error components. The most notable change is observed at 450 GeV, where for example the systematic sextupole component almost doubles due to the change in persistent current contribution. In Tab. 3.11, the minimum DA for the field quality table assuming more realistic conductor parameters is presented.

Given the substantial degradation of most field components at 450 GeV, the minimum DA decreases in both layouts by about 2 σ. For the other injection energy cases, the changes in the error components are less drastic and as such the minimum DA

Lattice	Injection Energy [GeV]		
	450	900	1300
18 arc cells	3.2 σ	8.4 σ	11.2 σ
23 arc cells	5.9 σ	13.1 σ	16.3 σ

TABLE 3.11: Minimum DA for both HE-LHC lattices and at different injection energies using all field errors presented in Tab. A.3 and correction for the b_3, b_4, and b_5 component.

found differs only slightly to the more optimistic conductor scenario. Subsequently, conclusions on the feasibility of the different scenarios remain as before.

Before any further studies were conducted, the dipole design and its field quality were updated to account for a new design with an increased beam-separation of 250 mm compared to the 204 mm used in the previous design. Furthermore, an asymmetric coil layout was used, which in turn introduces systematic field harmonics previously considered non-allowed. Both changes aim to reduce the systematic quadrupole component at top energy, as its correction significantly pushes the required main quadrupoles strength [109]. To account for the correction of this component, the length of the quadrupole would need to be increased to provide for the required integrated strength, in turn leading to a decrease of the available space for dipoles in turn leading to a potential decrease of the maximum available collision energy. As such, in the updated dipole designs, the quadrupole component is reduced from $-56.6 \cdot 10^{-4}$ to $-0.025 \cdot 10^{-4}$, significantly relaxing the quadrupole strength requirements at the expense of introducing other components. Again, two error tables are available, one assuming ideal conductor parameters (Tab. A.4) and one assuming a less efficient correction of the persistent current contribution (Tab. A.5). Comparing both tables, previously considered allowed harmonics such as b_3 and b_5 change by less than 4 units, whereas harmonics such as b_4 deemed non-allowed in the previous dipole design see an increase by an order of magnitude or more, yet in all but one case staying under 1 unit.

In Tab. 3.12 and Tab. 3.13, the minimum DA for both new error tables is presented.

Lattice	Injection Energy [GeV]		
	450	900	1300
18 arc cells	5.2 σ	8.8 σ	12.0 σ
23 arc cells	7.9 σ	12.9 σ	16.9 σ

TABLE 3.12: Minimum DA for both HE-LHC lattices and at different injection energies using all field errors presented in Tab. A.4 and correction for the b_3, b_4, and b_5 component.

As with the previous design, scenarios deemed feasible are the 23x90 at injection energies above 900 GeV, irrespective of the conductor properties, and 18x90 lattices at 1300 GeV for the case of optimistic conductor parameters without any changes to correction system. Given the small changes in the harmonics b_3 and b_5, which were previously shown to have a strong impact on the DA even with correction, the results in terms of DA are similar to those using the error tables for the symmetric coil layout. In return, the introduction of systematic b_6 and b_8 harmonics appears to only have a small impact on the results, suggesting that no specific correction might be

Lattice	Injection Energy [GeV]		
	450	900	1300
18 arc cells	2.7 σ	7.4 σ	11.2 σ
23 arc cells	5.4 σ	12.8 σ	15.9 σ

TABLE 3.13: Minimum DA for both HE-LHC lattices and at different injection energies using all field errors presented in Tab. A.5 and correction for the b_3, b_4, and b_5 component.

necessary. To conclude on the necessity of higher order correctors for certain components further studies were performed for cases where the DA is significantly below the target threshold. Studies here were only performed with the error table A.5 representing the realistic conductor parameters. Given that the biggest changes between the error table for realistic and for optimistic conductor parameters is a factor 2 between the systematic b_3 and b_5 components, two additional study cases were included were the systematic component of one harmonic is reduced while keeping the other at the same level.

The results for these studies and a comparison to the nominal minimum DA is presented in Tab. 3.14.

Injection Energy [GeV]	18 arc cells 450	18 arc cells 900	23 arc cells 450
nominal minimum DA	2.7 σ	7.4 σ	5.4 σ
50% b_{3S}	4.4 σ	8.1 σ	7.0 σ
50% b_{5S}	2.8 σ	7.7 σ	5.4 σ
no b_3 correction	0.0 σ	1.7 σ	0.8 σ
no b_4 correction	2.6 σ	7.7 σ	6.4 σ
no b_5 correction	1.1 σ	4.1 σ	2.0 σ
$b_{6S} = 0$	2.7 σ	7.4 σ	5.5 σ
$b_{7S} = 0$	2.9 σ	8.2 σ	5.5 σ
$b_{9S} = 0$	2.7 σ	7.7 σ	5.3 σ

TABLE 3.14: Minimum DA for studies with individual harmonics altered to evaluate its impact.

The studies with the reduced systematic b_3 component (dubbed 50% b_{3S} in Tab. 3.14) show a drastic increase in DA, in particular at 450 GeV, coming to within 1 σ to the results of the error table with the optimistic conductor parameters, while keeping all other components as before. Reducing the systematic b_5 component on the other hand does not show a significant increase in the DA, in particular the results in both lattices at 450 GeV barely change. As such, following also the previous studies comparing amplitude detuning for error table A.1 and A.2, the high systematic sextupole component of 50 units appears to be the main driver of the low DA in the 450 GeV injection energy cases.

Results corresponding to entries marked with *no b_n correction* represent studies where only the correctors for the *n th*-component were turned off to evaluate the need for this specific corrector circuit. As already concluded from previous studies, the local correction of the sextupole and decapole components is required as the DA

would otherwise would be significantly decreased. On the other hand, the correction of the octupole component does not appear necessary, in particular as in two cases the minimum DA slightly improves. These improvements are thought to stem from a favourable change of the amplitude detuning due to the uncorrected octupole contribution, but were not further investigated.

Lastly, studies were performed where the systematic component of the $n\,th$-harmonic was set to 0 to emulate an ideal correction and assess its need. Harmonics b_6, b_7, and b_9 were selected for these studies, with b_7 and b_9 the next strongest components above a decapole, and b_6 being the largest component introduced by the asymmetric coil design. In all cases, the minimum DA remains largely the same or increases only slightly, with the largest improvement being less than 1 σ, as such indicating that no specific correction of these components, either by a revised dipole design or by installation of corrector magnets, is necessary.

3.5 Effect of sorting on the dynamic aperture

In the previous section, the minimum DA for different operating scenarios of the HE-LHC were investigated, based on the field quality estimates of its main dipole. It was found that using the correction scheme of the LHC, both studied layouts do not meet the defined threshold DA at 450 GeV, as such excluding scenarios where the current SPS could be used as an injector. Even with an upgrade of the SPS to inject at an energy of 900 GeV, the `18x90` layout does not appear fit for implementation as the DA is about a factor 1.5 below the threshold. Additionally, at this injection energy the layout does not meet the target beam stay clear of the HL-LHC. Particularly for the 450 GeV scenario, one of the main drivers of the insufficient DA appears to be the large systematic sextupole component in the dipoles. However, for all studies presented above, the pessimistic assumption was made that during the installation of the dipoles, no care is taken on where each unit will be installed, in turn also not requiring any additional information on alignment or field quality from previous measurements. On the other hand, in the LHC, where the field quality of the main dipoles met most of the specifications and providing sufficient DA with the above mentioned pessimistic assumptions, before the installation in the tunnel commenced, magnet measurements were conducted to assess both field quality and mechanical tolerances and an installation strategy was devised to optimize machine performance [89, 110]. While sorting in this case was performed not focusing only on optimizing DA but also to improve the mechanical acceptance of the arcs, an increase of the DA of about 1.5 σ is seen in simulations due to these measures.

Given the precedence set by the LHC, it is thus only natural to assume similar measures will be in place during the installation of the HE-LHC. As such, studies were conducted evaluating the potential impact of the sorting for the different HE-LHC scenarios. In these studies, the sole focus lies on improving the minimum DA, in particular the effect of sorting dipoles by their b_3 component given that this component has shown to have the largest impact on the DA. No other effects such as other field components or mechanical tolerances are considered in the following sorting algorithms. Furthermore, another simplification made in the following is that magnet assemblies are indistinguishable unlike to the LHC where a distinction is made in the sorting algorithm between dipoles with and without the attached nested octupole/decapole spool piece corrector. Lastly, in the following sorting approach, it

is assumed that all dipoles are measured and available for installation. This was not the case for the LHC, where only a few dipoles were measured at their operating temperature of 1.9 K. All other dipoles were measured at room temperature and established warm-to-cold relations were used to infer the field quality at 1.9 K [111, 112]. Furthermore, magnets were delivered in batches and installed shortly after the delivery, thus preventing optimal global sorting. The results aim to illustrate an upper bound of what could be achieved in terms of DA, which make scenarios not meeting the target DA despite these optimistic sorting unlikely to be feasible for implementation.

Given the strong dependence of the DA on the random sextupole component in the first error table A.1, first studies looked into the effect of sorting for this error table. As the high random sextupole component, together with the powering scheme only allowing to correct for the average sextupole component in each arc, is believed to allow for a significant residual error which causes the low DA, the aim is to reduce the variance of the sextupole component per arc. In the first studies, this was accomplished by simply ordering the dipoles according to their sextupole component, as such reducing the variance by pairing sextupole with a similar sextupole component in the same arc. The distribution of the sextupole components and octupole components for one seed before and after this simple sorting is presented in Fig. 3.10a, with the mean and variance of both components illustrated in Fig. 3.10b.

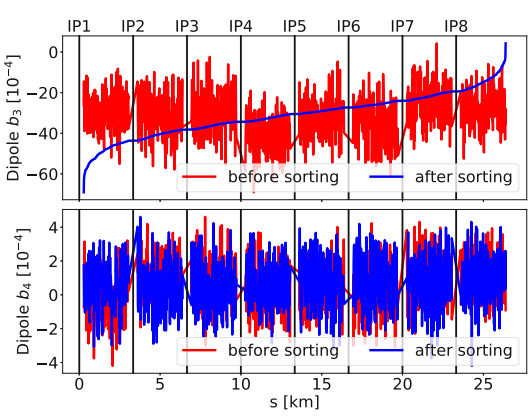

(A) Sextupole and octupole component for one seed before and after sorting.

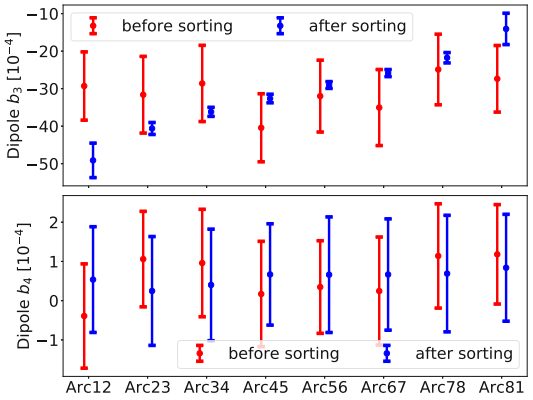

(B) Mean and variance per arc for the sextupole and octupole component in one seed before and after sorting.

FIGURE 3.10: Illustration of the simple sorting on the sextupole and octupole component using one seed of the tracking studies for the 23x90 lattice.

Thanks to this simple sorting, a drastic reduction of the variance of the sextupole component is found across all arcs. Given the simplistic nature of the sorting algorithm, which does only allow for sorting on one variable, and with no correlation between components assumed when assigning the field errors, the variance per arc of all other components remains on a similar level.

Before looking into the DA, the positive impact of the sorting can already be seen when comparing the amplitude detuning before and after sorting. In Fig. 3.11 and Fig. 3.12, the reduction of the amplitude detuning due to the sorting is illustrated for the 18x90 and 23x90 lattices, respectively.

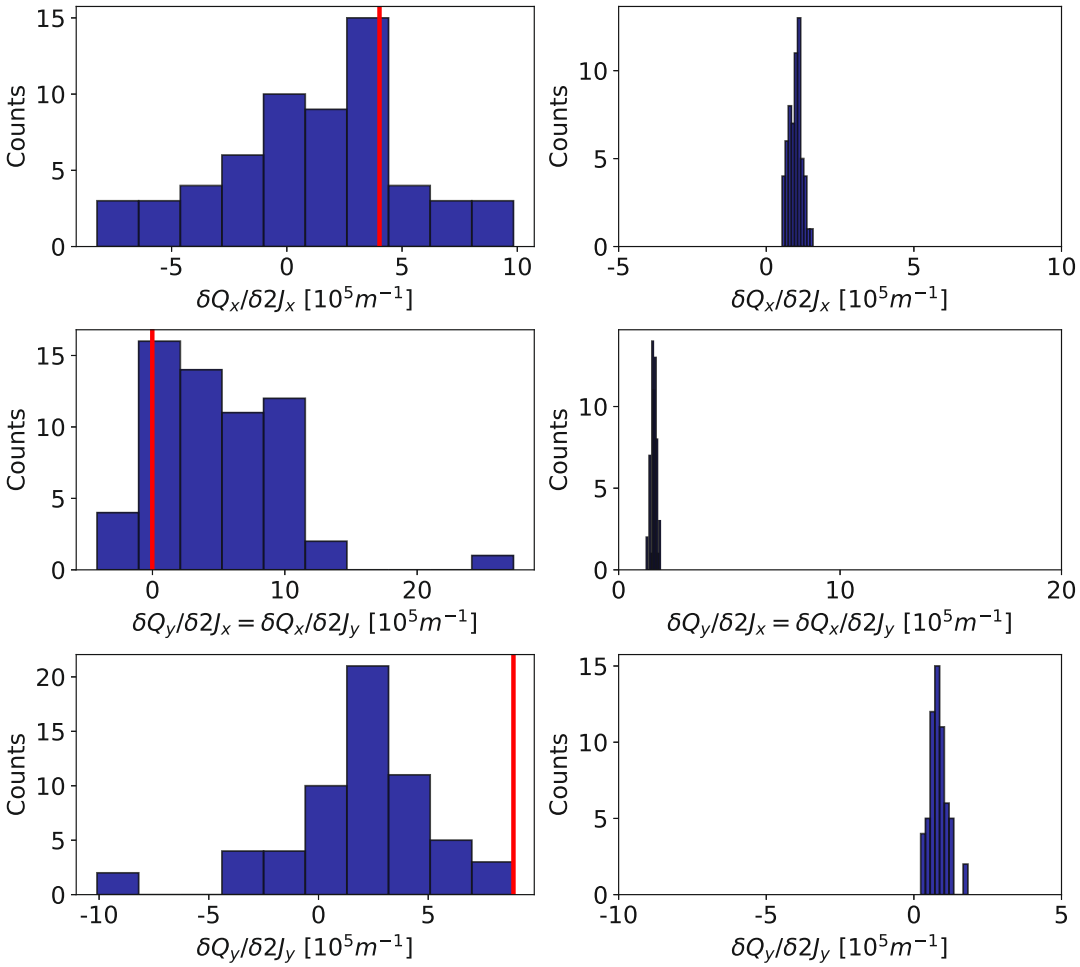

(A) Amplitude detuning without sorting.

(B) Amplitude detuning with sorting

FIGURE 3.11: Amplitude detuning for 60 different realizations of the 18x90 lattice at an injection energy of 450 GeV, using the field quality from Tab. A.1.

In the presented case for 450 GeV, in both lattices a significant reduction of all three amplitude detuning terms is observed, with the 18x90 showing a larger relative decrease of the standard deviation than the 23x90. This effect is predominately attributed to the sorting of the sextupole component and the associated reduction of the residual sextupole errors. In Tab. 3.15, the minimum DA results for both lattices and at the three considered injection energies are presented.

Studies using the simple sorting approach yield an increase of up to 5 σ, with the largest improvement at 450 GeV, where also the random sextupole component is largest. Comparing to studies presented in Tab.3.8, the improvement for the case of the 18x90 lattice at 450 GeV due to the sorting yields similar results to the case of a reduced random sextupole component between 2 to 6 units, but including also higher order components. However, using the same 12 σ threshold as in the previous section, still only the case of the 23x90 lattice at an injection energy of 1.3 TeV can be deemed feasible, irrespective of the use of sorting.

Additionally, this sorting approach only takes into account the sextupole component

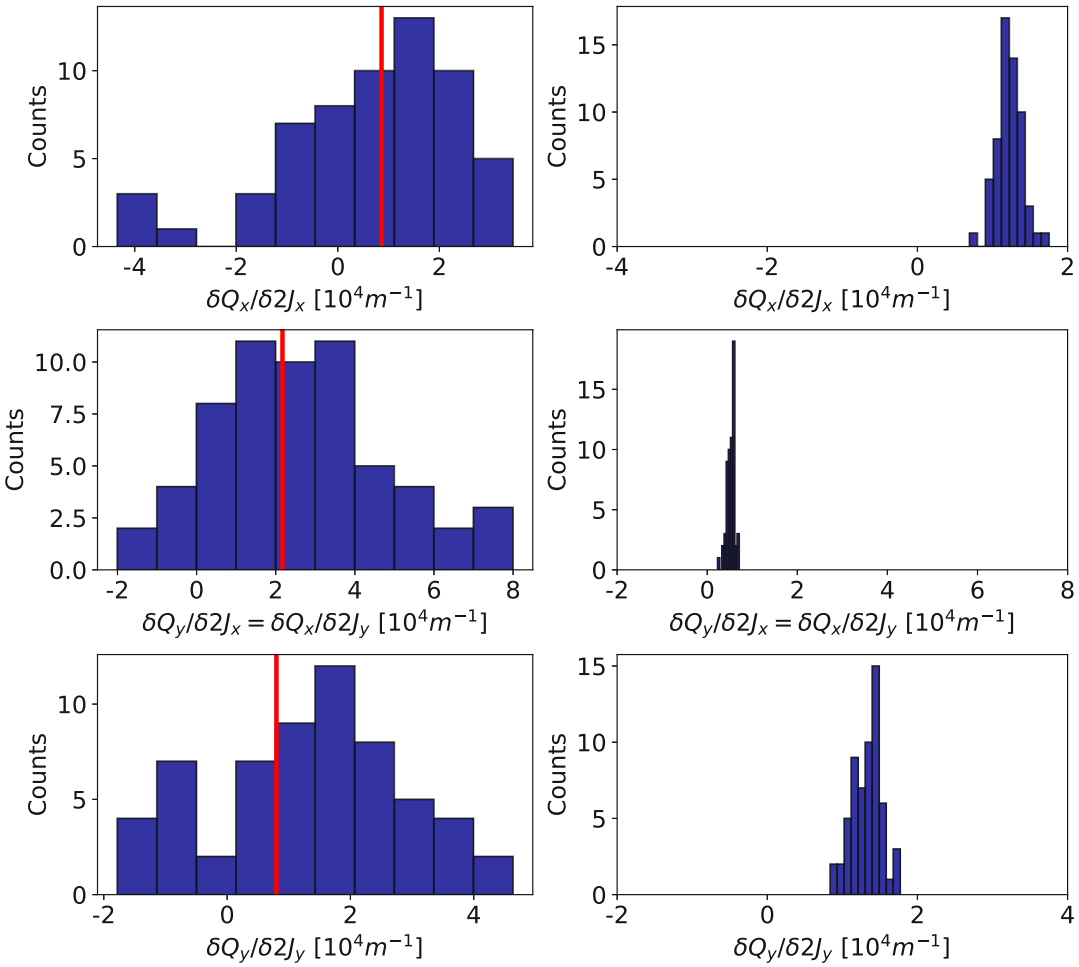

(A) Amplitude detuning without sorting.

(B) Amplitude detuning with sorting

FIGURE 3.12: Amplitude detuning for 60 different realizations of the 23x90 lattice at an injection energy of 450 GeV, using the field quality from Tab. A.1.

of one beam. This approach is feasible for the LHC dipoles, where a strong correlation of the sextupole component between both apertures was found [110]. This correlation is further illustrated in Tab. 3.16, where the correlation also for higher order components is illustrated, using measurement data for the LHC dipoles.

Notably, not only a strong correlation between the sextupole components of the two apertures is found, but the same holds also true for other allowed harmonics such as b_5, b_7, and b_9. Compared to other cases, also a relatively strong correlation between different allowed harmonics between apertures is noted, such as b_3 in aperture 1 and b_5 in aperture 2. However, no distinct cause for the correlation between the two apertures has been found and as such cannot be assumed to also be the case for the HE-LHC dipoles. As such, an alternative sorting algorithm is investigated, allowing sorting on the sextupole components in both apertures. For the given task, the K-means clustering algorithm [114] was chosen. This algorithm, given a set of points in an n-dimensional space, starts off by randomly distributing k points m_k, where k is the number of cluster and is specified on initialization. For the case of the HE-LHC, k equals 8 being the number of arcs, and using only the sextupole components of the two apertures the dimension $n = 2$. In the following step, the distance between

Lattice		Injection energy [GeV]		
		450 GeV	900 GeV	1300 GeV
18 arc cells	without sorting	1.5 σ	4.2 σ	7.6 σ
	with sorting	5.5 σ	6.6 σ	11.1 σ
23 arc cells	without sorting	2.7 σ	7.0 σ	12.1 σ
	with sorting	7.7 σ	10.8 σ	13.1 σ

TABLE 3.15: Comparison of minimum DA with and without the use of a simple sorting algorithm for both HE-LHC lattices at different injection energies and using field quality specified in Tab. A.1.

		Aperture 2						
		b_3	b_4	b_5	b_6	b_7	b_8	b_9
Aperture 1	b_3	0.88	-0.03	0.43	0.01	0.23	0.02	0.13
	b_4	-0.07	-0.31	-0.05	-0.14	0.04	-0.05	0.05
	b_5	0.42	-0.12	0.93	-0.04	0.27	0.18	0.58
	b_6	-0.15	-0.08	-0.21	-0.14	-0.30	-0.06	-0.20
	b_7	0.22	-0.09	0.26	0.17	0.90	0.05	0.54
	b_8	0.08	-0.12	0.04	-0.03	0.12	-0.01	0.09
	b_9	0.11	-0.19	0.58	-0.02	0.55	0.14	0.89

TABLE 3.16: Pearson product-moment correlation coefficients between the harmonics of the two apertures using the WISE seeds [113].

each data point to the points m_k is evaluated, and each data point is assigned to one cluster corresponding to a point m_i which is closest to the data point. Once all data points are assigned a cluster, the points m_k are recalculated as the mean over all data points belonging to one cluster. These two steps are repeated until convergence is achieved or the maximum number of iterations is exceeded. While the regular K-means algorithm creates clusters of unequal size, each arc of the HE-LHC has the same number of dipoles and as such an adapted K-means algorithm was used, able to provide clusters of equal size [115]. An illustration of the distribution of sextupole components in both apertures and the results of the equal cluster-size K-means are illustrated in Fig. 3.13.

Note that the K-means algorithm would also allow to extend the sorting to more components, e.g. sorting on b_3 and b_5 in both apertures, however this has not been tried yet. A comparison of the DA results between the simple sorting scheme and when using the K-means sorting are presented in Tab. 3.17.

As expected, due to additional consideration of the second aperture and the thus less efficient sorting of the sextupole component, the resulting DA falls in between the unsorted case and using the simple sorting. Note that the results presented here are only for the case of tracking in Beam 1 as no optics for Beam 2 is available for these layouts. However, comparing again the variance of the sextupole and octupole component before and after sorting, a clear reduction is observed in both beams, as is displayed in Fig. 3.14 for one seed of the 18x90 layout and in Fig. 3.15 for the 23x90 layout.

Given this reduction of the variance of the sextupole component also in Beam 2, it is

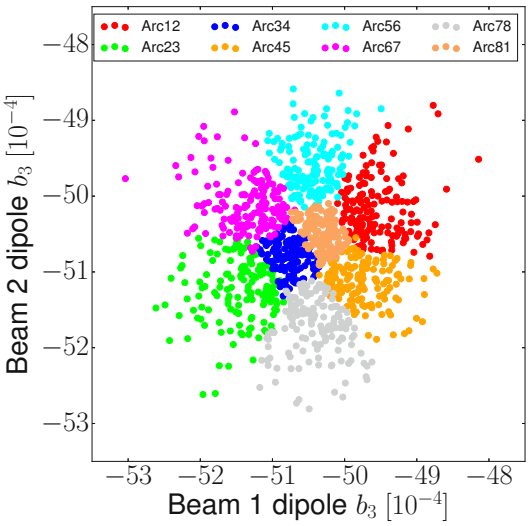

FIGURE 3.13: Illustration of the K-means clustering for sorting on the sextupole component of the main dipole in both apertures.

Lattice		**Injection energy [GeV]**		
		450 GeV	900 GeV	1300 GeV
18 arc cells	without sorting	1.5 σ	4.2 σ	7.6 σ
	with sorting	5.5 σ	6.6 σ	11.1 σ
	K-means	3.4 σ	5.8 σ	10.6 σ
23 arc cells	without sorting	2.7 σ	7.0 σ	12.1 σ
	with sorting	7.7 σ	10.8 σ	13.1 σ
	K-means	5.7 σ	9.3 σ	12.7 σ

TABLE 3.17: Comparison of minimum DA for different sorting algorithms for both HE-LHC lattices at different injection energies and using field quality specified in Tab. A.1.

thus believed that DA results here are also likely to improve, under the assumption that the DA is dominated by the effect of the sextupole component in the dipoles. However, the exact increase of the DA in Beam 2 still should be determined once optics for both beams are available.

Both sorting schemes have also been tried with the updated field quality table A.2, which for one features a significantly lower random sextupole component at the lowest injection energy. As such, the effect of the sorting is expected to show a less drastic increase compared to the previous case. DA results for all three cases and for the both HE-LHC lattices at the three injection energies are presented in Tab. 3.18.

As expected, all cases show only a modest increase in DA for both sorting schemes, showing at least an improvement of 1 σ. Independent of the used sorting approach, in no case is the improvement significant enough to change the previous conclusions on the feasibility of the individual scenarios from the DA point of view.

For completeness, the DA results with and without the use of the K-means sorting algorithm are presented in Tab. 3.19 for error table A.4, which assumes optimistic conductor parameters, and in Tab. 3.20 for the error table A.5 using the realistic

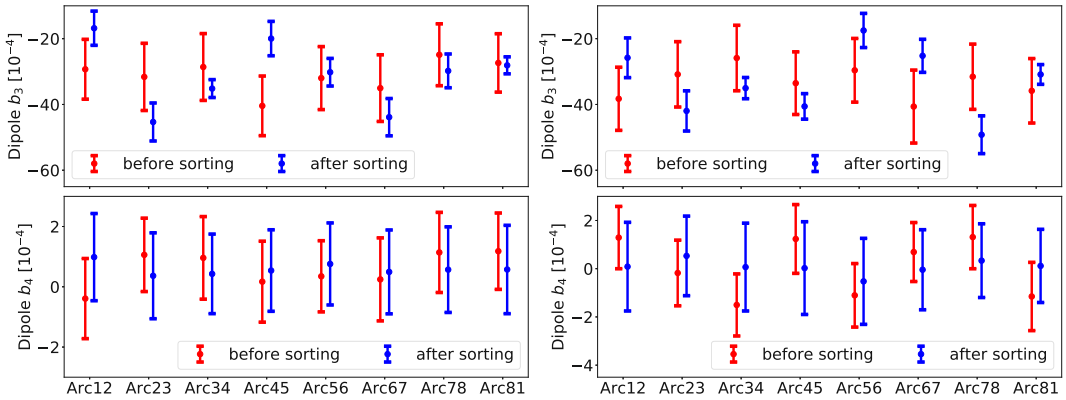

(A) Effect of sorting in Beam 1.

(B) Effect of sorting in Beam 2.

FIGURE 3.14: Effect of sorting using the K-means clustering on the variance of the sextupole and octupole component on a per arc basis in the 18x90 layout.

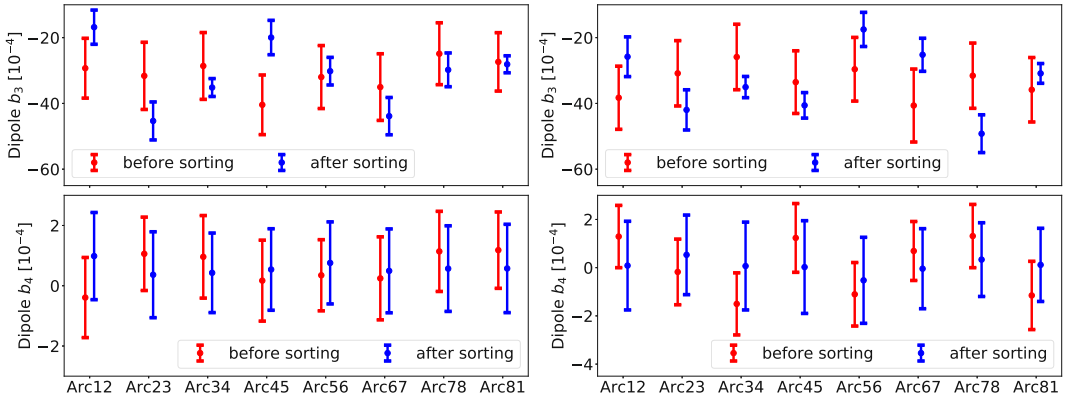

(A) Effect of sorting in Beam 1.

(B) Effect of sorting in Beam 2.

FIGURE 3.15: Effect of sorting using the K-means clustering on the variance of the sextupole and octupole component on a per arc basis in the 23x90 layout.

conductor parameters.

Again, using the K-means sorting approach yields an increase of the DA in simulations of at least 1 σ. However, while before the 18x90 satisfied the DA requirements only in case of the optimistic conductor parameters, thanks to the improvements using the sorting algorithm, also the more realistic case is now a viable option. Furthermore, with the sorting also an injection energy of 900 GeV becomes a feasible option for the 18x90 layout, albeit only for the more optimistic error table. However, even with sorting, at an injection energy of 450 GeV neither lattice meets the DA requirements nor show presently deemed sufficient beam stay clear.

3.6 Conclusions

In this chapter the motivation and considerations for one of the potential successors to the currently highest energy particle collider, the LHC, have been presented. The High Energy LHC (HE-LHC) aims at almost doubling the collision energy whilst

Lattice		Injection energy [GeV]		
		450 GeV	900 GeV	1300 GeV
18 arc cells	without sorting	5.3 σ	8.8 σ	11.3 σ
	with sorting	6.9 σ	11.5 σ	14.6 σ
	K-means	6.6 σ	11.4 σ	14.7 σ
23 arc cells	without sorting	8.4 σ	12.7 σ	15.3 σ
	with sorting	9.6 σ	14.2 σ	16.8 σ
	K-means	9.5 σ	13.8 σ	16.8 σ

TABLE 3.18: Comparison of minimum DA with and without the use of a simple sorting algorithm for both HE-LHC lattices at different injection energies and using field quality specified in Tab. A.2.

Lattice		Injection energy [GeV]		
		450 GeV	900 GeV	1300 GeV
18 arc cells	without sorting	5.2 σ	8.8 σ	12.0 σ
	K-means	5.8 σ	12.6 σ	17.4 σ
23 arc cells	without sorting	7.9 σ	12.9 σ	16.9 σ
	K-means	8.7 σ	15.2 σ	21.8 σ

TABLE 3.19: Comparison of minimum DA using a simple sorting algorithm and the K-means clustering algorithm for both HE-LHC lattices at different injection energies and using field quality specified in Tab. A.4.

reusing the same tunnel currently occupied by the LHC and before that by the LEP. This ambitious goal, together with the condition of no major modifications to the tunnel and the potential reuse of the LHC injector chain without any upgrades, put severe constraints on the design, which is reflected in the various scenarios considered. Next to the requirements on the deviation from the survey of the LHC and on the minimum available physical aperture at injection energy, another key quantity is the dynamic aperture (DA) at injection energy, which has been the focus of the last two sections. Herein, the minimum DA was studied in simulations for all considered scenarios, taking into account only the field quality of the main dipoles. Studies were performed for multiple iterations of the main dipole design and using

Lattice		Injection energy [GeV]		
		450 GeV	900 GeV	1300 GeV
18 arc cells	without sorting	2.7 σ	7.4 σ	11.2 σ
	K-means	3.8 σ	9.0 σ	14.4 σ
23 arc cells	without sorting	5.4 σ	12.8 σ	15.9 σ
	K-means	6.2 σ	13.9 σ	18.1 σ

TABLE 3.20: Comparison of minimum DA using a simple sorting algorithm and the K-means clustering algorithm for both HE-LHC lattices at different injection energies and using field quality specified in Tab. A.5.

the same threshold as used during the design of the LHC, the feasibility of all scenarios was evaluated in order to eventually conclude on one operational scenario to be studied in more detail if a technical implementation is targeted. Based on these studies, reusing the SPS without any further upgrade and injecting with an energy of 450 GeV seems an unlikely scenario, as the dynamic aperture in all dipole designs did not meet the required threshold, setting aside also issues with the physical aperture at this injection energy. As such, all currently feasible solutions include an energy upgrade of the SPS, with a doubling of the injection energy allowing operation with an LHC-like layout which does not achieve the targeted collision energy, while a tripling of the injection energy would allow for use of a layout able to achieve the full collision energy of 27 TeV. Implications and limitations of said upgrade of the SPS have not been studied so far. In all studied scenarios, the strong expected sextupole component of these dipoles is found to be the dominant factor. As a mitigation strategy, the effect of sorting on the minimum DA was studied, taking into account also that harmonics between the two apertures of the dipole may be uncorrelated, which was not the case for the LHC. Both sorting approaches show an increase of the minimum DA, however even without taking into account any further constraints from e.g. mechanical tolerances, at an injection energy of 450 GeV the minimum DA does not meet the requirements. While the main dipoles are believed to have the strongest impact on the DA at injection energy, future studies may also look into the change of the minimum DA when including field errors of other magnets such as the main quadrupoles, which were not available for these studies. Studied scenarios also assumed perfect knowledge of the field quality of each dipole and ideal corrections settings. As such, the effect of a miscorrection on the DA to evaluate the robustness of certain scenarios should be looked into.

Chapter 4

Dynamic Aperture in the LHC in the presence of large sextupole errors

The hadron collider options currently investigated as part of the FCC study rely on the use of dipoles with a field strength of 16 T or above in order to achieve the targeted collision energy. From simulations of the current design of these dipoles, a systematic sextupole component of up to factor 10 larger than in the LHC dipoles could be present in these magnets. A similar systematic mispowering of the corrector circuits as is assumed in the LHC may thus have a significantly larger impact on the dynamic aperture and in turn potentially also on the operational performance. In this experimental study, the dynamic aperture in the presence of large sextupole fields in the LHC at injection energy was measured. By deliberately mispowering the sextupole spool pieces attached to each dipole, a large systematic b_3 component is generated and the subsequent change in chromaticity is corrected by the chromaticity sextupoles. Using both the aperture kicker and the AC-dipole as exciters, free and forced dynamic aperture as well as amplitude detuning were measured. Additional linear optics measurements provide insight into the contributions to coupling from the sextupole spool pieces.

4.1 Introduction

In the LHC as well as in other colliders using superconducting magnets, the correction of the systematic sextupole component of the main dipoles is critical both in terms of operation and dynamic aperture. This systematic field harmonic stems both from static contributions such as the coil geometry and persistent currents in the conductor as well as dynamic contributions from current redistributions in the superconducting cables leading to a change of the allowed harmonics such as the sextupole component at static current called decay. Once the ramping of the current starts, another dynamic change is observed, where the sextupole component changes back to the value before the decay, an effect which is called snap-back. Due to the large amount of dipoles, the integrated sextupole contribution would, if uncorrected, lead to a large chromaticity. Though easily correctable with chromaticity sextupoles and a feedforward system, the presence of this strong sextupole fields in turn also drives multiple resonances as well as leads to the generation of higher order chromaticity and amplitude detuning. In the LHC, a local correction provided by sextupole spool pieces (MCS) attached to each dipole [106] together with a dipole

sorting strategy [110] was implemented. In addition, a large effort was put into assessing the field quality of the main dipoles, as well as understanding the influencing factors to the evolution of the harmonics. The results, aggregated in a magnetic model called FiDeL (Field Description for the LHC) [116], allow to predict the required corrector settings along the LHC cycle in order to compensate field errors.

To achieve the target 16 T in the dipoles for the FCC-hh and the HE-LHC, a change of the superconductor from the NbTi, which was used in the LHC dipoles, to Nb_3Sn is necessary. This superconductor features a larger filament size, which leads to a different persistent current contribution [117, 118], which is a major contribution to the field quality of the 16 T dipoles. In the case of the HE-LHC, where the option of injecting from the current Super Proton Synchrotron (SPS) at CERN with an injection energy of 450 GeV is considered, the large foreseen energy swing leads to another increase of the persistent current contribution at low field. To reduce this effect, measures were taken such as the reduction of the filament size from 50 µm to 20 µm and the inclusion of artificial pinning centers to reduce the magnetization at low fields. For the LHC dipoles, where NbTi is used, the filament size is around 7 µm [67]. The field quality tables for the 16 T dipoles, showing both the systematic and persistent current contributions, are presented in [83].

Due to this large sextupole component of e.g. 50 units (at a reference radius of 17 mm) at 450 GeV [83] in the HE-LHC, a similar systematic setting error of the MCS of 10 %, as was assumed for the LHC [82], would result in a drastically more challenging situation. For comparison, in the LHC a systematic b_3 between 4.5 to 5.7 units (with one notable exception being arc 78 with 2.5 units) is corrected for [119]. MCS setting errors could potentially occur due to a limited magnetic measurement accuracy, imperfect models of the dynamic contributions as well as from a rapid change in the order of a few seconds [120] coming from the snap-back. Again, while the first order chromaticity generated from this uncorrected sextupole component is easily corrected, for the other effects such as amplitude detuning the identification of the contribution in the presence of other multipoles and subsequent correction might prove significantly more difficult. This temporary situation of a large local b_3 could represent the overall limitation for the DA during the cycle, and as such possibly the overall collider performance.

A large systematic b_3 was studied in the LHC in this experimental study. Due to the better field quality of the LHC dipoles in comparison to what is expected for the 16 T Nb_3Sn dipoles, the MCS are used to mimic a large systematic b_3 in the dipoles. The chromaticity was then corrected using the main sextupoles (MS). Following the change in the spool piece corrector powering, the dynamic aperture was measured and results are presented in this report.

The change of powering of the MCS also allows to study possible changes in the linear optics and coupling due to misalignments of the sextupole spool piece correctors.

4.2 Measurement procedure

The experimental study was performed at the injection energy of 450 GeV using one pilot bunch (with a beam intensity $\approx 5 \cdot 10^9$ p^+) and the nominal injection optics. The fractional tunes were set to 0.28/0.31 and chromaticity was corrected to

$Q'_{x,y} = 3$ units. Upon the start of the study, collimators including the injection protection were retracted to coarse settings to provide ample aperture for AC-dipole and aperture kicker (MKA) excitation. Before the change of powering, the initial coupling was assessed, and a coupling correction was deemed not necessary (residual coupling equivalent to coupling knob settings [121] of $C^- = -2.3 \cdot 10^{-3} - 1.3i \cdot 10^{-3}$ in an ideal machine). Starting with Arc12, the current for the MCS was set to 0 arc by arc, as illustrated in Fig. 4.1.

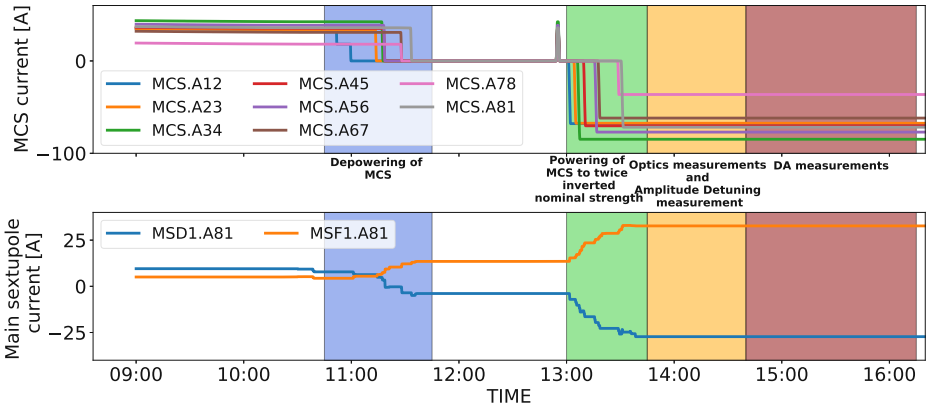

FIGURE 4.1: Evolution the current from the power supplies of the sextupole spool piece (MCS) correctors (top) and of the arc sextupole, grouped into sextupoles close to the focusing (MSF) and defocusing quadrupoles (MSD) (bottom). Here, only the current for the MS in Arc81 is displayed. The MS in the other arcs were powered with the same current.

After each sector depowering, the chromaticity was corrected using the arc sextupoles. Due to issues with the beam quality traced backed to injection oscillations, transfer line steering was carried out at this point. Additionally, linear optics measurements using the AC-dipole were conducted after the depowering of all MCS. In the following, the MCS currents were set to twice the nominal strength but with opposite polarity. After each change in the circuit powering, the chromaticity was corrected with the MS. Linear optics measurement were performed to assess the impact of a possible misalignment of the MCS on coupling and beta-beating. These were followed by single plane AC-dipole excitation to assess amplitude detuning and also for potential assessment of forced dynamic aperture. Lastly, large amplitude excitation with the aperture kicker (MKA) were performed to assess the free dynamic aperture. Before each MKA kick, the previous pilot bunch was dumped and a new bunch was injected. The kick strength of the MKA was limited to 7 $\sigma_{nominal}$ and 9.5 $\sigma_{nominal}$ in the horizontal and vertical planes, respectively, where $\sigma_{nominal}$ refers to the beam size using the LHC design normalized emittance of ϵ_n =3.75 µm.

4.3 Results

As the optics at the beginning of the study is the nominal injection optics, which has already been thoroughly analysed during the LHC commissioning phase, no in-depth optics measurements were conducted at this point. A comparison between the beta-beating obtained from a single kick at the beginning of the experimental shift to the beta-beating assessed during the LHC optics commissioning in April 2018 is

presented in Fig. 4.2. As expected, no significant difference is observed. As for cou-

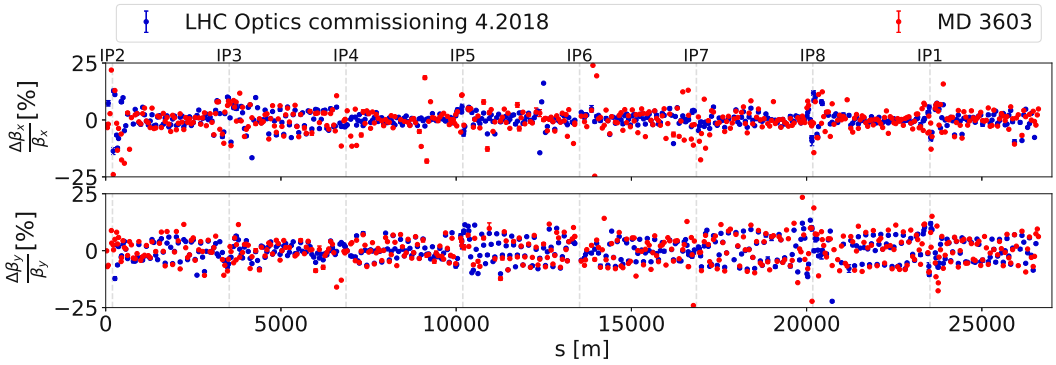

FIGURE 4.2: Comparison between beta-beating measured for injection optics during the LHC optics commissioning in April 2018 and in the beginning of the shift.

pling, a small difference in the amplitude is observed, shown in Fig. 4.3. During

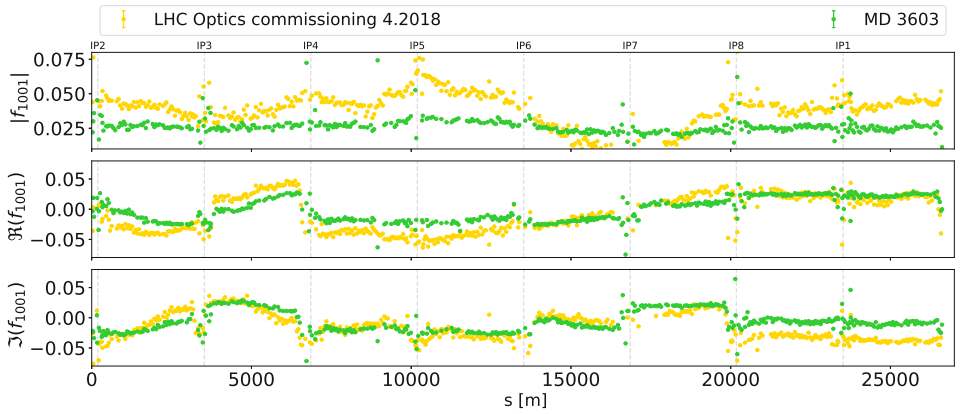

FIGURE 4.3: Comparison between difference coupling resonance driving term measured for injection optics during the LHC optics commissioning in April 2018 and in the beginning of the shift.

the experimental study, the fractional tunes were set to 0.28/0.31, whereas during commissioning the injection tunes 0.275/0.295 were used. No notable difference in the coupling structure is observed. Assuming that coupling sources have remained the same between commissioning in April 2018 and experimental study conducted in July 2018 and neglecting the slight change of the β-functions, this change of the tunes leads to a change of the resonance driving term (RDT) amplitude of the difference resonance ($Q_x - Q_y = p$) between these two measurements of about a factor

$$\left| \frac{1 - e^{2\pi i (Q_x^{Exp} - Q_y^{Exp})}}{1 - e^{2\pi i (Q_x^{commissioning} - Q_y^{commissioning})}} \right| \approx 1.5 \,. \tag{4.1}$$

Single AC-dipole excitations were performed after some arc depowering steps to assess the change in coupling. One example is presented in Fig. 4.4 for the case of Arc12. A drastic increase of about a factor 2 is observed in $|f_{1001}|$ before any coupling corrections were applied, highlighting the contribution of the MCS to the

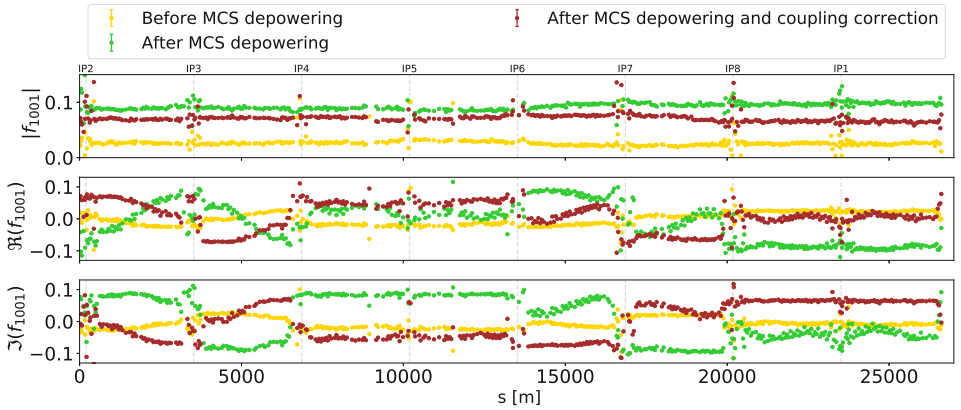

FIGURE 4.4: Change in Coupling after depowering the MCS in Arc12.

coupling in the LHC [122]. After reaching the final MCS powering and the subsequent chromaticity correction with the main sextupoles linear optics measurements were conducted, which are presented in Fig. 4.5 together with the beta-beating for the nominal MCS powering. In the mispowered MCS configuration a significantly

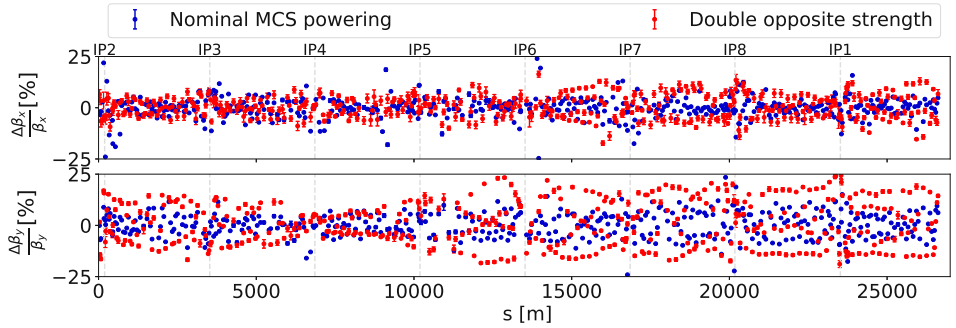

FIGURE 4.5: Comparison of beta-beating between the nominal MCS setting and powered with twice the strength and opposite sign.

higher beta-beating than in the nominal case is observed, especially in the vertical plane where a maximum beta-beating of 25% is obtained. The change in the linear optics can mostly be attributed to feed-down via horizontal misalignment of the sextupole spool pieces or main sextupoles. Similarly, a change in the coupling structure between the two MCS powering cases, as presented in Fig. 4.6, can be noted. However, the overall coupling is similar between the two cases and no special correction was considered necessary. Presented in Fig. 4.7 and Fig. 4.8, no drastic change in the closed orbit is observed.

The amplitude detuning measurements were analysed following the same algorithm as described in [123]. During the measurements, a tune drift was observed, for which the measurements were corrected for. In Fig. 4.9, the horizontal and vertical tunes, measured by the BBQ [124], during the horizontal excitations are presented, showing a tune drift of roughly 10^{-3} over a time span of 20 minutes. The results of the amplitude detuning measurements are presented in Fig. 4.10.

In Fig. 4.11, the spectrum at the BPM.10L1.B1 is presented during one vertical AC-dipole excitation. In both planes, spectral lines corresponding to decapolar reso-

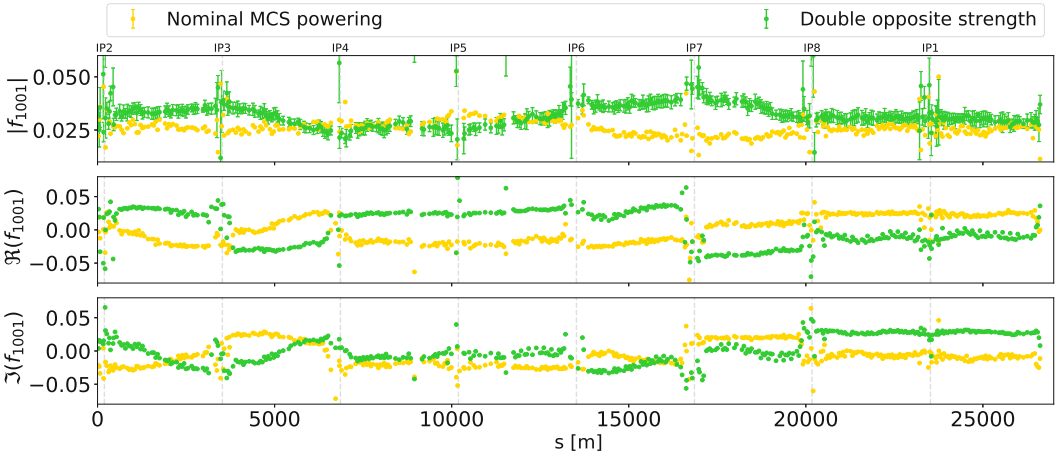

FIGURE 4.6: Comparison of coupling between the nominal MCS setting and powered with twice the strength and opposite sign.

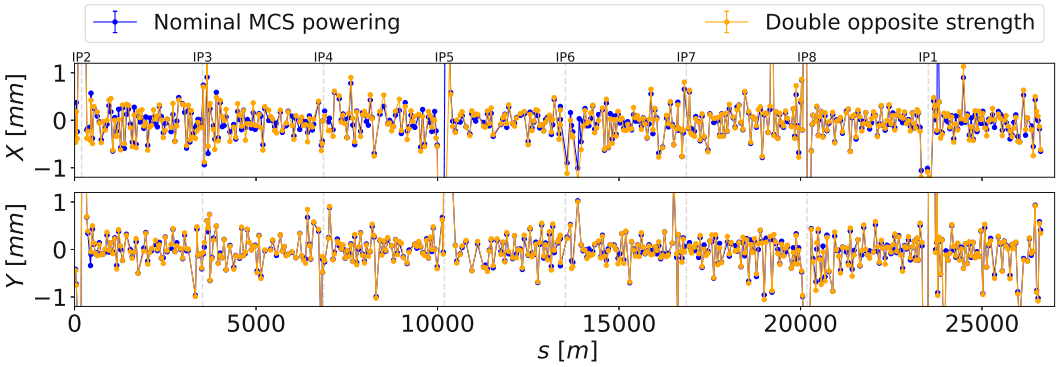

FIGURE 4.7: Comparison of closed orbit between the nominal MCS setting and powered with twice the strength and opposite sign.

nances are found close to the natural tunes. In the horizontal plane, the $4Q_y^{AC}$ spectral line, where $Q_y^{AC} = Q_y + 0.012$ is the driven tune of the AC-Dipole, is found close to the natural tune Q_x. The driven tune in the horizontal plane is $Q_x^{AC} = Q_x - 0.01$. For the vertical case, Q_y is in the vicinity of the $-Q_x^{AC} + 3Q_y^{AC}$ spectral line. However, these do not disturb the amplitude detuning measurements as the resolution of the frequency analysis is sufficient to distinguish between the lines. Strong decapolar lines, disturbing amplitude detuning measurements have already been reported in [123], although at a beam energy of 6.5 TeV.

During the vertical kicks, increasing losses are visible in the intensity, measured by the fast beam current transformer (FBCT) [67] and displayed in Fig. 4.12. Such losses were not seen in the preceding horizontal kicks, where the highest amplitude kicks were more than a factor 2 smaller than the largest vertical excitations.

Given the kick amplitude below $6\sigma_{nominal}$ and the fully retracted collimators, these losses during the vertical excitations with the AC-dipole are attributed to particles crossing the boundary of stable motion, called forced dynamic aperture [126]. In a

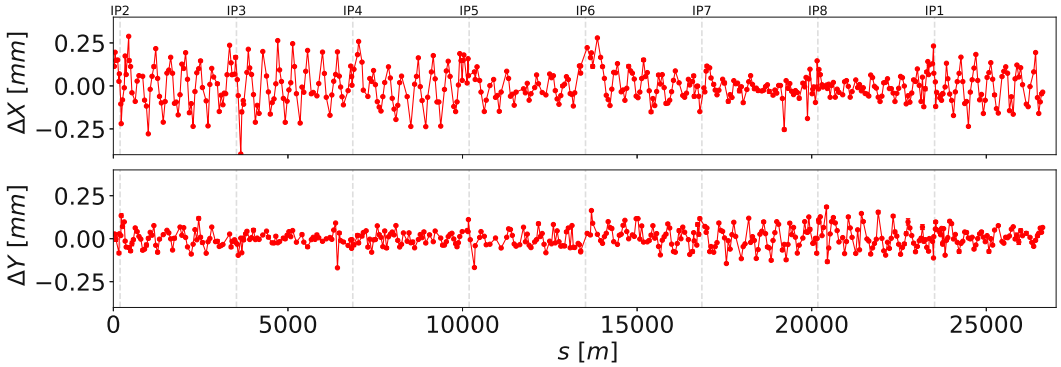

FIGURE 4.8: Difference between the closed orbit of the nominal MCS setting and when powered with twice the strength and opposite sign.

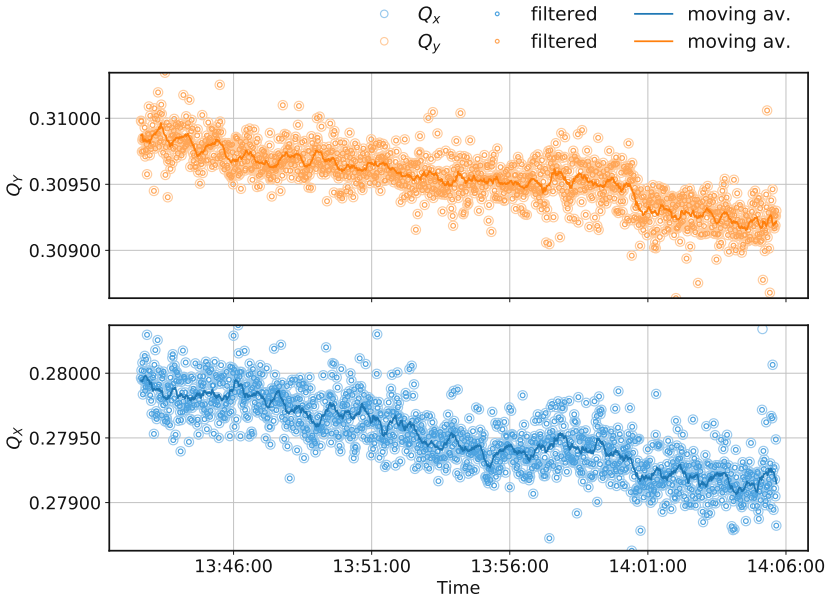

FIGURE 4.9: BBQ tune measurement during AC-Dipole excitations in the horizontal plane.

simplified one dimensional model the forced dynamic aperture relates to the intensity losses via

$$DA^{forced} = J_z^{forced} - \epsilon_z \ln \frac{\Delta I}{I}, \tag{4.2}$$

where $\frac{\Delta I}{I}$ is the relative intensity loss, z the excitation plane, J_z^{forced} the action of the excitation and ϵ_z the emittance of the bunch.

The emittance in between the kicks was logged using the BSRT and beforehand a reference measurement using the wire scanner (BWS) was performed. Horizontal and vertical normalized emittance during the amplitude detuning measurements are displayed in Fig. 4.13.

The emittance measured with the BWS beforehand agrees well with the BSRT measurements and no correction has been applied to the BSRT measurements. For the calculation of the forced DA, a moving average of the measured BSRT emittance was performed using the current value and three measurements before and after the

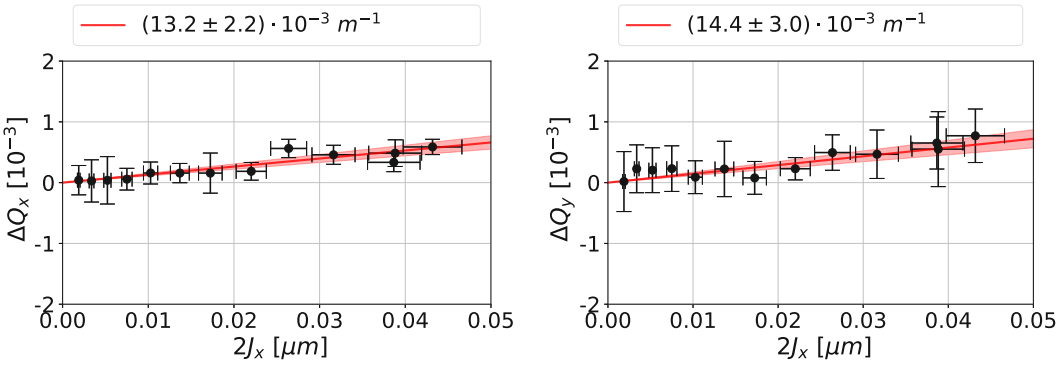

(A) $\delta Q_x / \delta 2J_x$

(B) $\delta Q_y / \delta 2J_x$

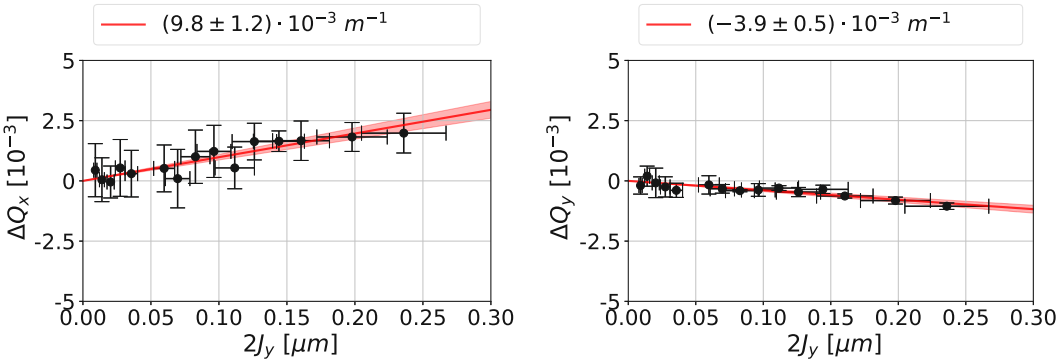

(C) $\delta Q_x / \delta 2J_y$

(D) $\delta Q_y / \delta 2J_y$

FIGURE 4.10: Measured amplitude detuning for the targeted MCS powering. Note that here the direct amplitude detuning is factor 2 larger compared to the case of free excitations due to the use of the AC-Dipole [125].

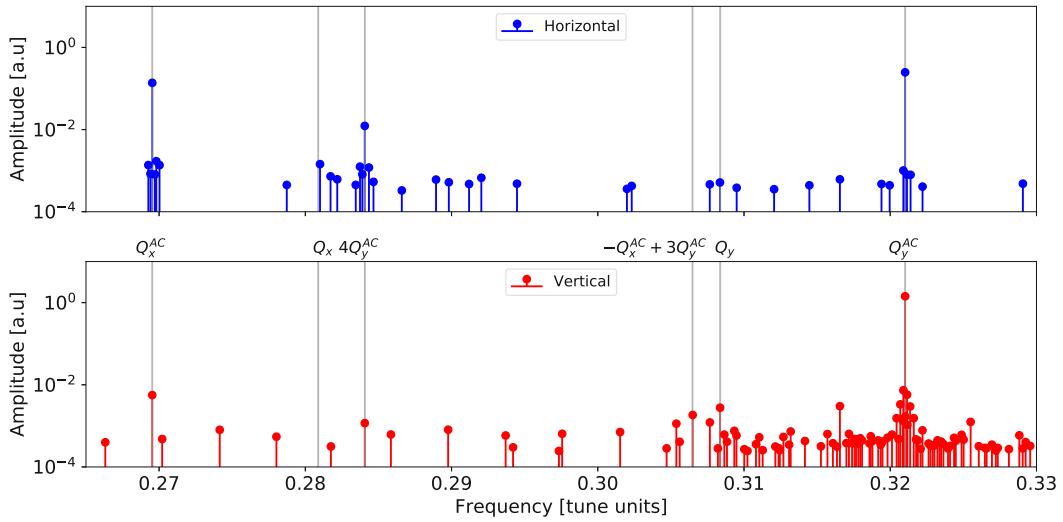

FIGURE 4.11: Horizontal and vertical spectrum of BPM.10L1.B1 for one AC-Dipole excitation.

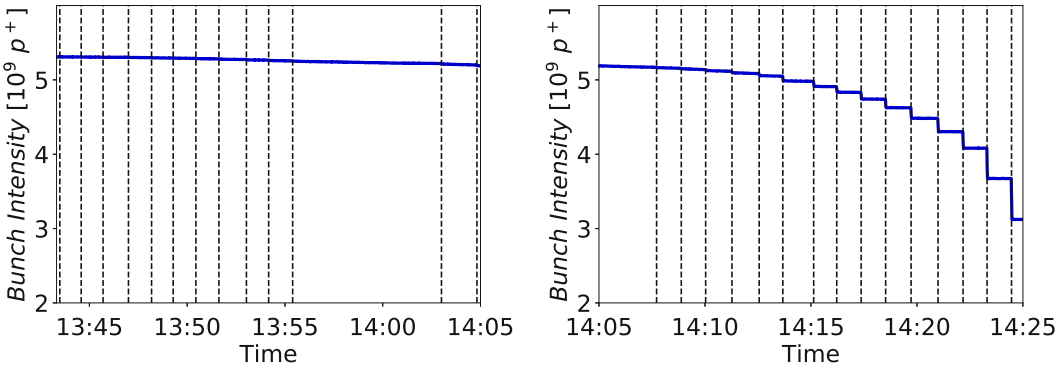

(A) Intensity during horizontal excitations (B) Intensity during vertical excitations

FIGURE 4.12: Losses in the beam intensity during AC-dipole excitations.

current timestamp. Beforehand, sudden drops of emittance were removed from the dataset, these being assumed to be false readings caused by the AC-dipole excitation. Notably, the emittance in both planes increases drastically during the two last horizontal AC-dipole excitations. This is observed in both BSRT and BWS measurements. Following the vertical kicks, a decrease of the normalized emittance of about a factor 3 in the horizontal plane and about factor 2 in the vertical plane is observed. In Fig. 4.14, the projection of the image captured by the BSRT to the horizontal and vertical planes is displayed, together with mean and standard deviation of the fitted Gaussian profile, indicated by white lines. At around 14:04, a sudden dip of the peak signal is observed, together with a sudden increase of the standard deviation, more visible in the horizontal plane. In Fig. 4.15, the measured density and the fitted Gaussian profile are displayed before the emittance blowup, during the vertical AC-dipole excitations and afterwards.

From Fig. 4.15b top, the increase of the spotsize in the horizontal plane is observed

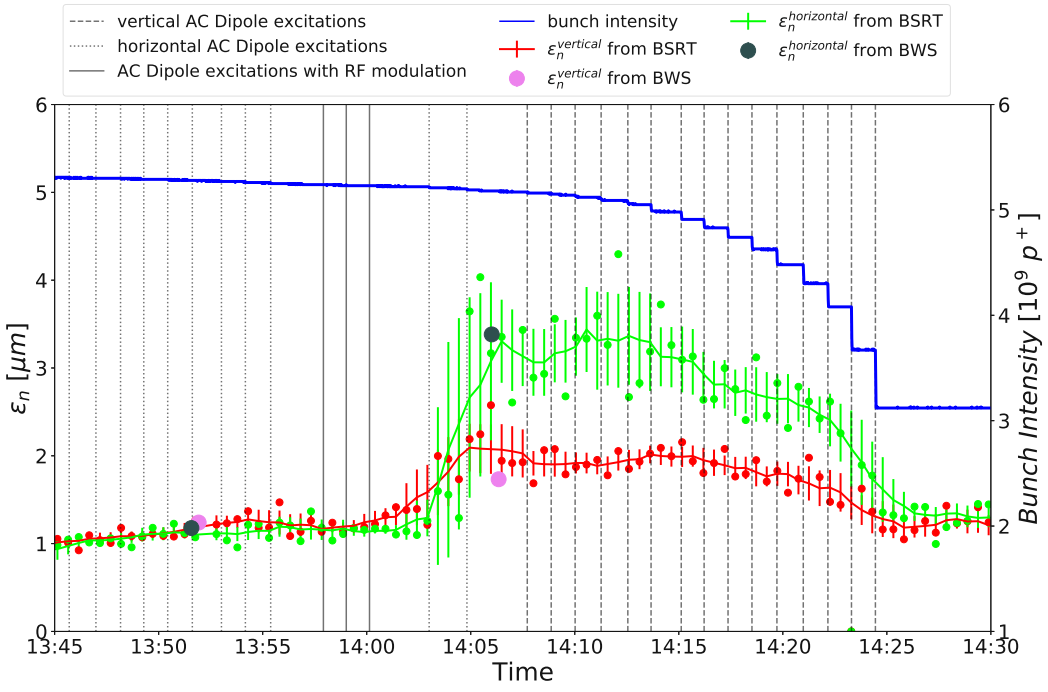

FIGURE 4.13: Measured normalized emittance as measured by the BSRT and the BWS during the AC-dipole excitations and the beam intensity from the FBCT. The kick times are displayed as vertical dashed lines.

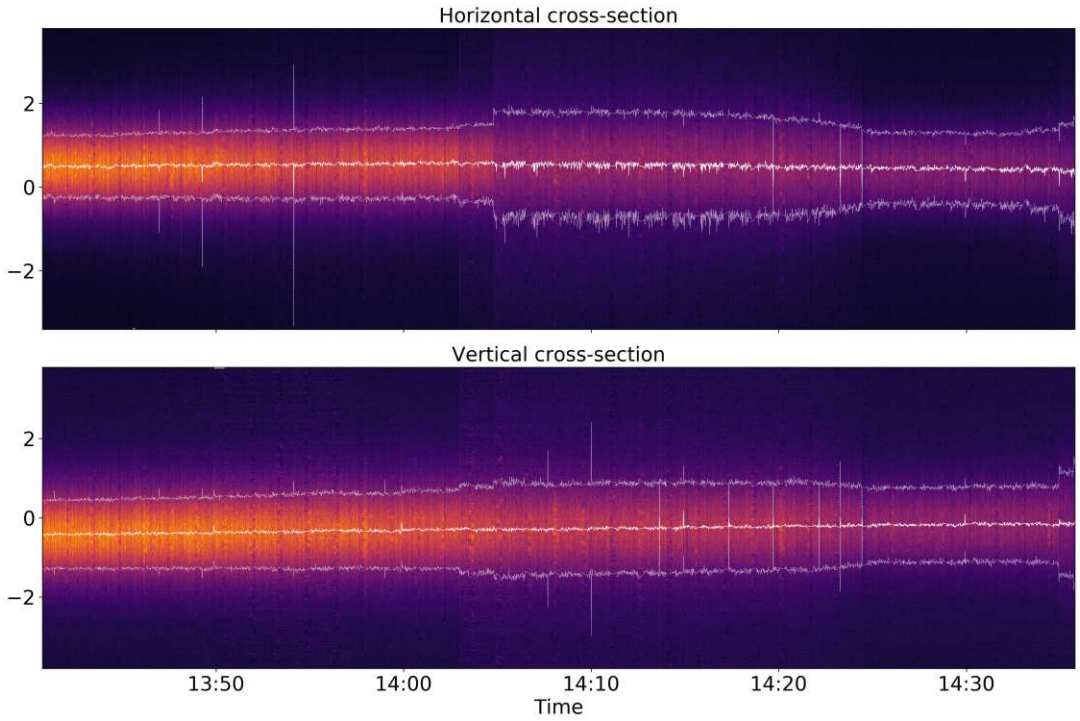

FIGURE 4.14: Logged cross-section from BSRT.

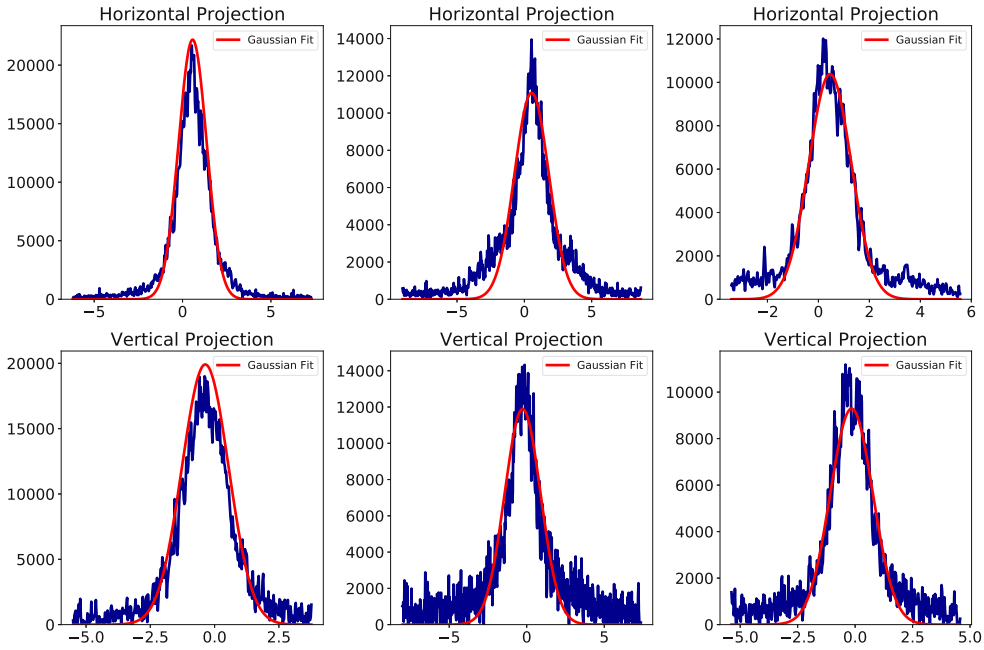

(A) Logged cross-section at 13:50 (B) Logged cross-section at 14:09 (C) Logged cross-section at 14:30

FIGURE 4.15: Projections of the logged BSRT signal to the horizontal and vertical plane.

together with an overpopulation of the tails. The subsequent decrease of the horizontal spotsize may stem from particles with large horizontal action being lost due to an excitation, either through coupling with the vertical plane, due to a small excitation provided by the AC-dipole also in the horizontal plane to allow for measuring the crossplane amplitude detuning, as is already described in [127], or, given the positive measured cross plane amplitude detuning and thus particles with large horizontal action being closer to the driven vertical tune Q_y^{AC}, receiving a stronger kick from the AC-Dipole and subsequently being lost. As the readings in vertical plane appear to have been less distorted by this effect, no correction to the measured emittance in the vertical plane was applied. The unwanted beam blow-up went unnoticed during the shift and as such, no corrective measures such as reinjecting a new pilot bunch were taken. In Fig. 4.16 the relative losses of the beam intensity are shown. Unfortunately, the overpopulation of tails in the horizontal plane and loss of these particle with large horizontal action spoil the measurement of the vertical forced dynamic aperture. Given the significant contribution to the beam losses from the horizontal large amplitude particles, from the given data is not possible to extract just the beam loss of particles with large vertical amplitude and as such no vertical forced dynamic aperture fitting the observed beam loss could be found, showing a clear point to watch for in future forced DA measurements. Using the last point as reference, it can however be stated that the forced dynamic aperture is above $5.61 \pm 0.35\ \sigma_{nominal}$, assuming a nominal normalized emittance of 3.75 µm. Due to occurrence of additional resonances as well as an increase of the amplitude detuning during forced oscillations [125], the forced DA is in general smaller than the free dynamic aperture [126].

Following the AC-dipole kicks, the free dynamic aperture was measured using the MKA. After each excitation, the beam was dumped and a new beam was injected.

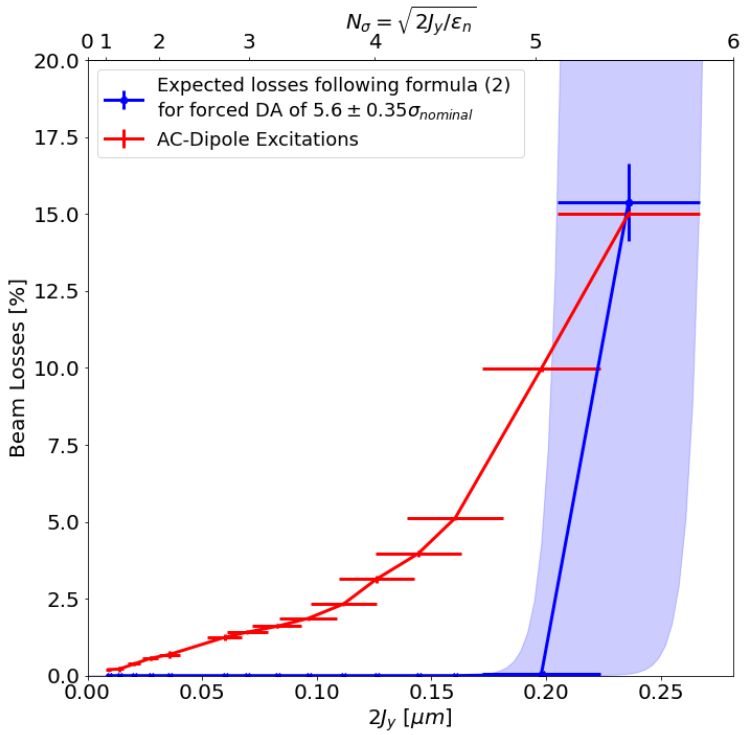

FIGURE 4.16: Measured losses of beam intensity during vertical AC-dipole excitation together with expected losses following formula (4.2).

The beam losses were calculated using the intensity from the FBCT before the excitation and 11 s after the excitation. The kick amplitudes and the associated beam intensity losses are shown in Fig. 4.17.

Here, significant losses can only be seen for diagonal excitations above a kick-amplitude of 9 $\sigma_{nominal}$. For horizontal excitations no losses are observed even at the maximum amplitude the MKA could provide during the measurement session. Assuming an uncertainty of 1% on the losses measured with the BCT for the largest horizontal excitation with a kick amplitude of N_σ together with [127]

$$\frac{DA - N_\sigma}{\sqrt{2}} = \mathrm{erf}^{-1}\left[1 - 2\frac{\Delta I}{I}\right] \tag{4.3}$$

would put the DA in this plane above 9.8 $\sigma_{nominal}$. Due to time constraints, no single kick excitations in the vertical plane were conducted. Using the data obtained from the diagonal excitations the free DA can be calculated following the same procedure as in [102]. Two datasets of kicks were used, one using kick angles between 40° and 50° and another one between 47° and 63°. The measured losses for these kicks are presented in Fig. 4.18.

For both datasets, the free DA obtained via fitting gives results above 10 $\sigma_{nominal}$.

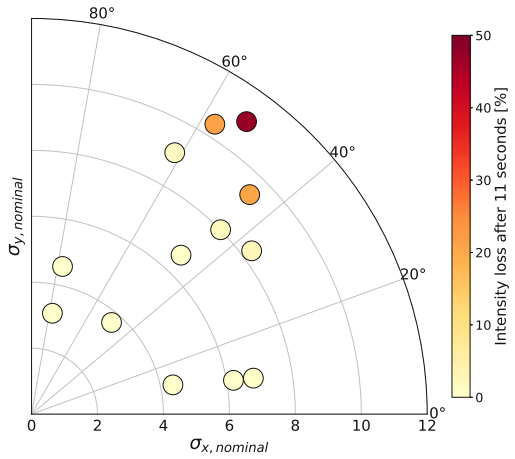

FIGURE 4.17: Excitations with the MKA and corresponding intensity losses from the FBCT.

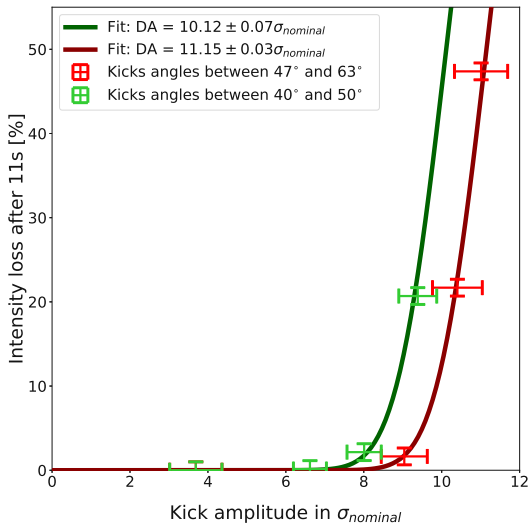

FIGURE 4.18: Measured beam intensity losses during the diagonal excitations and fit for obtaining free DA.

4.4 Comparison to simulation

Tracking studies using the tracking code SixTrack [95] were performed to provide an estimate for the DA expected during the experimental study. The nominal injection optics as used during the experiments is used in the model, with both Landau octupoles and octupole spool pieces depowered as was also the case during the measurements. Tunes were set to 0.28/0.31 and the chromaticity was corrected to +3 units using the MS, following the same procedure as used for the experimental setup. For the errors in the magnets, 60 WISE [113] seeds were used, excluding linear errors such as coupling and β-beating. In the model, the sextupole spool piece correctors and decapole spool piece corrector circuits were used to correct for the average sextupole and decapole field errors of the dipoles in each arc. Particles were tracked for 10^5 turns, equivalent to 11 s in the LHC, and using 5 angles in x-y-space. Due to the exclusion of linear errors in the magnets as well as no misalignments, these simulations were considered optimistic. The resulting DA from these tracking studies with the double inverted MCS powering is compared to the case with the MCS powered with the nominal settings in Fig. 4.19.

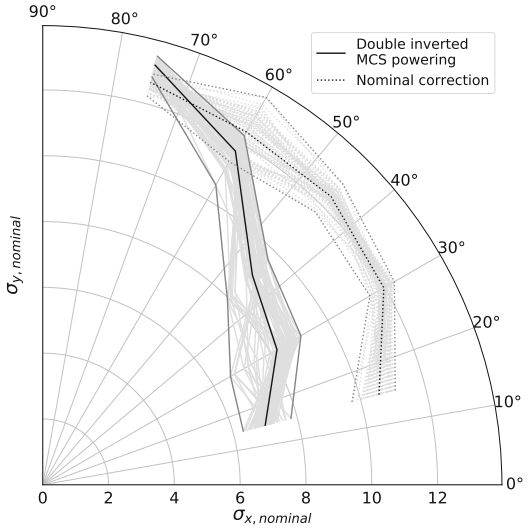

FIGURE 4.19: Dynamic Aperture from tracking studies with 10^5 turns using the WISE model with MCS and MS powered as in the experimental study and with nominal powering.

A clear reduction in the horizontal plane is observed of about 4 $\sigma_{nominal}$. For horizontal excitations, a dynamic aperture below 6 $\sigma_{nominal}$ to 8 $\sigma_{nominal}$ was expected, whereas during the measurements, no significant losses even at 7 $\sigma_{nominal}$ kick amplitude were observed. With the estimated DA in the vertical plane being above 12 $\sigma_{nominal}$, no dedicated free DA measurements were conducted during the shift as it would lie significantly above the maximum possible kick amplitude. For diagonal excitations, the measured DA of ≥ 10 $\sigma_{nominal}$ tends to be on the upper bound of the tracking studies results. As such, even the simple model, expected to provide an optimistic estimate, seems to rather underestimate the DA in the LHC. Comparing the results from the amplitude detuning measurements to the amplitude detuning in the models, calculated using PTC, shows a significant discrepancy in the vertical detuning term. The comparison for all terms is presented in Fig. 4.20.

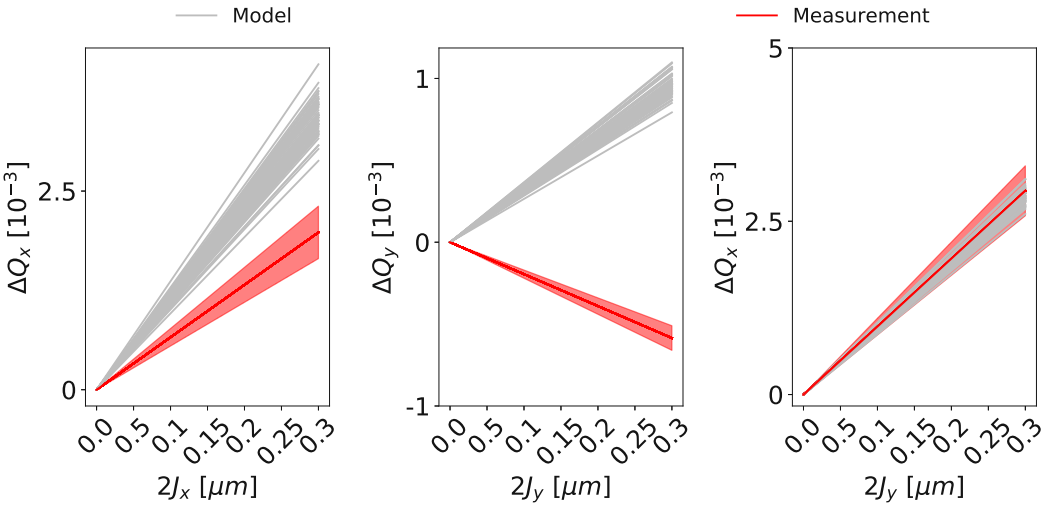

FIGURE 4.20: Comparison between the measured amplitude detuning and the amplitude detuning for the WISE seeds.

As the Landau octupoles are depowered in the model, three major sources of amplitude detuning detuning remain. The first contribution comes from the uncorrected octupole errors from the dipoles, which are already taken into account by the WISE model. The second contribution is from feed-down of the decapole spool piece correctors, due to misalignment or orbit excursions. From non-linear chromaticity studies, presented in [128], it was concluded that in the LHC a systematic horizontal misalignment of the decapole spool piece correctors (MCD) of about 0.2 mm should be taken into account. The last potential contribution, particularly relevant for this experiment, is the second order contribution from the sextupoles to amplitude detuning. While the first two options with its measurement uncertainties are easily implemented in the model, in the third option care has to be taken to properly adjust the phase advances between the sextupole sources to allow for comparing the model amplitude detuning and measured one. In these simulations, the amplitude detuning coming from the uncorrected dipole octupole errors and the misalignment of the MCD were shown to be negligible compared to the contribution from the sextupoles. As a simple study to evaluate the impact on the DA from the change in amplitude detuning without adjusting phase advance between sextupoles, the Landau octupoles were used instead to match the amplitude detuning to the measured values. The tracking results using the updated model together with the DA from measurements are presented in Fig. 4.21.

Compared to the previous results, an increase of the dynamic aperture in the horizontal plane is noted whereas in the vertical plane and for diagonal excitations a slight decrease of the DA occurs. The measured DA is now in good agreement with the simulations. The amplitude detuning was therefore a key ingredient for particle stability. In Fig. 4.22, the forced dynamic aperture from single particle tracking simulations is presented using the same model as employed also for the free dynamic aperture studies. Contrary to those studies however, only one realization of the magnetic errors (seed) is used. The AC-Dipole settings were set as was used during the measurements. The driven tunes were $Q_x^{ac} = Q_x - 0.01$ in the horizontal and $Q_y^{ac} = Q_y + 0.012$ in the vertical plane. The oscillation amplitude is ramped up over 2000 turns and is kept constant for 6000 turns. The action is then obtained by

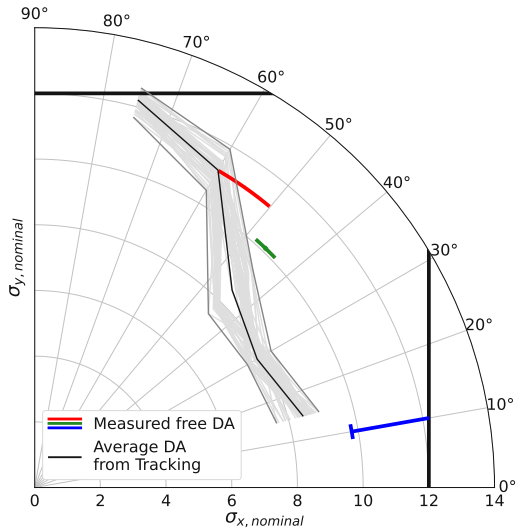

FIGURE 4.21: Dynamic Aperture from tracking studies with 10^5 turns using the WISE model and matched amplitude detuning to the measured values together with DA inferred from the measurements. The physical aperture is indicated with black lines.

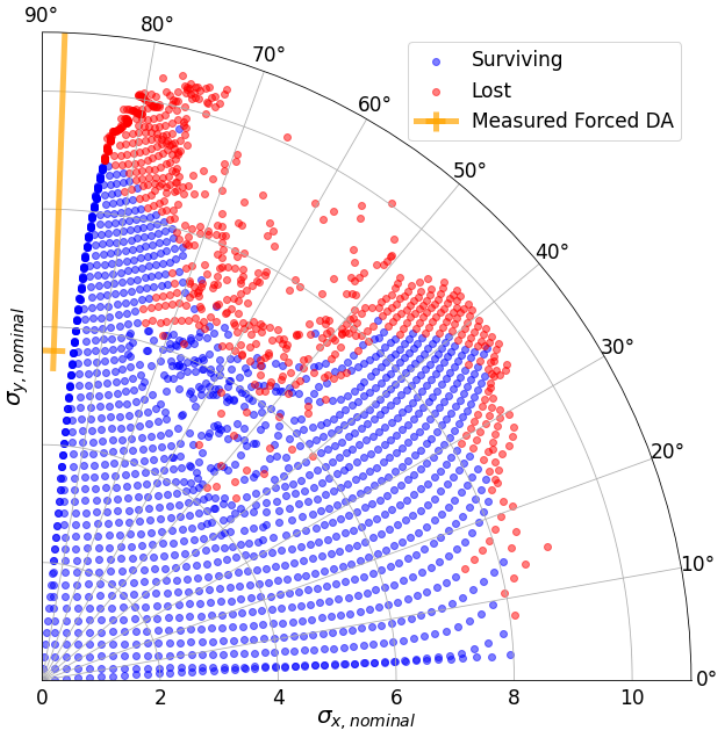

FIGURE 4.22: Forced Dynamic Aperture from tracking studies using the WISE model and matched amplitude detuning to the measured values

performing a frequency analysis on the first 200 turns, captured at the beam position monitor $BPM.22L1.B1$, at flattop and scaling the amplitude of the mainline with the β-function. The obtained action is then normalized using the nominal emittance of 3.75 µm. The tracking simulation show a forced DA above 9 $\sigma_{nominal}$ for a pure vertical excitation. Given the aforementioned issues during the forced dynamic aperture measurements, no conclusion on the validity of the model can be drawn. Using Eq. 4.2 and the vertical forced DA from the simulations, no loss should have been observed at the maximum kick amplitude of 5.4 $\sigma_{nominal}$.

4.5 Conclusions

In this experimental study, the dynamic aperture in the presence of strong local sextupole fields was successfully assessed. The measurements of free and forced dynamic aperture show a DA above 7 $\sigma_{nominal}$ for horizontal excitations, above 10 $\sigma_{nominal}$ for diagonal excitation and a forced DA above 5.6 $\sigma_{nominal}$ in case of vertical forced excitations. Initial tracking studies using a simple model, thought to provide optimistic estimates, were shown to actually provide lower values than what is measured. One key difference between the simple model and measurement was identified to be the amplitude detuning. Once corrected for in the model, simulation and measurement tend to agree better, showing that the DA in the LHC in the presence of large uncorrected sextupole error is of no concern. In turn, the situation for the HE-LHC or FCC-hh does not seem as severe as initially estimated. As for this case, the amplitude detuning, in part stemming from the strong sextupolar sources, was identified to have the largest impact on DA, a careful assessment of this could allow to find a correction using the octupoles to allow for minimal impact on the operational performance.

Chapter 5

Effect of local linear coupling on linear and nonlinear observables in circular accelerators

The contents of this chapter have also been published under the same title in *Physical Review Accelerator and Beams*, Volume **23**, Issue 9, 094001 on the 28th of September, 2020.

Operation of particle accelerators and correction of unavoidable magnet or alignment errors critically depend on the assessment of both global and local observables such as tune or resonance driving terms. With most of the observables being a sum of different error sources, careful disentangling is necessary in order to establish an optimal correction and allow for smooth operation. In the LHC, linear coupling has been proven to have a major impact on the beam dynamics and is taken to be one of the main sources of uncertainty when establishing corrections. In this paper an approach to evaluate the change of the Hamiltonian terms with linear coupling is presented. The validity of derived equations is demonstrated on a number of observables and benchmarked against simulations.

5.1 Introduction

Beam-based corrections of linear optics and nonlinear dynamics in current and future accelerator projects is of paramount importance to achieve their increasingly ambitious design goals. The evaluation of different error sources such as misalignment or magnetic field errors is based on measurements of either global quantities like the tune, chromaticity, and detuning terms or on local deviation from model values such as β-beating or resonance driving terms (RDT). In general, in the early commissioning phase of an accelerator focus is put on linear optics and coupling correction, both being major contributing factors in the performance of both hadron and lepton accelerators. Correction of linear coupling is usually based on either minimization of the global impact through reduction of the minimum possible tune separation or based on linear coupling RDTs or both.

The global effect of linear coupling is quantified by the closest tune approach ΔQ_{min}, that is, the minimum achievable distance between the fractional parts of the tunes [129]. More recently, this concept has been extended to include the effects of octupoles which lead to an amplitude dependence of the ΔQ_{min} [130, 131]. To

identify sources of linear coupling, the coupling RDTs f_{1001} and f_{1010} can be inferred from turn-by-turn data and serve as a basis for a local coupling correction. The relation between the coupling RDTs and ΔQ_{min} can be found in [132]. While significant efforts have been made in recent years to improve measurement and correction techniques for linear (and nonlinear) coupling [133], the residual coupling left after corrections still retains an important role when describing the dynamics in the accelerator.

For example, in the LHC in late 2018, it was observed that while global coupling was well corrected, an erroneous local coupling bump in one interaction region had a significant impact on the beam size and thus on the luminosity [134, 135]. Measurements of the β-function using the K-Modulation method did however not show any change in the tune shift generated from modulating the quadrupole gradient. Currently, no analytical derivation is available which may explain this insensitivity. A change of tune is not only used during the K-Modulation method, but also to determine nonlinear magnetic field errors in the triplet quadrupoles via feed down to a quadrupole gradient when changing the orbit in the quadrupoles [85, 136].

Linear coupling is also assumed to be the single biggest source of uncertainty when trying to model the nonlinear behaviour in the LHC. In [137], it was shown how nonlinear observables like detuning with amplitude are affected by linear coupling. This effect has been qualitatively demonstrated in [138] in simulations, where the impact of linear coupling on amplitude detuning is highlighted and how it may affect coherent instabilities in the LHC. Measurements of amplitude detuning are also used to establish corrections of nonlinear field errors in the triplet quadrupoles in the LHC [139]. Suboptimal correction of such may prove detrimental to beam lifetime and overall performance of the collider. To establish better corrections, the ability to determine the contribution of the local coupling to the measured amplitude detuning thus may prove quite helpful.

It was further shown in [137] that also measured RDTs change with linear coupling. In [140] it is shown how a skew sextupole resonance can be driven in the absence of any skew sextupole sources and away from the resonant condition due to interplay between the sextupoles and linear coupling. However, it is not apparent in this case how coupling would affect for example sextupole RDTs in the absence of skew sextupoles.

The studies presented in this chapter aim to quantify the effect that local linear coupling has on these global and local observables. Section 5.2 gives a brief introduction into the Normal form formalism, concluding with a description of the particle motion under the influence of local coupling, as was already presented in [141]. In section 5.3, the coupled eigenvalues then allow to express the effect on global and local observables under the influence of local coupling. This is then used in section 5.3.1 to show the impact on the change of tune during K-Modulation. The change of amplitude detuning generated by a single octupole in the presence of local coupling is treated in section 5.3.3. Section 5.3.4 then showcases the impact of local coupling on the RDT generated by a given multipole using as example sextupole RDTs.

5.2 Normal form and resonance driving term formalism

In circular accelerators, the one-turn motion of a single particle with the 4D coordinates $\mathbf{X} = (x, p_x, y, p_y)$ is described by

$$\mathbf{X_{s+C}} = \mathcal{M}_\mathbf{s}\mathbf{X_s}, \tag{5.1}$$

where $\mathcal{M}_s$ is the (sympletic) map of the accelerator lattice. For the sake of brevity, the dependence of the coordinates and following quantities on the longitudinal position s is omitted in the following. For a lattice consisting of W multipole elements the one-turn map is

$$\mathcal{M} = M_{W+1}e^{:H_{W,n_W}:}M_W ... e^{:H_{2,n_2}:}M_2 e^{:H_{1,n_1}:}M_1, \tag{5.2}$$

where M_w is the linear transfer map of a given element w. $H_{w,n}$ is the Hamiltonian for a magnetic multipole as given by

$$H_{w,n} = \frac{1}{n!}\Re\Big[(K_{w,n} + iK^S_{w,n})(x_w + iy_w)^n\Big], \tag{5.3}$$

with $e^{:H_{w,n}:}$ being the corresponding Lie-operator and $K_{w,n}$ and $K^S_{w,n}$ being the integrated magnetic strength of a normal and skew multipole, respectively. Here n denotes the order of the multipole of the element w with $n = 2$ corresponding to a quadrupole. The transverse coordinates at the element w are indicated with x_w and y_w.

In the following, the resonance basis

$$\mathbf{h} = (h_{x,+}, h_{x,-}, h_{y,+}, h_{y,-}) \tag{5.4}$$

is used with the definition

$$h_{q,\pm} = \hat{q} \pm i\hat{p}_q = \sqrt{2J_q}e^{\pm i\psi_q},\ q \in \{x, y\}, \tag{5.5}$$

where $\hat{q}$ and $\hat{p}_q$ are the normalised Courant-Snyder coordinates, defined as

$$\begin{pmatrix}\hat{q}\\ \hat{p}_q\end{pmatrix} = \begin{pmatrix}\frac{1}{\sqrt{\beta_q}} & 0\\ \frac{\alpha_q}{\sqrt{\beta_q}} & \sqrt{\beta_q}\end{pmatrix}\begin{pmatrix}q\\ p_q\end{pmatrix}, \tag{5.6}$$

and J_q and ψ_q the action and angle coordinates, respectively. The subscript $_w$ for the coordinates, introduced in Eq. (5.3), has been omitted here and in the following as the information on the element in question is implicitly specified via the s-dependence of the β-functions.

Following the derivations in [49], the map $\mathcal{M}$ from Eq. (5.2) can be rewritten as

$$\mathcal{M} = e^{:\tilde{H}_{1,n_1}:}e^{:\tilde{H}_{2,n_2}:}...e^{:\tilde{H}_{W,n_W}:}R, \tag{5.7}$$

where R is a rotation matrix. The Hamiltonian $\tilde{H}_{w,n}$ of a given element w of order n expressed in the resonance basis $\mathbf{h}$ is defined by

$$\tilde{H}_{w,n} = \sum_{jklm}^{n=j+k+l+m} h_{w,jklm} e^{i[(j-k)\Delta\phi_{w,x}+(l-m)\Delta\phi_{w,y}]} h_{x,+}^{j} h_{x,-}^{k} h_{y,+}^{l} h_{y,-}^{m}, \tag{5.8}$$

where $\Delta\phi_{w,x}$ and $\Delta\phi_{w,y}$ are the phase advances from the element w to an observation point in the horizontal and vertical plane, respectively. The coefficient $h_{w,jklm}$ is expressed by

$$h_{w,jklm} = \frac{\Re(i^{l+m}[K_{w,n} + iK_{w,n}^{S}])}{j!k!l!m!2^{n}} (\beta_{w,x})^{\frac{j+k}{2}} (\beta_{w,y})^{\frac{l+m}{2}}. \tag{5.9}$$

Using the Baker-Campbell-Hausdorff formula

$$e^{A}e^{B} = e^{A+B+\frac{1}{2}[A,B]+\cdots}, \tag{5.10}$$

Eq. (5.7) can be expressed as

$$e^{:\tilde{H}_{1,n_1}:} e^{:\tilde{H}_{2,n_2}:} \ldots e^{:\tilde{H}_{W,n_W}:} e^{\sum_{w}^{W} \tilde{H}_{w,n_w} + \frac{1}{2}\sum_{w}^{W}\sum_{v}^{w-1}[\tilde{H}_{w,n_w},\tilde{H}_{v,n_v}]+\cdots}, \tag{5.11}$$

where $\cdots$ indicates terms of order 3 and higher. In the normal form approach, the basis $\mathbf{h}$ is then transformed into the new basis $\boldsymbol{\zeta}$ following [142]

$$\boldsymbol{\zeta} = e^{-:F:}\mathbf{h}, \tag{5.12}$$

using a polynomial generating function

$$F = \sum_{jklm} f_{jklm} \zeta_{x,+}^{j} \zeta_{x,-}^{k} \zeta_{y,+}^{l} \zeta_{y,-}^{m}, \tag{5.13}$$

where $\zeta_{q,\pm} = \sqrt{2I_q} e^{\pm i\phi_q}$ and f_{jklm} denotes the resonance driving term.

It can be shown that the RDT f_{jklm} in first order is

$$f_{jklm} = \frac{\sum_w h_{w,jklm} e^{i[(j-k)\Delta\phi_{w,x}+(l-m)\Delta\phi_{w,y}]}}{1 - e^{2\pi i[(j-k)Q_x+(l-m)Q_y]}}, \tag{5.14}$$

where $h_{w,jklm}$ from Eq. (5.9) is used, which is obtained when approximating Eq. (5.11) as

$$e^{:\tilde{H}_{1,n_1}:} e^{:\tilde{H}_{2,n_2}:} \ldots e^{:\tilde{H}_{W,n_W}:} \approx e^{\sum_{w}^{W} \tilde{H}_{w,n_w}}. \tag{5.15}$$

The expansion to second order can be found in [49, 140].

5.2.1 Particle motion under the influence of coupling

Following Eq. (5.12), the transformation between normal form coordinates and Courant-Snyder coordinates reads

$$\begin{aligned} h_{q,\pm} = \hat{q} \pm i\hat{p}_q &= \sqrt{2J_q} e^{\pm i\psi_q} = \\ e^{:F:}\zeta_{q,\pm} &\approx \zeta_{q,\pm} + [F, \zeta_{q,\pm}] + \frac{1}{2!}[F,[F,\zeta_{q,\pm}]] + \ldots . \end{aligned} \tag{5.16}$$

In [141], it was shown that for the case of taking into account only linear perturbations such as either β-beating or linear coupling, a closed form of this transformation exists. In the case of linear coupling, the generating function F reads

$$F = f_{1001}\zeta_{x,+}\zeta_{y,-} + f_{1010}\zeta_{x,+}\zeta_{y,+} + f^*_{1001}\zeta_{x,-}\zeta_{y,+} + f^*_{1010}\zeta_{x,-}\zeta_{y,-}, \tag{5.17}$$

where the RDT f_{1001} drives the difference resonance $(Q_x - Q_y) = p$ and f_{1010} corresponds to the sum resonance $(Q_x + Q_y) = p$. Notably, this generating function only accounts for the geometric distortion due to coupling resonances and not for any change due to terms like f_{2000} which are excited by second and higher order interplay between skew quadrupoles. Using Eq. (5.16) together with the generating function F from Eq. (5.17) and

$$[\zeta^u_{q,+}, \zeta_{q,-}] = -2iu\zeta^{u-1}_{q,+}, \tag{5.18}$$

it is shown in [141] that the components of the resonance basis $\mathbf{h}$ can be expressed as

$$\begin{aligned}
h_{x,-} &= \zeta_{x,-}\cosh 2\mathcal{P} - i\frac{\sinh 2\mathcal{P}}{\mathcal{P}}(f_{1001}\zeta_{y,-} + f_{1010}\zeta_{y,+})\\
h_{x,+} &= \zeta_{x,+}\cosh 2\mathcal{P} + i\frac{\sinh 2\mathcal{P}}{\mathcal{P}}(f^*_{1010}\zeta_{y,-} + f^*_{1001}\zeta_{y,+})\\
h_{y,-} &= \zeta_{y,-}\cosh 2\mathcal{P} - i\frac{\sinh 2\mathcal{P}}{\mathcal{P}}(f^*_{1001}\zeta_{x,-} + f_{1010}\zeta_{x,+})\\
h_{y,+} &= \zeta_{y,+}\cosh 2\mathcal{P} + i\frac{\sinh 2\mathcal{P}}{\mathcal{P}}(f^*_{1010}\zeta_{x,-} + f_{1001}\zeta_{x,+})
\end{aligned} \tag{5.19}$$

where $2\mathcal{P} = \sqrt{|2f_{1010}|^2 - |2f_{1001}|^2}$. The particle coordinate q is given by

$$q = \frac{\sqrt{\beta_q}}{2}(h_{q,+} + h_{q,-}). \tag{5.20}$$

Using Eq. (5.19) and Eq. (5.20) the particles coordinates now read

$$\begin{aligned}
x &= \frac{\sqrt{\beta_x}}{2}\left[\zeta_{x,+}\mathcal{C} + \zeta_{x,-}\mathcal{C} + i\zeta_{y,+}\hat{F}^*_{yx} - i\zeta_{y,-}\hat{F}_{yx}\right], \qquad (5.21)\\
y &= \frac{\sqrt{\beta_y}}{2}\left[\zeta_{y,+}\mathcal{C} + \zeta_{y,-}\mathcal{C} + i\zeta_{x,+}\hat{F}^*_{xy} - i\zeta_{x,-}\hat{F}_{xy}\right],
\end{aligned}$$

where the superscript * denotes the complex conjugate and

$$\mathcal{C} = \cosh 2\mathcal{P}, \tag{5.22}$$

$$\hat{F}_{yx} = \frac{\sinh 2\mathcal{P}}{\mathcal{P}}(f^*_{1001} - f^*_{1010}), \tag{5.23}$$

$$\hat{F}_{xy} = \frac{\sinh 2\mathcal{P}}{\mathcal{P}}(f_{1001} - f^*_{1010}) \tag{5.24}$$

have been introduced. Equations (5.23) and (5.24) represent the combined coupling RDTs presented in [140] scaled by a factor $\frac{\sinh 2\mathcal{P}}{\mathcal{P}}$. In case of $|f_{1001}| = |f_{1010}|$, $\mathcal{C}$ and $\frac{\sinh 2\mathcal{P}}{\mathcal{P}}$ reduce to 1 and 2, respectively. It should be noted that in the following section for the benchmarking of the derivations, the coupling RDTs f_{1001} and f_{1010} have

been evaluated by expressing them as functions of the coupling matrix, as is shown in [143]. This way, all orders of the coupling RDTs are also taken into account and due to the closed form of the transformation (5.16), by using the generating function from Eq. (5.17), also the transformation is accurate to arbitrary order.

5.3 Change of observables due to coupling

In [49], contributions to tune and amplitude detuning up to second order have been derived. Similarly so, in [140], resonance driving term coefficients up to second order are presented. In both cases, it is apparent that the first order contributions from e.g. octupole to amplitude detuning is not modified in the presence of coupling and changes stem from other contributions such as skew octupoles in conjunction with coupling. Yet simulation work presented in [138] clearly shows that amplitude detuning generated by octupoles is affected in the presence of local coupling, also in the absence of other skew elements.

These findings indicate that the observed effect could stem from third order contributions or higher. As higher order expansion become more and more cumbersome, here an alternative approach is presented, which is specifically applicable to linear coupling. Using the coupled coordinates from Eq. (5.21), the Hamiltonian from Eq. (5.3) can be expanded leading to

$$
\begin{aligned}
\tilde{H}^{c}_{w,n} = \quad & \tfrac{1}{n!}\tfrac{1}{2}\Bigg\{\left(K_{w,n} + iK^{S}_{w,n}\right)\times \\
& \Bigg[\zeta_{x,+}\quad\left(\frac{\sqrt{\beta_x}}{2}\mathcal{C} - \frac{\sqrt{\beta_y}}{2}\hat{F}^{*}_{xy}\right) + \zeta_{x,-}\quad\left(\frac{\sqrt{\beta_x}}{2}\mathcal{C} + \frac{\sqrt{\beta_y}}{2}\hat{F}_{xy}\right) \\
& +i\zeta_{y,+}\quad\left(\frac{\sqrt{\beta_y}}{2}\mathcal{C} + \frac{\sqrt{\beta_x}}{2}\hat{F}^{*}_{yx}\right) + i\zeta_{y,-}\quad\left(\frac{\sqrt{\beta_y}}{2}\mathcal{C} - \frac{\sqrt{\beta_x}}{2}\hat{F}_{yx}\right)\Bigg]^{n} \\
& +\left(K_{w,n} - iK^{S}_{w,n}\right)\times \\
& \Bigg[\zeta_{x,-}\quad\left(\frac{\sqrt{\beta_x}}{2}\mathcal{C} - \frac{\sqrt{\beta_y}}{2}\hat{F}_{xy}\right) + \zeta_{x,+}\quad\left(\frac{\sqrt{\beta_x}}{2}\mathcal{C} + \frac{\sqrt{\beta_y}}{2}\hat{F}^{*}_{xy}\right) \\
& -i\zeta_{y,-}\quad\left(\frac{\sqrt{\beta_y}}{2}\mathcal{C} + \frac{\sqrt{\beta_x}}{2}\hat{F}_{yx}\right) - i\zeta_{y,+}\quad\left(\frac{\sqrt{\beta_y}}{2}\mathcal{C} - \frac{\sqrt{\beta_x}}{2}\hat{F}^{*}_{yx}\right)\Bigg]^{n}\Bigg\},
\end{aligned}
\tag{5.25}
$$

where $\Re(z) = \frac{z+z^*}{2}$ and $\zeta^{*}_{q,\pm} = \zeta_{q,\mp}$ has been used. Here the superscript ^{c} has been introduced as to distinguish from the Hamiltonian using the uncoupled basis. Following the multinomial theorem

$$
(x_1 + x_2 + ... + x_m)^n = \sum_{k_1+k_2+...k_m=n} \frac{n!}{k_1!k_2!...k_m!}\prod_{t=1}^{m} x_t^{k_t} \tag{5.26}
$$

the Hamiltonian is rewritten as

$$\begin{aligned}\tilde{H}^c_{w,n} \quad = \quad & \sum_{jklm}^{n=j+k+l+m} \\ & \left[\frac{i^{l+m}(K_{w,n}+iK^S_{w,n})}{j!k!l!m!2^{n+1}}\zeta^j_{x,+}\zeta^k_{x,-}\zeta^l_{y,+}\zeta^m_{y,-}\times\right. \\ & \left.(\sqrt{\beta_x}\mathcal{C}-\sqrt{\beta_y}\hat{F}^*_{xy})^j(\sqrt{\beta_x}\mathcal{C}+\sqrt{\beta_y}\hat{F}_{xy})^k(\sqrt{\beta_y}\mathcal{C}+\sqrt{\beta_x}\hat{F}^*_{yx})^l(\sqrt{\beta_y}\mathcal{C}-\sqrt{\beta_x}\hat{F}_{yx})^m\right]+ \\ & \left[\frac{(-i)^{l+m}(K_{w,n}-iK^S_{w,n})}{j!k!l!m!2^{n+1}}\zeta^j_{x,+}\zeta^k_{x,-}\zeta^l_{y,+}\zeta^m_{y,-}\times\right. \\ & \left.(\sqrt{\beta_x}\mathcal{C}+\sqrt{\beta_y}\hat{F}^*_{xy})^j(\sqrt{\beta_x}\mathcal{C}-\sqrt{\beta_y}\hat{F}_{xy})^k(\sqrt{\beta_y}\mathcal{C}-\sqrt{\beta_x}\hat{F}^*_{yx})^l(\sqrt{\beta_y}\mathcal{C}+\sqrt{\beta_x}\hat{F}_{yx})^m\right].\end{aligned} \tag{5.27}$$

It follows that the coefficient $h^c_{w,jklm}$ from Eq. (5.9) in the presence of coupling can then be rewritten as

$$\begin{aligned}h^c_{w,jklm} \quad = \quad & \frac{i^{l+m}[K_{w,n}+iK^S_{w,n}]}{j!k!l!m!2^{n+1}}\times \\ \Big[(\sqrt{\beta_x}\mathcal{C} \quad & -\sqrt{\beta_y}\hat{F}^*_{xy})^j(\sqrt{\beta_x}\mathcal{C}+\sqrt{\beta_y}\hat{F}_{xy})^k(\sqrt{\beta_y}\mathcal{C}+\sqrt{\beta_x}\hat{F}^*_{yx})^l(\sqrt{\beta_y}\mathcal{C}-\sqrt{\beta_x}\hat{F}_{yx})^m\Big] \\ + \quad & \frac{(-i)^{l+m}[K_{w,n}-iK^S_{w,n}]}{j!k!l!m!2^{n+1}}\times \\ \Big[(\sqrt{\beta_x}\mathcal{C} \quad & +\sqrt{\beta_y}\hat{F}^*_{xy})^j(\sqrt{\beta_x}\mathcal{C}-\sqrt{\beta_y}\hat{F}_{xy})^k(\sqrt{\beta_y}\mathcal{C}-\sqrt{\beta_x}\hat{F}^*_{yx})^l(\sqrt{\beta_y}\mathcal{C}+\sqrt{\beta_x}\hat{F}_{yx})^m\Big]\end{aligned} \tag{5.28}$$

and similar so to obtain f^c_{jklm} following Eq. (5.14). In the following, only the first order in strength of the natural source will be used in the evaluation of the Hamiltonian, however, a higher-order expansion analogously to [140] is possible as well. It should also be mentioned that by including a dispersion term $D_q\delta_p$ in the coupled coordinates from Eq. (5.21), also the behavior of the off-momentum Hamiltonian can be studied.

5.3.1 Impact of local coupling on K-Modulation

As a first application of the previous derivation, the impact of local coupling on the tune change from a change in quadrupole is examined. This change of tune is for example used during K-Modulation to determine the average β-function in quadrupoles, but has also been used in the LHC to determine nonlinear field errors in the triplet quadrupoles by changing the orbit and observing the tune change due to feed down. In general, the tune shift for a given Hamiltonian $\tilde{H}$ is

$$\Delta Q_q = \frac{1}{2\pi}\frac{\partial\langle\tilde{H}\rangle}{\partial J_q} \tag{5.29}$$

where $\langle\tilde{H}\rangle$ is the Hamiltonian average over the phase variables. As such, only phase-independent terms in the Hamiltonian will contribute. In the case of a horizontal (vertical) tune change for a quadrupole, this term corresponds to h_{1100} (h_{0011}).

Taking the Hamilton from Eq. (5.27) for the case of a thin quadrupole ($n = 2$) together with Eq. (5.29), the tune shift in the presence of local coupling is then

$$\Delta Q_x^c = \frac{\Delta K_2}{4\pi}\left[\beta_x \mathcal{C}^2 - \beta_y |\hat{F}_{xy}|^2\right], \tag{5.30}$$
$$\Delta Q_y^c = -\frac{\Delta K_2}{4\pi}\left[\beta_y \mathcal{C}^2 - \beta_x |\hat{F}_{yx}|^2\right],$$

where the subscript $_w$ has been omitted as here the case for only one element is examined. From this equation, it is apparent that any local coupling will tend to result in a decrease of the induced tune change.

We note that in the case of no local coupling ($f_{1001} = f_{1010} = 0$), these formulas reduce to the case of a thin quadrupole excitation

$$\Delta Q_{x,y}^{\text{approx}} = \pm\frac{\Delta K_2 \beta_{x,y}}{4\pi}, \tag{5.31}$$

which is an approximation of

$$\Delta Q_{x,y}^{\text{exact}} = -Q_{x,y} \tag{5.32}$$
$$+\frac{1}{2\pi}\arccos\left[\cos\left(2\pi Q_{x,y}\right) \mp \frac{\beta_{x,y}\Delta K_2}{2}\sin\left(2\pi Q_{x,y}\right)\right],$$

the approximation being valid in case of a small excitation ΔK_2 and sufficiently far from the integer and half-integer resonance [43]. To overcome these limitations, the first part of Eq. (5.30) can be replaced by Eq. (5.32) yielding

$$\Delta Q_x^c = \Delta Q_x^{\text{exact}} \mathcal{C}^2 - \frac{\Delta K_2}{4\pi}\beta_y |\hat{F}_{xy}|^2$$
$$\Delta Q_y^c = \Delta Q_y^{\text{exact}} \mathcal{C}^2 + \frac{\Delta K_2}{4\pi}\beta_x |\hat{F}_{yx}|^2. \tag{5.33}$$

We note that both Eq. (5.30) and (5.33) still only include the first-order contribution of ΔK_2 to tune shift, which is only exact in case of a thin quadrupole. In [144], a derivation is presented including the second-order contribution in ΔK_2 in case of a thick quadrupole.

To check the validity of the derived formulas and impact of higher-order contributions, MAD-X simulations were conducted using the LHC lattice. To mitigate interference from effects such as changes in the β-function through thick elements, a lattice composed of thin (zero length) elements was used.

For the conducted studies the inner triplet of the experimental insertion in LHC Point 1 was used. The location was chosen as in the LHC the β-function at the interaction point (β^*) is usually inferred from K-Modulation, a method which allows to calculate the average β-function in a quadrupole by measuring the tune change ΔQ under a modulation of the quadrupole gradient ΔK_2.

A change of this ΔQ due to local linear coupling at the location of the quadruple may thus affect the accuracy with which β^* can be reconstructed.

It is also here where due to the large β-function, an erroneous rotation of a triplet quadrupole around the longitudinal axis may give rise to a considerable skew quadrupole component. A closed coupling bump is created by using the skew

quadrupole correctors located between the second and third quadrupole of the final focus triplet left and right of the interaction point (IP), as illustrated in Fig. 5.1.

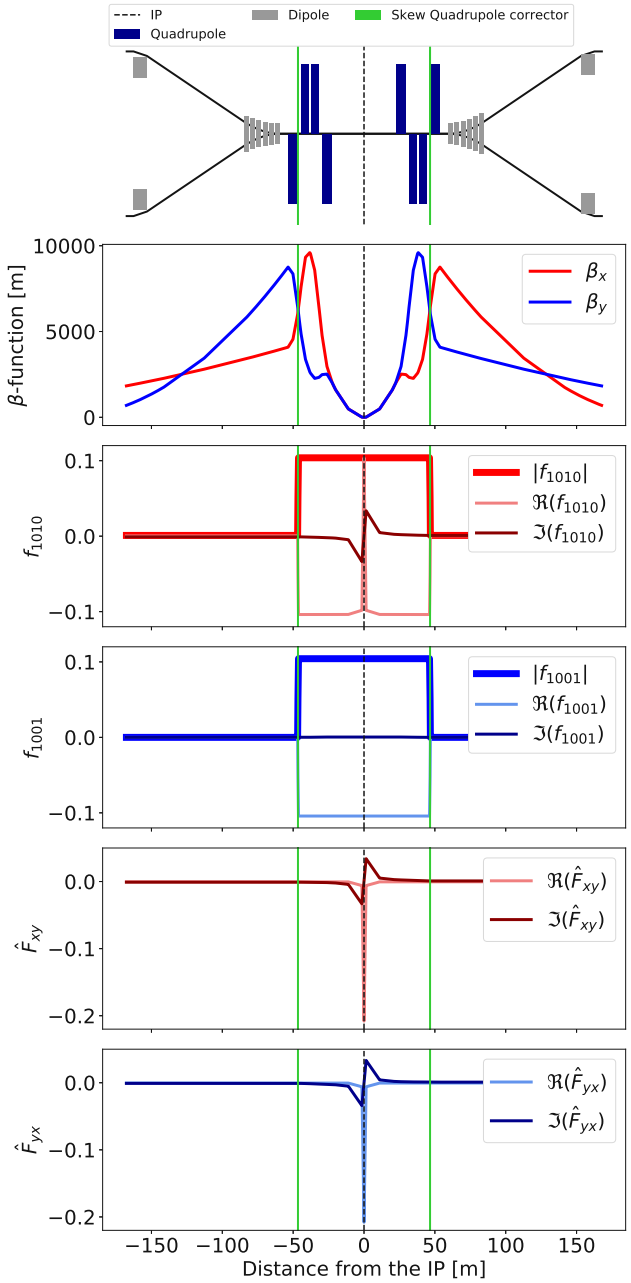

FIGURE 5.1: Illustration of a LHC interaction region. The optics presented here corresponds to β^*=25 cm and the strength of the skew quadrupole correctors (shown in green) was set to $K_2^S L = 6.7 \cdot 10^{-5}\ \mathrm{m}^{-2}$.

Due to the phase difference between the left and right skew quadrupole corrector being close to 180°, and if powered with opposite strength, the perturbation of the first skew quadrupole is canceled by the second one and ΔQ_{min} is marginally affected. After application of the skew quadrupole correctors, the tunes were rematched to the original values of $Q_x = 0.28$ and $Q_y = 0.31$ to compensate for the small second-order contribution of the correctors to tune. In this configuration however, the two

coupling terms cannot be controlled independently and $|f_{1010}| = |f_{1001}|$.

The gradient of one slice of the first quadrupole right of the interaction point was changed to induce a tune change in the uncoupled case of ≈ 0.01 in the plane with the larger β-function. The sign of the gradient change was chosen such that the tunes drift apart to mitigate any interference of a possible closest tune approach. A comparison between both formulas to results from MAD-X simulations is presented in Fig. 5.2. We note that Eq. (5.30) presents an offset even in case of no coupling. This

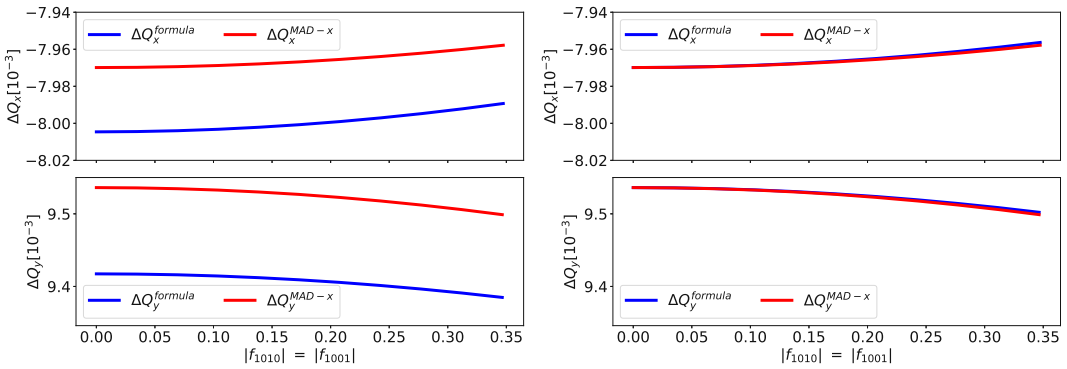

(A) Tune change from Eq. (5.30) compared to MAD-X simulations.

(B) Tune change from Eq. (5.33) compared to MAD-X simulations.

FIGURE 5.2: Comparison of tune change from quadrupole modulation with coupling to MAD-X simulations.

offset is attributed to the use of the approximation Eq. (5.31) in Eq. (5.30). Equation (5.33), which does not rely on this approximation, does not present this offset anymore and shows good agreement for the probed levels of coupling. In Fig. 5.3 the reduction in percent is presented for different ratios of $\frac{\beta_x}{\beta_y}$. Notably, for an amplitude of $|f_{1010}|$ around 0.15, the change of tune is below 0.1% in both planes with respect to the uncoupled case.

5.3.2 Effect on beam size

In late 2018, it was observed that a strong local coupling in the interaction point 2 in the LHC, introduced by an erroneous swap of two corrector settings, lead to a reduction of the luminosity of about a factor 2 [134, 135]. In the previous section, it was shown that even for a sizable local coupling, no significant change in ΔQ is observed. As such, K-Modulation measurements are only weakly affected by the presence of local coupling, which has also been demonstrated in a dedicated experiment in the LHC [145]. On the other hand, tracking studies presented in [146] show a drastic increase of the beam size at the IP if the local coupling bump is introduced, able to explain most of observed luminosity loss.

In the following, it will be shown how for the same setup as used for the tune change a significant increase in beam size can be calculated. The derivations presented here follow those in [147]. Assuming a centered Gaussian beam distribution, the second

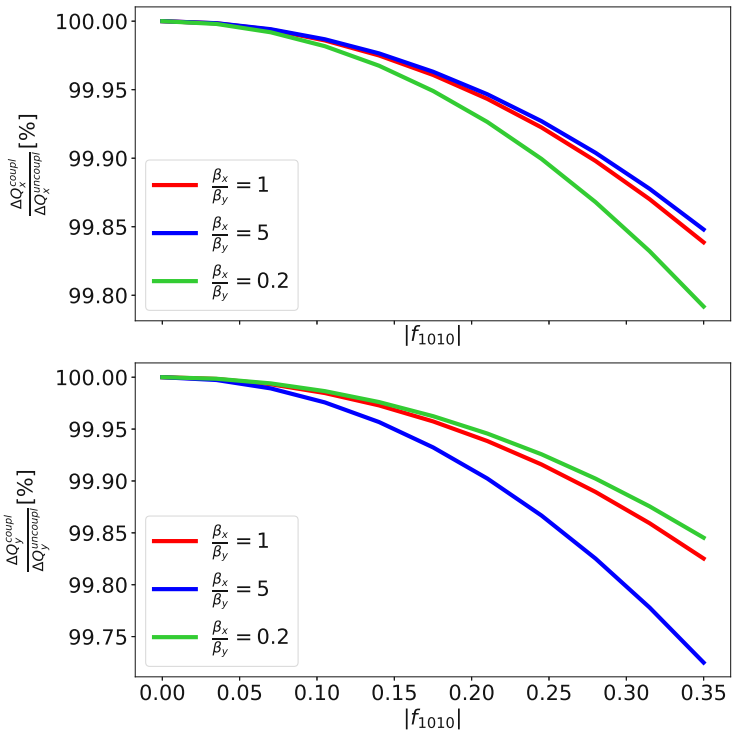

FIGURE 5.3: Change of the induced tune change from change of quadrupole gradient with local coupling amplitude.

order moment reads

$$\langle x^2 \rangle = \sigma_x^2 = \frac{1}{4\pi^2 \epsilon_x \epsilon_y} \int_0^\infty \int_0^\infty \int_0^{2\pi} \int_0^{2\pi} x^2 e^{-\frac{J_x}{\epsilon_x} - \frac{J_y}{\epsilon_y}} dJ_x dJ_y d\psi_x d\psi_y \tag{5.34}$$

where $\epsilon_{x,y}$ is the uncoupled RMS emittance in the horizontal and vertical plane, respectively. Using Eq. (5.21) one then obtains

$$\sigma_x^c = \sqrt{\langle x^2 \rangle} = \left[\beta_x \epsilon_x \mathcal{C}^2 + \beta_x \epsilon_y |\hat{F}_{yx}|^2 \right]^{\frac{1}{2}}. \tag{5.35}$$

Note that here the emittance exchange effect on the RMS emittances, described in [141] using the RDT formalism, is not taken into account. In a similar fashion, the beam size in the vertical plane reads

$$\sigma_y^c = \sqrt{\langle y^2 \rangle} = \left[\beta_y \epsilon_y \mathcal{C}^2 + \beta_y \epsilon_x |\hat{F}_{xy}|^2 \right]^{\frac{1}{2}}. \tag{5.36}$$

Local coupling will not only result in an increase of beamsize but can also introduce a tilt angle in the x-y-plane, as shown in [148]. The tilt angle ψ relates to the elements of the sigma matrix via

$$\tan(2\psi) = \frac{2\langle xy \rangle}{\langle x^2 \rangle - \langle y^2 \rangle} \tag{5.37}$$

where

$$\langle xy \rangle = \left[\sqrt{\beta_x \beta_y} \mathcal{C} \left(\epsilon_x \Im \hat{F}_{xy} + \epsilon_y \Im \hat{F}_{yx} \right) \right] \tag{5.38}$$

is used.

A comparison of the increase in beam size in the IP predicted by the formula with the MAD-X tracking simulations, using the setup described in the previous section, is presented in Fig. 5.4. For this tracking studies 10000 particles were tracked for 256

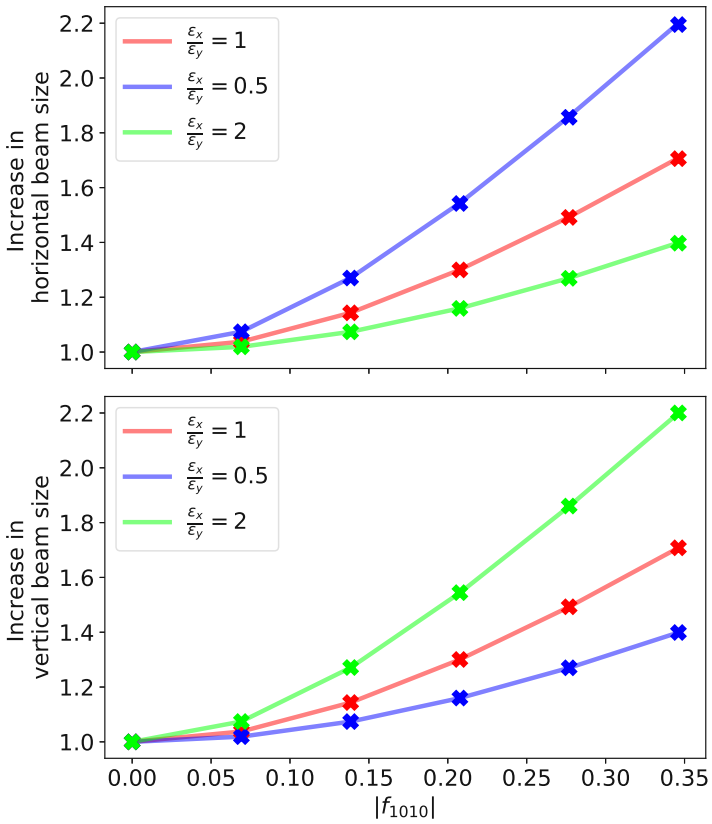

FIGURE 5.4: Increase of beam size in IP1 as a function of the absolute value of the coupling RDT.

turns using MAD-X. Notably, for $|f_{1010}|$ in a range where a tune change of below 0.1 % is observed, the beam size at the IP can increase by almost 20 % for equal emittances in both planes.

Observing Fig. 5.1, one can see that due to the jump of the f_{1010} coupling RDT and in the following also $\hat{F}_{xy}$ and $\hat{F}_{yx}$ at the IP, the local coupling leads to a large effect on the beam size at this position. On the other hand, $\hat{F}_{xy}$ and $\hat{F}_{yx}$ at the position of the innermost quadrupoles are significantly lower, thus explaining the small impact on the K-Modulation measurements.

Based on these formulas, the beam size inferred from optics measurements can be corrected to accurately represent the real beam size if local coupling is evaluated by other means. This could for example be used to correct the inferred emittance based on beam size measurements provided by instruments such as synchrotron light monitors.

5.3.3 Impact on amplitude detuning generated by octupoles

A second global observable of particular importance in the LHC is the detuning with amplitude generated by octupoles due to its role in damping coherent instabilities. Previous studies presented in [138] have already shown how linear coupling may lead to a loss of Landau damping. However, no analytical relation between local coupling and the decrease in amplitude detuning has been established.

Similar to the derivation of the change of tune presented in the previous section, we derive here equations to describe the impact of coupling on the amplitude detuning generated by octupoles. The amplitude detuning for a given Hamiltonian $\tilde{H}$ is calculated by

$$\frac{\partial Q_q}{\partial J_u} = \frac{1}{2\pi}\frac{\partial^2 \langle \tilde{H} \rangle}{\partial J_q \partial J_u}. \tag{5.39}$$

Using the previous equation together with the Hamiltonian from Eq. (5.27) for the case of a thin octupole, the direct and cross-plane amplitude detuning terms in the presence of linear coupling read

$$\frac{\partial Q_x^c}{\partial J_x} = \frac{K_4}{16\pi}\left[\beta_x^2\mathcal{C}^4 + \beta_y^2|\hat{F}_{xy}|^4 - 2\beta_x\beta_y\mathcal{C}^2\left(|\hat{F}_{xy}|^2 + 2(\Im\hat{F}_{xy})^2\right)\right], \tag{5.40}$$

$$\frac{\partial Q_y^c}{\partial J_y} = \frac{K_4}{16\pi}\left[\beta_y^2\mathcal{C}^4 + \beta_x^2|\hat{F}_{yx}|^4 - 2\beta_x\beta_y\mathcal{C}^2\left(|\hat{F}_{yx}|^2 + 2(\Im\hat{F}_{yx})^2\right)\right], \tag{5.41}$$

$$\frac{\partial Q_x^c}{\partial J_y} = \frac{\partial Q_y^c}{\partial J_x} = \frac{K_4}{8\pi}\left[\beta_x^2\mathcal{C}^2|\hat{F}_{yx}|^2 + \beta_y^2\mathcal{C}^2|\hat{F}_{xy}|^2 - \beta_x\beta_y\left(\mathcal{C}^4 - 4\mathcal{C}^2\Im\hat{F}_{yx}\Im\hat{F}_{xy} + |\hat{F}_{yx}|^2|\hat{F}_{xy}|^2\right)\right], \tag{5.42}$$

where again the subscript $_w$ has been omitted. Unlike the previous case for the tune change, here no general tendency leading to a reduction is observed, with the change being rather dependent on the ratio of the β-functions. However, for a case like the LHC where the Landau octupoles are positioned next to main quadrupoles in the arc and, as such, the β-function in one plane is significantly larger than that in the other plane, the direct amplitude detuning term in the focusing plane of the quadrupole as well as the crossterm detuning will decrease.

To benchmark the derived formulas, again studies using a thin LHC lattice as testbed were conducted using MAD-X-PTC. Similar to studies presented in [138], 4 skew quadrupoles were installed in the dispersion suppressor left and right of arc 12 in the LHC to create a closed coupling bump. This is illustrated in Fig. 5.5. One octupole next to a defocusing quadrupole was then powered to three quarter of its maximum gradient of $6.3 \cdot 10^4$ T/m^3 and the amplitude detuning with and without the coupling bump was determined. In both cases, all other nonlinear elements have been turned off to avoid contributions from other sources. Tunes were rematched to the original values of $Q_x = 0.28$ and $Q_y = 0.31$ after application of the coupling bump using quadrupoles located outside of the bump. The results are presented in Tab. 5.1. To show that this effect is caused by the local coupling, the amplitude detuning generated by another octupole in the neighbouring arc 23 is presented in

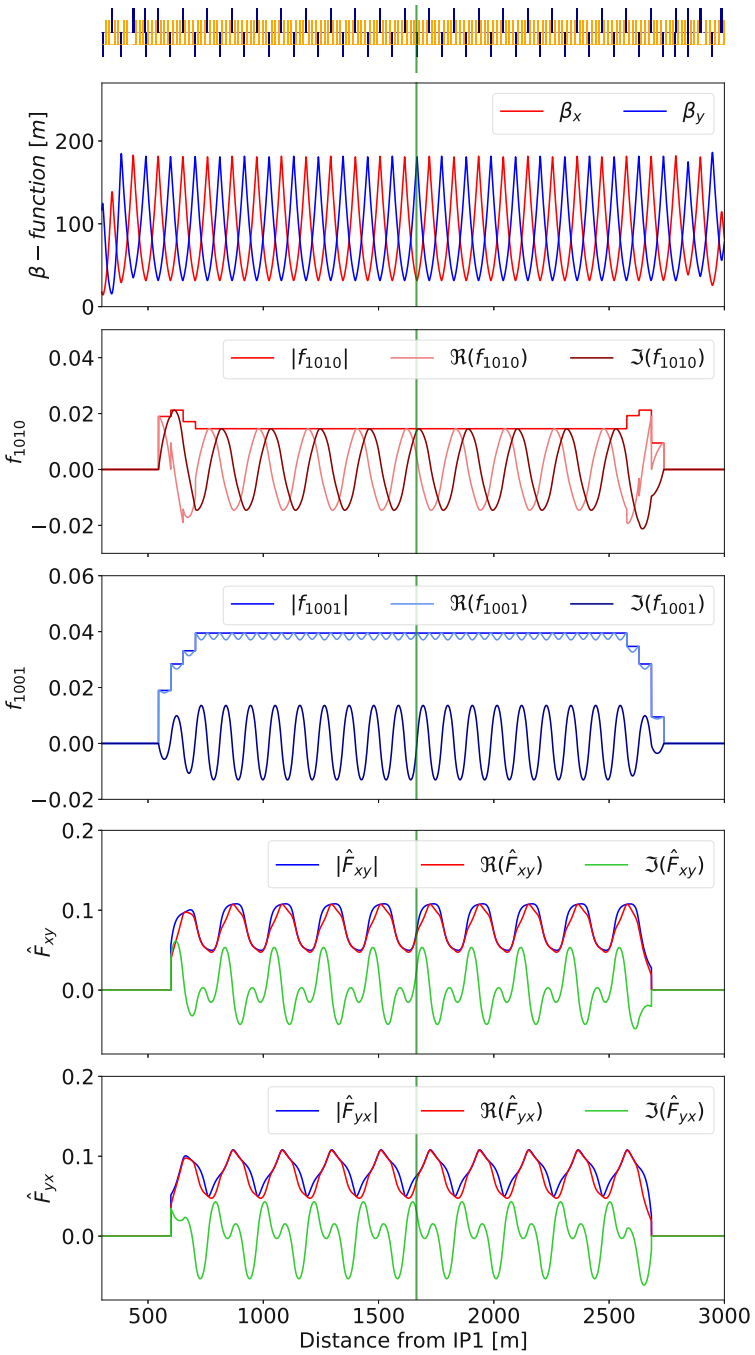

FIGURE 5.5: Illustration of the four corrector coupling bump created through the arc 12 right of IP1. The position of the octupole is indicated with a green line.

Tab. 5.2.

The small change in amplitude detuning between the case of no coupling bump and with a coupling bump in arc 12 in Tab. 5.2 is explained by the second order effect of the skew quadrupoles on the optics. Here, the β-function at the octupole in arc 23 changes by 0.15 % and -0.09 % in the horizontal and vertical plane, respectively. As for the case of amplitude detuning generated by the octupole in the coupling bump,

	no Coupling Bump		with Coupling Bump	
	Formula	PTC	Formula	PTC
dQ_x/dJ_x	$2.16 \cdot 10^2$	$2.16 \cdot 10^2$	$1.98 \cdot 10^2$	$1.95 \cdot 10^2$
dQ_y/dJ_y	$6.17 \cdot 10^3$	$6.17 \cdot 10^3$	$6.05 \cdot 10^3$	$6.05 \cdot 10^3$
dQ_x/dJ_y	$-2.31 \cdot 10^3$	$-2.31 \cdot 10^3$	$-2.19 \cdot 10^2$	$-2.20 \cdot 10^2$

TABLE 5.1: Amplitude detuning from single octupole in arc 12.

	no Coupling Bump		with Coupling Bump	
	Formula	PTC	Formula	PTC
dQ_x/dJ_x	$2.16 \cdot 10^2$	$2.16 \cdot 10^2$	$2.11 \cdot 10^2$	$2.11 \cdot 10^2$
dQ_y/dJ_y	$6.17 \cdot 10^3$	$6.17 \cdot 10^3$	$6.20 \cdot 10^3$	$6.20 \cdot 10^3$
dQ_x/dJ_y	$-2.31 \cdot 10^3$	$-2.31 \cdot 10^3$	$-2.29 \cdot 10^3$	$-2.29 \cdot 10^3$

TABLE 5.2: Amplitude detuning from single octupole in arc 23.

a difference between the derived formulas and MAD-X-PTC is observed, in particular in the cross term (dQ_x/dJ_y) and in the direct term of the horizontal plane, which is also the plane where the β-function is smaller. Using instead an octupole closer to a focusing quadrupole ($\beta_x \gg \beta_y$), the deviation in the horizontal amplitude detuning is reduced while it increases for the detuning with amplitude in the vertical plane. In Tab. 5.3, a comparison between the analytical derivations and MAD-X-PTC is presented again for amplitude detuning of an octupole close to a defocusing quadrupole but with the amplitude of coupling bump being a factor 5 larger compared to the case presented in Fig. 5.5. Here the relative error between formulas and

	no Coupling Bump		with Coupling Bump	
	Formula	PTC	Formula	PTC
dQ_x/dJ_x	$2.16 \cdot 10^2$	$2.16 \cdot 10^2$	$-4.07 \cdot 10^1$	$-6.95 \cdot 10^1$
dQ_y/dJ_y	$6.17 \cdot 10^3$	$6.17 \cdot 10^3$	$3.54 \cdot 10^3$	$3.73 \cdot 10^3$
dQ_x/dJ_y	$-2.31 \cdot 10^3$	$-2.31 \cdot 10^3$	$5.26 \cdot 10^1$	$-2.19 \cdot 10^2$

TABLE 5.3: Amplitude detuning from single octupole in arc 12 with increased levels of local coupling.

MAD-X-PTC is larger for all terms compared to the previous case with again both the cross term and the direct detuning in the horizontal plane showing a larger relative deviation compared to the vertical detuning with amplitude. Notably, for the same level of local coupling, the relative difference between the derived formulas and the results from MAD-X-PTC is not affected by the strength of octupole. Furthermore, the relative deviation only changes slightly for working points with a smaller tune separation, suggesting that the influence of a possible (amplitude-dependent) closest tune approach is negligible. Due to these aforementioned considerations, the derived formulas represent well the change of amplitude detuning in the presence of local linear coupling to leading order and deviation may arise from additional terms proportional to the level of the local coupling which are not accounted for in the presented derivation.

5.3.4 Impact on local RDTs

In [137], it was not only shown that coupling affects global quantities such as amplitude detuning but also a shift of the amplitude of measured skew sextupole RDTs is

observed. As derived in [140] this shift could be partially explained by taking into account second order contributions from coupling in conjunction with normal sextupoles. However, from these derivations it is not apparent if the skew sextupole RDT would change in the absence of normal sextupoles.

Using the Hamiltonian for a normal sextupole as an example, in the following it is shown how the generated RDTs are affected under local coupling in the absence of other skew multipoles. The coefficients from Eq. (5.28) in the presence of local linear coupling for the sextupole RDTs f_{3000} and f_{2100} read

$$h^c_{w,3000} = \frac{K_{w,3}}{48}\left[\beta_x^{\frac{3}{2}}\mathcal{C}^3 + \sqrt{\beta_x}\beta_y\mathcal{C}|\hat{F}_{xy}|^2\right] \tag{5.43}$$

and

$$h^c_{w,2100} = \frac{K_{w,3}}{8}\left[\beta_x^{\frac{3}{2}}\mathcal{C}^3 - \sqrt{\beta_x}\beta_y\mathcal{C}|\hat{F}_{xy}|^2\right]. \tag{5.44}$$

In the uncoupled case, both terms stem from the x^3 term in the sextupole Hamiltonian

$$H_3 = \frac{K_3}{3!}(x^3 - 3xy^2) \tag{5.45}$$

whereas in the coupled case an additional contribution from the xy^2 term is observed.

To benchmark the derived formulas, the same setup was used as in the study for the amplitude detuning. Two sextupoles with a phase difference of 2π in both planes were powered to 3/4 of their maximum gradient to create a closed sextupole RDT bump. In Fig. 5.6 and Fig. 5.7, a comparison between MAD-X-PTC and the analytical formula for the case with and without coupling is presented.

As also in the case of the amplitude detuning, in general a good agreement between the derived formulas and MAD-X-PTC is observed. The difference, which is more pronounced for the RDT f_{2100}, is again thought to stem from additional terms in the strength of local coupling.

5.4 Conclusions

Equations relating the impact of local coupling on global and local observables have been presented. While these effects are though to come from third and higher order contributions, here instead of performing the higher order expansion an alternative approach is presented, using the coupled coordinates. To illustrate the impact of local linear coupling, the reduction of the amplitude detuning generated by one octupole has been shown for the LHC case as well as the change of resonance driving terms generated by sextupoles. Comparison between the derived analytical formulas and tracking studies show good agreement in the range of interest, with the observed deviations from the tracking code results appearing to stem from additional terms which are not taken into account in the presented approach. Given the impact on e.g. beam size and subsequently possible luminosity decrease, these formulas allow to establish an upper bound for tolerable local coupling in an accelerator.

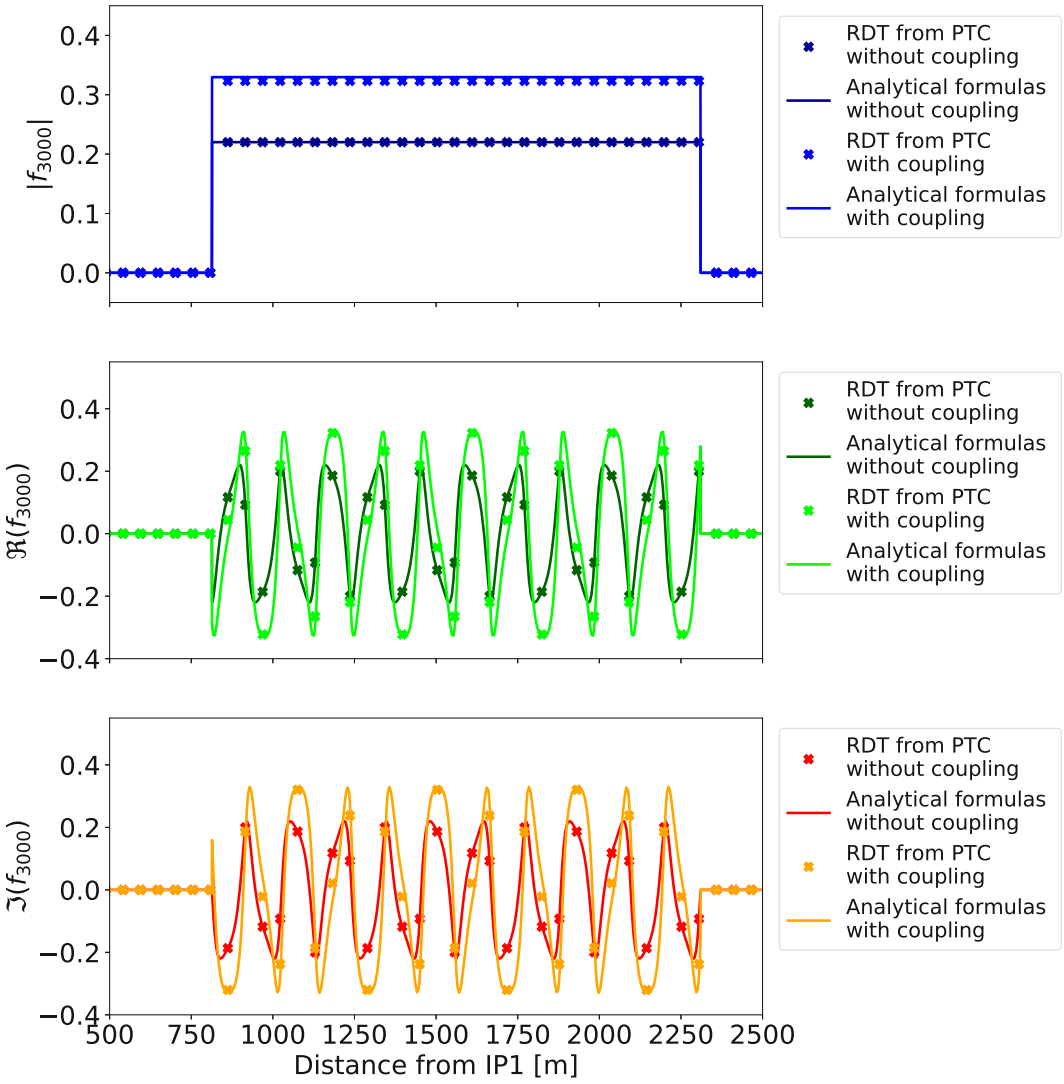

FIGURE 5.6: Comparison for the sextupole RDT f_{3000} between MAD-X-PTC and derived formulas.

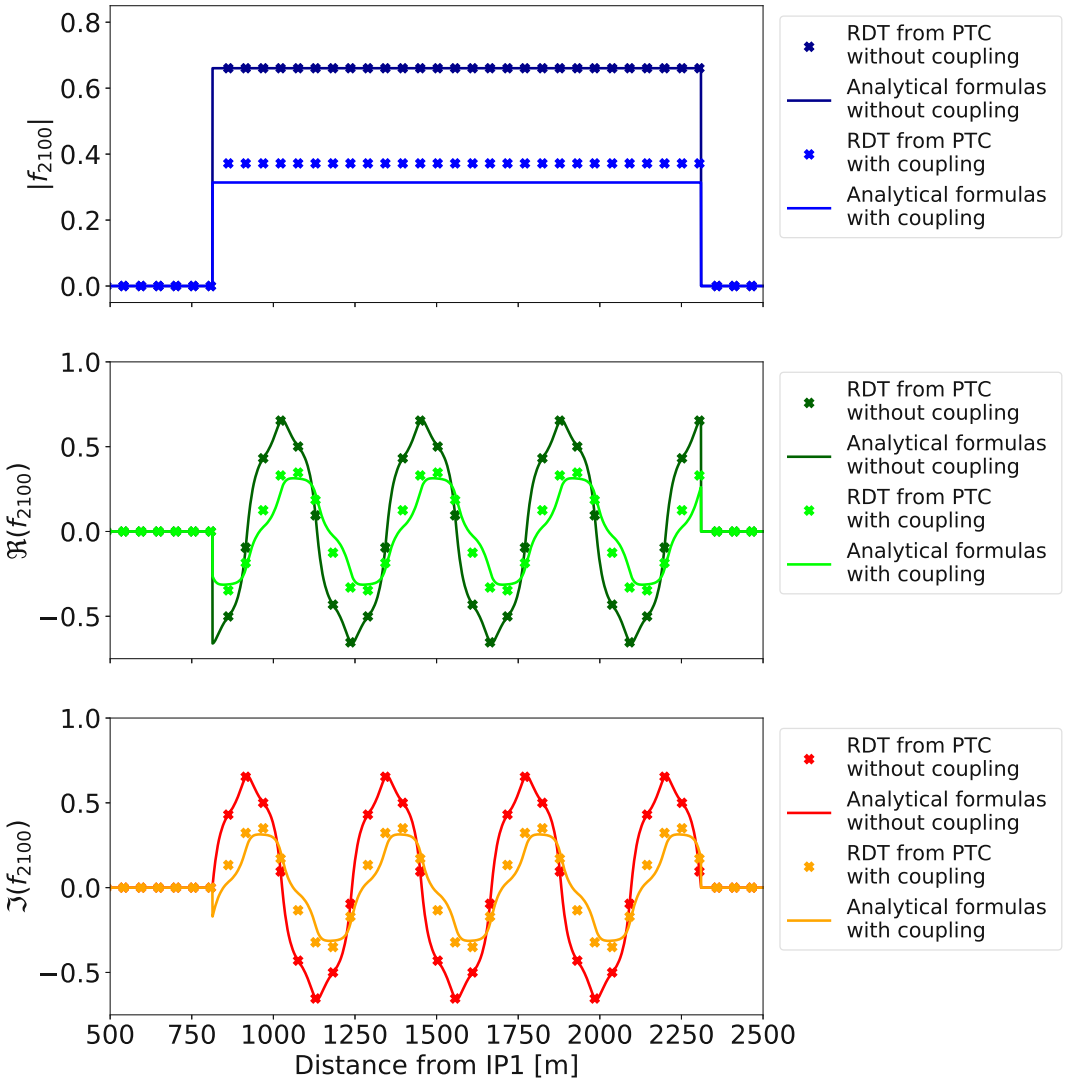

FIGURE 5.7: Comparison for the sextupole RDT f_{2100} between MAD-X-PTC and derived formulas.

Chapter 6

Optics measurements in IOTA

Nonlinear integrable optics is a recently proposed accelerator lattice design approach which allows to generate an amplitude dependent tune shift which is needed in high brightness accelerators to mitigate fast coherent instabilities. Whereas usually octupoles are used to achieve this task, this concept allows doing so without exciting any resonances, in turn preventing any particle loss. The concept is based around a special magnet design, together with specific constraints on the optics of the accelerator. To study such a system, the Integrable Optics Test Accelerator (IOTA) was recently constructed and commissioned at Fermilab. For the assessment of the performance of this concept, good knowledge of the optics and the (non-)linear dynamics without the special magnet is of key importance. As such, measurements were conducted in the IOTA ring, using the captured turn-by-turn data by the beam position monitors after excitation to infer quantities such as amplitude detuning and resonance driving terms. In this note, first results of these measurements are presented.

6.1 Introduction

In order to push the performance of current and potential future accelerator projects, the assessment of nonlinear beam dynamics has become a mainstay in the design and commissioning in these machines. In synchrotrons, nonlinear magnetic elements may have a detrimental impact on the machine performance due to for example excitation of strong resonances and reduction of dynamic aperture. As such, care is taken already in the design phase of many machines to evaluate the impact of higher order multipoles to define feasible correction strategies [149]. Once a machine is set up and running, it is equally important to check the validity of the prior models through dedicated measurements to ensure thorough understanding of involved dynamics in the accelerator and as solid starting point for machine tuning. A variety of measurement techniques are available to identify specific error sources, which can be conducted either via beam-based methods such as assessing feed-down effects via closed orbit modifications [85, 136] or based on turn-by-turn data [142], which was the method of choice for the studies presented in this note.

By performing spectral analysis on the turn-by-turn motion of a transversally excited particle bunch, not only the main spectral lines (corresponding to the tunes) may be observed but also higher order lines. These spectral lines, associated with specific resonances, allow to determine the distortion of the phase-space compared to the ideal linear case due to those resonances via the resonance driving term (RDT)

formalism. The evolution of amplitude of specific RDTs around the accelerator ring also allows to determine location and strength of nonlinear magnets [150].

The study of the nonlinear dynamics and assessment of nonlinear magnetic fields is of particular interest in accelerators based on the concept of nonlinear integrable optics [37]. Here, by using a magnet with a particular magnetic field shape, particles experience specific nonlinear effects such as amplitude detuning while in the ideal case no resonances are excited, in turn preventing any particle loss. The feasibility of this concept is currently being tested at the Integrable Optics Test Accelerator (IOTA) at Fermilab [38].

The presented concept to allow for nonlinear integrable optics imposes strict constraints on the accelerator characteristics, such as equal tunes in both planes $Q_x = Q_y$, layout, and in particular also on dynamics outside of the section where the NL-magnet is located. Specifically, a linear transfer map is assumed between the ends of this straight section in the original derivations, which due to the presence of chromaticity sextupoles or potential field errors is not the case in the IOTA accelerator. Given these specific constraints on the optics and the general goal of the demonstration of nonlinear integrable optics, an assessment of sources of nonlinear magnetic fields is thus important for this feasibility study, further potentially allowing for a clear attribution of the sources of particle loss.

The aim of this chapter is to present a first look into the nonlinear dynamics of the IOTA accelerator, generated by elements other than the dedicated nonlinear channels. In Sec. 6.2, a brief introduction to the concept of nonlinear integrable optics is presented, aiming to motivate why the knowledge and control of nonlinear magnets is critical here. An overview over the IOTA accelerator is then presented in the following Sec 6.3. Here, focus will be put on hardware and operational aspects relevant for the conducted experiments and results, which will be presented in Sec 6.4.

6.2 Nonlinear integrable optics

In modern synchrotrons, the use of nonlinear magnets has become a necessity in order to achieve the ever increasing performance goals while itself also possibly posing a limiting factor. One such example would be the necessity to use octupole magnets in the LHC to suppress collective instabilities via Landau damping due to an amplitude-dependant tune-spread while these also excite resonances which may lead to particle loss. As such, a trade-off has to be found between the stabilizing effect of the generated amplitude detuning and the excitation of resonances with an associated negative impact on the dynamic aperture (DA), which is the maximum amplitude up to which bounded motion of the particles for a given time span occurs.

To overcome the problem of the particle loss associated with nonlinear magnetic fields and associated resonances, in [37] a novel approach is discussed to find a nonlinear system with integrable motion which is feasible to be implemented in a particle accelerator. A fully integrable system is characterized by regular bounded motion of particles independent of their initial conditions or, conversely, a system with same number of conserved quantities as degrees of freedom, which for a 4D system requires two invariants. An accelerator can be described by a Hamiltonian as

$$H = \frac{p_x^2}{2} + \frac{p_y^2}{2} + K(s)\left(\frac{x^2}{2} + \frac{y^2}{2}\right) + V(x, y, s)\,, \tag{6.1}$$

where $K(s)$ represents the linear focusing component and $V(x,y,s)$ an $s-$dependent nonlinear potential. In order to find a system with two invariants of motion which can be can be achieved with magnets, the system is moved from an s-dependent system to a system dependent on the phase ψ, which is then expressed in normalized coordinates

$$z_N = \frac{z}{\sqrt{\beta_z(s)}},\ p_N = p\sqrt{\beta_z(s)} - \frac{\beta_z'(s)}{2\sqrt{\beta_z(s)}},\ z \in \{x,y\}\ . \tag{6.2}$$

The Hamiltonian then takes the following form

$$H_N = \frac{p_{x_N}^2 + p_{y_N}^2}{2} + \frac{x_N^2 + y_N^2}{2} + U(x_N, y_N)\ , \tag{6.3}$$

with the specific potential

$$U(x_N, y_N) = \beta(\psi) V\left(x_N\sqrt{\beta(\psi)}, y_N\sqrt{\beta(\psi)}, s(\psi)\right) \tag{6.4}$$

to be found which may yield a second invariant next to the time-independent Hamilton from Eq. (6.3) itself. In [37], families of solution for different coordinate system are presented, most notably for elliptic coordinates

$$\xi = \frac{\sqrt{(x+c)^2+y^2} + \sqrt{(x-c)^2+y^2}}{2c}\ , \tag{6.5}$$

$$\eta = \frac{\sqrt{(x+c)^2+y^2} - \sqrt{(x-c)^2+y^2}}{2c}\ , \tag{6.6}$$

where a potential of the form

$$U(x_n, y_n) = \frac{f(\xi) + g(\eta)}{\xi^2 - \eta^2} \tag{6.7}$$

with f and g defined as

$$f(\xi) = \xi\sqrt{\xi^2-1}\left[d + t\cosh^{-1}(\xi)\right]\ , \tag{6.8}$$

$$g(\eta) = \eta\sqrt{1-\eta^2}\left[b + t\cos^{-1}(\eta)\right]\ , \tag{6.9}$$

which allow for the realization using magnetic fields given that this potential also satisfies the Laplace Equation. The form of the Hamilton of Eq. (6.1) with the axial symmetric focusing imposes some constraint on the lattice design. One potential solution is displayed in Fig. 6.1, where the lattice is split into two parts, a drift-space of length L with equal β-functions in both planes and where the special nonlinear potential is installed and a so called T-insert, being a linear transfer-map.

In turn, also the choice of the working point of the accelerator is limited to $Q_x = Q_y$. Implementing such a system in an accelerator would allow for the generation of a tune spread whilst not exciting any resonances, in turn avoiding any particle loss and thus overcoming potential performance limitations due to coherent instabilities.

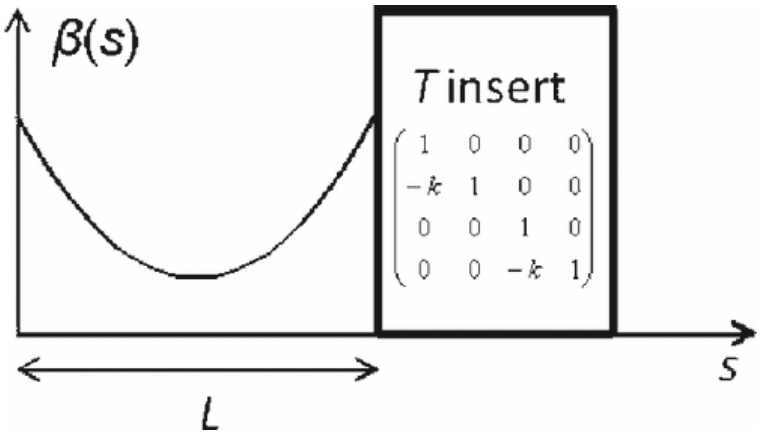

FIGURE 6.1: Schematic illustration of a lattice required to provide nonlinear integrable motion as described in [37].

However, effects such as chromaticity may lead to a violation of the imposed constraints, in turn restricting any beneficial effects to particles within a limited momentum deviation range. In [151], it was shown that a chromaticity correction using sextupoles can restore integrability for off-momentum particles. This however violates the aforementioned constraint of the linear transfer-map outside of the nonlinear channel and in turn resonances will be excited. Similarly so, nonlinear magnetic field imperfections may add to this.

Furthermore, as presented in [152], it can be shown that the first term of the multipole expansion of the potential in Eq. (6.7) for a given set of parameters b and d represents a quadrupole. As such, the powering of the NL-magnet will entail a change of the tunes, as illustrated in Fig. 6.2. As such, the choice of the working point, or conversely the strength t of the NL-magnet, may be limited due to the two sextupole resonances in the vicinity of the tune curve. Similarly so, even for working points sufficiently far away from those resonances, due to the significant amplitude detuning created by the NL-magnet, these resonances might be approached by particles and may lead to a subsequent particle loss. Depending on the number of allowed particle losses, the impact of these resonances could thus be a limiting factor for the created tune spread.

Due to the aforementioned arguments, the identification of nonlinear elements in an accelerator lattice built around the concept of nonlinear integrable optics, characterisation of critical resonances and possible optimization of any powering or correction scheme to reduce the resonance strength may thus assist in restoring near-integrability of the nonlinear motion and reducing particle loss.

6.3 The IOTA accelerator

One of the first accelerators built around the concept of nonlinear integrable optics is the Integrable Optics Test Accelerator (IOTA) at Fermilab. Housed at Fermilab Accelerator Science and Technology (FAST) facility, the storage ring with a circumference of 40 m, together with the already established superconducting FAST linac and the proton injector currently in development, allows not only for studies on nonlinear integrable optics but also, amongst others, demonstration of optical stochastic cooling and experiments with electron lenses. A comprehensive overview over the

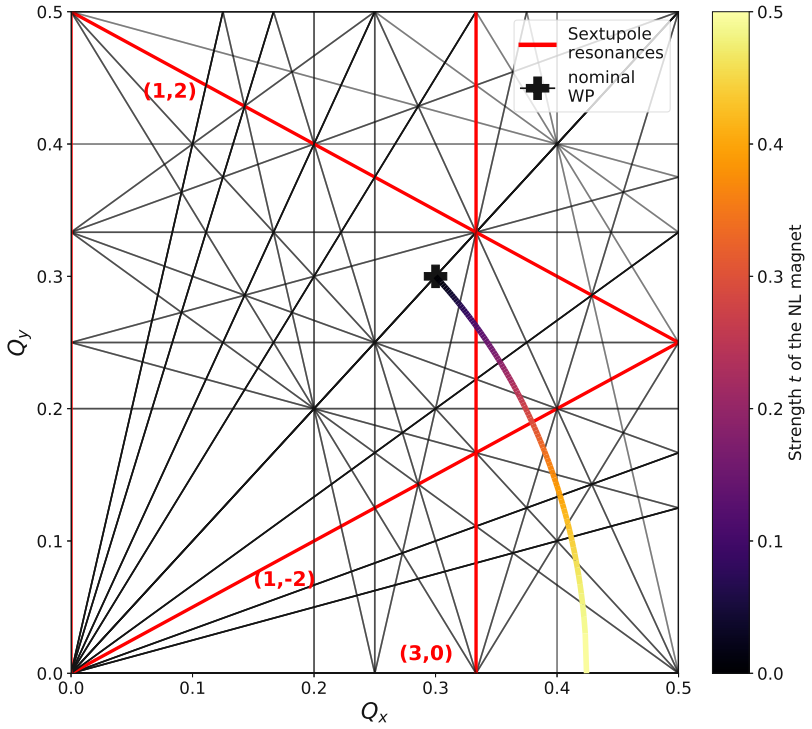

FIGURE 6.2: Change of the horizontal/vertical tune during different strengths t of the NL-magnet and resonances up to fifth order. Marked in red are normal sextupole resonances. The working point of the bare lattice with the NL-magnet depowered was assumed to be $Q_{x,y} = 5.30$.

facility can be found in [38]. In the following, only a brief overview of the characteristics of the IOTA storage ring, relevant to the studies presented in the next section, is presented. In Fig. 6.3, the layout of the accelerator is presented.

It consists of 8 straight sections, separated by dipoles with a bending angle of either 30° or 60°. The straight sections on the top left and top right house the so called octupole string, consisting of 17 individually powered octupoles, and the special nonlinear magnet, implementing a potential as described in Eq. (6.7), respectively. The beam is injected in the center straight on the top, which is also where the horizontal and vertical kicker [153] are located, used to bring the injected beam on the closed orbit or excite the particle bunch transversally. During Run II, in total 4 sextupoles were used to correct chromaticity in the ring, 2 in each of the short straight sections, located in between the 60° dipoles. The sextupoles in the same straight section are separated by a phase advance of $0.06 \cdot 2\pi$ $[rad]$ in the horizontal and $0.25 \cdot 2\pi$ $[rad]$ in the vertical plane, while the phase advance between the sextupoles further away from the injection straight is $0.99 \cdot 2\pi$ $[rad]$ and $0.36 \cdot 2\pi$ $[rad]$ for the horizontal and the vertical plane, respectively. For acquiring turn-by-turn data after a beam excitation, 21 beam position monitors are installed in the IOTA ring, with at least two BPMs per straight section.

In Fig. 6.4, the baseline optics for the nonlinear integrable optics studies in the IOTA ring is presented, with a working point of $Q_{x,y} = 5.3$.

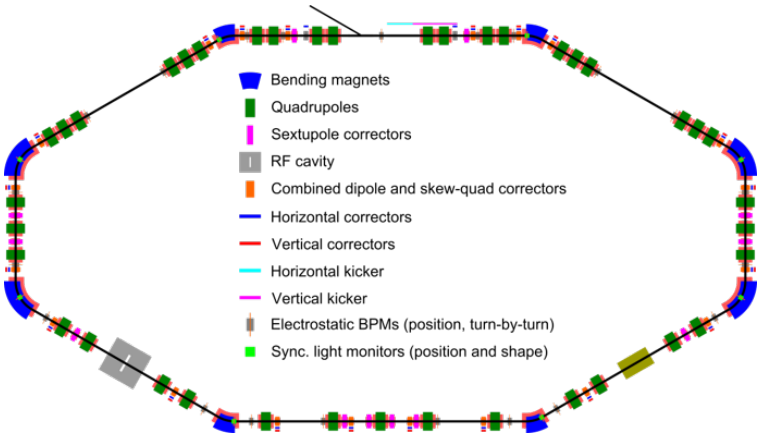

FIGURE 6.3: Layout of the IOTA ring.

The sections marked in light grey and light green illustrate the location of the NL-magnet and the octupole string, respectively, with both fulfilling the constraint illustrated in Fig. 6.1, of equal β-functions in both planes. The phase-advance over each insertion is matched to $\mu_{x,y} = 0.3$. The phase advance between the right hand side of the grey marked section to the left hand side of the same section is matched to an integer phase-advance. The same holds true for the section containing the octupole string, marked in green.

6.4 Experimental setup and measurements

Various methods exist for the assessment and localisation of nonlinear magnetic fields in an accelerator. For the studies presented in this note, a beam-based approach is chosen, in particular looking into the turn-by-turn motion of a transversally excited particle bunch. The spectral content of transverse beam position evolution after the excitation, recorded around the ring by the 21 Beam Position Monitors (BPM), provides insights into the linear optics and the characterisation of the nonlinear motion via (combined-) resonance driving terms (RDT) [154]. By combining the data from different locations around the ring, the location of strong sources may be inferred.

The turn-by-turn measurements were conducted during 3 non-consecutive shifts, where both the NL-magnet and the octupole channel were turned off to allow for bare lattice measurements. Where not specifically mentioned otherwise, the sextupoles were split in two families, pairing both the sextupoles closer to the injection point and those further away, and chromaticity was corrected to $Q'_x = Q'_y = 0$. Notably, the natural chromaticity of the accelerator does not match the model values, the working assumption being an additional sextupole component from the 60° dipoles. Both measures aim to reduce decoherence to allow for a sufficient number of turns. In Fig. 6.5, a typical example of turn-by-turn motion recorded by one BPM is illustrated. Here, the number of usable turns before the signal is damped down is about 900 turns. As the synchrotron radiation damping time is relatively long ($> 10^7$ turns) [38], the damping mainly stems from the decoherence, and here in particular from decoherence due to amplitude detuning, as chromaticity is matched to 0 [155].

Data was taken using either the baseline optics with a working point of $Q_x = Q_y = 5.3$ or with working points with larger tune separation, namely using

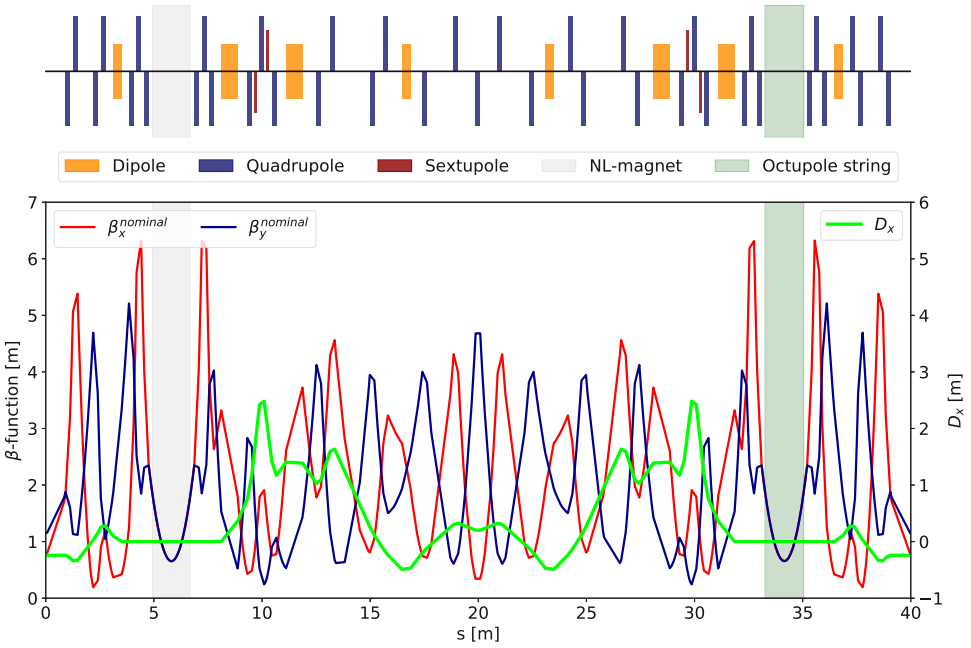

FIGURE 6.4: Baseline optics for the nonlinear integrable optics studies, starting from the injection point.

$Q_x = 5.28/Q_y = 5.31$ and $Q_x = 5.32/Q_y = 5.29$. The tunes were changed using the knobs as presented in Tab. 6.1.

The working point change is achieved by mostly adjusting the β-function in the injection straight, as is displayed in Fig. 6.6, with the maximum change of the β-function below 10%.

Working points other than the nominal one were chosen for measurements of (C-)RDTs as to distinguish between certain lines more easily. An example is displayed in Fig. 6.7.

Here, for the case of the nominal working point, for example, the sextupole lines $H(-2,0)$ and $H(0,-2)$ overlap and the octupole line $H(-1,2)$ lies in the shadow of

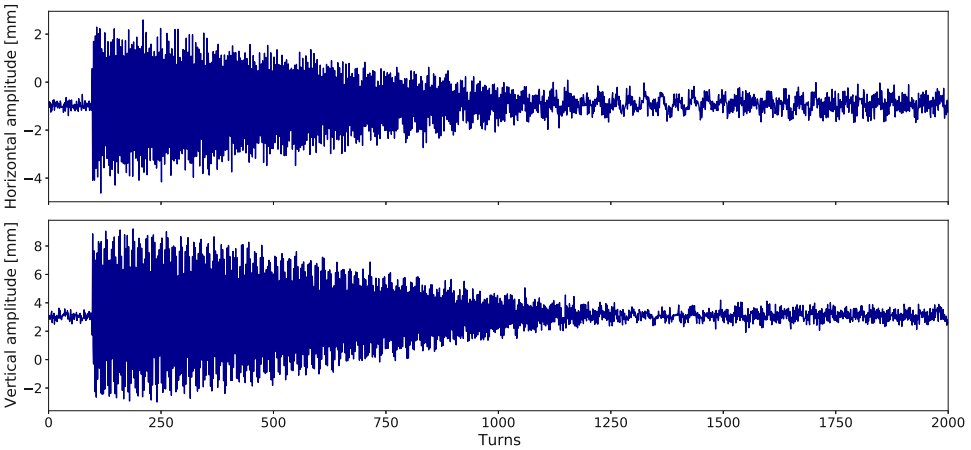

FIGURE 6.5: Turn-by-turn motion after one excitation recorded by the IBPMB2L.

Magnet	$\Delta K/\Delta Q_x$ $[10^{-3}/m^2]$	$\Delta K/\Delta Q_y$ $[10^{-3}/m^2]$
QA1R	−2.56	7.62
QA2R	16.84	−2.54
QA3R	4.36	11.61
QA4R	−23.34	−3.40
QB1R	−0.17	−32.40
QB2R	11.83	8.80
QB3R	−0.64	−1.30
QB4R	−2.87	−6.11
QB5R	4.25	9.01
QB6R	−6.11	−12.95

TABLE 6.1: Knobs used to change horizontal and vertical tune. Note that due to symmetric optics, the same change is applied in the quadrupoles on the left hand side.

the main tune line, making the reconstruction rather difficult or next to impossible, which is not the case for the separated working point. However, the change in working point also entails a change of the amplitude of the (C-)RDTs and subsequently the amplitude of the spectral lines is changed between these two cases. Thus, the derived resonance strength is not representative for the case of the nominal optics. Still, the measurements allow to benchmark the nonlinear model and infer location and strength of nonlinear magnetic fields.

The presented measurements were analysed using the `python 3.7` based OMC3 software suite [156], and crosschecked with its predecessor [157], implemented in `python 2.7`. The turn-by-turn data was cleaned before spectral composition, using a variety of cut-based methods, e.g. removing BPMs where the oscillation exceeds a given threshold, and removing noise by performing a singular value decomposition, retaining only a number of modes with the largest singular values [158]. The number of modes was chosen based on the analysis, with the (C-)RDT analysis using a significantly higher number compared to the linear optics one to be able to show local phenomena [159].

6.4.1 Linear Optics

As demonstrated in [160], good control of the linear optics is among the key issues, critical to achieving a large tune spread while keeping particle losses minimal. Similarly so, good knowledge of the linear optics is also critical as a precursor to evaluating nonlinear observables. For the commissioning of the linear optics, a LOCO algorithm is regularly used [161], with good results achieved in the previous run [162]. Complementary to the LOCO based approach, as a first step before analysing higher order modes in the spectral components of the motion, the linear optics is inferred from the captured turn-by-turn data. Two methods were used to infer the linear optics, one based on the measured phase advance between BPMs and one based on the amplitude of the oscillation.

For the phase advanced based approach, the N-BPM method [163, 164] is employed, using combinations of 7 surrounding BPMs to the one probed. This approach uses

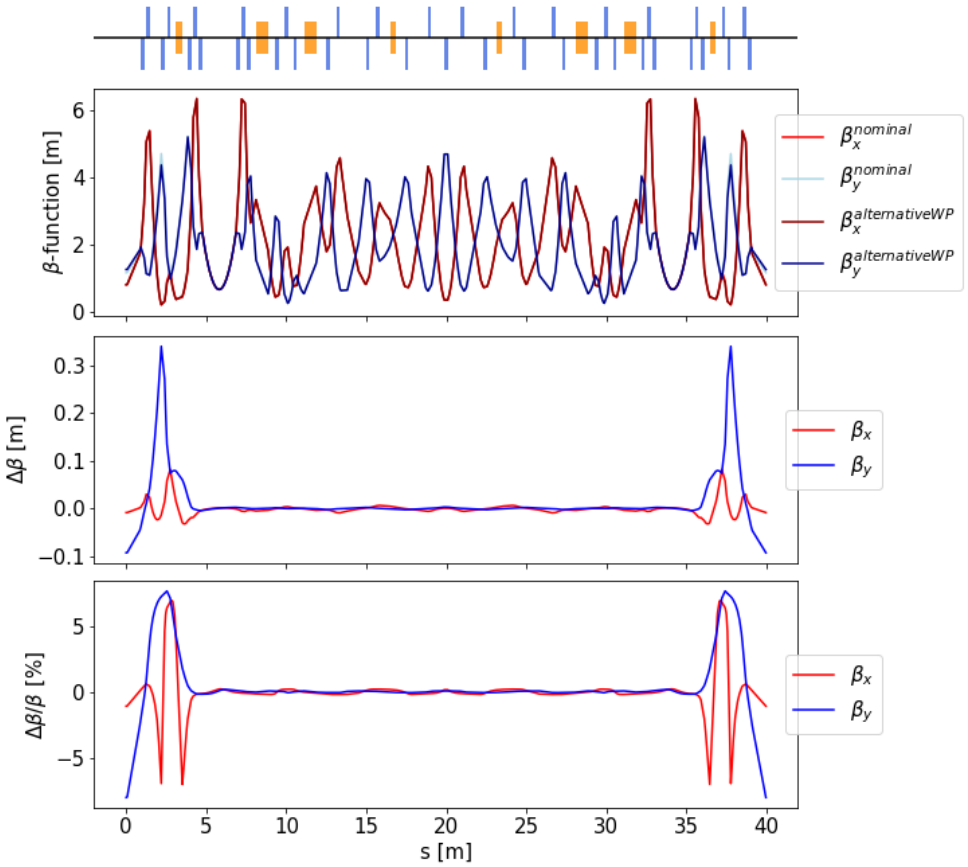

FIGURE 6.6: Change of the optics when moving from the nominal optics to a working point of $Q_x = 5.28$, $Q_y = 5.31$.

measured and model phase advances between BPMs together with the model β-functions at the BPMs to determine the β-function at a certain BPM. In Fig. 6.8, the difference between model and measured phases between consecutive BPMs is presented.

The phase advance in the nonlinear channel on the left hand side of the plot is well controlled, approaching the desired 10^{-3} level. In the octupole channel on the right side of the plot on the other hand, a larger phase difference is noted. It has to be noted that this measurements were conducted with a non-nominal optics at a working point of $Q_x = 5.28$, $Q_y = 5.31$ and without any prior corrections applied, as such not being able to accurately reflect the levels reached in operation.

Using the the measured phase difference as input and the aforementioned N-BPM algorithm, the β-functions were determined and are displayed in Fig. 6.9.

Although no optics correction were performed after the application of the tune knob, the presented results show a peak β-beating below 12 % around the IOTA ring, above the target accuracy for the experiments with the NL-magnet, but well with the parameters for experiments with the octupole channel [162]. Notably, the results in the horizontal plane are worse, likely due to reduced number of usable turns in this plane and thus reduced phase accuracy.

The other approach for determining the optics functions around the ring, using the

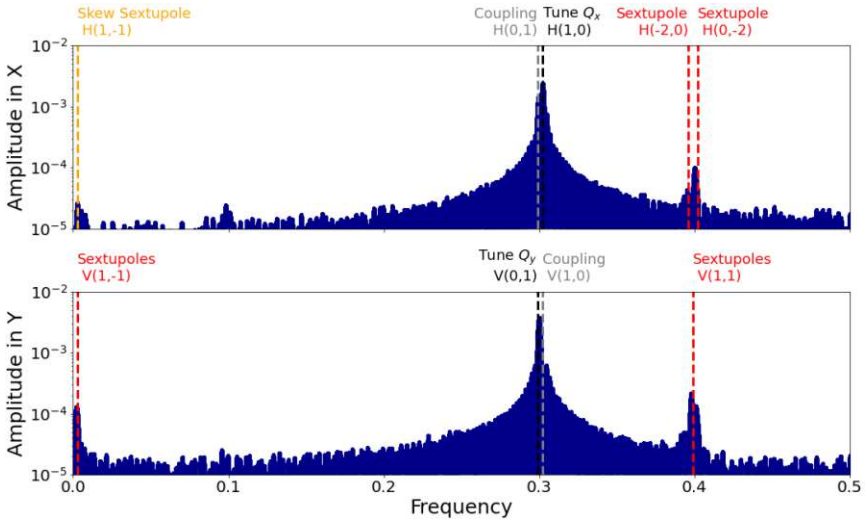

(A) Working point $Q_x = Q_y = 5.30$

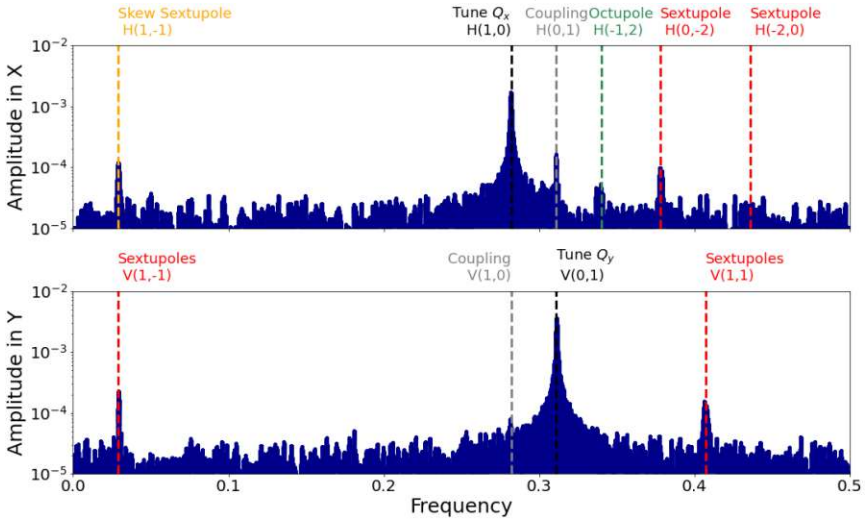

(B) Working point $Q_x = 5.28$, $Q_y = 5.31$

FIGURE 6.7: Comparison between spectra for the nominal working point ($Q_x = Q_y = 5.30$) and a working point with a larger tune separation.

oscillation amplitude of the betatron motion, dubbed β from amplitude [165], critically depends on the calibration of the individual BPMs and on the accuracy of the kick action determination. The kick action is determined using

$$2J_{x,y} = \frac{\sum_{BPMs}(0.5A_{x,y})^2/C_{x,y}^2\beta_{x,y}}{N_{BPMs}}, \tag{6.10}$$

where $A_{x,y}$ is the peak-to-peak amplitude of the oscillation at the given BPM, $\beta_{x,y}$ the beta-function from the model at the respective BPM, N_{BPMs} the number of the BPMs, and $C_{x,y}$ represents the, a priori unknown, calibration factor of the given BPM. The underlying assumptions for the use of this formula are that the effect of linear coupling on the action, as well as that the phase space distortion from higher order resonances are negligible, and that by averaging over all BPMs, first order effects from optics errors are canceled and the remaining higher order having no significant

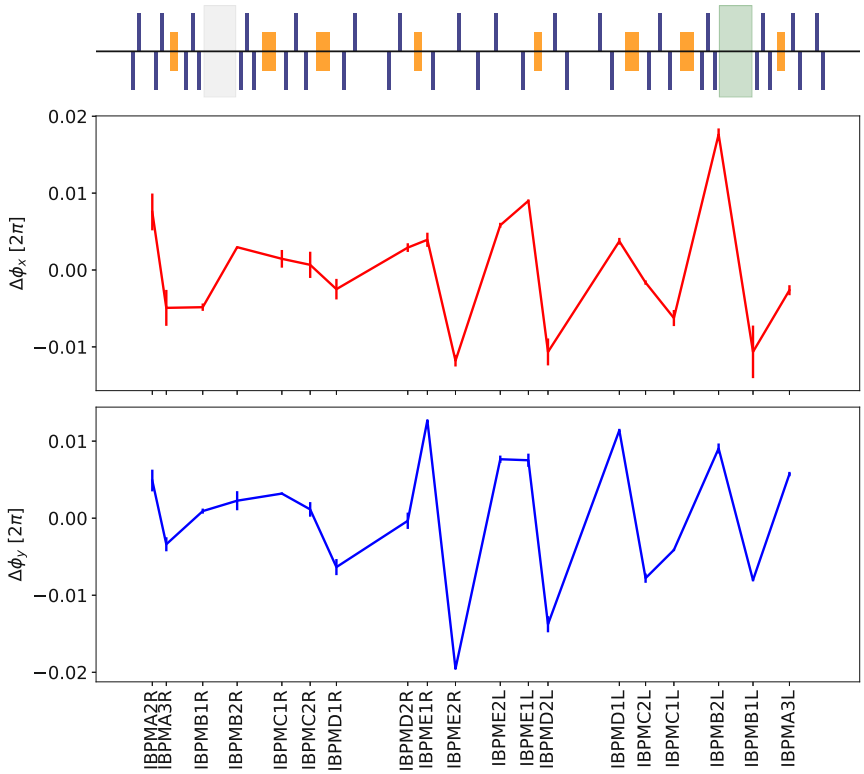

FIGURE 6.8: Difference between measured and model phase advance. The phase difference at given BPM represents the difference with respect to the next BPM.

impact. The β-function at a given BPM is then inferred via

$$\beta_{x,y} = \frac{A_{x,y}^2}{C_{x,y}^2 2J_{x,y}} \,. \tag{6.11}$$

The calibration factor may be inferred later by comparing to trusted optics measurements from LOCO. However, given the exploratory nature of the presented measurements, the determination of the calibration factors and validation was deemed outside of the scope of this work. In Fig. 6.10, the results using the β from amplitude method are displayed.

For the presented measurements, the BPM `IMBPMA1C` has been excluded, as across all measurements it has shown a significantly lower β-function, which is attributed to this BPM featuring an alternate design with a wider aperture [38] and its position readout not adapted to the different geometry compared to the other BPMs. Compared to the previously presented β from phase result, the β from amplitude measurements show a higher β-beating, with a peak deviation of about 15 % compared to the 12 % found before. As mentioned before, this could partly be attributed to the calibration issues in BPMs. Additionally, the action calculation may be improved by using measured β-function from LOCO measurements. However, in both measurements a significant beating is found close to the octupole string and in the injection straight, where also the optics was changed to achieve the change in tunes. Similar results have also been obtained for data sets from later measurements shift using the same working point.

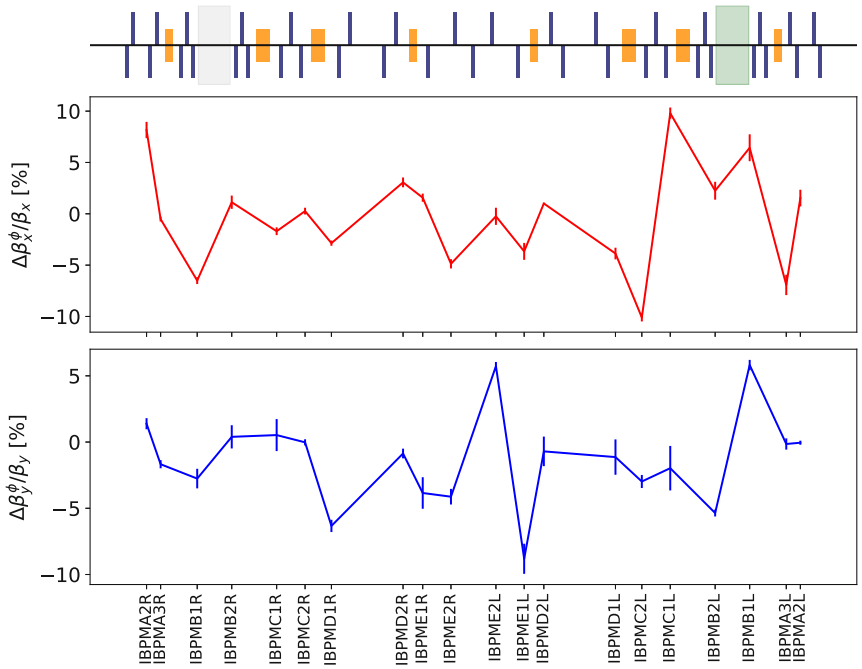

FIGURE 6.9: Measured β-beating using the analytical N-BPM method.

Notably, in both analyses, multiple data sets show erratic behaviour, not present in the kick immediately before and after this data set. No immediate explanation for these transients has been been found and data sets with large deviations in the optics have been dropped.

While not definite results and with potential for further improvements, studies and cross-checks with LOCO, the results indicate that, as expected, the linear optics is sufficiently well controlled for the following studies and no special precaution were deemed necessary for the following analysis. However, the target β-beating below 1% is not yet observed using turn-by-turn based methods for measuring the linear optics.

6.4.2 Amplitude detuning

The nonlinear integrable optics concept is based on generating a tune spread via detuning with amplitude, which allows mitigation of coherent instabilities. As such, to determine the amplitude detuning from the nonlinear inserts, it is also of particular interest to determine the detuning of the bare accelerator with both nonlinear inserts turned off. Given that detuning from the nonlinear inserts and from other sources of the accelerator is to first order independent, the impact of the lattice sources could then be used together with the measured detuning with the nonlinear inserts to allow for comparison with theoretical estimates. In Tab. 6.2, the expected amplitude detuning from the model is shown for the case where the sextupoles are used in their nominal configuration and for the case of a sextupole component in all 60° dipoles of $k_3L = 4.55\ \mathrm{m}^{-2}$, compared to $k_3L = -40\ \mathrm{m}^{-2}$ and $k_3L = 55\ \mathrm{m}^{-2}$ of the chromaticity sextupole when powered in their nominal correction scheme. The sextupole component in the dipoles has been implemented such that it matches with the measured chromaticity in the IOTA ring when the chromaticity sextupoles are turned off.

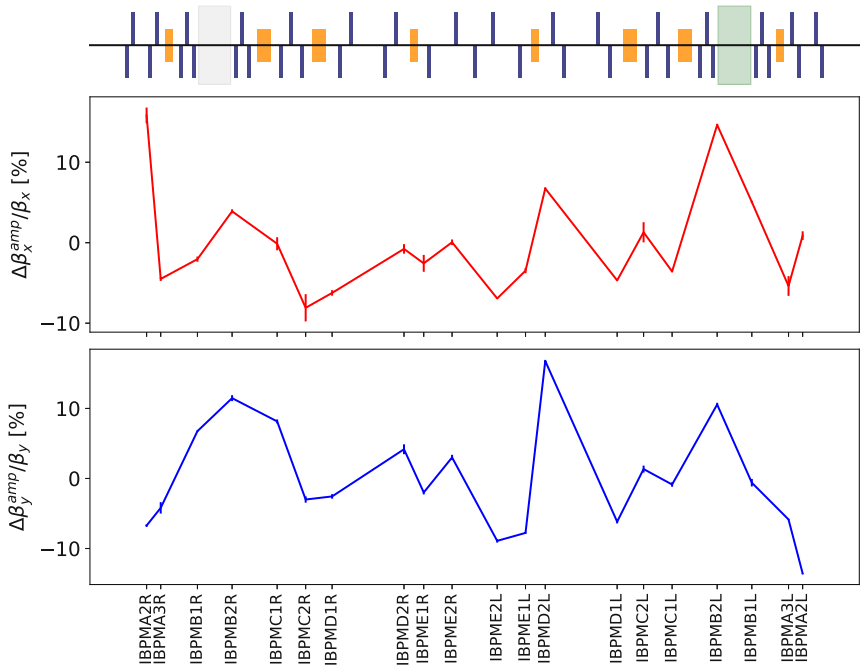

FIGURE 6.10: Measured β-beating using the β from amplitude method.

Sources	**chromaticity sextupoles**	**chromaticity sextupoles + dipole b_3 errors**	**NL-magnet with t=0.29**
$dQ_x/d2J_x$	150	19	575
$dQ_x/d2J_y$	294	209	-2207
$dQ_y/d2J_y$	100	100	2126

TABLE 6.2: Amplitude detuning in the IOTA ring for different sources.

Additionally, for comparison, the amplitude detuning for an ideal lattice without sextupoles and the nonlinear insert powered to $t = 0.29$ is presented here too. Notably, the effect of the b_3 errors is most pronounced in the direct horizontal detuning, showing a decrease of almost a factor 10 from the unperturbed case. Similarly so, based on the model, the powering of the chromaticity sextupole generates up to 20% of the amplitude detuning generated by the NL-magnet, in particular for the direct term in the horizontal plane, and to a lesser extent in the cross-plane detuning. In simulations, the amplitude detuning generated by the chromaticity sextupoles decreases the horizontal direct term by 25% when changing to a working point with split tunes such as $Q_x = 5.28$, $Q_y = 5.31$, with the other terms changing by less than 5%.

For the measurements of the detuning in the bare lattice, the beam was excited in both planes. The strength in one plane is stepwise increased while the kick strength in the opposite plane remains the same throughout the measurement. This was done as to provide enough excitation in the non-ramped plane to determine the tune in this plane, such that the cross-plane detuning may also be determined. Given the small and constant excitation strength in the cross-plane, any change of the tune here is then fully attributed to the excitation of the plane where the excitation strength

is ramped up. In turn, a potential contribution due to linear coupling is hereby neglected in this approach.

As noted in the previous section, the kick action $2J$ is then inferred for plane where the kick strength has been gradually ramped up. Again, in order not to distort the action calculation, for the analysed data sets, the turn-by-turn data of `IBPMA1C` has been dropped.

Measurements were conducted using an optics with a working point of $Q_x = 5.28$, $Q_y = 5.31$. Sextupoles were set such that the chromaticity is matched to 0. The measured amplitude detuning is presented in Fig. 6.11.

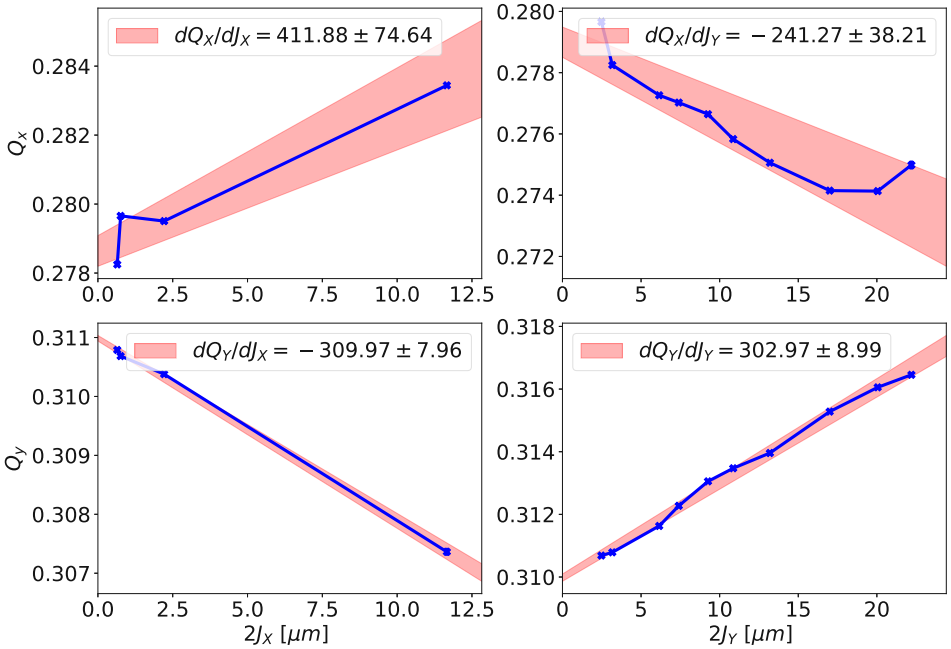

FIGURE 6.11: Measured amplitude detuning using an optics with a working point of $Q_x = 5.28$, $Q_y = 5.31$. A linear fit over the presented data is displayed in red, together with the amplitude detuning obtained from the fit.

It has to be noted that only a smaller number of kicks was available at this working point, in particular for the horizontal kicks. Furthermore, no online continuous tune measurements system is present, such that data could not be corrected for any possible tune drift. Notably, the measured detuning does not agree with the previously presented expected detuning from the two models. The summary of the measurement and a comparison to the model values for the working point $Q_x = 5.28$, $Q_y = 5.31$ is given in Tab. 6.3.

Although measurements with horizontal kicks are sparse, the horizontal detuning is about a factor 4 larger than what is expected and is about the size as the direct horizontal detuning from the NL-magnet at $t = 0.29$. Furthermore, the cross term detuning in both cases shows an opposite sign of what is expected from the model and approximately the same order of magnitude, hinting at possible extra sources of detuning in the bare lattice. While inconsistent with behaviour expected if sextupoles are the main contributors to the detuning, the measured detuning is more consistent with an octupole as main source. From these measurements however,

Sources	**chromaticity sextupoles**	**chromaticity sextupoles + dipole b_3 errors**	**Measurement**
$dQ_x/d2J_x$	112	10	412 ± 75
$dQ_x/d2J_y$	287	202	-241 ± 38
$dQ_y/d2J_x$	287	202	-310 ± 8
$dQ_y/d2J_y$	95	96	303 ± 9

TABLE 6.3: Measured amplitude detuning in the IOTA ring together with a comparison to the detuning expected from the model.

the number and strength of octupole sources cannot be concluded. One potential candidate could be hysteresis effects in the octupole string. It should be noted that before these measurements were conducted, the center octupole was degaussed and another one was disconnected due to issues with the powering.

Further amplitude detuning analysis was performed for data obtained from a later shift, using an optics with the same working point of $Q_x = 5.28$, $Q_y = 5.31$. As this data was primarily taken for (C-)RDT analysis, kick amplitudes were not optimized for amplitude detuning analysis and the kick strength in the non-ramped plane was unnecessarily high. Due to this, a non negligible contribution from the kick action of the off plane may arise, potentially spoiling the measurement accuracy. Additionally, a non-nominal sextupole configuration was used, with only two sextupole from the same straight section used to correct for chromaticity. In Fig. 6.12, the results of the amplitude detuning analysis are shown, with a comparison to the expected model detuning presented in Tab. 6.4.

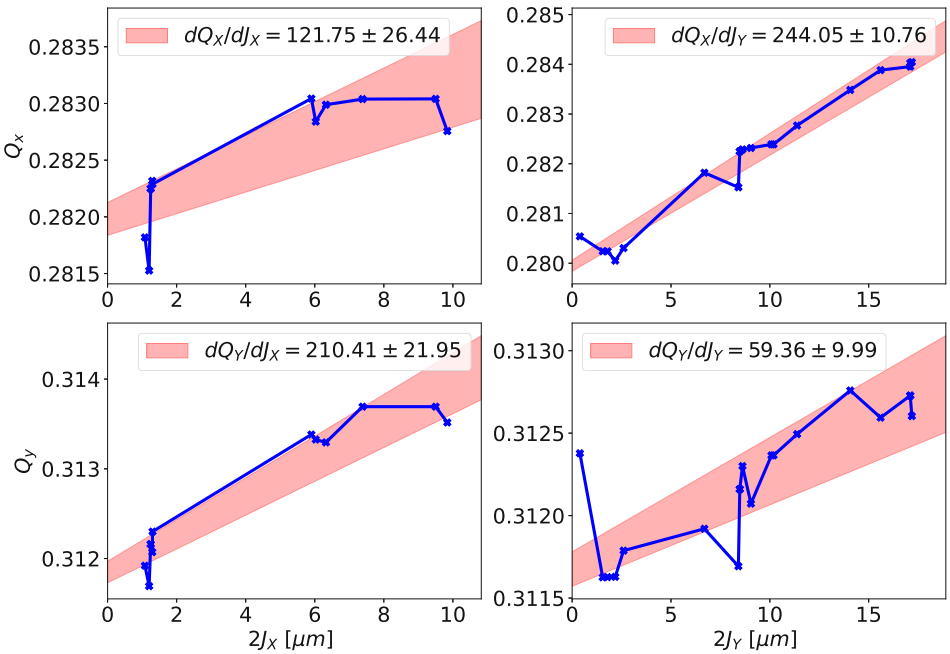

FIGURE 6.12: Measured amplitude detuning using an optics with a working point of $Q_x = 5.28$, $Q_y = 5.31$ and using only sextupoles from the left hand straight section for chromaticity correction. A linear fit over the presented data is displayed in red, together with the amplitude detuning obtained from the fit.

Sources	**chromaticity sextupoles**	**chromaticity sextupoles + dipole b_3 errors**	**Measurement**
$dQ_x/d2J_x$	150	45	121 ± 26
$dQ_x/d2J_y$	302	209	244 ± 11
$dQ_y/d2J_x$	302	209	210 ± 22
$dQ_y/d2J_y$	225	199	59 ± 10

TABLE 6.4: Measured amplitude detuning at a working point of $Q_x = 5.28$, $Q_y = 5.31$ and using only sextupoles from the left hand straight section for chromaticity correction, together with a comparison to the detuning expected from the model.

Compared to the previous analysis, a better agreement with the model values is observed in this case. In particular, no opposite sign in the cross detuning is found, thus it is assumed that sextupole are the main contributor to the detuning in this scenario and no strong spurious octupole source appears to be present during that shift. These results also add to the previous suspicion that the previously observed strong octupole contribution might be linked to the intervention performed before the measurements. While this measurements only provide a snapshot over a short time span, based on these results, no persistent strong spurious octupole source appears present and, bar any hardware issues, amplitude detuning seems mostly by the chromaticity sextupoles.

6.4.3 (Combined-) Resonance Driving terms

As motivated in Sec. 6.2, good knowledge of the nonlinear elements outside of the nonlinear channel is of great importance for assessing the performance of NL-magnet. Using a nonlinear model, validated by the measurements, allows for more realistic simulation to estimate the performance. In the following, also potential correction strategies may be tried in simulation and, provided a viable solution is found, then be implemented in the accelerator.

For assessing the validity of the IOTA model, as a first measure the so-called combined resonance driving terms [154] were assessed. In this method, the spectral line amplitude for certain resonances is used to infer a linear combination of two resonance driving terms. As such, the strength of individual RDTs cannot be inferred from the measurements. Furthermore, this method relies on the use of dual plane BPMs, which is the case in IOTA.

The C-RDT are measured by determining the kick action and amplitude of a specific spectral line at each BPM. The C-RDT is then obtained by performing a linear fit for various measurements with different kick action and line amplitudes using the relations for the individual C-RDT as presented in [154] and as is illustrated in Fig. 6.13. It has to be noted that for the analysis here, spectral lines were normalised with the main line of the respective plane to account for first order calibration errors. As such, during the fitting process, an additional contribution from the kick action has to be taken into account.

Note that in the following, a different notation compared to the original paper [154] will be adapted, namely, C-RDT will be addressed by their corresponding line. As example, the C-RDT F_{NS3} will be addressed by $H(-2,0)$, corresponding to the line $-2Q_x$ in the horizontal spectrum.

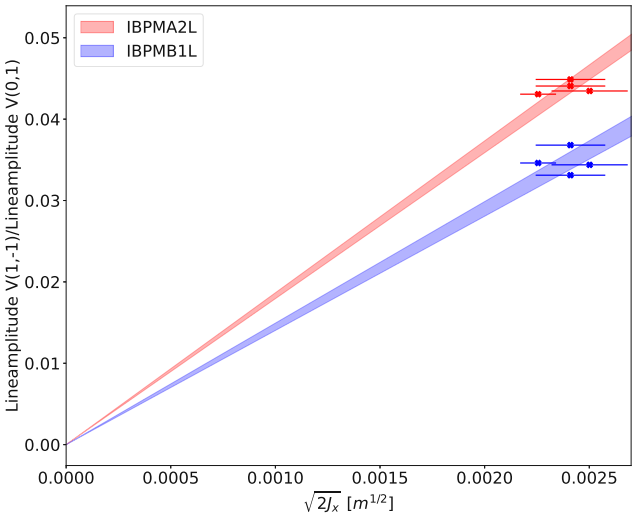

FIGURE 6.13: Amplitude of the V(1,-1) line for different kicks at 2 BPMs. Overlayed a linear fit to obtain the CRDT at the given BPMs.

First C-RDT measurements were performed at a working point of $Q_x = 5.28$, $Q_y = 5.31$ and using a nominal sextupole configuration. C-RDTs were only investigated for lines which were clearly above the noise level in all BPMs, which limit the analysis to coupling, sextupoles, skew sextupoles, and octupole C-RDTs. In Fig. 6.14, the measured coupling C-RDTs are presented. A notable excursion is observed in the injection straight for the C-RDT $H(0,1)$. Following the derivations presented in [147, 166], this indicates a strong influence of the horizontal motion on the vertical one here. This may be of concern as both the horizontal and vertical kicker are located here.

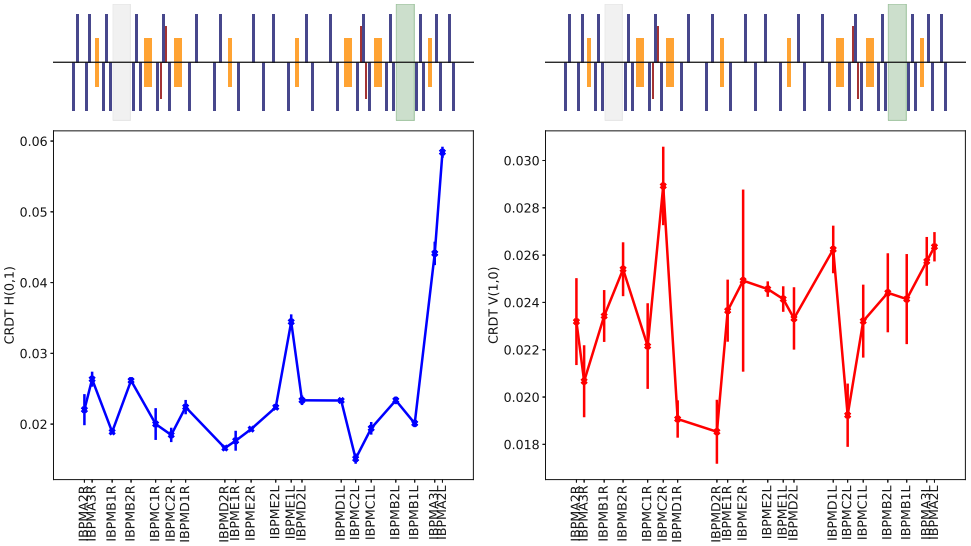

FIGURE 6.14: Measured coupling C-RDTs at a working point of $Q_x = 5.28$, $Q_y = 5.31$ and using a nominal sextupole configuration.

In Fig. 6.15, the amplitude of the sextupole C-RDTs are presented.

Here, the C-RDT corresponding to the line $H(-2,0)$ is not presented, as the line

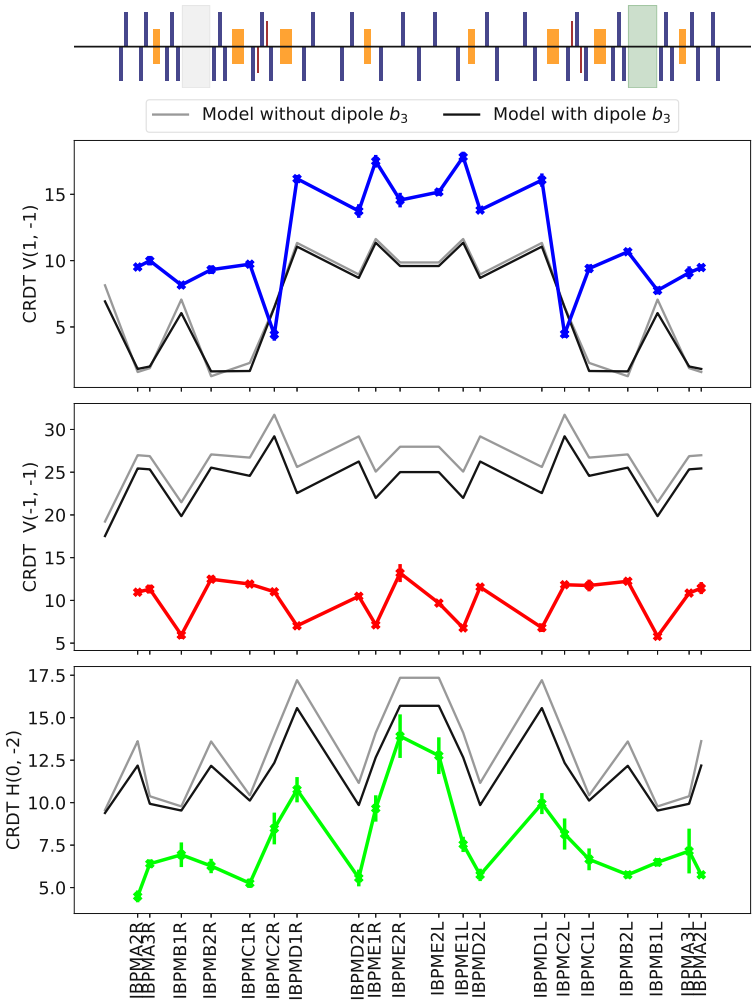

FIGURE 6.15: Measured sextupole C-RDTs at a working point of $Q_x = 5.28$, $Q_y = 5.31$ and using a nominal sextupole configuration, together with a comparison to the expected model values.

was not observed in the spectra. Additionally, the model sextupole C-RDTs, evaluated using MAD-X PTC, are included for the case of the nominal chromaticity correction and when including a sextupole component in the 60° dipoles. Notably, a discrepancy between the model amplitude and measured amplitude is observed in all cases. However, it has to be noted that the different decoherence factor for the spectral lines [150] have not been applied yet to the data. However, a good qualitative agreement in the longitudinal evolution of the C-RDTs is observed. Given the small expected change from a potential sextupole component in the dipoles and the discrepancy in the amplitude, no conclusion on the presence of such errors can be made at the moment.

One skew sextupole line was consistently observed in all BPMs and for different kicks and the corresponding C-RDT is presented in Fig. 6.16.

Notably, given that by design no skew sextupole sources are present in the IOTA-ring, the presence of such line can be explained either by sextupole tilts, by an interplay between linear coupling and the regular sextupole sources, or any combination

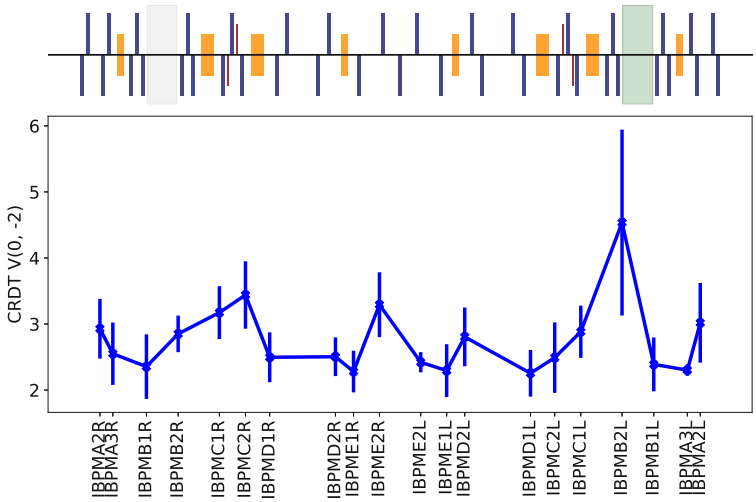

FIGURE 6.16: Measured skew sextupole C-RDT at a working point of $Q_x = 5.28$, $Q_y = 5.31$ and using a nominal sextupole configuration.

of those two effects. Similar to the sextupole lines, no decoherence factors were applied so far and thus the data cannot be used yet to determine the origin.

Lastly, in Fig. 6.17, the C-RDT corresponding to the line $H(-1,2)$, observed in all BPMs is presented.

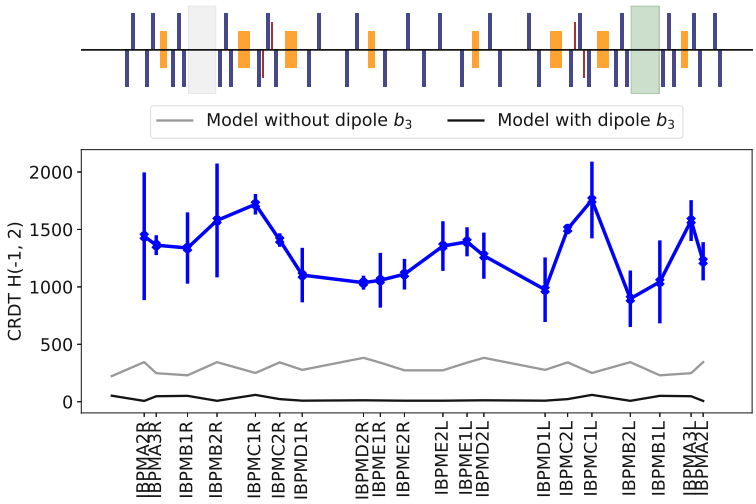

FIGURE 6.17: Measured octupole C-RDT at a working point of $Q_x = 5.28$, $Q_y = 5.31$ and using a nominal sextupole configuration, together with a comparison to the expected model values.

As octupole lines may also arise from, amongst others, a second order contribution from normal sextupoles, model values have been included here. Again, due to the lack of the decoherence correction, no comparison on the amplitude between model and measurement can be made. However, a difference in the evolution of the C-RDT amplitude is observed, unlike in the previous case for the sextupoles. Further investigation may thus investigate if a spurious octupole source may explain this difference. Notably, this data was taken during a different shift than the amplitude detuning data, as such hinting at a potential consistent octupole source.

In a further shift, studies were performed using a different sextupole powering scheme to potentially better identify any sextupole component in the 60° dipoles. In particular, the sextupoles in the straight section on the right hand side of IOTA-ring, as illustrated in Fig. 6.3, were turned off and the chromaticity in the ring was corrected using the remaining two sextupoles. Measurements were conducted at a working point of $Q_x = 5.28$, $Q_y = 5.31$, to compare to the measurements conducted in a previous shift, and at working point of $Q_x = 5.32$, $Q_y = 5.29$ and $Q_x = 5.325$, $Q_y = 5.29$. These different working points were chosen due to their proximity to $3Q_x$ resonance and thus increased C-RDTs linked to this resonance.

In Fig. 6.18-6.21, C-RDTs for coupling, sextupole, skew sextupole, and octupole sources are presented.

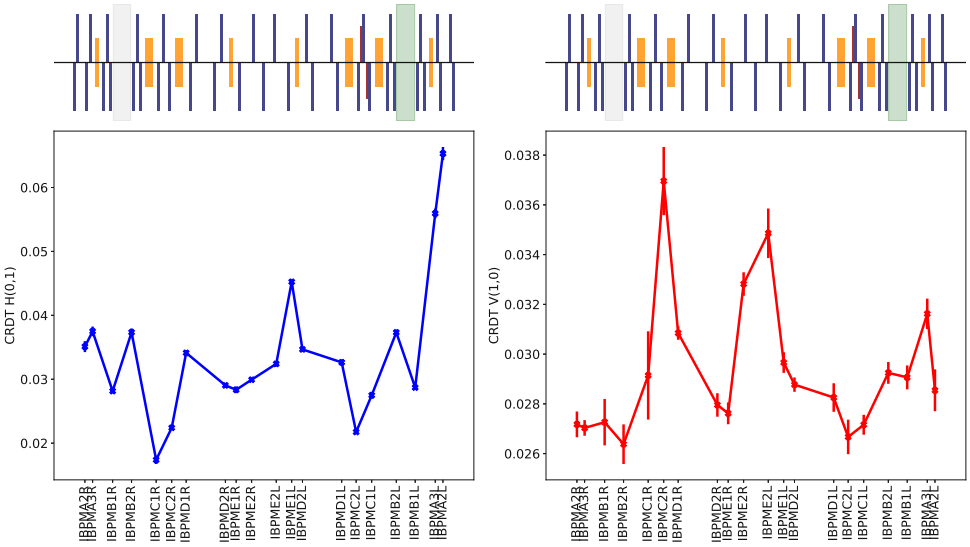

FIGURE 6.18: Measured coupling C-RDTs at a working point of $Q_x = 5.28$, $Q_y = 5.31$ and using only sextupoles in the left hand straight section for chromaticity correction.

For the coupling C-RDT $H(0,1)$, a similar excursion in the injection straight is observed as in the previous dataset, although gathered on different days and shifts. Similar so, a bump in the C-RDT $V(1,0)$ is observed around `IBPMC2R`.

For the sextupole C-RDTs, similar conclusions as for the previous results hold. While again a good quantitative agreement in the evolution is observed, for a comparison between the model values and the measurements, the difference due to decoherence factors needs to be taken into account. The C-RDT corresponding to the skew sextupole line $V(0,-2)$ does show some consistent behaviour between the two shifts, bar the excursion observed at `IBPMB2L` for the nominal sextupole configuration. Given the similar behaviour of the coupling C-RDTs between the two shifts, no further conclusion on the origin can be made. For the octupole C-RDT, while the amplitude of the C-RDT remains the same between the measurements, the evolution of the C-RDT is different between the two measurements. Given that hardware interventions on the octupole string took place in between the measurements shifts, future studies using the data corrected for the decoherence may thus look into potential effects of these interventions on the origin of the octupole line and linking it to specific measures taken.

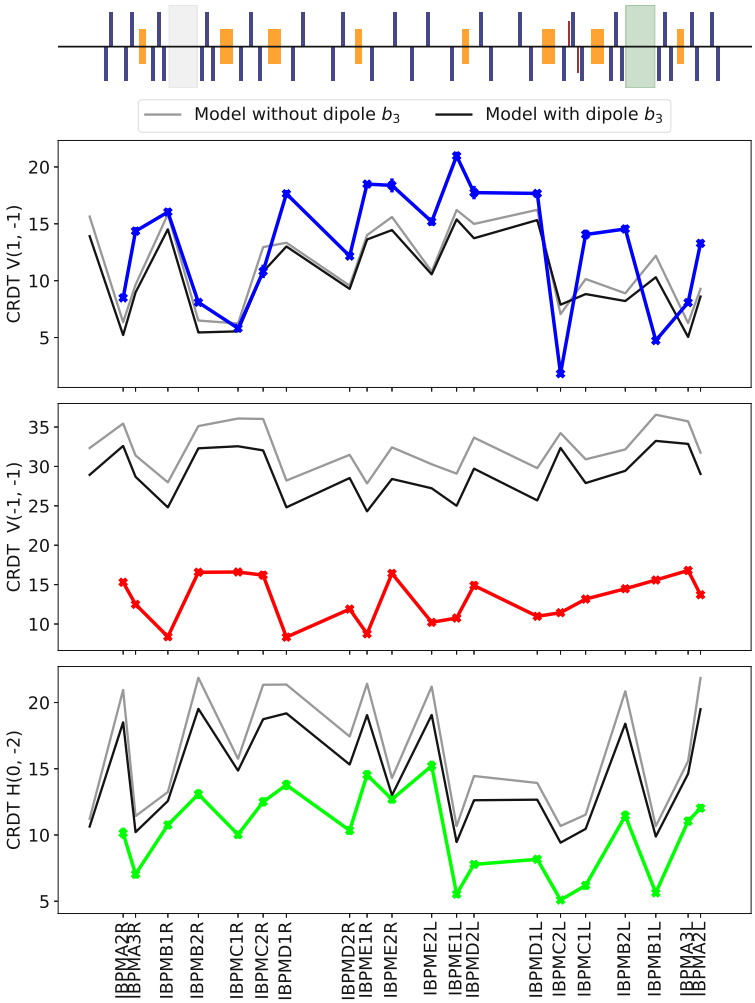

FIGURE 6.19: Measured sextupole C-RDTs at a working point of $Q_x = 5.28$, $Q_y = 5.31$ and using only sextupoles in the left hand straight section for chromaticity correction, together with a comparison to the expected model values.

Lastly, C-RDTs for measurements at the working point of $Q_x = 5.32$, $Q_y = 5.29$ are presented in Figs. 6.22-6.24. Results have been compared to the results at $Q_x = 5.325$, $Q_y = 5.29$, with no particular difference observed.

Notably, a slight change in the structure pf the coupling C-RDTs is observed between the measurements for the working point of $Q_x = 5.28$, $Q_y = 5.31$ and at $Q_x = 5.32$, $Q_y = 5.29$. In particular, the change of the C-RDTs in the CR-straight section is noticeable, which could stem from a tilt of the quadrupoles used to achieve the tune change. In both cases a tune split of $\Delta Q = 0.03$ is used, and thus no significant change of the C-RDT amplitude is expected nor observed. Additionally, in this data sets no skew sextupole line is observed, which may be partly explained by Q_y further away from the $3Q_y$ resonance. For sextupole C-RDTs, a similar good qualitative agreement is observed between model and measurement as for the previous measurements. Although taken back to back, a change in the octupole C-RDT $H(-1,2)$ is observed for the measurements at $Q_x = 5.28$, $Q_y = 5.31$ and at $Q_x = 5.32$, $Q_y = 5.29$, where in both cases only the sextupoles in the left hand straight section were powered. This change might then be explained by the change of the optics due to the

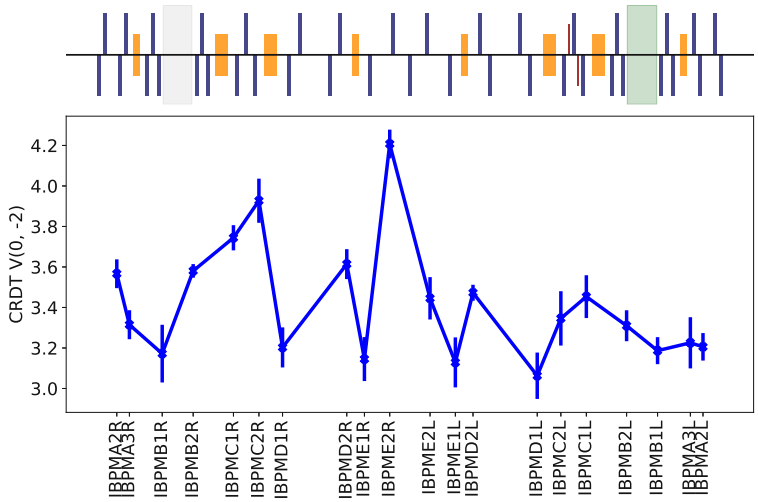

FIGURE 6.20: Measured skew sextupole C-RDT at a working point of $Q_x = 5.28$, $Q_y = 5.31$ and using only sextupoles in the left hand straight section for chromaticity correction.

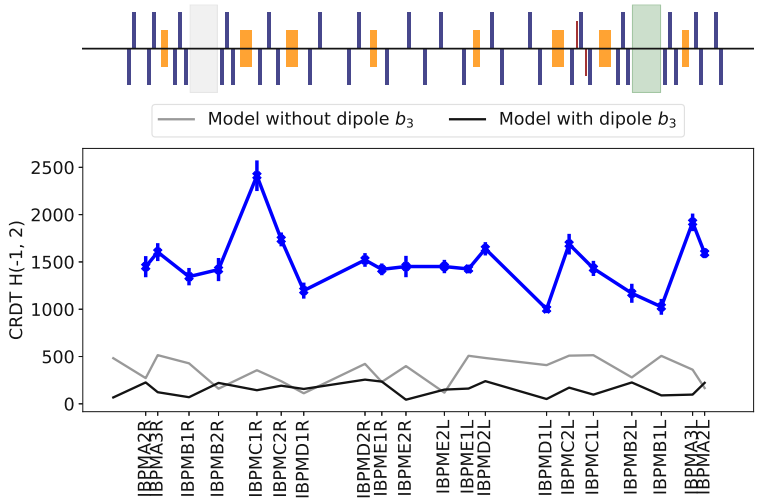

FIGURE 6.21: Measured octupole C-RDT at a working point of $Q_x = 5.28$, $Q_y = 5.31$ and using only sextupoles in the left hand straight section for chromaticity correction, together with a comparison to the expected model values.

tune knob, under assumption that the strength of any potential spurious octupole source has not changed between these measurements.

No analysis of resonance driving terms has been performed up until this point, as similarly to the C-RDT analysis, data has to be corrected for the decoherence first.

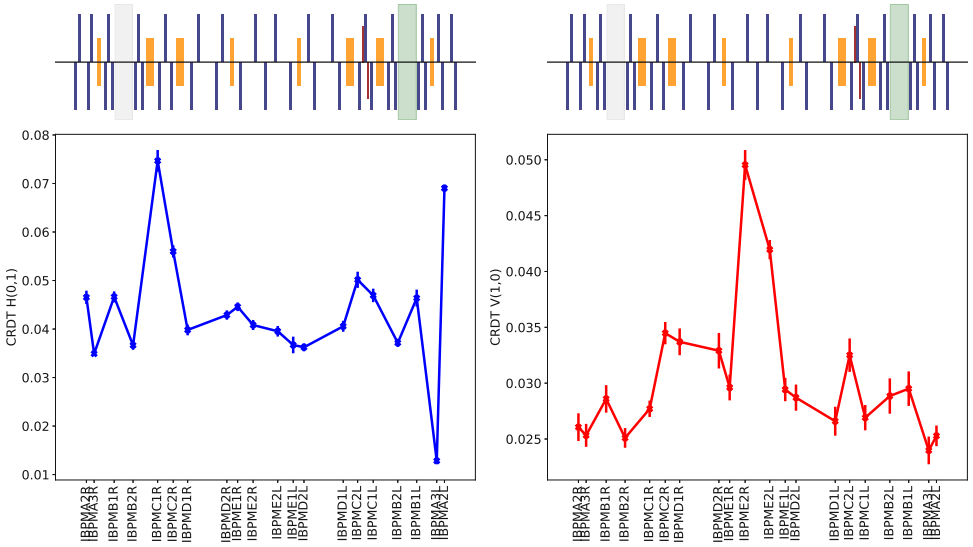

FIGURE 6.22: Measured coupling C-RDTs at a working point of $Q_x = 5.32$, $Q_y = 5.29$ and using only sextupoles in the left hand straight section for chromaticity correction.

6.5 Conclusions

Assessment of nonlinear magnetic fields, present either by design or by erroneous introduction, is one key task during the design and operation for many accelerators due to their potential performance limiting effects. One accelerator concept where this may be off particular importance is the recently proposed nonlinear integrable optics. It is based on introducing a nonlinear magnet with a particular potential which together with a special accelerator layout allows to generate an amplitude dependent tune shift, while not exciting any resonances. Other nonlinear fields in the accelerator may violate the required conditions and careful assessment is required to account for particle losses due to such sources. In this note, first studies on nonlinearities outside of the specific nonlinear channel have been presented for the case of the IOTA accelerator at Fermilab, one of the first machines built around the concept of nonlinear integrable optics. Using turn-by-turn data from the beam position monitors, acquired after an excitation with the kicker magnets, first a look in the linear optics is presented. Linear optics is in general well controlled in the IOTA accelerator, with a peak β-beating under 10 %. Following studies have looked into the amplitude detuning from the bare lattice without either the NL-magnet nor the octupole channel turned on. While initial measurements show discrepancies with the values expected from simulations, attributed to a spurious octupole source, measurements from a later shift show better agreement with the model values. The discrepancy is assumed to stem from hardware modification conducted before the first measurements, and no persistent spurious octupole source appears present in the IOTA-ring. Lastly, measurements of the combined resonance driving terms (C-RDT) have been presented for different working points and sextupole configurations. Good qualitative agreement for the sextupole C-RDTs has been observed between the model and measurements for the different configurations. Further studies are looking into the role of the decoherence of the specific spectral lines to account for the difference in amplitude between the model and measurements, to allow for a better comparison between those and in view of a potential use to assess the location and strength of

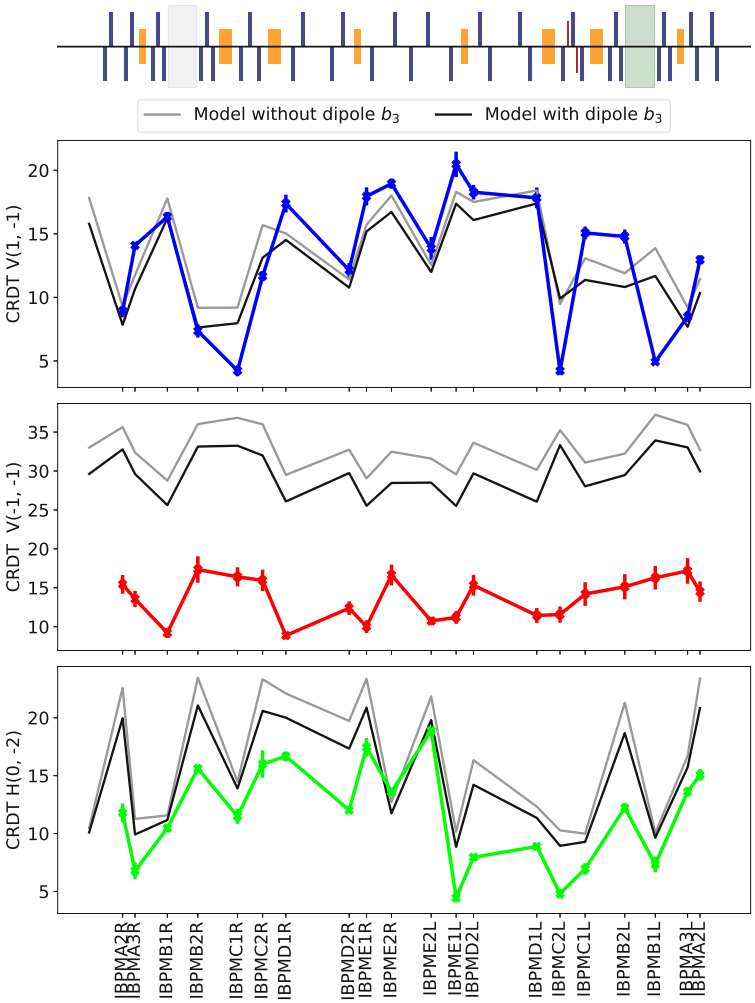

FIGURE 6.23: Measured sextupole C-RDTs at a working point of $Q_x = 5.32$, $Q_y = 5.29$ and using only sextupoles in the left hand straight section for chromaticity correction, together with a comparison to the expected model values.

the nonlinear magnetic fields.

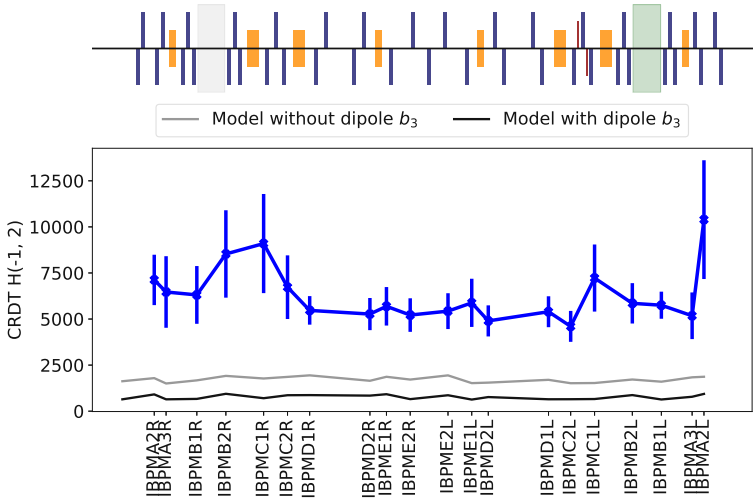

FIGURE 6.24: Measured octupole C-RDT at a working point of $Q_x = 5.32$, $Q_y = 5.29$ and using only sextupoles in the left hand straight section for chromaticity correction, together with a comparison to the expected model values.

Summary and outlook

Nonlinear magnetic fields have been shown in the past to have a profound impact on the operations of particle accelerators and are expected to do so even more in future machines which aim to achieve higher energies with more intense beams. Given their potential to both prevent mechanisms that would reduce the beam intensity but also itself potentially being the cause of significant beam loss has made them a rich field of study, with each new accelerator adding another facet.

In this thesis, the impact of nonlinear magnetic fields on the beam dynamics is studied under various circumstances, specifically investigating situations relevant to the operation of future accelerators. Using a number of observables, derived from either simulations or experiments, the main effects are quantified and give insights into ways of overcoming potential issues.

In Chapter 3, the dynamic aperture in the HE-LHC at injection energy has been studied. Multiple operation scenarios have been considered, taking into account the field quality of the main dipole magnets for the different cases. Based on early results, the main limitations have been identified and served as input into the following magnet design iterations. Viable scenarios in terms of dynamic aperture have been identified and allowed to define the requirements under which the HE-LHC may be built. While giving a solid first look at the feasibility of the considered scenarios, further studies should evaluate the dynamic aperture including also the field quality of other magnetic elements such as the main quadrupoles, which was not available for these studies, and also taking into account adverse effects resulting in a miscorrection to define additional tolerances.

Following the assessment of the previous Chapter that the sextupole component in the main dipoles is the key component, an experimental study was proposed and its results are presented in Chapter 4. The aim of the experiment was to assess the dynamic aperture in the presence of a strong, uncorrected sextupole component of the dipoles. Such a situation is expected to occur in a machine such as the HE-LHC in case of setting errors of the corrector circuits or dynamic changes of the sextupole component of the dipoles. The experiment was conducted in the LHC, being the natural predecessor to the HE-LHC, and the sextupole correctors were set such to emulate a situation expected in the HE-LHC. While initial simulations using a simplified model showed a significant decrease of the dynamic aperture, the measured dynamic aperture was found to be significantly higher. The main discrepancy between the model and the situation in the LHC was identified to be the amplitude detuning stemming from the second order effect of the sextupoles. With the amplitude detuning in the model adjusted to the measured values, the dynamic aperture between simulation and measurement agrees well. In turn, the case for the HE-LHC does not appear as dire as initially estimated, with adjustments of the amplitude detuning using octupole magnets potentially allowing to minimize the

decrease of the dynamic aperture due to miscorrection of the main dipole sextupole component.

To quantify the nonlinear content of a machine, either in experiments or in simulations, and to establish corrections, global and local observables such as amplitude detuning or resonance driving terms may be used. One common source of uncertainty of these is the coupling between the two transverse planes, elicit by either skew quadrupole or solenoid fields. In Chapter 5, a formalism is presented to evaluate the impact of coupling on these observables. The derived formulas have been benchmarked against simulations and have shown good agreement and allow to estimate the impact of coupling on measured values. In addition, given the impact on the beam size in the interaction point of the experiments in the LHC and subsequently the luminosity, tolerances on the local coupling can be established.

Many accelerators are built around the principle of linear optics and nonlinear magnetic elements are added on top, intended to be small perturbations, yet provide effects beneficial to the beam stability whilst also being a potential major source of beam loss. Chapter 6 presents studies in an accelerator based around a different concept, where one special nonlinear element is integrated such that no resonances are excited, thus preventing any beam loss, while still retaining the intended beneficial effects. This concept relies on the absence of other nonlinear magnetic elements such as sextupoles to allow for the best performance possible. Measurements of the impact on the beam dynamics from nonlinear magnetic fields other than the special nonlinear magnet are presented for the case of the first accelerator built around this concept, the IOTA accelerator at Fermilab. In general, no significant difference between the measurements and quantities derived from the model is found. While good qualitative agreement is observed, further studies are needed to eliminate known sources of uncertainty such as decoherence to allow for an accurate localization of additional sources.

In conclusion, the studies and results presented in this thesis represent significant improvements in the understanding of the impact of nonlinear magnetic fields in synchrotrons and may serve as vital input for design studies of potential future accelerators.

Appendix A

Field quality of the main dipoles in the HE-LHC

Field quality tables as used for the tracking studies presented in Ch. 3.

	Systematic			**Uncertainty**			**Random**		
Injection Energy [GeV]	450	900	1300	450	900	1300	450	900	1300
b_2	-2.230	-2.230	-2.230	0.922	0.922	0.922	0.922	0.922	0.922
b_3	-35.000	-55.000	-40.000	10.000	4.000	3.000	10.000	4.000	3.000
b_4	0.000	0.000	0.000	0.449	0.449	0.449	0.449	0.449	0.449
b_5	8.000	8.000	4.000	1.500	1.500	0.800	1.500	1.500	0.800
b_6	0.000	0.000	0.000	0.176	0.176	0.176	0.176	0.176	0.176
b_7	0.200	0.600	1.100	0.211	0.211	0.211	0.211	0.211	0.211
b_8	0.000	0.000	0.000	0.071	0.071	0.071	0.071	0.071	0.071
b_9	3.800	4.200	2.900	0.500	0.500	0.200	0.500	0.500	0.200
b_{10}	0.000	0.000	0.000	0.027	0.027	0.027	0.027	0.027	0.027
b_{11}	0.750	0.860	1.000	0.028	0.028	0.028	0.028	0.028	0.028
b_{12}	0.000	0.000	0.000	0.009	0.009	0.009	0.009	0.009	0.009
b_{13}	0.000	0.000	0.000	0.011	0.011	0.011	0.011	0.011	0.011
b_{14}	0.000	0.000	0.000	0.003	0.003	0.003	0.003	0.003	0.003
b_{15}	0.000	0.000	0.000	0.004	0.004	0.004	0.004	0.004	0.004
a_2	0.000	0.000	0.000	1.040	1.040	1.040	1.040	1.040	1.040
a_3	0.000	0.000	0.000	0.678	0.678	0.678	0.678	0.678	0.678
a_4	0.000	0.000	0.000	0.450	0.450	0.450	0.450	0.450	0.450
a_5	0.000	0.000	0.000	0.317	0.317	0.317	0.317	0.317	0.317
a_6	0.000	0.000	0.000	0.205	0.205	0.205	0.205	0.205	0.205
a_7	0.000	0.000	0.000	0.116	0.116	0.116	0.116	0.116	0.116
a_8	0.000	0.000	0.000	0.071	0.071	0.071	0.071	0.071	0.071
a_9	0.000	0.000	0.000	0.041	0.041	0.041	0.041	0.041	0.041
a_{10}	0.000	0.000	0.000	0.025	0.025	0.025	0.025	0.025	0.025
a_{11}	0.000	0.000	0.000	0.016	0.016	0.016	0.016	0.016	0.016
a_{12}	0.000	0.000	0.000	0.000	0.000	0.000	0.009	0.009	0.009
a_{13}	0.000	0.000	0.000	0.000	0.000	0.000	0.005	0.005	0.005
a_{14}	0.000	0.000	0.000	0.000	0.000	0.000	0.003	0.003	0.003
a_{15}	0.000	0.000	0.000	0.000	0.000	0.000	0.002	0.002	0.002

TABLE A.1: Normal and skew coefficients for MB dipoles for different injection energies in the HE-LHC. Harmonics correspond to the dipole design from 24.01.2018 and at a reference radius of $R_r = 16.7\,\text{mm}$.

	Systematic			**Uncertainty**			**Random**		
Injection Energy [GeV]	450	900	1300	450	900	1300	450	900	1300
b_2	-2.200	-2.200	-2.200	0.922	0.922	0.922	0.922	0.922	0.922
b_3	-26.761	-16.433	-13.211	1.351	1.351	1.351	1.351	1.351	1.351
b_4	-0.081	-0.081	-0.081	0.449	0.449	0.449	0.449	0.449	0.449
b_5	3.732	1.417	0.703	0.541	0.541	0.541	0.541	0.541	0.541
b_6	-0.001	-0.001	-0.001	0.176	0.176	0.176	0.176	0.176	0.176
b_7	1.142	1.409	1.493	0.211	0.211	0.211	0.211	0.211	0.211
b_8	0.000	0.000	0.000	0.071	0.071	0.071	0.071	0.071	0.071
b_9	2.798	2.042	1.804	0.092	0.092	0.092	0.092	0.092	0.092
b_{10}	0.000	0.000	0.000	0.027	0.027	0.027	0.027	0.027	0.027
b_{11}	0.997	0.999	1.000	0.028	0.028	0.028	0.028	0.028	0.028
b_{12}	0.000	0.000	0.000	0.009	0.009	0.009	0.009	0.009	0.009
b_{13}	0.000	0.000	0.000	0.011	0.011	0.011	0.011	0.011	0.011
b_{14}	0.000	0.000	0.000	0.003	0.003	0.003	0.003	0.003	0.003
b_{15}	0.000	0.000	0.000	0.004	0.004	0.004	0.004	0.004	0.004
a_2	0.000	0.000	0.000	1.040	1.040	1.040	1.040	1.040	1.040
a_3	0.000	0.000	0.000	0.678	0.678	0.678	0.678	0.678	0.678
a_4	0.000	0.000	0.000	0.450	0.450	0.450	0.450	0.450	0.450
a_5	0.000	0.000	0.000	0.317	0.317	0.317	0.317	0.317	0.317
a_6	0.000	0.000	0.000	0.205	0.205	0.205	0.205	0.205	0.205
a_7	0.000	0.000	0.000	0.116	0.116	0.116	0.116	0.116	0.116
a_8	0.000	0.000	0.000	0.071	0.071	0.071	0.071	0.071	0.071
a_9	0.000	0.000	0.000	0.041	0.041	0.041	0.041	0.041	0.041
a_{10}	0.000	0.000	0.000	0.025	0.025	0.025	0.025	0.025	0.025
a_{11}	0.000	0.000	0.000	0.016	0.016	0.016	0.016	0.016	0.016
a_{12}	0.000	0.000	0.000	0.000	0.000	0.000	0.009	0.009	0.009
a_{13}	0.000	0.000	0.000	0.000	0.000	0.000	0.005	0.005	0.005
a_{14}	0.000	0.000	0.000	0.000	0.000	0.000	0.003	0.003	0.003
a_{15}	0.000	0.000	0.000	0.000	0.000	0.000	0.002	0.002	0.002

TABLE A.2: Normal and skew coefficients for MB dipoles for different injection energies in the HE-LHC. Harmonics correspond to the dipole design from 12.06.2018 and at a reference radius of $R_r = 16.7$ mm. All values are presented in units of 10^{-4}.

	Systematic			Uncertainty			Random		
Injection Energy [GeV]	450	900	1300	450	900	1300	450	900	1300
b_2	-2.200	-2.200	-2.200	0.922	0.922	0.922	0.922	0.922	0.922
b_3	-50.549	-27.643	-19.653	1.351	1.351	1.351	1.351	1.351	1.351
b_4	-0.081	-0.081	-0.081	0.449	0.449	0.449	0.449	0.449	0.449
b_5	10.429	3.784	1.982	0.541	0.541	0.541	0.541	0.541	0.541
b_6	-0.001	-0.001	-0.001	0.176	0.176	0.176	0.176	0.176	0.176
b_7	0.294	1.150	1.352	0.211	0.211	0.211	0.211	0.211	0.211
b_8	0.000	0.000	0.000	0.071	0.071	0.071	0.071	0.071	0.071
b_9	4.834	2.821	2.238	0.092	0.092	0.092	0.092	0.092	0.092
b_{10}	0.000	0.000	0.000	0.027	0.027	0.027	0.027	0.027	0.027
b_{11}	0.976	1.003	1.002	0.028	0.028	0.028	0.028	0.028	0.028
b_{12}	0.000	0.000	0.000	0.009	0.009	0.009	0.009	0.009	0.009
b_{13}	-0.192	-0.192	-0.192	0.011	0.011	0.011	0.011	0.011	0.011
b_{14}	0.000	0.000	0.000	0.003	0.003	0.003	0.003	0.003	0.003
b_{15}	0.011	0.011	0.011	0.004	0.004	0.004	0.004	0.004	0.004
a_2	0.000	0.000	0.000	1.040	1.040	1.040	1.040	1.040	1.040
a_3	0.000	0.000	0.000	0.678	0.678	0.678	0.678	0.678	0.678
a_4	0.000	0.000	0.000	0.450	0.450	0.450	0.450	0.450	0.450
a_5	0.000	0.000	0.000	0.317	0.317	0.317	0.317	0.317	0.317
a_6	0.000	0.000	0.000	0.205	0.205	0.205	0.205	0.205	0.205
a_7	0.000	0.000	0.000	0.116	0.116	0.116	0.116	0.116	0.116
a_8	0.000	0.000	0.000	0.071	0.071	0.071	0.071	0.071	0.071
a_9	0.000	0.000	0.000	0.041	0.041	0.041	0.041	0.041	0.041
a_{10}	0.000	0.000	0.000	0.025	0.025	0.025	0.025	0.025	0.025
a_{11}	0.000	0.000	0.000	0.016	0.016	0.016	0.016	0.016	0.016
a_{12}	0.000	0.000	0.000	0.000	0.000	0.000	0.009	0.009	0.009
a_{13}	0.000	0.000	0.000	0.000	0.000	0.000	0.005	0.005	0.005
a_{14}	0.000	0.000	0.000	0.000	0.000	0.000	0.003	0.003	0.003
a_{15}	0.000	0.000	0.000	0.000	0.000	0.000	0.002	0.002	0.002

TABLE A.3: Normal and skew coefficients for MB dipoles for different injection energies in the HE-LHC. Harmonics correspond to the dipole design from 12.09.2018 and at a reference radius of $R_r = 16.7$ mm. All values are presented in units of 10^{-4}.

	Systematic			Uncertainty			Random		
Injection Energy [GeV]	450	900	1300	450	900	1300	450	900	1300
b_2	5.466	4.511	4.233	0.929	0.929	0.929	0.929	0.929	0.929
b_3	-23.928	-12.756	-9.246	0.668	0.668	0.668	0.668	0.668	0.668
b_4	0.804	0.878	0.904	0.467	0.467	0.467	0.467	0.467	0.467
b_5	5.049	2.561	1.799	0.283	0.283	0.283	0.283	0.283	0.283
b_6	0.657	0.494	0.444	0.187	0.187	0.187	0.187	0.187	0.187
b_7	-1.303	-0.536	-0.299	0.109	0.109	0.109	0.109	0.109	0.109
b_8	0.458	0.400	0.381	0.072	0.072	0.072	0.072	0.072	0.072
b_9	2.009	1.241	0.999	0.047	0.047	0.047	0.047	0.047	0.047
b_{10}	0.217	0.167	0.152	0.028	0.028	0.028	0.028	0.028	0.028
b_{11}	1.042	1.030	1.030	0.015	0.015	0.015	0.015	0.015	0.015
b_{12}	0.081	0.081	0.081	0.010	0.010	0.010	0.010	0.010	0.010
b_{13}	-0.227	-0.227	-0.227	0.005	0.005	0.005	0.005	0.005	0.005
b_{14}	0.026	0.026	0.026	0.003	0.003	0.003	0.003	0.003	0.003
b_{15}	-0.020	-0.020	-0.020	0.002	0.002	0.002	0.002	0.002	0.002
a_2	0.000	0.000	0.000	1.103	1.103	1.103	1.103	1.103	1.103
a_3	0.000	0.000	0.000	0.754	0.754	0.754	0.754	0.754	0.754
a_4	0.000	0.000	0.000	0.473	0.473	0.473	0.473	0.473	0.473
a_5	0.000	0.000	0.000	0.329	0.329	0.329	0.329	0.329	0.329
a_6	0.000	0.000	0.000	0.205	0.205	0.205	0.205	0.205	0.205
a_7	0.000	0.000	0.000	0.114	0.114	0.114	0.114	0.114	0.114
a_8	0.000	0.000	0.000	0.069	0.069	0.069	0.069	0.069	0.069
a_9	0.000	0.000	0.000	0.038	0.038	0.038	0.038	0.038	0.038
a_{10}	0.000	0.000	0.000	0.023	0.023	0.023	0.023	0.023	0.023
a_{11}	0.000	0.000	0.000	0.015	0.015	0.015	0.015	0.015	0.015
a_{12}	0.000	0.000	0.000	0.008	0.008	0.008	0.008	0.008	0.008
a_{13}	0.000	0.000	0.000	0.005	0.005	0.005	0.005	0.005	0.005
a_{14}	0.000	0.000	0.000	0.003	0.003	0.003	0.003	0.003	0.003
a_{15}	0.000	0.000	0.000	0.002	0.002	0.002	0.002	0.002	0.002

TABLE A.4: Normal and skew coefficients for MB dipoles for different injection energies in the HE-LHC. Harmonics correspond to the dipole design from 28.09.2018, assuming a full artificial pinning efficiency, and at a reference radius of $R_r = 16.7\,\text{mm}$. All values are presented in units of 10^{-4}.

	Systematic			Uncertainty			Random		
Injection Energy [GeV]	450	900	1300	450	900	1300	450	900	1300
b_2	7.828	5.607	4.785	0.929	0.929	0.929	0.929	0.929	0.929
b_3	-50.764	-24.856	-16.197	0.668	0.668	0.668	0.668	0.668	0.668
b_4	0.638	0.797	0.850	0.467	0.467	0.467	0.467	0.467	0.467
b_5	12.263	5.109	3.187	0.283	0.283	0.283	0.283	0.283	0.283
b_6	1.077	0.669	0.541	0.187	0.187	0.187	0.187	0.187	0.187
b_7	-3.501	-1.312	-0.728	0.109	0.109	0.109	0.109	0.109	0.109
b_8	0.612	0.461	0.416	0.072	0.072	0.072	0.072	0.072	0.072
b_9	4.142	2.036	1.440	0.047	0.047	0.047	0.047	0.047	0.047
b_{10}	0.357	0.220	0.180	0.028	0.028	0.028	0.028	0.028	0.028
b_{11}	1.052	1.048	1.038	0.015	0.015	0.015	0.015	0.015	0.015
b_{12}	0.081	0.081	0.081	0.010	0.010	0.010	0.010	0.010	0.010
b_{13}	-0.227	-0.227	-0.227	0.005	0.005	0.005	0.005	0.005	0.005
b_{14}	0.026	0.026	0.026	0.003	0.003	0.003	0.003	0.003	0.003
b_{15}	-0.020	-0.020	-0.020	0.002	0.002	0.002	0.002	0.002	0.002
a_2	0.000	0.000	0.000	1.103	1.103	1.103	1.103	1.103	1.103
a_3	0.000	0.000	0.000	0.754	0.754	0.754	0.754	0.754	0.754
a_4	0.000	0.000	0.000	0.473	0.473	0.473	0.473	0.473	0.473
a_5	0.000	0.000	0.000	0.329	0.329	0.329	0.329	0.329	0.329
a_6	0.000	0.000	0.000	0.205	0.205	0.205	0.205	0.205	0.205
a_7	0.000	0.000	0.000	0.114	0.114	0.114	0.114	0.114	0.114
a_8	0.000	0.000	0.000	0.069	0.069	0.069	0.069	0.069	0.069
a_9	0.000	0.000	0.000	0.038	0.038	0.038	0.038	0.038	0.038
a_{10}	0.000	0.000	0.000	0.023	0.023	0.023	0.023	0.023	0.023
a_{11}	0.000	0.000	0.000	0.015	0.015	0.015	0.015	0.015	0.015
a_{12}	0.000	0.000	0.000	0.008	0.008	0.008	0.008	0.008	0.008
a_{13}	0.000	0.000	0.000	0.005	0.005	0.005	0.005	0.005	0.005
a_{14}	0.000	0.000	0.000	0.003	0.003	0.003	0.003	0.003	0.003
a_{15}	0.000	0.000	0.000	0.002	0.002	0.002	0.002	0.002	0.002

TABLE A.5: Normal and skew coefficients for MB dipoles for different injection energies in the HE-LHC. Harmonics correspond to the dipole design from 28.09.2018, assuming a half artificial pinning efficiency, and at a reference radius of $R_r = 16.7\,\text{mm}$. All values are presented in units of 10^{-4}.

Bibliography

[1] E.D Courant and H.S Snyder. "Theory of the alternating-gradient synchrotron". In: *Annals of Physics* 3.1 (1958), pp. 1 –48. ISSN: 0003-4916. DOI: https://doi.org/10.1016/0003-4916(58)90012-5. URL: http://www.sciencedirect.com/science/article/pii/0003491658900125 (cit. on p. 1).

[2] C. Smith. "How the LHC came to be". In: *Nature* 448 (2007), 281–284. DOI: 10.1038/nature06076 (cit. on p. 3).

[3] Stephen Myers. *The LEP Collider, from design to approval and commissioning*. John Adams' Lecture. Delivered at CERN, 26 Nov 1990. Geneva: CERN, 1991. DOI: 10.5170/CERN-1991-008. URL: http://cds.cern.ch/record/226776 (cit. on p. 3).

[4] Ralph Assmann, Mike Lamont, and Steve Myers. "A brief history of the LEP collider". In: *Nuclear Physics B - Proceedings Supplements* 109.2 (2002). Proceedings of the 7th Topical Seminar, pp. 17 –31. ISSN: 0920-5632. DOI: https://doi.org/10.1016/S0920-5632(02)90005-8. URL: http://www.sciencedirect.com/science/article/pii/S0920563202900058 (cit. on p. 3).

[5] Gerald F Dugan and James R Sanford. *Superconducting Super Collider: a retrospective summary 1989-1993*. Dallas, TX: SSC, 1994. URL: https://cds.cern.ch/record/270210 (cit. on p. 3).

[6] CERN Media and Press team. *First beam in the LHC - accelerating science*. https://home.cern/news/press-release/cern/first-beam-lhc-accelerating-science. 2008 (cit. on p. 3).

[7] Mike Lamont. "The First Years of LHC Operation for Luminosity Production". In: (2013), MOYAB101. 5 p. URL: https://cds.cern.ch/record/2010134 (cit. on p. 3).

[8] *Design Report Tevatron 1 project*. Tech. rep. FERMILAB-DESIGN-1984-01. 1984. URL: https://cds.cern.ch/record/1478620 (cit. on p. 3).

[9] ATLAS Collaboration. "Observation of a new particle in the search for the Standard Model Higgs boson with the ATLAS detector at the LHC". In: *Physics Letters B* 716.1 (2012), pp. 1 –29. ISSN: 0370-2693. DOI: https://doi.org/10.1016/j.physletb.2012.08.020. URL: http://www.sciencedirect.com/science/article/pii/S037026931200857X (cit. on p. 3).

[10] CMS Collaboration. "Observation of a new boson at a mass of 125 GeV with the CMS experiment at the LHC". In: *Physics Letters B* 716.1 (2012), pp. 30 –61. ISSN: 0370-2693. DOI: https://doi.org/10.1016/j.physletb.2012.08.021. URL: http://www.sciencedirect.com/science/article/pii/S0370269312008581 (cit. on p. 3).

[11] ATLAS Collaboration. *ATLAS: technical proposal for a general-purpose pp experiment at the Large Hadron Collider at CERN*. LHC Tech. Proposal. Geneva: CERN, 1994. URL: http://cds.cern.ch/record/290968 (cit. on p. 3).

[12] CMS Collaboration. *CMS Physics: Technical Design Report Volume 1: Detector Performance and Software*. Technical Design Report CMS. Geneva: CERN, 2006. URL: http://cds.cern.ch/record/922757 (cit. on p. 3).

[13] ALICE Collaboration. *ALICE: Physics Performance Report*. Tech. rep. CERN-LHCC-2003-049. Geneva: CERN, Nov. 2003. DOI: 10.1088/0954-3899/30/11/001. URL: http://cds.cern.ch/record/643556 (cit. on p. 3).

[14] LHCb Collaboration. *LHCb : Technical Proposal*. Tech. Proposal. Geneva: CERN, 1998. URL: https://cds.cern.ch/record/622031 (cit. on p. 3).

[15] Lucio Rossi and Oliver Brüning. *The High Luminosity Large Hadron Collider: the new machine for illuminating the mysteries of Universe*. Advanced series on directions in high energy physics. Hackensack, NJ: World Scientific, 2015. DOI: 10.1142/9581. URL: http://cds.cern.ch/record/1995532 (cit. on p. 3).

[16] O. Brüning and L. Rossi. "The High-Luminosity Large Hadron Collider". In: *Nat Rev Phys* 1 (2019), 241–243. DOI: 10.1038/s42254-019-0050-6 (cit. on p. 3).

[17] "The European Strategy for Particle Physics Update 2013. La stratégie européenne pour la physique des particules Mise à jour 2013. 16th Session of European Strategy Council". In: (May 2013). URL: https://cds.cern.ch/record/1567258 (cit. on p. 4).

[18] "Minutes. Procès-verbal. 16th Session of European Strategy Council". In: (Dec. 2013). URL: https://cds.cern.ch/record/1646092 (cit. on p. 4).

[19] M. Benedikt. "Overview of the Future Circular Collider study". presented at the FCC Week 2019, June 24-28, 2019, Brussels, https://indico.cern.ch/event/727555 (cit. on p. 4).

[20] R. Assmann. "LEP Operation and Performance with Electron-Positron Collisions at 209 GeV". In: (2001). URL: https://cds.cern.ch/record/567226 (cit. on p. 4).

[21] Michael Benedikt et al. *Future Circular Collider - European Strategy Update Documents*. Tech. rep. CERN-ACC-2019-0007. Geneva: CERN, Jan. 2019. URL: https://cds.cern.ch/record/2653673 (cit. on p. 4).

[22] Michelangelo Mangano et al. *FCC Physics Opportunities: Future Circular Collider Conceptual Design Report Volume 1. Future Circular Collider*. Tech. rep. CERN-ACC-2018-0056. 6. Geneva: CERN, Dec. 2018. DOI: 10.1140/epjc/s10052-019-6904-3. URL: https://cds.cern.ch/record/2651294 (cit. on p. 4).

[23] Michael Benedikt et al. *FCC-ee: The Lepton Collider: Future Circular Collider Conceptual Design Report Volume 2. Future Circular Collider*. Tech. rep. CERN-ACC-2018-0057. 2. Geneva: CERN, Dec. 2018. DOI: 10.1140/epjst/e2019-900045-4. URL: https://cds.cern.ch/record/2651299 (cit. on p. 4).

[24] Michael Benedikt et al. *FCC-hh: The Hadron Collider: Future Circular Collider Conceptual Design Report Volume 3. Future Circular Collider*. Tech. rep. CERN-ACC-2018-0058. Geneva: CERN, Dec. 2018. DOI: 10.1140/epjst/e2019-900087-0. URL: https://cds.cern.ch/record/2651300 (cit. on pp. 4, 36).

[25] Frank Zimmermann et al. *HE-LHC: The High-Energy Large Hadron Collider: Future Circular Collider Conceptual Design Report Volume 4. Future Circular Collider*. Tech. rep. CERN-ACC-2018-0059. Geneva: CERN, Dec. 2018. DOI: 10.1140/epjst/e2019-900088-6. URL: https://cds.cern.ch/record/2651305 (cit. on pp. 4, 31, 40).

[26] M. Benedikt. "FCC feasibility study and FCCIS H2020 project". presented at the FCC November Week 2020, November 9-13, 2020, https://indico.cern.ch/event/923801 (cit. on p. 4).

[27] The CEPC Study Group. *CEPC Conceptual Design Report: Volume 1 - Accelerator*. 2018. arXiv: 1809.00285 [physics.acc-ph] (cit. on p. 4).

[28] Hitoshi Yamamoto. "The International Linear Collider Project—Its Physics and Status". In: *Symmetry* 13.4 (2021). ISSN: 2073-8994. DOI: 10.3390/sym13040674. URL: https://www.mdpi.com/2073-8994/13/4/674 (cit. on p. 5).

[29] Chris Adolphsen et al. *The International Linear Collider Technical Design Report - Volume 3.I: Accelerator R&D in the Technical Design Phase*. 2013. arXiv: 1306.6353 [physics.acc-ph] (cit. on p. 5).

[30] A. Robson et al. *The Compact Linear e^+e^- Collider (CLIC): Accelerator and Detector*. 2018. arXiv: 1812.07987 [physics.acc-ph] (cit. on p. 5).

[31] Oliver Bruning and Max Klein. *The Large Hadron-Electron Collider at the HL-LHC*. Tech. rep. arXiv:2007.14491. Submitted to J.Phys. Geneva: CERN, Jan. 2020. URL: http://cds.cern.ch/record/2706220 (cit. on p. 5).

[32] E. C. Aschenauer et al. *eRHIC Design Study: An Electron-Ion Collider at BNL*. 2014. arXiv: 1409.1633 [physics.acc-ph] (cit. on p. 5).

[33] E. Syresin et al. "NICA Accelerator Complex at JINR". In: *Proc. 10th International Particle Accelerator Conference (IPAC'19), Melbourne, Australia, 19-24 May 2019* (Melbourne, Australia). International Particle Accelerator Conference 10. https://doi.org/10.18429/JACoW-IPAC2019-MOPMP014. Geneva, Switzerland: JACoW Publishing, June 2019, pp. 452–454. ISBN: 978-3-95450-208-0. DOI: doi:10.18429/JACoW-IPAC2019-MOPMP014. URL: http://jacow.org/ipac2019/papers/mopmp014.pdf (cit. on p. 5).

[34] "FAIR Baseline Technical Report (Volume 1)". In: (2006) (cit. on p. 5).

[35] "The PIP-II Reference Design Report". In: (June 2015). Ed. by Valeri Lebedev. DOI: 10.2172/1365571 (cit. on p. 5).

[36] J. Eldred, V. Lebedev, and A. Valishev. "Rapid-cycling synchrotron for multi-megawatt proton facility at Fermilab". In: *Journal of Instrumentation* 14.07 (July 2019), P07021–P07021. ISSN: 1748-0221. DOI: 10.1088/1748-0221/14/07/p07021. URL: http://dx.doi.org/10.1088/1748-0221/14/07/P07021 (cit. on p. 5).

[37] V. Danilov and S. Nagaitsev. "Nonlinear accelerator lattices with one and two analytic invariants". In: *Phys. Rev. ST Accel. Beams* 13 (8 Aug. 2010), p. 084002. DOI: 10.1103/PhysRevSTAB.13.084002. URL: https://link.aps.org/doi/10.1103/PhysRevSTAB.13.084002 (cit. on pp. 5, 98–100).

[38] S. Antipov et al. "IOTA (Integrable Optics Test Accelerator): facility and experimental beam physics program". In: *Journal of Instrumentation* 12.03 (Mar. 2017), T03002–T03002. DOI: 10.1088/1748-0221/12/03/t03002. URL: https://doi.org/10.1088%2F1748-0221%2F12%2F03%2Ft03002 (cit. on pp. 5, 98, 101, 102, 107).

[39] Andrzej Wolski. *Beam dynamics in high energy particle accelerators*. London: Imperial College Press, 2014. DOI: 10.1142/p899. URL: https://cds.cern.ch/record/1622200 (cit. on p. 7).

[40] Helmut Wiedemann. *Particle accelerator physics; 4th ed.* Berlin: Springer, 2015. DOI: 10.1007/978-3-319-18317-6. URL: https://cds.cern.ch/record/2034423 (cit. on pp. 7, 19, 25).

[41] Alexander Wu Chao. *Lectures on accelerator physics*. Singapore: World Scientific, 2020. URL: https://cds.cern.ch/record/2743448 (cit. on p. 7).

[42] S Y Lee. *Accelerator physics; 4th ed.* Singapore: World Scientific, 2019. DOI: 10.1142/11111. URL: https://cds.cern.ch/record/2651939 (cit. on p. 7).

[43] Michiko G Minty and Frank Zimmermann. *Measurement and control of charged particle beams*. Particle acceleration and detection. Berlin: Springer, 2003. URL: http://cds.cern.ch/record/629879 (cit. on pp. 7, 86).

[44] Martin Reiser. *Theory and design of charged particle beams; 2nd ed.* Weinheim: Wiley, 2008. DOI: 10.1002/9783527622047. URL: https://cds.cern.ch/record/1113306 (cit. on p. 8).

[45] W. Herr, ed. *CAS - CERN Accelerator School: Advanced Accelerator Physics: Trondheim, Norway 18 - 29 Aug 2013. CAS - CERN Accelerator School: Advanced Accelerator Physics Course*. Organisers: Dr. Roger Bailey (Head of CAS); Barbara Strasser (CAS Assistant). CERN. Geneva: CERN, Jan. 2016. DOI: 10.5170/CERN-2014-009. URL: https://cds.cern.ch/record/1507631 (cit. on p. 16).

[46] Edmund J N Wilson. "Nonlinear resonances (particle accelerators)". In: (1995). DOI: 10.5170/CERN-1995-006.15. URL: https://cds.cern.ch/record/302492 (cit. on p. 18).

[47] V. Lebedev and S. Bogacz. "Betatron Motion with Coupling of Horizontal and Vertical Degrees of Freedom". In: *JINST* 5 (2010), P10010. DOI: 10.1088/1748-0221/5/10/P10010. arXiv: 1207.5526 [physics.acc-ph] (cit. on p. 19).

[48] Gilbert Guignard. "Betatron coupling and related impact of radiation". In: *Phys. Rev. E* 51 (1995), pp. 6104–6118. DOI: 10.5170/CERN-1995-006.43. URL: https://cds.cern.ch/record/300856 (cit. on p. 19).

[49] J. Bengtsson J. Irwin. "Analytical calculations of smear and tune shift". In: (1990) (cit. on pp. 22, 81, 82, 84).

[50] Michel Henon and Carl Heiles. "The Applicability of the Third Integral of Motion: Some Numerical Experiments". In: *Astron. J.* 69 (1964), pp. 73–79. DOI: 10.1086/109234 (cit. on p. 23).

[51] A. Bazzani et al. "Advances on the modeling of the time evolution of dynamic aperture of hadron circular accelerators". In: *Phys. Rev. Accel. Beams* 22 (10 Oct. 2019), p. 104003. DOI: 10.1103/PhysRevAccelBeams.22.104003. URL: https://link.aps.org/doi/10.1103/PhysRevAccelBeams.22.104003 (cit. on p. 23).

[52] H. Burkhardt et al. "Improved TEAPOT Method and Tracking with Thick Quadrupoles for the LHC and its Upgrade". In: *Proc. IPAC'13* (Shanghai, China, May 2013). JACoW Publishing, Geneva, Switzerland, pp. 945–947. URL: https://jacow.org/IPAC2013/papers/MOPWO027.pdf (cit. on p. 23).

[53] F Schmidt. *SIXTRACK version 1.2: single particle tracking code treating transverse motion with synchrotron oscillations in a symplectic manner; user's reference manual*. Tech. rep. CERN-SL-94-56. CERN-SL-94-56-AP. Geneva: CERN, Sept. 1994. URL: https://cds.cern.ch/record/269474 (cit. on pp. 23, 40, 41).

[54] M. Böge and F. Schmidt. "Estimates for Long-term stability for the LHC". In: *AIP Conf. Proc.* 405 (1998), 201–210. 9 p. DOI: 10.1063/1.53486. URL: https://cds.cern.ch/record/327774 (cit. on p. 23).

[55] M. Benedikt. "LHC Pilot Bunches from the CERN PS Booster". In: *Proc. PAC'03* (Portland, OR, USA, May 2003). JACoW Publishing, Geneva, Switzerland. URL: https://jacow.org/p03/papers/TPPE004.pdf (cit. on p. 24).

[56] O. et al. Aberle. *High-Luminosity Large Hadron Collider (HL-LHC): Technical design report*. CERN Yellow Reports: Monographs. Geneva: CERN, 2020. DOI: 10.23731/CYRM-2020-0010. URL: https://cds.cern.ch/record/2749422 (cit. on p. 24).

[57] I.V. Pinayev et al. "Experiments with undulator radiation of a single electron". In: *Nuclear Instruments and Methods in Physics Research Section A: Accelerators, Spectrometers, Detectors and Associated Equipment* 341.1 (1994), pp. 17–20. ISSN: 0168-9002. DOI: https://doi.org/10.1016/0168-9002(94)90308-5. URL: https://www.sciencedirect.com/science/article/pii/0168900294903085 (cit. on p. 24).

[58] Roman Klein et al. "Operation of the Metrology Light Source as a primary radiation source standard". In: *Phys. Rev. ST Accel. Beams* 11 (11 Nov. 2008), p. 110701. DOI: 10.1103/PhysRevSTAB.11.110701. URL: https://link.aps.org/doi/10.1103/PhysRevSTAB.11.110701 (cit. on p. 24).

[59] I. Lobach et al. "Single electron in a storage ring: a probe into the fundamental properties of synchrotron radiation and a powerful diagnostic tool". In: *Journal of Instrumentation* 17.02 (Feb. 2022), P02014. DOI: 10.1088/1748-0221/17/02/p02014. URL: https://doi.org/10.1088/1748-0221/17/02/p02014 (cit. on p. 24).

[60] R. Tomás. "Adiabaticity of the ramping process of an ac dipole". In: *Phys. Rev. ST Accel. Beams* 8 (2 Feb. 2005), p. 024401. DOI: 10.1103/PhysRevSTAB.8.024401. URL: https://link.aps.org/doi/10.1103/PhysRevSTAB.8.024401 (cit. on p. 25).

[61] Werner Herr and B Muratori. "Concept of luminosity". In: (2006). DOI: 10.5170/CERN-2006-002.361. URL: https://cds.cern.ch/record/941318 (cit. on p. 26).

[62] Peter M McIntyre and Akhdiyor Sattarov. "On the Feasibility of a Tripler Upgrade for LHC". In: CARE-CONF-05-004-HHH. CARE-CONF-2005-004-HHH (2005). URL: https://cds.cern.ch/record/926779 (cit. on p. 31).

[63] R Assmann et al. *First Thoughts on a Higher-Energy LHC*. Tech. rep. CERN-ATS-2010-177. Geneva: CERN, Aug. 2010. URL: https://cds.cern.ch/record/1284326 (cit. on p. 31).

[64] E. Todesco, ed. *EuCARD-AccNet-EuroLumi Workshop : The High-Energy Large Hadron Collider: Villa Bighi, Malta, Republic of Malta 14 - 16 Oct 2010. Proceedings, EuCARD-AccNet-EuroLumi Workshop: The High-Energy Large Hadron Collider (HE-LHC10). Villa Bighi, Malta, Republic of Malta, October 14-16, 2010. EuCARD-AccNet-EuroLumi Workshop: The High-Energy Large Hadron Collider*. 29 lectures, 156 pages, published as CERN Yellow Report. CERN. Geneva: CERN, 2011. DOI: 10.5170/CERN-2011-003. URL: https://cds.cern.ch/record/1344820 (cit. on p. 31).

[65] Y.M. Nosochkov et al. "Optimized Arc Optics for the HE-LHC". In: *Proc. 9th International Particle Accelerator Conference (IPAC'18), Vancouver, BC, Canada, April 29-May 4, 2018* (Vancouver, BC, Canada). International Particle Accelerator Conference 9. https://doi.org/10.18429/JACoW-IPAC2018-MOPMF067. Geneva, Switzerland: JACoW Publishing, June 2018, pp. 277–280. ISBN: 978-3-95450-184-7. DOI: doi:10.18429/JACoW-IPAC2018-MOPMF067. URL: http://jacow.org/ipac2018/papers/mopmf067.pdf (cit. on p. 32).

[66] D. Zhou. "Arc Optics and Geometry". presented in the HE LHC review meeting, https://indico.cern.ch/event/674475 (cit. on p. 32).

[67] Oliver Sim Brüning et al. *LHC Design Report*. CERN Yellow Reports: Monographs. Geneva: CERN, 2004. DOI: 10.5170/CERN-2004-003-V-1. URL: https://cds.cern.ch/record/782076 (cit. on pp. 32, 33, 62, 66).

[68] Laurent Deniau; Hans Grote; Ghislain Roy; Frank Schmidt; Iselin F.C.; Herr W. and many other contributors. *MADX*. http://mad.web.cern.ch/mad/ (cit. on pp. 32, 40).

[69] Roderik Bruce et al. *Parameters for aperture calculations at injection for HL-LHC**. Tech. rep. CERN-ACC-2016-0328. *Research supported by EU FP7 HiLumi LHC Grant agreement 284404. Geneva: CERN, Feb. 2016. URL: https://cds.cern.ch/record/2237427 (cit. on p. 32).

[70] R. Kersevan. "Beam screen design & Vacuum constraints". presented in the HE LHC review meeting, https://indico.cern.ch/event/674475 (cit. on p. 32).

[71] I. Bellafont and R. Kersevan. "Studies on the beam induced effects in the FCC-hh". presented at the 3rd EuroCirCol Meeting,October 9th 2017, https://indico.cern.ch/event/655013 (cit. on p. 32).

[72] Wolfgang Bartmann et al. "LHC injection losses for tighter collimator settings in view of HE-LHC". In: (July 2020). URL: https://cds.cern.ch/record/2733016 (cit. on p. 33).

[73] L. van Riesen-Haupt et al. "Optics for RF Acceleration Section for the High Energy Large Hadron Collider". In: *Proc. 9th International Particle Accelerator Conference (IPAC'18), Vancouver, BC, Canada, April 29-May 4, 2018* (Vancouver, BC, Canada). International Particle Accelerator Conference 9. https://doi.org/10.18429/JACoW-IPAC2018-MOPMK001. Geneva, Switzerland: JACoW Publishing, June 2018, pp. 345–347. ISBN: 978-3-95450-184-7. DOI: doi:10.18429/JACoW-IPAC2018-MOPMK001. URL: http://jacow.org/ipac2018/papers/mopmk001.pdf (cit. on pp. 33, 35).

[74] L. van Riesen-Haupt et al. "Experimental Interaction Region Optics for the High Energy LHC". In: *Proc. 9th International Particle Accelerator Conference (IPAC'18), Vancouver, BC, Canada, April 29-May 4, 2018* (Vancouver, BC, Canada). International Particle Accelerator Conference 9. https://doi.org/10.18429/JACoW-IPAC2018-MOPMK006. Geneva, Switzerland: JACoW Publishing, June 2018, pp. 360–363. ISBN: 978-3-95450-184-7. DOI: doi:10.18429/JACoW-IPAC2018-MOPMK006. URL: http://jacow.org/ipac2018/papers/mopmk006.pdf (cit. on p. 33).

[75] "HE-LHC lattices V0.3". /afs/cern.ch/eng/lhc/optics/HELHC/V0.3 (cit. on p. 35).

[76] Jacqueline Keintzel. "Optics Design and Performance Aspects of the HE-LHC". Presented 21 Sep 2018. 2018. URL: https://cds.cern.ch/record/2640684 (cit. on p. 35).

[77] Jacqueline Keintzel. *Arc cell options for the HE-LHC*. Tech. rep. CERN-ACC-2018-0020. Geneva: CERN, June 2018. URL: https://cds.cern.ch/record/2624282 (cit. on p. 35).

[78] J. Keintzel. "HE-LHC Lattice Design and Optics Integration". presented at the FCC Week 2019, June 24-28, 2019, Brussels, https://indico.cern.ch/event/727555 (cit. on p. 35).

[79] Stephan Russenschuck. *Field computation for accelerator magnets: analytical and numerical methods for electromagnetic design and optimization*. Weinheim: Wiley, 2010. DOI: 10.1002/9783527635467. URL: https://cds.cern.ch/record/1221810 (cit. on p. 35).

[80] *CAS - CERN Accelerator School : Measurement and Alignment of Accelerator and Detector Magnets: Anacapri, Italy 11 - 17 Apr 1997. CAS - CERN Accelerator School : Measurement and Alignment of Accelerator and Detector Magnets*. CERN. Geneva: CERN, 1998. DOI: 10.5170/CERN-1998-005. URL: https://cds.cern.ch/record/318977 (cit. on p. 35).

[81] Rob Wolf. *Field Error Naming Convnetions for LHC Magnet*. Tech. rep. EDMS Doc. 90250. Geneva: CERN, Oct. 2001 (cit. on pp. 36, 41).

[82] O. Brüning and S. Fartoukh. *Field Quality Specification for the LHC Main Dipole Magnets*. Tech. rep. LHC-Project-Report-501. CERN-LHC-Project-Report-501. Geneva: CERN, Oct. 2001. URL: https://cds.cern.ch/record/522049 (cit. on pp. 37, 38, 62).

[83] S.I. Bermudez and D. Tommasini. "Field Quality Table Update for EuroCirCol 16 T design". presented in the 33rd HE-LHC design meeting, https://indico.cern.ch/event/761900/ (cit. on pp. 37, 62).

[84] Oliver Sim Brüning et al. *Dynamic Aperture Studies for the LHC Separation Dipoles*. Tech. rep. LHC-Project-Note-349. CERN-LHC-Project-Note-349. Geneva: CERN, June 2004. URL: https://cds.cern.ch/record/742967 (cit. on p. 38).

[85] E. H. Maclean et al. "First measurement and correction of nonlinear errors in the experimental insertions of the CERN Large Hadron Collider". In: *Phys. Rev. ST Accel. Beams* 18 (12 Dec. 2015), p. 121002. DOI: 10.1103/PhysRevSTAB.18.121002. URL: https://link.aps.org/doi/10.1103/PhysRevSTAB.18.121002 (cit. on pp. 38, 80, 97).

[86] Stéphane David Fartoukh. *Chromatic Coupling Induced by Skew Sextupolar Field Errors in the LHC Main Dipoles and its Correction*. Tech. rep. LHC-Project-Report-278. CERN-LHC-Project-Report-278. Geneva: CERN, Mar. 1999. URL: https://cds.cern.ch/record/383926 (cit. on p. 39).

[87] Stéphane David Fartoukh. *Second order chromaticity correction of LHC V 6.0 at collision*. Tech. rep. LHC-Project-Report-308. CERN-LHC-Project-Report-308. Geneva: CERN, Oct. 1999. URL: https://cds.cern.ch/record/403591 (cit. on p. 39).

[88] Stephane Fartoukh. "Impact and possible mitigation measures in case of failure of lattice sextupole and octupole circuits in Run 3". In: (Oct. 2020). URL: https://cds.cern.ch/record/2742896 (cit. on p. 39).

[89] S. Fartoukh and M. Giovannozzi. "Dynamic aperture computation for the as-built CERN Large Hadron Collider and impact of main dipoles sorting". In: *Nuclear Instruments and Methods in Physics Research Section A: Accelerators, Spectrometers, Detectors and Associated Equipment* 671 (2012), pp. 10 – 23. ISSN: 0168-9002. DOI: https://doi.org/10.1016/j.nima.2011.12.052. URL: http://www.sciencedirect.com/science/article/pii/S0168900211022613 (cit. on pp. 39, 51).

[90] Léon van Riesen-Haupt et al. "Developments in the experimental interaction regions of the High Energy LHC". In: (2019), MOPMP039. 4 p. DOI: 10.18429/JACoW-IPAC2019-MOPMP039. URL: https://cds.cern.ch/record/2695239 (cit. on p. 39).

[91] M Hayes and F Schmidt. *Run Environment for SixTrack*. Tech. rep. LHC-PROJECT-NOTE-300. Geneva: CERN, July 2002. URL: https://cds.cern.ch/record/691785 (cit. on p. 40).

[92] E McIntosh and R De Maria. "The SixDesk Run Environment for SixTrack". In: (Nov. 2012). URL: https://cds.cern.ch/record/1491626 (cit. on p. 40).

[93] "SixDesk: SixTrack running enviroment". https://github.com/SixTrack/SixDesk (cit. on p. 40).

[94] G Ripken and F Schmidt. *A symplectic six-dimensional thin-lens formalism for tracking*. Tech. rep. CERN-SL-95-12. CERN-SL-95-12-AP. DESY-95-063. Geneva: CERN, Apr. 1995. URL: https://cds.cern.ch/record/281283 (cit. on p. 40).

[95] *SixTrack*. http://sixtrack.web.cern.ch/SixTrack/, https://github.com/SixTrack/SixTrack.git (cit. on pp. 40, 74).

[96] F Schmidt, F Willeke, and Frank Zimmermann. "Comparison of methods to determine long-term stability in proton storage rings. Comparison of methods to prove long term stability in proton storage rings". In: *Part. Accel.* 35.CERN-SL-91-14-AP. DESY-HERA-91-07 (Apr. 1991), 249–256. 9 p. URL: https://cds.cern.ch/record/218662 (cit. on p. 40).

[97] D Jacquet. "Injection". In: (2016), 49–52. 4 p. URL: https://cds.cern.ch/record/2294514 (cit. on p. 40).

[98] M Hayes, E McIntosh, and F Schmidt. *The Influence of Computer Errors on Dynamic Aperture Results Using SixTrack*. Tech. rep. LHC-PROJECT-NOTE-309. Geneva: CERN, Jan. 2003. URL: https://cds.cern.ch/record/692073 (cit. on p. 40).

[99] Massimo Giovannozzi and Eric McIntosh. "Parameter scans and accuracy estimates of the dynamical aperture of the CERN LHC". In: LHC-PROJECT-Report-925. CERN-LHC-Project-Report-925 (July 2006). revised version submitted on 2006-09-15 14:42:31, 4 p. URL: https://cds.cern.ch/record/972343 (cit. on p. 40).

[100] "SixDeskDB". https://github.com/SixTrack/SixDeskDB (cit. on p. 41).

[101] Jean-Pierre Koutchouk. "The LHC dynamic aperture". In: LHC-Project-Report-296. CERN-LHC-Project-Report-296 (Apr. 1999). revised version submitted on 2004-08-20 17:40:29, 6 p. URL: https://cds.cern.ch/record/386687 (cit. on p. 41).

[102] E. H. Maclean et al. "Measurement of nonlinear observables in the Large Hadron Collider using kicked beams". In: *Phys. Rev. ST Accel. Beams* 17 (8 Aug. 2014), p. 081002. DOI: 10.1103/PhysRevSTAB.17.081002. URL: https://link.aps.org/doi/10.1103/PhysRevSTAB.17.081002 (cit. on pp. 41, 72).

[103] E. H. Maclean, M. Giovannozzi, and R. B. Appleby. "Innovative method to measure the extent of the stable phase-space region of proton synchrotrons". In: *Phys. Rev. Accel. Beams* 22 (3 Mar. 2019), p. 034002. DOI: 10.1103/PhysRevAccelBeams.22.034002. URL: https://link.aps.org/doi/10.1103/PhysRevAccelBeams.22.034002 (cit. on p. 41).

[104] K. Paraschou. "Beam Lifetime simulations". presented at the 1st Non-Linear Beam Dynamics WG Meeting https://indico.cern.ch/event/860386/ (cit. on p. 41).

[105] Mattias Fjellstrom. "Particle Tracking in Circular Accelerators Using the Exact Hamiltonian in SixTrack". Presented 13 Dec 2013. Dec. 2013. URL: https://cds.cern.ch/record/1642385 (cit. on p. 41).

[106] Stéphane David Fartoukh. *LHC Installation Scenarios and Dynamic Aperture*. Tech. rep. LHC-Project-Report-449. CERN-LHC-Project-Report-449. Geneva: CERN, Dec. 2000. URL: https://cds.cern.ch/record/481065 (cit. on pp. 44, 61).

[107] S.I. Bermudez et al. "Field Quality Table Update for EuroCirCol 16 T designs". presented in the 31st HE-LHC design meeting, https://indico.cern.ch/event/739469/ (cit. on p. 44).

[108] Armando Bazzani et al. *A normal form approach to the theory of nonlinear betatronic motion*. CERN Yellow Reports: Monographs. Geneva: CERN, 1994. DOI: 10.5170/CERN-1994-002. URL: https://cds.cern.ch/record/262179 (cit. on pp. 45, 47).

[109] J. Keintzel. "Optics Integration". presented at the FCC Week 2018, April 8-13, 2018, Amsterdam, https://indico.cern.ch/event/656491 (cit. on p. 49).

[110] S. Fartoukh. "Installation Strategy for the Main Dipoles". In: *Proc. 9th European Particle Accelerator Conf. (EPAC'04), Lucerne, Switzerland, Jul. 2004*. 2004, pp. 176–178 (cit. on pp. 51, 54, 62).

[111] Ezio Todesco et al. "Steering field quality in the main dipole magnets of the Large Hadron Collider". In: *IEEE Trans. Appl. Supercond.* 14.LHC-Project-Report-704. CERN-LHC-Project-Report-704. 2 (Apr. 2004), 177–180. 5 p. DOI: 10.1109/TASC.2004.829039. URL: https://cds.cern.ch/record/732306 (cit. on p. 52).

[112] Walter Scandale et al. "Controlling Field Quality in Magnet Production". In: LHC-Project-Report-659. CERN-LHC-Project-Report-659 (July 2003), 4 p. URL: https://cds.cern.ch/record/630340 (cit. on p. 52).

[113] P. Hagen et al. "WISE: An Adaptative Simulation of the LHC Optics". In: LHC-PROJECT-Report-971. CERN-LHC-Project-Report-971 (Aug. 2006), 4 p. URL: https://cds.cern.ch/record/977794 (cit. on pp. 55, 74).

[114] J. MacQueen. "Some methods for classification and analysis of multivariate observations". In: *Proceedings of the Fifth Berkeley Symposium on Mathematical Statistics and Probability, Volume 1: Statistics*. Berkeley, Calif.: University of California Press, 1967, pp. 281–297. URL: https://projecteuclid.org/euclid.bsmsp/1200512992 (cit. on p. 54).

[115] *Equal Groups K-Means Clustering*. https://github.com/ndanielsen/Same-Size-K-Means (cit. on p. 55).

[116] N. J. Sammut, J. Micallef, and L. Bottura. "The field description for the Large Hadron Collider". Presented on 12 Oct 2006. PhD thesis. 2006. URL: http://cds.cern.ch/record/1007196 (cit. on p. 62).

[117] S. Izquierdo Bermudez, L. Bottura, and E. Todesco. "Persistent-Current Magnetization Effects in High-Field Superconducting Accelerator Magnets". In: *IEEE Transactions on Applied Superconductivity* 26.4 (June 2016), pp. 1–5. ISSN: 1051-8223. DOI: 10.1109/TASC.2016.2519006 (cit. on p. 62).

[118] V. V. Kashikhin and A. V. Zlobin. "Persistent Current Effect in 15-16 T Nb_3Sn Accelerator Dipoles and its Correction". In: *Proceedings, 2nd North American Particle Accelerator Conference (NAPAC2016): Chicago, Illinois, USA, October 9-14, 2016*. 2017, THA1CO04. DOI: 10.18429/JACoW-NAPAC2016-THA1CO04. URL: http://lss.fnal.gov/archive/2016/conf/fermilab-conf-16-519-td.pdf (cit. on p. 62).

[119] P. Hagen et al. *WISE: A Simulation of the LHC Optics including Magnet Geometrical Data*. Tech. rep. CERN-LHC-PROJECT-Report-1123. Aug. 2008. URL: http://cds.cern.ch/record/1123714 (cit. on p. 62).

[120] G. Ambrosio et al. "A scaling law for the snapback in Superconducting accelerator magnets". In: *IEEE Transactions on Applied Superconductivity* 15.2 (June 2005), pp. 1217–1220. ISSN: 1051-8223. DOI: 10.1109/TASC.2005.849535 (cit. on p. 62).

[121] R Tomas. "Optimizing the global coupling knobs for the LHC". In: (Feb. 2012). URL: https://cds.cern.ch/record/1422434 (cit. on p. 63).

[122] T.H.B. Persson et al. "LHC optics corrections in Run 2". presented at the 9th LHC Operations Evian Workshop (cit. on p. 65).

[123] Joschua Werner Dilly et al. "Report and Analysis from LHC MD 3311: Amplitude detuning at end-of-squeeze". In: (Mar. 2019). URL: https://cds.cern.ch/record/2692810 (cit. on pp. 65, 66).

[124] M Gasior and R Jones. *The principle and first results of betatron tune measurement by direct diode detection*. Tech. rep. LHC-Project-Report-853. CERN-LHC-Project-Report-853. revised version submitted on 2005-09-16 09:23:15. Geneva: CERN, Aug. 2005. URL: https://cds.cern.ch/record/883298 (cit. on p. 65).

[125] S. White, E. Maclean, and R. Tomás. "Direct amplitude detuning measurement with ac dipole". In: *Phys. Rev. ST Accel. Beams* 16 (7 July 2013), p. 071002. DOI: 10.1103/PhysRevSTAB.16.071002. URL: https://link.aps.org/doi/10.1103/PhysRevSTAB.16.071002 (cit. on pp. 68, 71).

[126] F. S. Carlier et al. "First experimental demonstration of forced dynamic aperture measurements with LHC ac dipoles". In: *Phys. Rev. Accel. Beams* 22 (3 Mar. 2019), p. 031002. DOI: 10.1103/PhysRevAccelBeams.22.031002. URL: https://link.aps.org/doi/10.1103/PhysRevAccelBeams.22.031002 (cit. on pp. 66, 71).

[127] E. H. Maclean. "Modelling and correction of the non-linear transverse dynamics of the LHC from beam-based measurements". PhD thesis. 2014. URL: http://cds.cern.ch/record/1951379 (cit. on pp. 71, 72).

[128] E. H. Maclean. "Optics measurements and misalignment of the b4-b5-spool pieces". presented in the FiDel meeting, https://indico.cern.ch/event/812944/ (cit. on p. 75).

[129] Gilbert Guignard. *The general theory of all sum and difference resonances in a three-dimensional magnetic field in a synchrotron*. CERN Yellow Reports: Monographs. Geneva: CERN, 1976. DOI: 10.5170/CERN-1976-006. URL: https://cds.cern.ch/record/185921 (cit. on p. 79).

[130] R. Tomás, T. H. B. Persson, and E. H. Maclean. "Amplitude dependent closest tune approach". In: *Phys. Rev. Accel. Beams* 19 (7 July 2016), p. 071003. DOI: 10.1103/PhysRevAccelBeams.19.071003. URL: https://link.aps.org/doi/10.1103/PhysRevAccelBeams.19.071003 (cit. on p. 79).

[131] E.H. Maclean, T. Persson, and R. Tomás. "Amplitude Dependent Closest Tune Approach Generated by Normal and Skew Octupoles". In: *Proc. of International Particle Accelerator Conference (IPAC'17), Copenhagen, Denmark, 14-19 May, 2017* (Copenhagen, Denmark). International Particle Accelerator Conference 8. https://doi.org/10.18429/JACoW-IPAC2017-WEPIK091. Geneva, Switzerland: JACoW, May 2017, pp. 3147–3150. ISBN: 978-3-95450-182-3. DOI: https://doi.org/10.18429/JACoW-IPAC2017-WEPIK091. URL: http://jacow.org/ipac2017/papers/wepik091.pdf (cit. on p. 79).

[132] T. Persson R. Tomás. "Improved control of the betatron coupling in the Large Hadron Collider". In: *Phys. Rev. ST Accel. Beams* 17 (5 May 2014), p. 051004. DOI: 10.1103/PhysRevSTAB.17.051004. URL: https://link.aps.org/doi/10.1103/PhysRevSTAB.17.051004 (cit. on p. 80).

[133] Rogelio Tomás et al. "Review of linear optics measurement and correction for charged particle accelerators". In: *Phys. Rev. Accel. Beams* 20 (5 May 2017),

p. 054801. DOI: 10.1103/PhysRevAccelBeams.20.054801. URL: https://link.aps.org/doi/10.1103/PhysRevAccelBeams.20.054801 (cit. on p. 80).

[134] J.M. Jowett et al. "The 2018 Heavy-Ion Run of the LHC". In: *Proc. 10th International Partile Accelerator Conference (IPAC'19), Melbourne, Australia, 19-24 May 2019* (Melbourne, Australia). International Partile Accelerator Conference 10. https://doi.org/10.18429/JACoW-IPAC2019-WEYYPLM2. Geneva, Switzerland: JACoW Publishing, June 2019, pp. 2258–2261. ISBN: 978-3-95450-208-0. DOI: doi:10.18429/JACoW-IPAC2019-WEYYPLM2. URL: http://jacow.org/ipac2019/papers/weyyplm2.pdf (cit. on pp. 80, 88).

[135] R. Tomás et al. "LHC Run 2 Optics Commissioning Experience in View of HL-LHC". In: *Proc. 10th International Partile Accelerator Conference (IPAC'19), Melbourne, Australia, 19-24 May 2019* (Melbourne, Australia). International Partile Accelerator Conference 10. https://doi.org/10.18429/JACoW-IPAC2019-MOPMP033. Geneva, Switzerland: JACoW Publishing, June 2019, pp. 508–511. ISBN: 978-3-95450-208-0. DOI: doi:10.18429/JACoW-IPAC2019-MOPMP033. URL: http://jacow.org/ipac2019/papers/mopmp033.pdf (cit. on pp. 80, 88).

[136] F. Pilat et al. "Beam-Based Non-Linear Optics Corrections in Colliders". In: *Proceedings of the 2005 Particle Accelerator Conference*. May 2005, pp. 601–605. DOI: 10.1109/PAC.2005.1590503 (cit. on pp. 80, 97).

[137] E.H. Maclean et al. "Effect of Linear Coupling on Nonlinear Observables at the LHC". In: *Proc. of International Particle Accelerator Conference (IPAC'17), Copenhagen, Denmark, 14-19 May, 2017* (Copenhagen, Denmark). International Particle Accelerator Conference 8. https://doi.org/10.18429/JACoW-IPAC2017-WEPIK092. Geneva, Switzerland: JACoW, May 2017, pp. 3151–3154. ISBN: 978-3-95450-182-3. DOI: https://doi.org/10.18429/JACoW-IPAC2017-WEPIK092. URL: http://jacow.org/ipac2017/papers/wepik092.pdf (cit. on pp. 80, 93).

[138] L. R. Carver et al. "Transverse beam instabilities in the presence of linear coupling in the Large Hadron Collider". In: *Phys. Rev. Accel. Beams* 21 (4 Apr. 2018), p. 044401. DOI: 10.1103/PhysRevAccelBeams.21.044401. URL: https://link.aps.org/doi/10.1103/PhysRevAccelBeams.21.044401 (cit. on pp. 80, 84, 91).

[139] E. H. Maclean et al. "New approach to LHC optics commissioning for the nonlinear era". In: *Phys. Rev. Accel. Beams* 22 (6 June 2019), p. 061004. DOI: 10.1103/PhysRevAccelBeams.22.061004. URL: https://link.aps.org/doi/10.1103/PhysRevAccelBeams.22.061004 (cit. on p. 80).

[140] A. Franchi et al. "First simultaneous measurement of sextupolar and octupolar resonance driving terms in a circular accelerator from turn-by-turn beam position monitor data". In: *Phys. Rev. ST Accel. Beams* 17.7 (2014), p. 074001. DOI: 10.1103/PhysRevSTAB.17.074001. arXiv: 1402.1461 [physics.acc-ph] (cit. on pp. 80, 82–85, 94).

[141] A. Franchi, E. Métral, and R. Tomás. "Emittance sharing and exchange driven by linear betatron coupling in circular accelerators". In: *Phys. Rev. ST Accel. Beams* 10 (6 June 2007), p. 064003. DOI: 10.1103/PhysRevSTAB.10.064003. URL: https://link.aps.org/doi/10.1103/PhysRevSTAB.10.064003 (cit. on pp. 80, 83, 89).

[142] F Bartolini R Schmidt. "Normal form via tracking or beam data". In: *Part. Accel.* 59.LHC-Project-Report-132. CERN-LHC-Project-Report-132 (Aug. 1997), 93–106. 10 p. URL: http://cds.cern.ch/record/333077 (cit. on pp. 82, 97).

[143] R. Calaga, R. Tomás, and A. Franchi. "Betatron coupling: Merging Hamiltonian and matrix approaches". In: *Phys. Rev. ST Accel. Beams* 8 (3 Mar. 2005), p. 034001. DOI: 10.1103/PhysRevSTAB.8.034001. URL: https://link.aps.org/doi/10.1103/PhysRevSTAB.8.034001 (cit. on p. 84).

[144] P. Thrane et al. "Measuring β^* in SuperKEKB with K modulation". In: *Phys. Rev. Accel. Beams* 23 (1 Jan. 2020), p. 012803. DOI: 10.1103/PhysRevAccelBeams.23.012803. URL: https://link.aps.org/doi/10.1103/PhysRevAccelBeams.23.012803 (cit. on p. 86).

[145] Tobias Hakan Bjorn Persson et al. "MD4944: Local linear coupling measurement at the IPs". In: (Jan. 2020). URL: http://cds.cern.ch/record/2710101 (cit. on p. 88).

[146] T. H. B. Persson. *Post-mortem analysis of IR2 coupling issue*. 372nd LHC machine committee meeting. 2019 (cit. on p. 88).

[147] A. Franchi et al. "Vertical emittance reduction and preservation in electron storage rings via resonance driving terms correction". In: *Phys. Rev. ST Accel. Beams* 14 (3 Mar. 2011), p. 034002. DOI: 10.1103/PhysRevSTAB.14.034002. URL: https://link.aps.org/doi/10.1103/PhysRevSTAB.14.034002 (cit. on pp. 88, 113).

[148] Y Cai. "Luminosity of Asymmetric e^+e^- Collider with Coupling Lattices". In: hep-ph/0007052. SLAC-PUB-8479 (July 2000). URL: http://cds.cern.ch/record/446251 (cit. on p. 89).

[149] J. Bengtsson. "The Sextupole Scheme for the Swiss Light Source (SLS): An Analytic Approach". In: *SLS Note 9/97* (1997). URL: https://ados.web.psi.ch/slsnotes/sls0997.pdf (cit. on p. 97).

[150] R Tomas-García. "Direct Measurement of Resonance Driving Terms in the Super Proton Synchrotron (SPS) of CERN using Beam Position Monitors". Presented on 30 Mar 2003. 2003. URL: https://cds.cern.ch/record/615164 (cit. on pp. 98, 114).

[151] Stephen D. Webb et al. *Chromatic and Dispersive Effects in Nonlinear Integrable Optics*. 2015. arXiv: 1504.05981 [physics.acc-ph] (cit. on p. 100).

[152] S. Nagaitsev, A. Valishev, and V. Danilov. "Nonlinear Optics as a Path to High-Intensity Circular Machines". In: *Proc. 46th ICFA Advanced Beam Dynamics Workshop on High-Intensity and High-Brightness Hadron Beams (HB10), Morschach, Switzerland, Sep.-Oct. 2010*, pp. 676–680 (cit. on p. 100).

[153] S. A. Antipov et al. "Stripline Kicker for Integrable Optics Test Accelerator". In: *Proc. 6th International Particle Accelerator Conference (IPAC'15), Richmond, VA, USA, May 3-8, 2015* (Richmond, VA, USA). International Particle Accelerator Conference 6. https://doi.org/10.18429/JACoW-IPAC2015-WEPTY051. Geneva, Switzerland: JACoW, June 2015, pp. 3390–3392. ISBN: 978-3-95450-168-7. DOI: https://doi.org/10.18429/JACoW-IPAC2015-WEPTY051. URL: http://jacow.org/ipac2015/papers/wepty051.pdf (cit. on p. 101).

[154] A. Franchi et al. "First simultaneous measurement of sextupolar and octupolar resonance driving terms in a circular accelerator from turn-by-turn beam position monitor data". In: *Phys. Rev. ST Accel. Beams* 17 (7 July 2014), p. 074001. DOI: 10.1103/PhysRevSTAB.17.074001. URL: https://link.aps.org/doi/10.1103/PhysRevSTAB.17.074001 (cit. on pp. 102, 112).

[155] R.E. Meller et al. "Decoherence of Kicked Beams". In: (May 1987) (cit. on p. 102).

[156] *OMC3 Accelerator Optics Analysis Suite*. https://github.com/pylhc/omc3 (cit. on p. 104).

[157] *Beta-Beat Source*. https://github.com/pylhc/Beta-Beat.src (cit. on p. 104).
[158] R. Calaga and R. Tomás. "Statistical analysis of RHIC beam position monitors performance". In: *Phys. Rev. ST Accel. Beams* 7 (4 Apr. 2004), p. 042801. DOI: 10.1103/PhysRevSTAB.7.042801. URL: https://link.aps.org/doi/10.1103/PhysRevSTAB.7.042801 (cit. on p. 104).
[159] E. Fol et al. "Detection of faulty beam position monitors using unsupervised learning". In: *Phys. Rev. Accel. Beams* 23 (10 Oct. 2020), p. 102805. DOI: 10.1103/PhysRevAccelBeams.23.102805. URL: https://link.aps.org/doi/10.1103/PhysRevAccelBeams.23.102805 (cit. on p. 104).
[160] A. Valishev et al. "Beam Physics of Integrable Optics Test Accelerator at Fermilab". In: *Proc. 3rd Int. Particle Accelerator Conf. (IPAC'12), New Orleans, LA, USA, May 2012*, pp. 1371–1373 (cit. on p. 104).
[161] A. L. Romanov. "Testing of Advanced Technique for Linear Lattice and Closed Orbit Correction by Modeling Its Application for IOTA Ring at Fermilab". In: *Proc. North American Particle Accelerator Conf. (NAPAC'16), Chicago, IL, USA, Oct. 2016*, pp. 1155–1157 (cit. on p. 104).
[162] A. Valishev on behalf of the IOTA collaboration. "Fighting nonlinear dynamics with nonlinear elements". In: *Mitigation Approaches for Storage Rings and Synchrotrons, ARIES-APEC workshop, GSI, June. 2020*. https://indico.gsi.de/event/10458/contributions/45017/attachments/31685/40147/2020-06-22_ARIES_APEC_Workshop.pdf (cit. on pp. 104, 105).
[163] A. Langner and R. Tomás. "Optics measurement algorithms and error analysis for the proton energy frontier". In: *Phys. Rev. ST Accel. Beams* 18 (3 Mar. 2015), p. 031002. DOI: 10.1103/PhysRevSTAB.18.031002. URL: https://link.aps.org/doi/10.1103/PhysRevSTAB.18.031002 (cit. on p. 104).
[164] A. Wegscheider et al. "Analytical *N* beam position monitor method". In: *Phys. Rev. Accel. Beams* 20 (11 Nov. 2017), p. 111002. DOI: 10.1103/PhysRevAccelBeams.20.111002. URL: https://link.aps.org/doi/10.1103/PhysRevAccelBeams.20.111002 (cit. on p. 104).
[165] A. García-Tabarés Valdivieso and R. Tomás. "Optics-measurement-based beam position monitor calibrations in the LHC insertion regions". In: *Phys. Rev. Accel. Beams* 23 (4 Apr. 2020), p. 042801. DOI: 10.1103/PhysRevAccelBeams.23.042801. URL: https://link.aps.org/doi/10.1103/PhysRevAccelBeams.23.042801 (cit. on p. 106).
[166] M. Hofer and R. Tomás. "Effect of local linear coupling on linear and nonlinear observables in circular accelerators". In: *Phys. Rev. Accel. Beams* 23 (9 Sept. 2020), p. 094001. DOI: 10.1103/PhysRevAccelBeams.23.094001. URL: https://link.aps.org/doi/10.1103/PhysRevAccelBeams.23.094001 (cit. on p. 113).

Acknowledgements

For me, starting a PhD was a journey into the unknown, and with many difficult and challenging problems to understand and overcome, having people around that I can rely on and their help has been invaluable to me. Here, I now want to take the time to acknowledge and thank the people around me for their support along the way.

First and foremost, I want to thank my supervisor at CERN, Dr. Rogelio Tomás García. Your infectious passion for accelerators, the seemingly never ending cheerfulness, and incredibly deep understanding of beam optics have always been a source of great inspiration. However confusing or disheartening the initial results may look, after every meeting we've had I came out with a new spark of motivation and countless new ideas. Thank you for taking me up as a student with no prior knowledge of accelerators, for giving me the chance to work on a variety of different interesting projects, and for your supervision and guidance through the last few years.

I would also like to express my gratitude to my university supervisor Dr. Michael Benedikt. Thank you for accepting me as your student, for enabling me to continue as a Doctoral Student at CERN, and for the continued support of my studies. I've always considered myself lucky to receive such great support, that amongst others allowed me to work at CERN, attend numerous conferences and schools, as well as to travel to Fermilab for conducting experiments, all of which I consider having a tremendous impact on my career.

I also want to thank the many members of the FCC collaboration. Special thanks go to Frank Zimmermann and Daniel Schulte, who have shown interest in my work early on, always had an open door for discussions, and with their keen observations having often left me wondering if I understood anything up to this point, only to come out with a deeper understanding of the matter afterwards. I would also like to acknowledge the fruitful and interesting discussions with Daniel Schörling and Susanna Izquierdo Bermudez from the Magnet Design Group. Moreover, I want to thank Antoine Chancé, Barbara Dalena, and Roman Martin who were a great help when starting in the field of accelerator optics and working on the FCC-hh. I also want to thank Léon van Riesen-Haupt, who I've gotten to work with on all the machines in the FCC-study and who has also become a good friend. That said, I will never not be mad about you sending my office utensils on an unscheduled journey to faraway control rooms.

I also want to thank the members of the OMC-team, for welcoming me in the team, everyone taking their time to explain how things work, and making night shifts in the CERN Control Room always a pleasant experience. In particular, I want to thank Ewen Hamish Maclean and Tobias Persson for their help with different studies and many enlightening discussions, some of those over a few beers. I would also like to thank Lukas Malina for the countless discussions on code development and for sharing his understanding of the analysis of measurement data. Joschua Dilly has not only been a great colleague and an enormous help when developing the analysis for different experiments but has also been a great friend outside of work. While having to fix either bicycles or codes is not something I particularly look forward to, it is more bearable to have an always helpful friend around. Luckily for both of us, we seem to be better at the latter than the former.

I also want to express my gratitude to the members of the IOTA collaboration, in particular Alexander Valishev, Giulio Stancari, Alexander Romanov, Nikita Kuklev, and Sebastian Szuskowstki. Thank you for hosting me at Fermilab, for taking the time to explain the ins and outs of the IOTA ring and infrastructure, and for providing a more holistic view of how accelerators work.

I also want to thank my office mates over the years, Matthew Crouch, Elena Fol, Stefania Papadopoulou, and Andreas Wegscheider, for enduring my at times quite energetic treatment of the keyboard, the countless coffee breaks we shared filled with jokes and in general for creating a fun environment to work in every day. I also owe my gratitude to many members of the CERN Accelerator and Beam Physics group, with everyone always happy to help and provide helpful suggestions.

I would also like to take the time to thank the people in my life outside work, be they in the Geneva area, back home in Austria, or on a different continent altogether. To my friends, Early, Christian, Laila, Benni, Markus, Fabien, and many others, thank you for your friendship, for always having an open ear and providing an outside view to everyday problems, and for making the effort to stay in touch even when due to distance and schedule this is often not easy.

Lastly, I want to thank my family and especially my parents Christa and Wolfgang for their never-ending support and their encouragement to follow my passion for science from an early age.

Thank you.